



TECHNISCHE
UNIVERSITÄT
WIEN

DISSERTATION

**A hybrid hydrolytic hydrogen storage system based on
catalyst sputter-coated hollow glass microspheres**

Ausgeführt zum Zwecke der Erlangung des akademischen Grades eines Doktors der
technischen Wissenschaften unter der Leitung von

Ao.Univ.Prof. Dipl.-Ing. Dr.techn. Christoph Eisenmenger-Sittner

E138

Institut für Festkörperphysik

eingereicht an der Technischen Universität Wien

Fakultät für Physik

von

Dipl.-Ing. Gerwin Holger Stefan Schmid

e0104646

Obere Donaustraße 73 1/1/3, 1020 Wien

Erstbegutachter

Ao.Univ.Prof. Dipl.-Ing. Dr.techn.
Christoph Eisenmenger-Sittner

Zweitbegutachter

Univ.Prof. Mag.rer.nat. Dr.rer.nat.
Günther Rupprechter

Author

Dipl.-Ing.
Gerwin Schmid

Ort, Datum, Unterschrift

Ort, Datum, Unterschrift

Ort, Datum, Unterschrift

Deutsche Kurzfassung

Hohle, wasserstoffbeladene Mikrogaskugeln kombiniert mit Hydriden (z.B. NaBH_4) bergen das Potential zur Wasserstoffspeicherung in praktikablem Ausmaß, wobei theoretisch Speicherdichten von 8-20 Gewichtsprozent oder $30\text{-}50\text{ kg/m}^3$ erreicht werden können. Zur Speicherung werden die etwa $20\text{ }\mu\text{m}$ großen Mikrogaskugeln mit 70 MPa Wasserstoff bedrückt und aufgeheizt, sodass der Wasserstoff ins Innere der Kugeln diffundieren kann. Werden die Kugeln wieder abgekühlt so kann der nun eingeschlossene Wasserstoff bei Raumtemperatur ohne größere Sicherheitsvorkehrungen aufbewahrt werden. Um den Wasserstoff wieder freizusetzen, muss erneut Wärme zur Erreichung von etwa $250\text{ }^\circ\text{C}$ appliziert werden. Diese Wärme kann durch eine exotherme chemische Reaktion bereitgestellt werden, in diesem Fall die Hydrolyse von Natriumborhydrid, welche außerdem noch weiteren Wasserstoff als Nebenprodukt freisetzt. Diese chemische Reaktion erfordert jedoch einen Katalysator, der auf die Kugeln aufgebracht werden muss.

Um die Kugeln gleichmäßig mit dem gewünschten Katalysator zu beschichten, wurde eine Anlage mit speziell geformter Beschichtungsschale, in welcher sich die zu beschichtenden Kugeln befinden, entwickelt. Diese Schale ist gekippt (vgl. Betonmischer) und rotiert unterhalb der Beschichtungsquelle, in diesem Fall eine Sputterquelle. Wie sich allerdings gezeigt hat, neigen die, auf diese Art beschichteten Kugeln, dazu zu verklumpen oder haften an der inneren Oberfläche der Schale an. Dies tritt verstärkt beim Aufbringen metallischer Schichten auf, aber kaum bei Oxidschichten. Das Verklumpen verhindert eine gleichmäßige Beschichtung, da nicht alle Kugeln dem Sputterstrahl ausgesetzt werden. Um dies zu lösen wurde ein Rüttelmechanismus entwickelt, der dazu führt, dass die Klumpen immer wieder aufbrechen und auch das am Schalenrand haftende Material immer wieder abgelöst wird. Auf diese Art konnten die Mikrogaskugeln gleichmäßig mit einem Katalysator beschichtet werden.

Die Katalysatoreffektivität hängt nicht nur von der Struktur des Katalysators ab, sondern auch vom Trägermaterial, auf das der Katalysator aufgebracht wird. Für die vorliegende Anwendung wurde Anatas, eine spezielle Phase des Titandioxids, als sehr geeignet identifiziert, weshalb derartige Schichten auf planem Glassubstrat und auf hohlen Mikrogaskugeln untersucht wurden. Die TiO_2 -Schichten wurden reaktiv mit einer bipolaren Gleichstromspannungsversorgung bei unterschiedlichen Argon- und Sauerstoff-Drücken und verschiedenen Pulsfrequenzen abgeschieden. Es konnten Anatas-Schichten auf planem Substraten abgeschieden werden, jedoch konnten auf Mikrogaskugeln auf Grund einer geringen Schichtdicke keine TiO_2 -schichten in Anatas-Phase mittels Röntgendiffraktometrie nachgewiesen werden.

Die Katalysator-Versuche wurden mit Ruthenium-, Platin- und Titandioxidschichten beziehungsweise Kombinationen dieser Materialien durchgeführt. Um den Katalysator zu charakterisieren wurden die Menge an freigesetztem Wasserstoff aus der hydrolytischen Reaktion und die dabei entstehende Temperatur gemessen. Ruthenium-Schichten erzielten dabei eine wesentlich höhere Wasserstoffausbeute als Platin, zeigten jedoch eine problematisch geringe Haftung an den Glaskugeln. Die Haftungsproblematik des Katalysators konnte mittels eines Mehrschichtsystems und auch durch gleichzeitiges Abscheiden von TiO_2 und Ruthenium behoben werden. Da die Effizienz aller getesteten Katalysatoren nach einmaligem Gebrauch sehr stark abnahm, der Katalysator also deaktiviert wurde, musste eine Methode entwickelt werden den Katalysator zu reaktivieren. Eine wiederholte Reaktivierung gelang durch die Behandlung der beschichteten Mikroglaskugeln mit Salzsäure.

Zusammenfassend ist ein erster Schritt zur Realisierung eines hybriden Hydrid-Glaskugel-Wasserstoffspeichersystems gelungen. Ein nächster Schritt wären Versuche mit wasserstoffbeladenen Mikroglaskugeln.

Abstract

Hydrogen pressurized hollow glass micro spheres in combination with NaBH₄ (soda borohydride) hydrolysis bear the potential of storing hydrogen in feasible amounts and could reach storage densities up to 8-20 wt% or 30-50 kg/m³ (theoretically). Therefore, the approximately 20 µm diameter spheres are heated up and pressurized with hydrogen at 70 MPa, so hydrogen diffuses into the spheres. After the spheres are cooled down, hydrogen can be stored at room temperature without excessive security measures. To release the trapped hydrogen, heat has to be applied again to reach the temperatures of about 250 °C. To reach this temperature an exothermal chemical reaction can be used, in this case a NaBH₄-water reaction, which produces hydrogen as a most welcome by-product. This chemical reaction has to be initialized by a catalyst deployed on the hollow glass microspheres.

To realise uniform coatings on the microspheres, an apparatus was designed with a special shaped coating vessel rotating beneath a deposition source, i.e. magnetron sputter source. However, in vacuum the particles tend to adhere to one another and to the surfaces of the containing vessel as coating proceeds, especially when depositing pure metal films. This prohibits most particles from being coated, since they are not exposed to the sputtering beam. To overcome these problems, a concussion mechanism was developed to break up the particle clusters. It will be shown that powder substrates of different kinds can be coated successfully.

Catalyst performance not only depends on the structure of the catalyst, but also on the support material of the catalyst. For the present application anatase phase TiO₂ was chosen as support, which is why these films have been studied on plane glass substrate and hollow glass microspheres. The TiO₂ films were reactively deposited with a bipolar pulsed DC power supply at different deposition pressures (Ar, O₂), reverse times and frequencies. It will be shown that even though anatase films could be deposited on plane substrates, it was not possible to detect anatase films on hollow glass microspheres by X-ray diffraction.

In addition, results of the catalytic experiments of Ru, Pt, TiO₂ films and combinations thereof will be presented. To characterise the catalyst the amount of released hydrogen and the reaction temperature were measured with a custom built experimental setup. Ruthenium films showed superior catalytic performance but inferior adhesion. The issue of adhesion was solved with multilayer and co-sputtered coatings. Since the activity of the catalysts decreased dramatically after the first test, a reactivation method had to be found. By hydrochloric acid treatment it was possible to repeatedly reactivate the catalyst.

In conclusion, a first step to realise a hybrid hydride hollow glass microsphere hydrogen storage system was taken. The next step would be experiments with hydrogen loaded microspheres.

Acknowledgement

First I want to thank my supervisor Professor Christoph Eisenmenger-Sittner, who made this work even possible. He was always there for discussions and helpful with good advice.

Furthermore I want to thank all my colleagues of our group for their help, ideas and the discussions I have had with them. It was not always work, but also fun to discuss problems or technical issues. I want to thank Johannes Hell, for he built the very first version of coating system and introduced me into the apparatus; Harald Mahr, who developed the method with which the film thickness on hollow glass microspheres could be determined; Andreas Eder, who scaled up the further developed coating system for much larger batches. With him I had a lot of fruitful discussions. I want to thank Martin Quirchmair, for his collaboration in TiO₂ film preparations, Jürgen Bauer, René Bachofner, Lukas Stöttinger and Reinhard Eder, for their important collaboration in the many catalytic experiments. I also want to thank Karin Whitmore, our expert in scanning electron microscopy and Lukas Belhadj, our well-behaving apprentice. Additionally, I want to thank Werner Artner, for operating the XRDs and his help in analysing the diffractograms. I want to thank, Hedda Drexler, for her additional advice in chemical questions. Further thanks go to USTEM, which made electron microscopy even possible and the Austrian Science Fund FWF for granting and supporting the project (P-22718).

I thank my father for supporting me, so that I could finish my diploma study and meet the requirements of a PhD thesis.

Above all I want to thank my fiancé, Heidrun Drexler, since she was always understanding, patient and caring, especially in the last months of my work.

Table of content

1.	Introduction.....	11
1.1.	Motivation.....	11
1.2.	What will be discussed.....	12
1.3.	What will not be discussed.....	13
2.	Hydrogen storage.....	14
2.1.	Hydrogen production and conversion	14
2.1.1.	Hydrogen Production	14
2.1.2.	Hydrogen Conversion	15
2.2.	Overview over hydrogen storage systems.....	16
2.2.1.	Physical hydrogen storage.....	17
	Compressed hydrogen.....	17
	Liquid hydrogen.....	18
	Cryocompressed hydrogen.....	19
	Low temperature adsorption.....	19
	Hollow glass microspheres, -capsules, -balloons or -cavities	20
2.2.2.	Hydrides	21
	Interstitial metal hydrides.....	21
	Complex metal hydrides.....	22
	Non-metal hydrides	23
	Irreversible hydrolytic systems	24
2.2.3.	Clathrate hydrates.....	24
2.3.	Summary of hydrogen storage systems.....	25
3.	Microspheres & Hydrolysis – A hybrid hydrogen storage system	26
3.1.	Overview of hollow glass micro spheres	27
3.1.1.	Loading hollow glass microspheres	28
3.1.2.	Storing hollow glass microspheres.....	29
3.1.3.	Unloading hollow glass microspheres.....	29
3.1.4.	Recycling of hollow glass microspheres	30
3.1.5.	Advantages and drawbacks of hollow glass microspheres.....	30
3.1.6.	Fabrication of hollow glass microspheres	30
	Spray pyrolysis process.....	31
	Liquid droplet method.....	31
3.2.	Storage capacity of microspheres and the releasing process.....	33
3.2.1.	Hydrogen storage capacity of hollow glass micro spheres.....	34

Tensile strength of hollow glass micro spheres.....	34
Maximum loading pressure for hollow glass micro spheres	35
Gravimetric and volumetric hydrogen storage density of S38 hollow glass micro spheres	37
Gravimetric and volumetric hydrogen storage density of hollow glass micro spheres with optimized radius and shell thickness	40
Storage densities as a function of the shell thickness.....	43
3.2.2. Hydrogen releasing process by temperature induced diffusion.....	44
3.3. Combination of glass microspheres with a hydrolytic system	50
3.3.1. Hydrolysis of sodium borohydride NaBH_4	50
Water requirements	51
Reaction kinetics	53
Recycling of NaBO_2 and pricing of NaBH_4	54
3.3.2. Description of the proposed hydrogen storage system.....	56
3.3.3. Study on combined glass sphere hydrolytic storage system	59
Restrictions and assumptions	60
System hydrogen storage densities.....	61
Stoichiometric restrictions for the ratio of hollow glass microspheres to hydride	64
Temperature restrictions.....	64
3.3.4. Discussion of resulting material storage densities of the proposed hybrid system	66
3.3.5. Costs of the hybrid system	71
Influence of hydrogen, hydride and hollow glass microspheres costs	74
3.3.6. Outlook on further increasing storage densities	75
3.3.7. Summary of hybrid system analysis.....	77
4. Coating of hollow glass microspheres	78
4.1. Overview of possible coating methods	78
4.1.1. Electroless deposition – Overview	79
Electroless nickel.....	79
4.1.2. Electroless plating on microspheres	80
4.1.3. Sol-gel deposition – Overview	81
4.1.4. Sol-gel coatings on microspheres.....	83
4.1.5. Ferrite plating	84
4.1.6. Chemical vapour deposition (CVD).....	84
4.1.7. Chemical vapour deposition on hollow glass microspheres.....	86
4.1.1. Magnetron Sputtering.....	89
4.2. Methods for coating hollow glass microspheres by magnetron sputtering	89
4.2.1. Magnetron Sputtering.....	89
Different sputter source configurations.....	91

4.2.2.	Magnetron sputtering on hollow glass microspheres - review	92
	Rotating Drums	93
	Good vibrations	95
	Tilted rotating vessels.....	95
4.3.	Experiments on coating hollow glass microspheres.....	96
4.3.1.	Substrate: S38 hollow glass microspheres S38	97
	S38 hollow glass microspheres as delivered by 3M™.....	97
	S38 sieved with 50 µm mesh.....	100
	S38 washed.....	101
4.3.2.	Coating vessel and concussion mechanism design	102
	Impact velocity of the coating vessel	104
4.3.3.	Coating material and parameters	106
4.3.4.	Trickling experiments	106
	Trickling experiments without concussion.....	107
	Trickling experiments with concussion.....	108
4.3.5.	Trickling behaviour of microspheres under sputter conditions	108
	Coating spheres with a rotating vessel	109
	Coating with concussed vessel.....	109
	The effect of oxygen on the trickling of hollow glass microspheres.....	113
4.3.6.	Film thickness measurement	113
4.3.7.	Film thickness estimation and rate determination	115
	Mean diameter of the powder particles	115
	Surface exposed to the sputtering beam	115
	Volume of powder put into the coating vessel V	117
	Packing density of powder f (packing factor).....	117
	Geometry factor of the powder f_{circ}	117
	Sputter rate at the coating vessel \dot{x}	117
	Deposition time t	118
4.3.1.	Conclusions on coating powders in the concussed coating vessel	118
5.	Reactive pulsed DC magnetron sputtering: Titanium dioxide TiO_2	120
5.1.	TiO_2 – properties and applications	120
5.1.1.	Applications	120
5.1.2.	Structure and properties	121
5.1.3.	Synthesis and phase transition.....	122
5.1.4.	TiO_2 thin film preparation methods.....	123
5.2.	TiO_2 films prepared by reactive pulsed DC magnetron sputtering	123
5.2.1.	Reactive Sputtering	123
	Flow control	124
	Partial pressure control.....	126

Other aspects of reactive sputtering	129
5.2.2. Pulsed DC magnetron sputtering.....	129
Arcing.....	130
Methods to prevent arcing.....	130
Minimum frequency to avoid arcing with RF or pulsed DC sputtering.....	131
Pulsed DC (direct current) sputtering.....	132
Other parameters that influence film properties of TiO ₂	134
5.2.3. Experimental setup.....	135
5.2.4. Sample preparation.....	136
Pre-treatment	136
Coating parameters.....	136
Post-treatment.....	136
5.3. TiO ₂ thin films – results and discussion.....	136
5.3.1. X-ray diffraction analysis and scanning electron microscope imaging....	137
5.3.2. Parameters correlating to structure and film thickness.....	143
5.4. TiO ₂ thin films on hollow glass microspheres	145
5.4.1. X-ray diffraction of TiO ₂ films on hollow glass microspheres	148
6. Catalyst characterisation	150
6.1. Overview of potential catalysts	150
6.1.1. Catalyst synthesis methods.....	151
Impregnation	152
Supercritical CO ₂ method.....	152
Pyrolysis	152
In situ formation of the catalyst.....	153
Electroless deposition.....	153
Pulsed laser deposition	153
6.1.2. Comparison of catalyst compounds	153
Noble metal comparison.....	153
Carrier comparison	154
Effect of pressure on catalytic activity	155
Influence of the preparation method	155
Catalyst overview conclusion.....	155
Sputterable catalysts (metallic):	156
Sputterable catalysts (oxides):.....	156
6.1.3. Catalyst choice	156
6.2. Experimental setup for catalyst characterisation.....	157
6.2.1. Experimental procedure	159
6.2.2. Error source analysis	159
Amount of NaBH ₄	159

Amount of hollow glass microspheres	159
Atmospheric pressure	160
Room temperature	160
Remaining NaBH ₄ in mixing flask or funnel	160
Air humidity	160
Systematic overestimation: pressure difference and water displacement	160
Conclusion regarding error sources	161
6.3. Sample preparation	162
6.3.1. Pre-treatment of hollow glass microspheres	162
Washing	162
Sieving	162
Other treatments	162
6.3.2. Catalyst-coating of hollow glass microspheres	163
Sputter geometries	163
Sputter conditions	164
6.3.3. Evaluation method	165
6.4. Results and discussion	166
6.4.1. Effect of film thickness - platinum	166
6.4.2. Platinum modifications & ruthenium	167
6.4.3. Film adhesion	168
6.4.4. Catalyst reusability and reactivation	171
6.4.5. Temperature behaviour	173
6.5. Conclusion of catalyst characterisation	174
7. Conclusion and outlook	175
8. References	178
9. Appendix	192
9.1. Microspheres and hydrolysis	192
9.1.1. Relation for a pressurized thick walled spheres	192
9.1.2. Pressure inside spheres at different loading and extraction temperatures	192
9.1.3. Hydrogen diffusion – pressure as a function of time	193
9.1.4. Amount of water to cover hollow glass microspheres and hydride	195
9.2. Sphere counting algorithm used in <i>ImageJ</i>	196
9.3. Construction drawings of the concussion mechanism	196
9.4. Mathematica model for concussion vessel movement	200
9.5. Sputter rates of different configurations	207

1. Introduction

1.1. Motivation

For decades people have dreamt of vehicles powered by hydrogen and emitting nothing but water. For CO₂ emissions have risen exponentially since the middle of the 19th century (Figure 1.1) and now, that fossil fuels are depleting, it has become imperative to look for new energy sources and ways to store that energy [1].

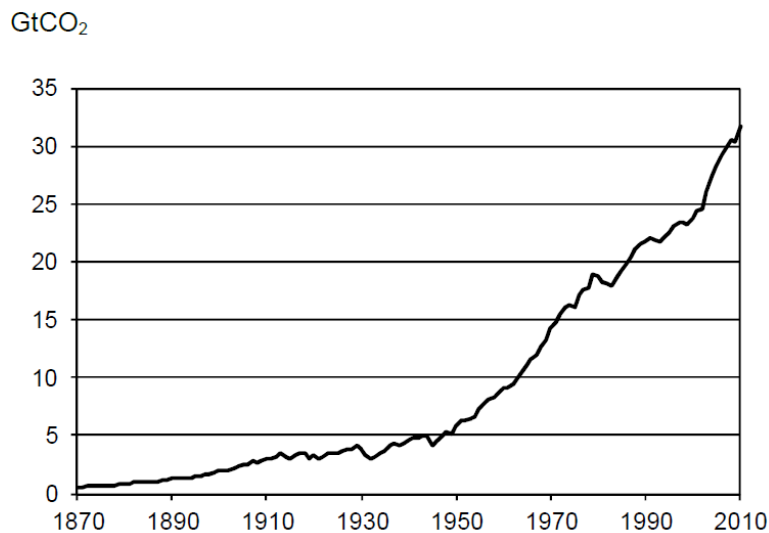


Figure 1.1: Trend of CO₂ emissions from fossil fuel combustion in GtCO₂/year [1]

Through analysis of different means of storing energy, it has become clear that only high-energy compounds are feasible. Mechanical energy storage systems or batteries do not have the

capacity to work as an energy reservoir for a whole national economy. This is also the reason why fossil fuels have become popular; they are easy to handle, easy to store and easy to convert [2].

Hydrogen might be a promising replacement energy storage molecule, because it has the highest energy density of all common fuels by weight. The lower heating value¹ of hydrogen is 120 MJ/kg while gasoline has only a specific energy of 42 MJ/kg [3]. On the other hand the energy density of hydrogen at ambient conditions is only 10 MJ/m³ while gasoline has an energy density of 32000 MJ/m³ [4, 5].

As a result, storing hydrogen at high volumetric energy densities and at the same time high gravimetric energy densities is one main challenge for a hydrogen society coming to life. Other challenges are the production and transportation of hydrogen and the efficient conversion into electricity in a fuel cell.

In this work a hybrid concept to store hydrogen will be proposed, consisting of catalyst sputter-coated hollow glass microspheres and sodium borohydride. The hollow spheres can be loaded with hydrogen by applying heat and hydrogen pressure of up to 70 MPa. Due to the elevated temperature of around 250 °C hydrogen diffuses through the glass wall into the spheres. After cooling down the hydrogen is trapped and can only be released by applying heat again. To do that an exothermal hydrolytic reaction can be used, e.g. sodium borohydride and water. However this reaction needs a catalyst in order to liberate all the hydrogen bound in the hydride and provide the necessary heat for the trapped hydrogen to diffuse out of the spheres. For thermal reasons and for the sake of recyclability, the catalyst has to be applied to the spheres surface.

As a result the main task of this work is to coat hollow glass microspheres with a proper working and stable catalyst.

1.2. What will be discussed

This work is structured as follows. First an overview of hydrogen storage systems will be given, including ways to produce and convert hydrogen. After that the proposed hybrid hydrogen storage system will be described in detail, starting with an overview of hollow glass microspheres and their production. After that the hydrogen storage capacity of hollow glass microspheres and of sodium borohydride will be discussed before giving a detailed analysis of the proposed hybrid system. This analysis includes gravimetric and volumetric storage

¹ The higher heating value corresponds to the heat of combustion of a substance at 25°C and can be calculated from the enthalpy of formation. The lower heating value now can be acquired by subtracting the evaporation enthalpy of water, assuming that the water is vaporous at the end of the combustion process. The higher heating value of hydrogen is 142 MJ/kg [3]

capacities, a comparison with storage density targets, thermal conditions and financial aspects. The system will be always compared with the challenging targets of the automotive industry.

The next section will deal with possible coating methods to apply a catalyst to hollow glass microspheres in general and by magnetron sputtering in special. After that the developed coating mechanism based on magnetron sputtering will be described, including results of deposited metallic and oxide films.

Since oxide films were deposited by reactive sputtering, the next section will deal with reactive pulsed DC magnetron sputtering of TiO_2 . The goal was to deposit anatase phase TiO_2 first on plane glass substrates and then on hollow glass microspheres. These films should work as a carrier material for the noble metal catalyst.

The last chapter discusses the main topic of this work, i.e. catalyst coated hollow glass microspheres for the hydrolytic reaction of sodium borohydride. The chapter starts with an overview of potential catalysts. After that the experimental setup will be described, before discussing results of the catalytic experiments.

1.3. What will not be discussed

This work does not include experiments with hydrogen loaded hollow glass microspheres. Whether the coating has an effect of hydrogen diffusion through the glass sphere wall remains to be investigated. Nor does this work include kinetic studies of the catalytic reaction. Both topics would have gone beyond the scope of this work.

2. Hydrogen storage

This section will give an overview of hydrogen storage technologies and explain the benefits and drawbacks of different ways to store hydrogen. Furthermore hydrogen production and fuel cells will be shortly discussed initially. The potential of storing hydrogen in hollow glass micro spheres will be investigated in chapter 3, including the hybrid concept of combining hollow glass micro spheres with a hydride.

2.1. Hydrogen production and conversion

This chapter shall give a short overview of hydrogen production technology and hydrogen conversion.

2.1.1. Hydrogen Production

“The production processes <of hydrogen> can be grouped into electrochemical, thermochemical, photochemical, and their combinations. In electrochemical processes, the energy input is given as electricity, which in turn is generated from various energy sources such as renewables (e.g., wind, solar, geothermal, hydro, biomass) and nonrenewables (e.g., fossil fuels, nuclear). In thermochemical processes, the energy input is given as high-temperature heat, which in turn is generated from various energy sources such as renewables (e.g., concentrated solar thermal, biomass combustion) and nonrenewables (e.g., fossil fuel combustion, nuclear heat). In photochemical processes, the energy input is by the direct absorption of photons of light. Combinations of these energy-intensive processes include

photoelectrochemical (e.g., artificial catalytic photosynthesis), photobiological (e.g., photosynthesis by microbial metabolic systems), thermoelectrochemical (e.g., high-temperature electrolysis), and hybrid methods involving multiple steps of the aforementioned processes (e.g., thermochemical and electrochemical splitting cycles).” Aldo Steinfeld, ETH Zurich, Paul Scherrer Institute in [4].

Presently, hydrogen is mostly produced from fossil fuels and used in the chemical industry, refineries to upgrade crude oil and in metallurgical processes. About 90% of hydrogen used worldwide is produced by consumer-owned plants for their own purposes and only about 10% are provided by industrial gas companies. To establish hydrogen as an energy carrier, production rates require an increase of several orders of magnitude [2, 4].

To overcome this issue and to help speed up the introduction of fuel cell powered vehicles, car manufacturers are working on on-board fuel processors in collaboration with oil- and fuel processing companies. These devices would allow the use of gasoline or methanol in a fuel-cell powered car. However, such fuel processors pose several engineering challenges and would still require fossil fuels [4].

Since water is a very cheap resource, it is the most logical source for large-scale hydrogen production. Methods of hydrogen production from water include electrolysis, direct thermal decomposition or thermolysis, thermochemical processes, and photolysis [4].

Typical efficiencies for electrolysis range from 72% to 82% and even 90% seem to be possible. For direct thermal decomposition of water, temperatures of 2000 °C – 3000 °C are necessary, reaching decomposition rates of up to 34%.

2.1.2. Hydrogen Conversion

Hydrogen can be converted either in internal combustion engines or in fuel cells.

For internal combustion engines with spark ignition, the intrinsic efficiency is about 30% higher than that of a gasoline engine, i.e. gasoline engine efficiency ~35%, hydrogen engine efficiency ~47%. Another advantage is, that hydrogen internal combustion engines have zero CO₂ and nearly zero NO_x emissions. However, due to the fact that hydrogen is injected as a gas and not as a liquid like gasoline, it requires a much higher volume in the combustion chamber. Thus the power density of the hydrogen powered engine drops to only 43% of a gasoline powered engine [6].

There exist five general classes of fuel cells to convert hydrogen into electrical energy. They differ primarily by the electrolyte used to perform the ion conduction and by the corresponding operation temperature. Table 2.1 gives the different types of fuel cells with electrical conversion efficiencies and operating temperatures [4, 6, 7, 8]. The listed efficiencies depend on operation conditions such as temperature, fuel type and fuel purity.

Fuel Cell Type	Mobile Ion	Electrical Efficiency	Operating Temperature
Proton-exchange membrane (PEMFC)	H ⁺	35-60%	50-100°C
Alkaline (AFC)	OH ⁻	60%	50-250°C
Phosphoric acid (PAFC)	H ⁺	40-42%	150-220°C
Molten carbonate (MCFC)	CO ₃ ²⁻	47-50%	600-700°C
Solid oxide (SOFC)	O ²⁻	45-60%	500-1000°C

Table 2.1: Types of fuel cells, their electrical efficiency and operating temperature [4, 6, 7, 8]

2.2. Overview over hydrogen storage systems

This chapter shall give an overview over existing and hydrogen storage technologies under development.

The main parameters to measure a hydrogen storage system are the gravimetric storage density γ_G and the volumetric storage density γ_V . The target storage densities for mobile applications are given in Table 2.2 [9]. These targets are published by the U.S. Department of Energy and are under constant revision.

DOE targets	2017	ultimate
γ_G (wt%)	5.5	7.5
γ_V (kg/m ³)	40.0	70.0

Table 2.2: DOE targets for hydrogen storage densities [9].

The targets were set to enable greater than 500 km range on most light-duty vehicles without making significant changes to the vehicle and being available at similar cost. They were formulated by comparing the performance of a fuel cell vehicle (FCV) to an advanced gasoline ICE vehicle as the baseline. Based on the lower heating value of hydrogen, 120 MJ/kg, the targets are for the whole storage system, including valves, tanks, regulators, etc.

Hydrogen storage systems can be divided into physical storage, reversible chemical storage, irreversible chemical storage and hydrocarbons, where not only hydrogen is utilized. Figure 2.1 gives an overview of these storage methods.

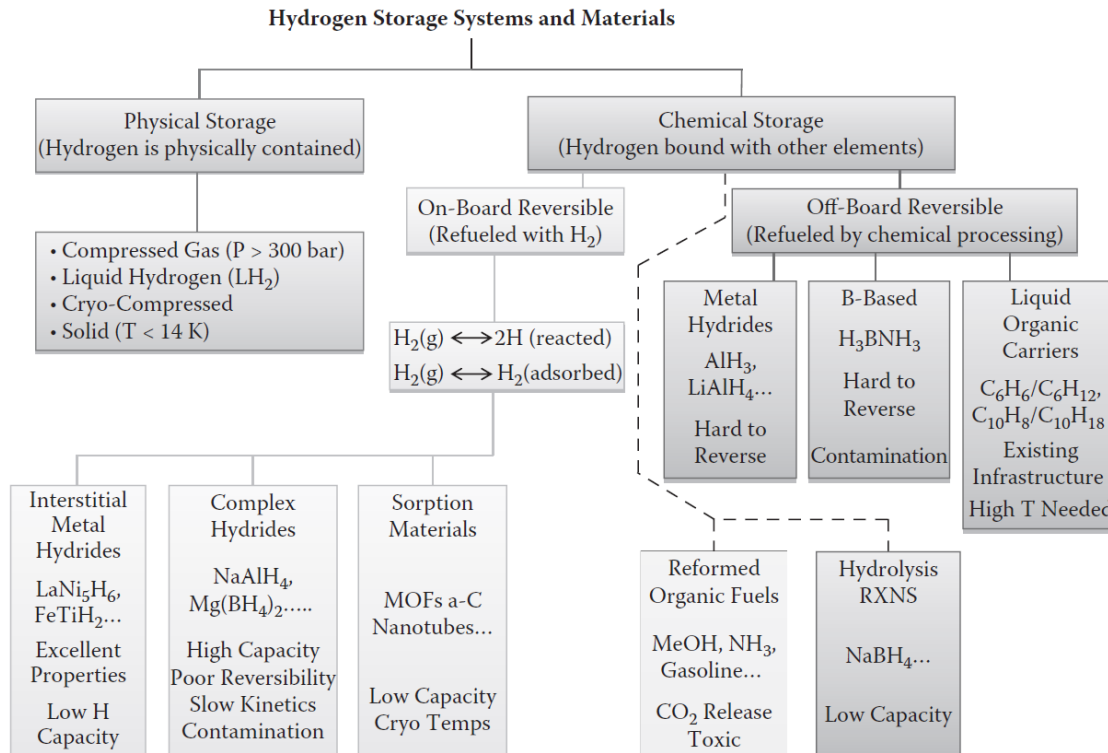


Figure 2.1: Overview of hydrogen storage systems and materials, taken from Klebanoff (2014) section 3, p. 67, [6].

2.2.1. Physical hydrogen storage

The physical states of hydrogen are well understood, so the first applications utilizing pure hydrogen were fed by hydrogen stored in compressed form or liquid. In recent years, cryocompression has also become a state of the art technique to store hydrogen.

Compressed hydrogen

The most obvious way to increase hydrogen density is compression. This technique is well developed and goes back as far as 1880, when the British used wrought-iron metal cylinders for transporting hydrogen to inflate war balloons during expeditions across Asia and Africa [4].

At near ambient conditions, hydrogen behaves like an ideal gas, at high pressures, however, it deviates from that behaviour due to Van-der-Waals forces. This behaviour is illustrated in Figure 2.2 at 20 °C as a function of applied pressure and compared with liquid hydrogen at different state points. At a pressure of 70 MPa an ideal hydrogen gas would have a density of $\rho = 58 \text{ kg/m}^3$ whereas in reality it only has a density of $\rho = 39.2 \text{ kg/m}^3$. This is an enormous decrease in the energy density due to real gas behaviour at high pressures. For calculating the real gas properties the relation in [10] was used.

Another issue is mechanical and thermal losses during the compression process. These two issues limit the compression of hydrogen and result in feasible maximum pressures of 70 MPa to 85 MPa. As an example, for reaching 35 MPa 12% of the lower heating value of hydrogen is lost to compression; for 70 MPa it is 15% and for 80 MPa 19% [2, 4].

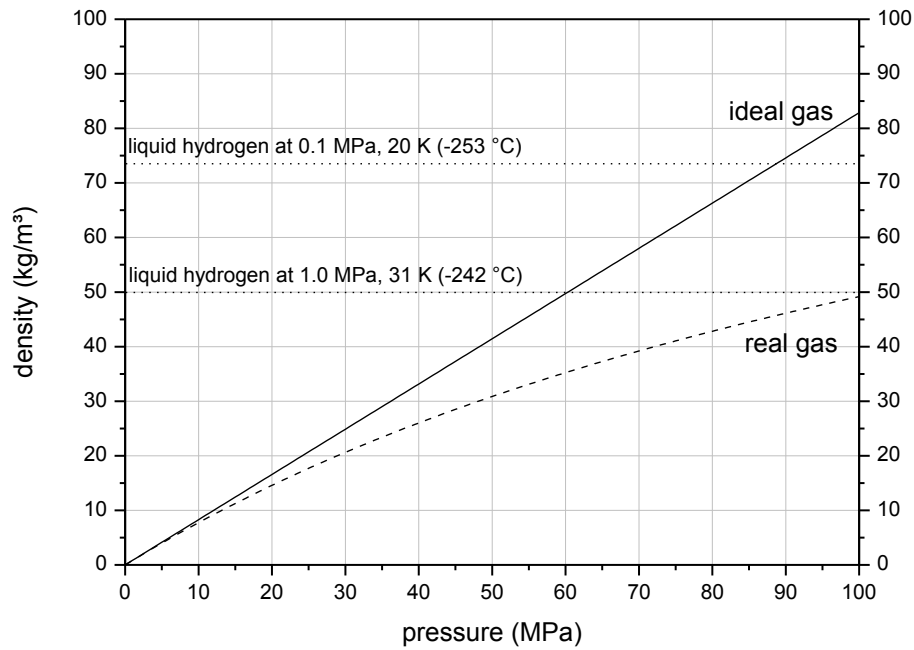


Figure 2.2: Hydrogen density as ideal gas and real gas at different working pressures; densities of liquid hydrogen are also illustrated [2]

Usually compressed hydrogen is stored in cylindrical vessels made of composite materials. A system to store 4.2 kg of hydrogen at 70 MPa within three carbon composite vessels weighs about 135 kg; made of steel it would weigh 600 kg. Using just one vessel would result in a gravimetric and volumetric storage densities of $\gamma_G = 4.8$ wt% and $\gamma_V = 23$ kg/m³ [2]. Toyota™ claims to have even higher storage densities of $\gamma_G = 5.7$ wt% and $\gamma_V = 38$ kg/m³ in the new Toyota™ Mirai car, which is powered by fuel cells [11].

Liquid hydrogen

The density of liquid hydrogen at 20 K is nearly double that of compressed hydrogen at 70 MPa at room temperature (see Figure 2.2). To keep this low temperature however, great effort has to be applied to insulate the vessel thermally. The cryogenic storage vessels must also safely manage the release of the evaporated gas due to heating from residual thermal leaks or the ortho-para conversion. Furthermore, the evaporation enthalpy of liquid hydrogen is very low, $\Delta h_{vap.} = 0.46$ kJ/mol, compared to the evaporation enthalpy of for example liquid gas $\Delta h_{vap.} = 8.19$ kJ/mol. So small thermal leakages already have a large effect and reduce

dormancy, which is the period of time when hydrogen has to be released in order to keep low pressure and temperature [6].

Another issue is the energy required to liquefy hydrogen, which is about 30-35% of the lower heating value. So 30-35% of the energy is already lost [2, 5].

Since both the storing and producing of liquid hydrogen still bears technical and energy issues, research has shifted to cryocompressed hydrogen [5].

Cryocompressed hydrogen

To increase the storage density of liquid hydrogen, it can be stored in insulated pressure vessels. This is due to the compressibility of liquid hydrogen: at 21 K, its density increases from 70 kg/m³ at ~0.1MPa to 87 kg/m³ at ~23.7 MPa [12]. Furthermore, high pressure vessels also allow venting at higher pressures, which is the main advantage of the system. The venting due to hydrogen evaporation stops when the tank reaches ambient temperature, which would result in an empty tank when using a liquid hydrogen storage vessel. When using a cryocompression system, there would be still about 30% of initial liquid hydrogen inside the tank after venting [5, 12]. However, there is still the problem of the energy necessary to liquefy hydrogen.

Ahluwalia et al. showed that such a system could reach storage densities of $\gamma_G = 6.5$ wt% and $\gamma_V = 47.8$ kg/m³. With better materials the gravimetric storage density might even be increased to $\gamma_G = 9.2$ wt% [12].

To save the energy for liquefying hydrogen, it could simply be cooled down to 77 K by liquid nitrogen. To store 4.1 kg of hydrogen in a 100 litre tank a pressure of 74 MPa is required at room temperature, but only 14.8 MPa is required to store the same amount at 77 K [5].

A possible scenario might be that for short trips only gaseous hydrogen is fuelled and for long trips liquid hydrogen would be used to extend the range.

Low temperature adsorption

Low temperature adsorption is another option for physical hydrogen storage. At temperatures of -193 °C hydrogen adsorbs on surfaces of zeolites, carbon nano-materials, metal organic frameworks (MOF) or polymers with intrinsic porosity [2].

The storage density is approximately proportional to the specific surface of the sorbent. With zeolites, storage densities of only 2.5 wt% are possible, which is well below any technical applicability. Eberle et. al [2] additionally concluded that carbon based nano-material would also never meet the requirements for a hydrogen storage material.

Metal organic frameworks have very large specific surfaces of around 5000 m²/g which makes them a suitable storing medium. According to Sherif et al. (2014) [4] and Langmi et al. (2014) [13] several groups have reported experimental measurements showing maximum excess

adsorption of ~6.5 to 8.6 wt% of hydrogen at 77 K and < 10 MPa on MOFs, polymers and various porous carbon materials. It is apparent that similar adsorption uptakes are observed for the best performing porous materials, e.g. total hydrogen uptakes for MOF-200 (16.3 wt%), MOF-210 (17.6 wt%) NOTT-112 (10 wt%) and UMCM-2 (12.4 wt%) at 8.0 MPa have been observed at 77 K. For storage applications, however, hydrogen capacity on a volume basis is also important. The materials with highest adsorption capacities on a volumetric basis are PCN-14 (55 kg/m³) and NOTT-112 (54 kg/m³) [4, 13].

Nonetheless, materials discovered so far have a hydrogen uptake of only about 2-3 wt% at atmospheric pressure level and 77 K. Thus, to reach high volumetric and gravimetric storage densities both, high pressure and low temperature must currently be applied [13].

Another issue of this technique is the adsorption enthalpy. Because of the high adsorption enthalpy it would be necessary to evaporate enormous amounts of liquid nitrogen to keep the temperature at ~70 K. For one kg hydrogen about 13 to 33 kg of nitrogen have to be evaporated [2].

In conclusion adsorption of hydrogen on porous materials is currently limited to cryogenic temperatures (77 K) and elevated pressures (5 - 10MPa). This limits the use of the technique in real practical transport application situations. The design of porous materials with enhanced adsorption capacity under ambient conditions would involve increased hydrogen–surface interactions [4, 13].

For an overview of investigated sorbents and hydrides Figure 2.3 shows the gravimetric storage density of some sorbents, chemical hydrides and metal hydrides.

Hollow glass microspheres, -capsules, -balloons or -cavities

The storage concept in hollow glass microspheres, microcapsules, microballoons or microcavities is based on the exponential temperature dependence on the permeability of hydrogen through glass. Hollow glass microspheres (approx. 20 – 200 µm) are heated and pressurized with hydrogen in an autoclave. Once the spheres are saturated with hydrogen the temperature is reduced, still under hydrogen pressure. When room temperature is reached, the hydrogen is trapped inside the spheres and the overpressure can be removed [14]. Theoretical calculations yield storage densities of up to 14.2 wt% and 17.3 kg/m² under realistic conditions (see section 3.2.1). The volumetric storage density is limited by the sphere packing density and the maximum feasible pressure from an energetic point of view.

Experimentally validated storage densities of hollow glass microspheres reported so far are given in Table 2.3 [4, 14, 15, 16, 17, 18]. A more detailed discussion will be given in section 3.1 and 3.2.

system and pressure	reported by	gravim. storage density (wt%)	volum. storage density (kg/m ³)
spheres 10.4 MPa	Tsugawa et. al 1976 [4]	2	-
spheres 55.1 MPa	Teitel 1981 [4]	5.3	12
spheres 45 MPa	Eklund and von Krusenstierna (1983) [14]	5-6	~10
cylinders - MPa	Yan et al. (1985) [15]	2	-
spheres 100 MPa	Duret and Saudin (1994) [16]	4	14
spheres 15-30 MPa	Kohli et al. (2008) [17]	15-17	-
spheres 1 MPa	Dalai et al. (2014) [18]	2.32	-

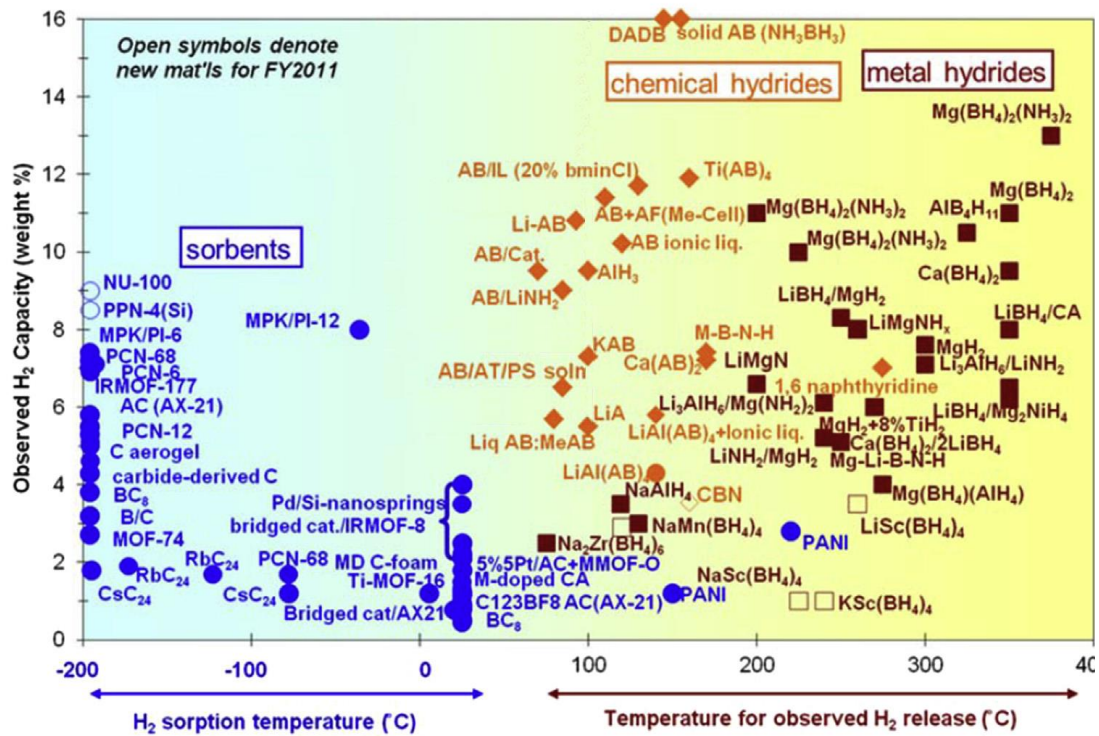
Table 2.3: Reported hydrogen storage densities in hollow glass microspheres, -capsules, -balloons or -cavities so far (DOE-targets are 7.5 wt% and 70 kg/m³)

2.2.2. Hydrides

Hydrides can be divided into interstitial metal hydrides, complex metal hydrides, irreversible hydrolytic systems and hydrocarbons. The principal distinction between metallic hydrides and complex hydrides is that complex hydrides form an ionic or covalent compound of the metals upon hydrogen absorption, whereas in metal hydrides hydrogen is absorbed by the intermetallic matrix [4]. Irreversible hydrolytic systems use complex hydrides for a hydrolytic reaction with water and thus cannot be reversed on-board a vehicle.

Interstitial metal hydrides

The mechanism of metallic hydrides works as follows: Hydrogen molecules physisorb at the metal surface. In order to chemisorb, the hydrogen molecule has to overcome an activation barrier to dissociate and create the hydrogen metal bond on the surface of the metal. After that the hydrogen atom can move into the lattice and diffuse to interstitial sites and be stored in the lattice. A typical relation of that mechanism can be expressed as $M + x/2 H_2 \leftrightarrow MH_x + \text{heat}$, where M represents the intermetallic matrix and H hydrogen [4]. There exist many different kinds of metal hydrides, i.e. binary metal hydrides like MgH_2 or AlH_3 and intermetallic hydrides with two metals like $NaAlH_4$ or more complex like $La_{0.7}Mg_{0.3}Ni_{2.8}Co_{0.5}$, often using transition metals. Whereas binary systems often need high working temperatures of about 300-400 °C, intermetallic systems also work under mild conditions [5] (see Figure 2.3).



Prepared by DOE: G. Thomas (2007), G. Sandrock (2008), B. Bowman (2009-10), S. McWhorter (2011)

Figure 2.3: Overview of hydrogen storage materials: sorbents, chemical hydrides and metallic hydrides; gravimetric storage densities and operation temperature, taken from [5]. In the text metal hydrides are referred to interstitial metal hydrides and chemical hydrides are referred to as complex hydrides.

As mentioned above, transition metals are often used for such systems, but since transition metals have a high molar weight when compared to hydrogen, the gravimetric storage density of metal hydrides is low and often does not exceed 3 wt% at mild conditions. The existing materials which have much higher gravimetric storage densities, e.g. MgH_2 7 wt%, often lack in reaction kinetics or require high working temperatures [2].

Currently investigations are focused especially on intermetallic alloys with more than two metals.

Complex metal hydrides

Complex metal hydrides contain hydrogen atoms that are partially covalently bound within a polyatomic anion. Typical covalent hydrides are carbon hydrides, boron hydrides, or germanium hydrides. They often have higher gravimetric capacities than simple hydrides.

There are two main categories of complex hydrides: nitrogen containing hydrides (amides or imides) and boron-containing hydrides (borohydrides). These are usually bound to lithium,

magnesium, sodium, calcium or, less commonly, transition metals. Multiple compounds can be combined to make systems with enhanced properties. Most compounds dissociate at higher temperatures [2, 4, 5].

Examples for nitrogen containing hydrides are lithium imide Li_2NH and magnesium amide $\text{Mg}(\text{NH}_2)_2$. Li_2NH adsorbs hydrogen at 0.1 MPa and 285 °C and stores hydrogen reversibly with 6.5 wt%. In order to release hydrogen, however, a heat generator would be necessary on-board the vehicle. $\text{Mg}(\text{NH}_2)_2$ already releases hydrogen at 200 °C but on the other hand has lower storage efficiencies. Another disadvantage is the forming of ammonia as by-product during the releasing process [19].

Examples for borohydrides are lithium borohydride LiBH_4 and sodium borohydride NaBH_4 . Both would be very promising with a gravimetric storage density of up to 18 wt%, but dehydrogenation temperatures are much too high at about 400 °C. A lot of work has been done in reducing that temperature e.g. changing the cation or incorporating additives to the fuel mixture [5, 20].

Another option is to use a hydrolytic reaction, which results in an irreversible process as will be discussed in the following.

Non-metal hydrides

The main groups of non-metal hydrides are hydrocarbon, boron hydrides and nitrogen hydrides. Since the main goal is to reduce CO_2 emission and be independent from fossil fuels, hydrocarbons must be produced from renewable sources (see section 2.1.1, p.14).

Most common non-metal hydrides based on boron and nitrogen are ammonia borane NH_3BH_3 , ammonia NH_3 and hydrazine N_2H_4 [5].

Ammonia borane is a promising compound due to its high hydrogen storage density of 19.6 wt%. However, it does not release H_2 until thermal decomposition at about 200 °C. The decomposition temperature can be lowered in organic solutions, ionic liquids, acid catalysed or with metal complex catalysts. Up to 18 wt% have been released at temperatures of approximately 60 °C. Unfortunately, ammonia borane dehydrogenation releases unwanted toxic borazine by-products [20].

Ammonia has the highest hydrogen content of all the nitro hydrides at 17.7 wt% and, in addition, the ammonia production technology already exists, which makes it a very interesting hydrogen storage material. However, ammonia decomposition is endothermic and requires high temperatures. Even with catalysts, the reaction temperature is about 400 °C and only 80% of hydrogen is released [20].

Hydrazine has a hydrogen content of 12.6 wt%, but is dangerous to work with because of its hypergolic properties, which means that it reacts explosively when brought into contact with

oxidizing agents. To overcome this issue, it has to be diluted in water or in an inert gas. Decomposition temperature is at 250 °C, however without a catalyst, it decomposes to ammonia [20].

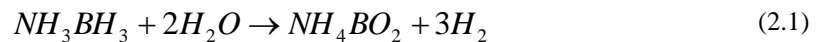
In conclusion hydrazine and an ammonium-lithium amide mixture are the most promising nitrogen-containing compounds; hydrogen content of amides is too low and ammonia requires too high operating temperatures [20].

Irreversible hydrolytic systems

Some hydrides can irreversibly react with water or alcohol, releasing hydrogen at mild conditions, which is the main advantage of such reactions. The reactions are known as hydrolysis or alcoholysis. The disadvantage is that the hydride has to be recycled off-board [2, 4, 5].

Two examples of hydrolysis or alcoholysis of already mentioned hydrides will be given: ammonium borane and sodium borohydride. Lithium borohydride is also a possibility, but not as easy to handle ($\gamma_G = 14.0$ wt%).

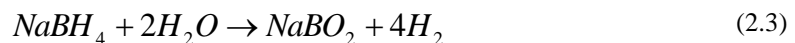
Ammonium borane hydrolysis [20], $\gamma_G = 12.4$ wt%:



Ammonium borane hydrolysis [20], $\gamma_G = 3.5$ wt%:



Sodium borohydride hydrolysis [20], $\gamma_G = 10.9$ wt%:



Sodium borohydride will be discussed in more detail in section 3.3.1, since its catalyst supported hydrolysis is one main topic of this work.

2.2.3. Clathrate hydrates

Clathrates are a chemical substances consisting of a lattice that traps or contains molecules. In clathrate hydrates the guest gas molecules are trapped in host water molecules. There are no chemical bonds and the gas molecule is only held inside the cavities physically. According to

Velusvamy et al. (2014) there have been considerable research efforts to improve the clathrate process for hydrogen storage. The advantages of clathrate hydrates are: (i) The clathrate process is environmentally benign as it uses only water and low concentration of promoters for improving the operating conditions. (ii) Hydrogen is stored in its molecular form and can be utilised simply by depressurization or minimal thermal stimulation. (iii) Another advantage is the moderate temperatures and pressure conditions for storage in the presence of low concentration of promoters. (iv) They bear a relatively high hydrogen content per unit mass/volume and (v) are not explosive [21].

The challenges encountered in storing hydrogen as clathrates are (i) the slow formation kinetics of hydrogen hydrates, (ii) the stability of hydrogen hydrates at ambient conditions and (iii) the low hydrogen storage capacity when used along with promoters, since the promoters occupy hydrate cages [21].

Up to now, gravimetric densities of 7.2 wt% were predicted at extreme conditions of pressure and temperature, which may not be feasible at large scale considering the associated energy requirement [21].

Research on clathrate hydrates has only begun in the 1990s, so there are still many unanswered questions.

2.3. Summary of hydrogen storage systems

It was shown that there are many different ways to store hydrogen, i.e.:

- Physical hydrogen storage: compressed, liquid, cryocompressed, low temperature adsorption, hollow glass microspheres
- Hydrides: interstitial metal hydrides, complex metal hydrides, non-metal hydrides irreversible hydrolysis systems
- Clathrates

There is still a significant body of research in progress to make hydrogen the new and clean energy carrier. The next chapter will deal with a combined system of hollow glass microspheres and NaBH_4 hydrolysis as a hybrid approach to merge the positive aspects of these two storage techniques.

3. Microspheres & Hydrolysis – A hybrid hydrogen storage system

Hollow glass micro spheres have a theoretical high gravimetric storage density and are relatively cheap compared to other storage solutions, i.e. metal hydrides or chemical hydrides. Furthermore no pressure vessel is needed for storing the spheres. However, they have quite a low volumetric storage density and bear the problem of releasing the hydrogen in feasible amount of time without consuming a lot of energy for the heating process.

Hydrolytic systems on the other hand have both a high gravimetric storage density and a high volumetric storage density, but are very expensive. Furthermore they produce enormous amounts of heat when releasing the hydrogen.

Combining those two complementary systems might be a satisfactory solution to overcome the problematic issues of both approaches [22]. The heat generated by the hydride can be used for heating the hollow glass micro spheres and thus inducing the diffusion process of hydrogen out of the hollow glass micro spheres. Another advantage is that costs are dramatically reduced compared to hydrolysis-only systems. Furthermore, encrustation of the educts is reduced due to lower hydride to total volume ratio.

However, a combination of hollow glass micro spheres and a hydride brings other problems:

- At room temperature the diffusion process must be very slow in order to keep the hydrogen inside, which can be achieved with larger spheres and thicker sphere shells, as will be shown in section 3.2.2.
- As a result a fast diffusion process would require high temperatures of about $T = 250 - 400$ °C [2, 4].

- The hydride reaction necessitates water, which vapour pressure increases with increasing temperature. At 300 °C the vapour pressure of water is 8.58 MPa [23], which would make a heavy pressure vessel indispensable.
- Another issue is that during heating up to high diffusion temperatures, the hydrogen pressure inside the hollow glass micro spheres is also increased, even before releasing significant amounts of hydrogen. The hollow glass micro spheres have to withstand this increased pressure, so the spheres shell thickness has to be higher than would be necessary at room temperature. A higher shell thickness decreases the gravimetric storage density.
- For keeping hydrogen inside the spheres, large spheres are necessary, but on the other hand large spheres promote their breakability, because of surface imperfections like scratches.

In the following chapters the before-mentioned issues and necessary compromises will be discussed in more detail as well as the feasibility of the system, storage densities and the theory behind it. First an overview of hollow glass microspheres will be given. Next the theoretical storage capacity of hollow glass microspheres will be calculated with assumptions as realistic as possible. After that the temperature dependent releasing process will be discussed, before describing the combined system of hollow glass microspheres and a hydrolytic reaction.

3.1. Overview of hollow glass micro spheres

The storage concept in hollow glass microspheres is based on the exponential temperature dependence of the permeability of hydrogen through glass. Hollow glass microspheres are heated and pressurized with hydrogen in an autoclave. Once the spheres are saturated with hydrogen the temperature is reduced, still under hydrogen pressure. When room temperature is reached the hydrogen is trapped inside the spheres and the hydrogen overpressure can be removed [14]. Glass microspheres can be pressurized to over 100 MPa which is due to the high tensile strength of glass [24, 25]. Moreover, glass has a much lower density than steel which makes hollow glass microspheres perfect pressure vessels. However, the size and quality of the spheres is of great importance, since imperfections decrease the effective tensile strength dramatically [26]. This matter will be discussed more thoroughly in section 3.2.1.

Hydrogen storage in hollow glass microspheres, microcapsules or microcavities was first proposed by Teitel in 1978 [15, 27, 28], where he describes a combination of a metal hydride and glass sphere hydrogen storage system. This system should have been able to provide hydrogen which is released during the cooling down process. The combination with the metal

hydride should also increase the volumetric storage density of the system. Since then hollow glass microspheres have been of great interest regarding hydrogen storage [27].

A proposed loading and unloading cycle of microspheres is illustrated in Figure 3.1 with (1) hydrogen loading, (2) storage and distribution, (3) on-board H_2 unloading and (4) screening and recycling of whole microspheres [4].

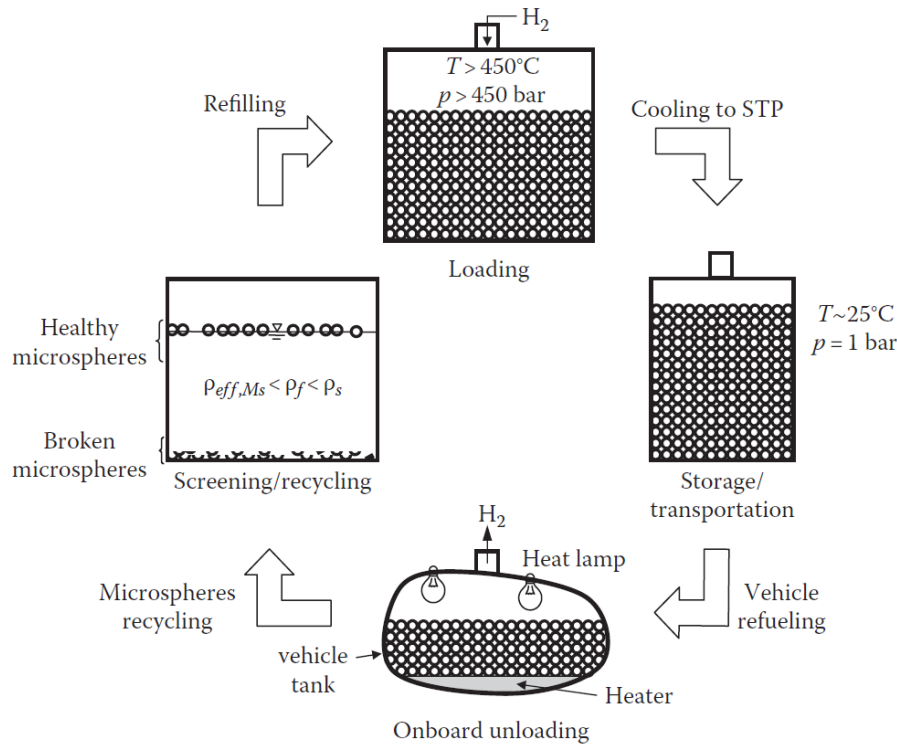


Figure 3.1: Life cycle of hollow glass microspheres: loading, storing, on-board unloading and recycling; taken from [4] p. 767

3.1.1. Loading hollow glass microspheres

The loading process could be easily performed in industrial autoclaves at high pressures and high temperatures, e.g. 200-400 °C and up to 85 MPa [14, 29]. Hydrogen diffuses through the glass into the hollow glass micro spheres. When cooled down the hydrogen is trapped inside the hollow glass micro spheres and can be released by applying heat again. Yet, to increase the storage density, it would be essential to be able to load the hollow glass microspheres at lower temperatures. This is due to the fact that the hydrogen density is much lower at elevated temperatures and thus storage densities are decreased. This behaviour was also reported by Halvordson and Shelby (2008) [30].

3.1.2. Storing hollow glass microspheres

Storage of hydrogen loaded hollow glass microspheres is very easy. Since every sphere is a tiny pressure vessel, no other provisions have to be arranged. The spheres can for example be put into a common plastic can or tank and transported at ambient conditions. It has been reported, that hydrogen loaded hollow glass microspheres can be stored for weeks without losing significant amounts of hydrogen [31, 32, 33]. However, it will be shown that this so-called dormancy strongly depends on the sphere dimensions and the permeability at ambient temperature (section 3.2.2).

3.1.3. Unloading hollow glass microspheres

The unloading process is crucial, which is why most research regarding hollow glass microspheres has focused on that topic. There are two approaches for the releasing process [30, 34, 35]:

- Light induced by an infrared lamp or
- Thermally induced by an electric heater.

A thermally driven release requires temperatures of 200 - 400 °C depending on required hydrogen flow rate, sphere material and dimension, such as radius and shell thickness. It can be realized as an electric heater or other means, if available. A more elegant way is to utilise an infrared lamp, since hollow glass microspheres respond very well to infrared radiation. This technique has been under research since 1998 to the present (2015). To enhance the response to infrared radiation, experiments have been carried out by many groups [30, 32, 34, 35, 36, 37]. In these experiments the raw materials were doped with different materials before fabricating the spheres from it, i.e. Fe_3O_4 , CoO , NiO , V_2O_5 , Cr_2O_3 .

Both methods, lamp heating and electric or furnace heating, are limited. Infrared and incandescent lamp heating is limited by the optical properties, since the radiation is absorbed and only sample thicknesses of up to 10 mm seem to be feasible [36]. Heating by a furnace or an electric heater is limited by the thermal conductivity of the hollow glass microspheres, which is about 0.05 – 0.26 W/m²K [25].

To enhance the diffusion process in general the glass properties can be altered by changing the glass composition. This was also done by several groups by adding Fe, Co, Mg, MgO, BaO, or Li_2O or by changing the ratio the common glass compounds SiO_2 , B_2O_3 , Na_2O , Fe_2O_3 , Al_2O_3 and K_2O [18, 38, 39, 40, 41].

The diffusion process will be discussed in more detail in section 3.2.2.

To release the hydrogen by simply destroying the microspheres is also a possibility, but is also the most expensive method and therefore not seriously pursued. Moreover, small pieces of broken microspheres could constitute a health hazard [42].

3.1.4. Recycling of hollow glass microspheres

Empty microspheres are removed from the tank and need to be separated into broken and whole spheres. After that the intact spheres can again undergo H₂ loading, distribution, and unloading again. The separation of broken microspheres from reusable ones can be done quite easily by the so called sink–float method. Putting the batch of spheres into water causes the broken spheres and small glass shards to sink down whereas the intact spheres will float on the surface. This method was also reported by Paul and Jones (1952) [43].

3.1.5. Advantages and drawbacks of hollow glass microspheres

- + Hollow glass microspheres are inexpensive in production and are already produced on industrial scale [4, 25, 33]
- + The storage system would be intrinsically safe [4, 33]
- + Good dormancy: weeks [31, 32, 33]
- + Good gravimetric storage density $\gamma_G > 10$ wt%
- Bad volumetric storage density $\gamma_V < 20$ kg/m³
- Requires quite high temperatures for hydrogen extraction, 200-400 °C [4]
- Requires recycling

3.1.6. Fabrication of hollow glass microspheres

“Extensive efforts have been devoted to the fabrication of hollow glass microspheres for applications ranging from thermal insulation and fire retardant to lightweight composite materials for flotation and reinforced materials. They have also been used for viscosity modification, shrinkage reduction, and chemical resistance enhancement of plastics or paints, as well as for radiation shield. Hollow microspheres made of materials other than glass have also been used to encapsulate drugs for controlled drug delivery or colorant or artificial flavour in food science. Thus, there exist numerous synthesis methods with different levels of control in the size distribution, shell thickness, material composition, mechanical properties, and throughput.” taken from Pilon (2014) in Sherif (2014) p. 791 [4].

This section will give just a very short overview of existing synthesis methods of hollow glass microspheres. A complete overview of patents and research activities regarding the fabrication of microspheres, -capsules,- containers, - cylinders etc. would go far beyond the

scope of discussion. The main fabrication methods are spray pyrolysis processes and liquid droplet methods.

Spray pyrolysis process

In the spray pyrolysis process, blowing agent containing glass frits, microspheres, or micropowders, the so called semiproducts, are sprayed into an oxy-fuel flame at temperatures between 1000 °C and 1200 °C. Due to the heat and thus reduced viscosity and surface tension, the semiproducts take a spherical shape. At a certain temperature the blowing agent (e.g. sulphate, urea) undergoes thermal decomposition and thus releases gases which results in the formation of a cavity. The resulting hollow sphere is rapidly cooled from outside to maintain their sphericity. Figure 3.2 illustrates the spray hydrolysis process. The size and composition of the semiproducts, i.e glass frits, spheres, etc., are most important for the final product [4].

The simplest semiproducts to produce are glass frits, since one basically just has to crush glass. However, because of irregular size and shape, the resulting hollow glass microspheres are non-uniform in size and shell thickness. To overcome this issue, the glass frits can be sieved. Another method for semiproduct fabrication is the dried-gel process. A gel of desired composition is dried and ground into small particles [4].

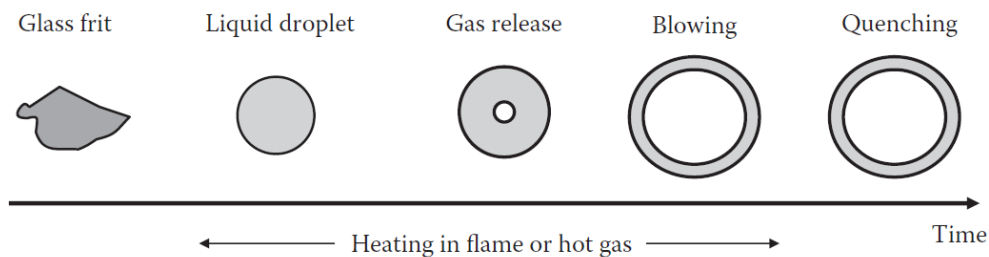


Figure 3.2: Schematic of a spray pyrolysis process to produce hollow glass microspheres; taken from Pilon (2014) in Sherif (2014) p. 792 [4]

Liquid droplet method

This method uses a drop tower, where the components fall through different temperature zones on the way down. Figure 3.3 illustrates the drop furnace with the different regions. First, glass-forming components are dissolved in an aqueous solution, which is then distributed as uniform-size droplets by a Rayleigh-Taylor generator or a vibrating nozzle. A controlled air flow passes from the top to the bottom of the furnace and transports the droplets. In region 1 the water from the surface of the droplets is removed due to a moderate temperature, which results in an elastic gel membrane that encapsulates the rest of the droplet. Then, in region 2, water

from the droplet evaporates and diffuses through the membrane resulting in dry solid gel particles. Due to higher temperatures in the lower region, the gel microspheres fuse to glass and collapse to form denser glass microspheres. In region 4 residual gases are released and diffuse through the shell. Due to the low viscosity at the elevated temperature and surface tension, the sphere shells become uniform like in the spray pyrolysis process. The hollow glass microspheres are then rapidly cooled (quenched) and collected [4].

The resulting hollow glass microspheres are nearly monodispersed with excellent sphericity and shell uniformity. Moreover the process allows regulation of the microspheres' diameter and shell thickness by controlling the liquid solution composition, the droplet formation process, the temperature profile in the column, and the liquid flow rate [4].

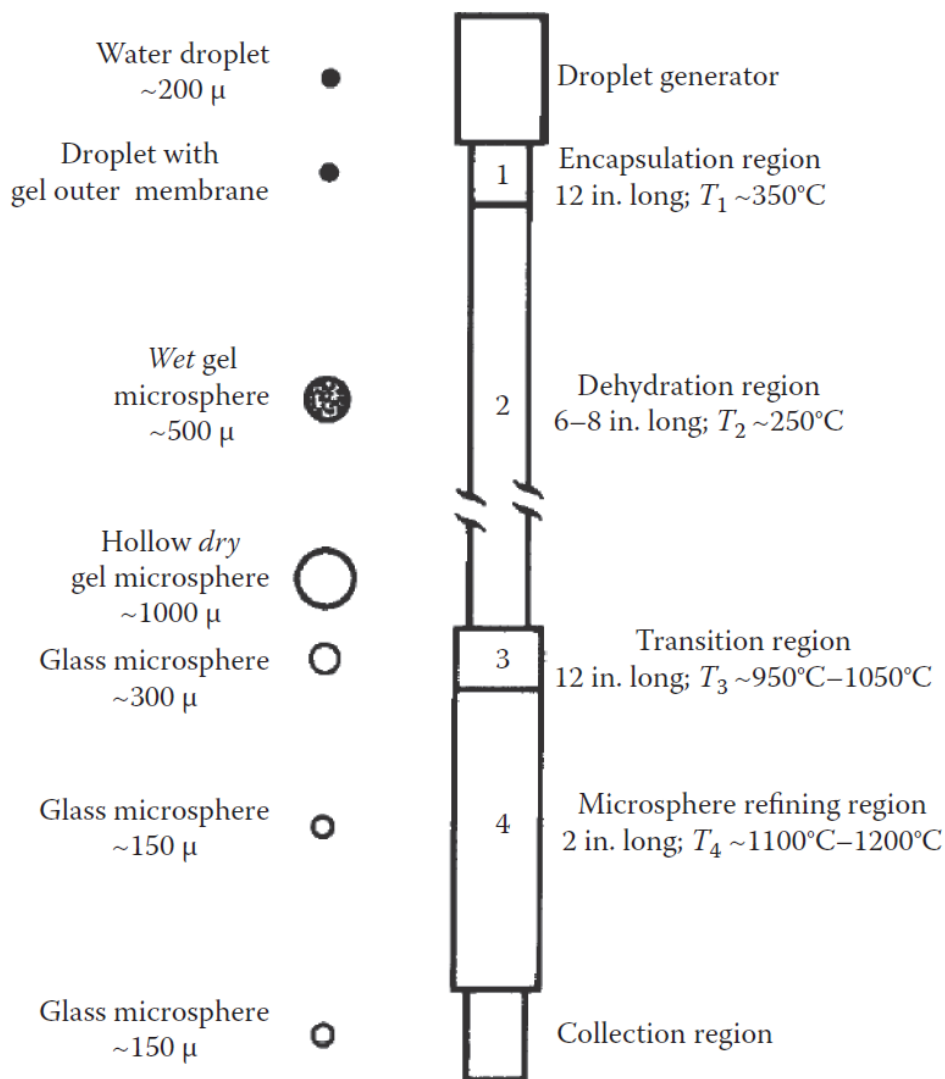


Figure 3.3: Schematic of a vertical-drop furnace used in liquid-droplet process (Reproduced from Hendricks, C.D., J. Nuclear Mater., 85–86(1), 107–111, 1979; Rosencwaig, A. et al., Laser fusion hollow glass microspheres by the liquid-droplet method, Lawrence Livermore Laboratory Report UCRL-81421, June 5, 1978.) [4]

Most research groups are using the spray pyrolysis process in combination with glass frits or sol-gel fabricated semiproducts, e.g. [26], [30], [37], [39], [44], but some also use drop towers [17]. For hydrogen storage the spheres have to fulfil additional requirements, such as optimal diameter to shell thickness ratio and glass permeability.

3.2.Storage capacity of microspheres and the releasing process

Hollow glass micro spheres can be loaded and unloaded with high pressure hydrogen by a temperature induced diffusion process. Therefore, the hollow glass micro spheres are heated up to approximately 250-400 °C and pressurized to about 85 MPa, so that hydrogen diffuses through the glass into the hollow glass micro spheres. When cooled down, the hydrogen is trapped inside the hollow glass micro spheres and can be released again by applying heat.

In this chapter the theoretical hydrogen storage capacity of hollow glass microspheres will be described in detail. This will include S38 hollow glass microspheres provided 3M™ [25] as they were used in this work as well as theoretical hollow glass micro spheres with an optimized ratio of sphere radius r to sphere shell thickness d . For reasons discussed in section 3.3, the extraction temperature will be assumed at $T_E = 250$ °C.

Furthermore this chapter will deal with the theoretical aspects of the diffusion and outgassing process of hydrogen loaded hollow glass micro spheres.

For all calculations the real gas law is implemented, since the ideal gas law no longer applies at high pressures such as in loaded hollow glass micro spheres (85 MPa). For the real gas law virial coefficients are used.

In the following table (Table 3.1) the used variables for calculating the storage capacity of hollow glass micro spheres and the outgassing process are given. The assumptions of the given values will be explained later in more detail:

Name	Variable	Value (assumed)	Unit
hydrogen loading pressure	p_L	8.5×10^7	Pa
tensile strength of glass spheres	σ	3.31×10^9	Pa
density of glass	ρ_{gl}	2230	kg/m ³
gas constant	R	8.314462	J/kgK
loading temperature	T_L	523.15	K
outgassing (extraction) temperature	T_E	523.15	K
molar mass of hydrogen molecule	M_{H_2}	2.02	g/mol
virial coefficient	B_1	2.01×10^{-6}	K/Pa
virial coefficient	B_2	-5.09×10^{-7}	K ² /Pa
total virial coefficient for loading	$B_L(T_L)$	-	1/Pa

total virial coefficient for extraction	$B_E(T_E)$	-	1/Pa
packing factor (random packing of spheres)	f	0.63	-
amount of spheres	V	0.06	m ³
hydrogen extraction pressure	p_E	-	Pa
ambient pressure	p_∞	1.0 x 10 ⁵	Pa
sphere radius	r	14	μm
sphere shell thickness	d	1	μm
compressibility factor	$Z(T,p)$	-	-
safety factor	S_f	1, 2, 4	-
sphere volume	V_{Sp}	-	m ³

Table 3.1: Variables for calculating the storage density of hollow glass micro spheres and the outgassing process

3.2.1. Hydrogen storage capacity of hollow glass micro spheres

The main parameters that influence the hydrogen storage capacity of hollow glass micro spheres are the tensile strength σ of the used glass and the ratio ε of the sphere shell thickness d to the sphere radius r . These parameters determine the maximum pressure p_{max} inside hollow glass micro spheres given in equation (3.1) also considering a safety factor S_f [4, 45, 46].

$$p_{max} = \frac{2\sigma d}{S_f r} \quad (3.1)$$

Equation (3.1) only applies to thin walled spheres. For thick walled spheres the relation is much more complex [45], but will not be used, also in prospect of analytical solvability of further relations. The error made by using this relation is about $d/(r-d)$ [45], so about 6.5 % for S38 hollow glass micro spheres and about 2.2 % for optimized hollow glass micro spheres. The relation for thick walled spheres is given in the appendix in section 9.1.1.

Tensile strength of hollow glass micro spheres

The mechanical properties of glass mainly depend on its composition, sample history and temperature. Glass is much stronger under compression loads than under tensile loads, because of the significant influence of surface imperfections. Breaks occur easily at these imperfections making them the limiting factor [4, 24, 26, 47, 48]. As a result it is important to use small sphere sizes to decrease the number of these weak points.

The theoretical values of the tensile strength of glass considered for hydrogen storage range from $\sigma = 14$ GPa for borosilicate pyrex to $\sigma = 24$ GPa for vitreous silica. These theoretical

values are up 60 % higher than experimental measurements have shown, due to the presence of surface imperfections [26, 48]. Roughly estimated, this gives a tensile strength of glass of about $\sigma(40\%) = 5.6\text{-}9.6$ GPa.

The S38 hollow glass micro spheres used in this work are made of borosilicate glass [25] [49] for which a tensile strength of $\sigma = 3.31$ GPa is given by 3M™ [50]. A comparison of all values is given in Table 3.2, with respect to surface imperfection (-60%) and experimental values (for 3M™ glass) in the second line. For all following calculations a value of $\sigma = 3.31$ GPa is assumed. Effects of the temperature on tensile strength will not be considered in detail but incorporated in the safety factor S_f , which will be assumed as $S_f = 2$. The commonly used value would be $S_f = 1.5$ [4].

	Vitreous Silica [24]	Soda-Lime Glass [24]	Borosilicate Pyrex [24]	3M™ Borosilicate Glass [50]
tensile strength σ (GPa), theoretical	24	16	14	-
tensile strength σ (GPa), reduced/ experimentally	9.6	6.4	5.6	3.31

Table 3.2: Comparison of tensile strengths of glass used in hollow glass microspheres. The second line gives the actual tensile strength of borosilicate glass used by 3M™ or rather reduced values (minus 60%) for theoretical tensile values.

Maximum loading pressure for hollow glass micro spheres

Using equation (3.1) the maximum pressure for S38 hollow glass micro spheres results to $p_{max} = 203$ MPa assuming a tensile strength of $\sigma = 3.31$ GPa, a radius $r = 14$ μm , a sphere shell thickness of $d = 0.75$ μm and a safety factor $S_f = 2$. According to the S38 data sheet from 3M™ [25] the target crush strength of S38 hollow glass micro spheres (90% survival) is at $p_{crush} = 27.5$ MPa. For thin walled spheres (as assumed) the maximum pressure applied outside or inside the spheres is the same. Thus, for storage density estimations regarding S38 spheres a maximum hydrogen pressure of $p_{max,S38} = 27.5$ MPa will be assumed.

For storage density estimations regarding idealized spheres however, a maximum hydrogen loading pressure of $p_L = 85$ MPa is assumed, since higher pressure appears unpractical from an energy consideration point of view [4]. For example, multistage compression from atmospheric pressure to 20 and 80 MPa requires 11.9% and 19.1% of the lower heating value of hydrogen, which is still less energy than needed for liquefying hydrogen [4]. State of the art hydrogen

compressors for automotive applications work up to pressures of $p = 85$ MPa to deliver hydrogen at $p = 70$ MPa [29, 51]. Higher pressures are not feasible from an engineering point of view. To sum up, in further calculations regarding the storage density, a hydrogen loading pressure of $p_L = 85$ MPa at loading temperature T_L will be assumed.

It must be mentioned that the pressure inside the hollow glass micro spheres will decrease during the cooling process and increase again during the extraction process, when heat is applied to release hydrogen out of the spheres. The pressure inside the hollow glass micro spheres during extraction p_E is critical for the sphere integrity (equation (3.1)), since there is no outside pressure. In contrast to this, the loading pressure is not critical, as during the cooling down phase after loading the hollow glass micro spheres are still in a ~ 85 MPa hydrogen environment. As a result there is no pressure difference between the inside and outside of the spheres after cooling down at the end of the loading process. The extraction pressure can be deducted from loading pressure p_L , loading temperature T_L and extraction temperature T_E as described in the appendix under section 9.1.2.

Since the loading process is not critical, the loading temperature T_L is assumed to be the same as the extraction temperature T_E and thus the extraction pressure p_E is the same as the loading pressure p_L .

The amount of hydrogen n inside one sphere is given by the real gas equation

$$p_L V_{Sp} = nRT_L Z_L(p_L, T_L) \quad (3.2)$$

with loading pressure p_L , sphere volume V_{Sp} , amount of mol n , gas constant R , loading temperature T_L and compressibility factor $Z_L(p, T)$ for loading conditions (equation (3.3)) [10]

$$Z_L = 1 + B_L p_L, \quad (3.3)$$

where $B_L(T)$ is the total virial coefficient for loading conditions, given by [10]

$$B_L = \frac{B_1}{T_L} + \frac{B_2}{T_L^2}. \quad (3.4)$$

Regarding the real gas equation (equation (3.2)) it must be mentioned that there exist different ways to express the compressibility factor [10, 52, 53]. Most correlations found do not apply for temperatures higher than 100 °C, but that found in [10], for temperatures up to 120 °C. This correlation was compared with hydrogen density values for temperatures of 0 °C to 300 °C

and pressures of 0.1 MPa to 100 MPa calculated with the free reference library *CoolProp* [23]. The maximum and mean relative error found were $max\ error = 1.89\ %$ at 0 °C and 100 MPa and $mean\ error = 0.66\ %$. The errors increase with pressure but decrease with temperature. Eventually the correlation of Chen (2009) [10] was applied. Another reason to use the correlation of Chen (2009) (equation (3.3) and (3.4)) was with the prospect of analytical solvability of further equations.

As already mentioned loading and extraction conditions are assumed to be the same and thus it will no longer be distinguished between loading and extraction temperatures or pressures.

Gravimetric and volumetric hydrogen storage density of S38 hollow glass micro spheres

The gravimetric storage density γ_G is given by

$$\gamma_G = \frac{\rho_{H_2}(r-d)^3}{\rho_{H_2}(r-d)^3 + \rho_{gl}(r^3 - (r-d)^3)}, \quad (3.5)$$

where ρ_{glass} is the glass density of the sphere shell, r the radius of the spheres, d the sphere shell thickness (see Figure 3.4) and ρ_{H_2} the hydrogen density at pressure p_E and temperature T_E given by

$$\rho_{H_2} = \frac{p_E M_{H_2}}{RT_E Z_E} = \frac{p_E M_{H_2}}{RT_E (1 + B_E p_E)}. \quad (3.6)$$

In the following, the ratio of sphere shell thickness to sphere radius will be used in order to simplify the equations. It is given by

$$\varepsilon = \frac{d}{r}. \quad (3.7)$$

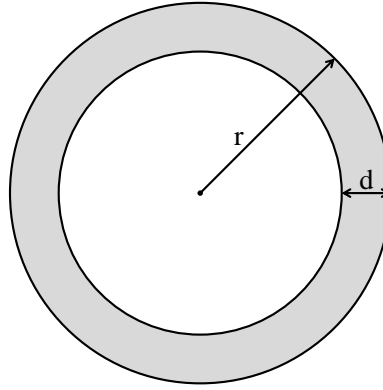


Figure 3.4: Sketch of a hollow glass microsphere

Inserting equation (3.6) into (3.5) and using relation (3.7) yields the gravimetric hydrogen storage density γ_G as a function of the extraction pressure, which is the hydrogen pressure inside the spheres at extraction temperature T_E ,

$$\gamma_G = \frac{1}{1 + \frac{\rho_{gl}RT_E}{M_{H_2}} \left(\frac{1}{(1-\varepsilon)^3} - 1 \right) \left(\frac{1}{p_E} + B_E \right)}. \quad (3.8)$$

Using an extraction pressure of $p_{max,S38} = 27.5$ MPa, which is the maximum pressure for S38 glass spheres, and an extraction temperature of 250 °C, a glass density of 2230 kg/m³ [24], sphere radius $r = 12$ μm and a shell thickness $d = 0.75$ μm the gravimetric hydrogen storage density becomes $\gamma_G = 2.4$ wt%. For a pressure of $p_E = 85$ MPa it would be $\gamma_G = 5.9$ wt%.

The radius r of the S38 hollow glass microspheres was determined by measuring the diameter of over a thousand spheres and weighting their radius volumetrically (equation (3.9)), because larger spheres contribute more to the storage density. The measurement was done with scanning electron micrographs (see Figure 3.5 left) and *ImageJ*-Software (v.1.48) [54]. The sphere shell thickness was determined in a similar way, but for that the spheres had to be crushed first in order to uncover the cross section of the sphere shell (see Figure 3.5 right).

$$r_{\bar{V}} = \sqrt[3]{\frac{\sum_i^k r_i^3}{k}} \quad (3.9)$$

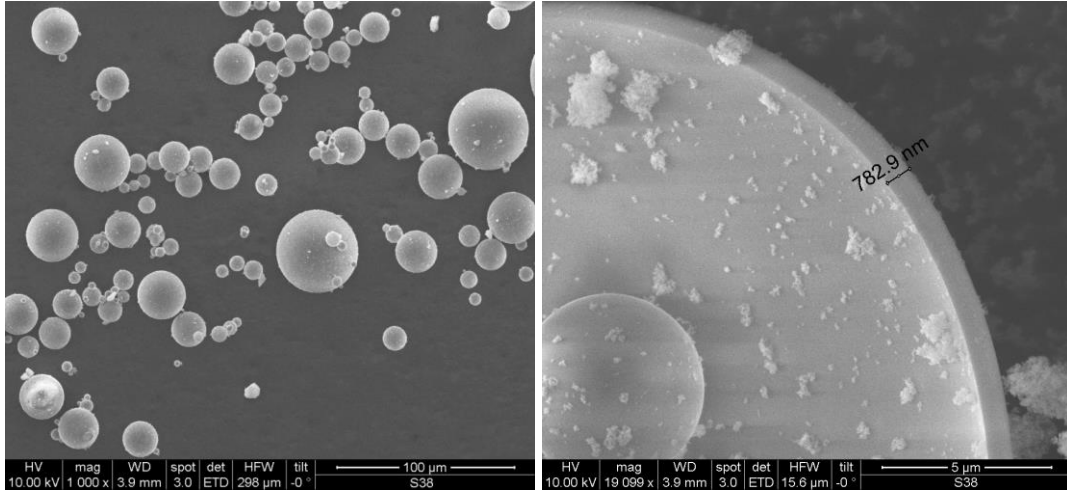


Figure 3.5: left, image of S38 hollow glass micro spheres taken with a scanning electron microscope; right, cross section of a hollow glass microsphere with measured sphere shell thickness,; the white powder between the spheres is silicic acid which works as anti-caking agent

The measured values for r and d correspond very well with the density given in the data sheet of the S38 hollow glass micro spheres of, where the packing factor is neglected [25]. $\rho_{3M} = 0.38 \text{ kg/m}^3$ versus $\rho_{measured} = 0.385 \text{ kg/m}^3$.

The volumetric storage density γ_V is given by

$$\gamma_V = f \frac{\rho_{H_2} (r - d)^3}{r^3}, \quad (3.10)$$

where f is the packing factor. For random packed monosized spheres the packing factor is usually about $f = 0.63$ [4, 55, 56]. Inserting equation (3.6) into (3.10) and using relation (3.7) yields the volumetric storage density

$$\gamma_V = f \frac{M_{H_2}}{RT_E} \frac{(1 - \varepsilon)^3}{\frac{1}{p_E} + B_E}. \quad (3.11)$$

For an extraction pressure of 27.5 MPa, extraction temperature of 250 °C, sphere radius $r = 12 \text{ }\mu\text{m}$ and a shell thickness $d = 0.75 \text{ }\mu\text{m}$ the volumetric hydrogen storage density is $\gamma_V = 6.0 \text{ kg/m}^3$. For a pressure $p_E = 85 \text{ MPa}$ it would be $\gamma_V = 15.44 \text{ kg/m}^3$.

Figure 3.6 shows the gravimetric storage density γ_G and the volumetric storage density γ_V of S38 hollow glass micro spheres as a function of the pressure at an extraction temperature of 250 °C.

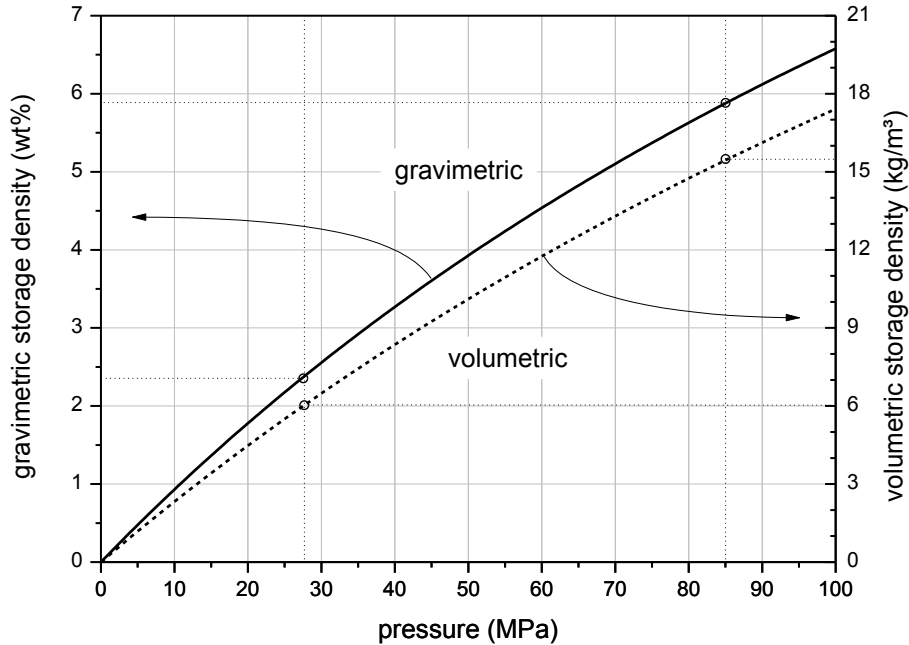


Figure 3.6: Theoretical gravimetric and volumetric storage density of S38 hollow glass micro spheres as a function of hydrogen pressure inside; $\gamma_G = 2.4$ wt% and $\gamma_V = 6.0$ kg/m³ at a pressure of 27.5 MPa and $\gamma_G = 5.9$ wt% and $\gamma_V = 15.4$ kg/m³ at a pressure of 85 MPa and an extraction temperature of 250 °C.

Gravimetric and volumetric hydrogen storage density of hollow glass micro spheres with optimized radius and shell thickness

Under the assumption of perfect spheres with no surface scratches or other imperfection, the spheres could withstand much higher pressures than the S38 as we have seen before. Such spheres can be manufactured and many research groups fabricate their own spheres as discussed in section 3.1.6.

When using optimized hollow glass micro spheres, the minimum sphere shell thickness d can be expressed by the sphere radius r and the tensile strength σ using the relation for a thin walled sphere under constant inner pressure [4, 45, 46].

$$\varepsilon_{opt} = \frac{d}{r} = \frac{S_f P_E}{2\sigma} \quad (3.12)$$

Using this relation for equation (3.8) and (3.11) gives the gravimetric and volumetric storage density ($\gamma_{G,opt}$, $\gamma_{V,opt}$) for hollow glass micro spheres with optimized ratio of radius r and shell thickness d .

$$\gamma_{G,opt} = \frac{1}{1 + \frac{\rho_{gt}RT}{M_{H_2}} \left(\frac{1}{\left(1 - \frac{S_f P_E}{2\sigma}\right)^3} - 1 \right) \left(\frac{1}{P_E} + B_E \right)} \quad (3.13)$$

$$\gamma_{V,opt} = f \frac{M_{H_2}}{RT} \frac{1}{\frac{1}{P_E} + B_E} \left(1 - \frac{S_f P_E}{2\sigma} \right)^3 \quad (3.14)$$

For a pressure of 85 MPa, an extraction temperature of 250 °C and a safety factor $S_f = 2$ this gives a gravimetric hydrogen storage density of $\gamma_{G,opt} = 14.2$ wt% and a volumetric hydrogen storage density of $\gamma_{V,opt} = 17.3$ kg/m³.

Figure 3.7 shows the gravimetric storage density $\gamma_{G,opt}$ and the volumetric storage density γ_V of hollow glass micro spheres with optimized shell thickness as a function of the pressure at an extraction temperature of 250 °C. Compared to S38 hollow glass micro spheres the optimized spheres have a much higher gravimetric storage density, but only a slightly higher volumetric storage density. The decrease of the gravimetric storage density with increasing pressure is surprising, but can be explained by the relation of glass density and hydrogen density. Increasing pressure necessitates thicker the sphere shells, which means basically more glass. With more glass the spheres become heavier and at the same time the hydrogen volume inside the sphere decreases. Only a hydrogen density higher or equal the glass density would cancel that effect, which is of course not possible.

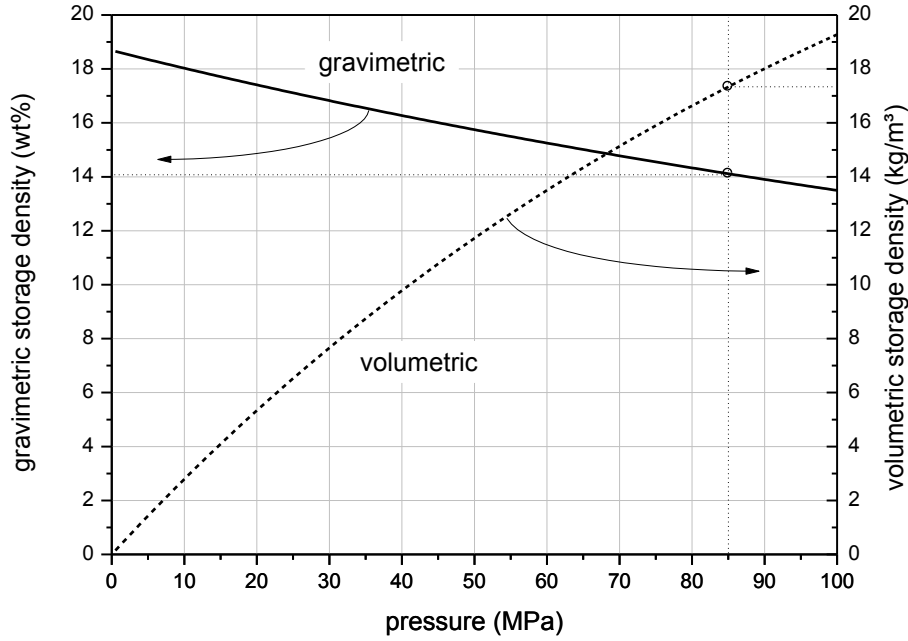


Figure 3.7: Theoretical gravimetric and volumetric storage density of optimized hollow glass micro spheres as a function of hydrogen pressure inside, $S_f = 2$; $\gamma_G = 14.2$ wt% and $\gamma_V = 17.3$ kg/m³ for a pressure of 85 MPa at an extraction temperature of 250 °C.

It can be concluded, that the gravimetric storage density of hollow glass micro spheres exceeds the DOE targets 2015, but that the volumetric storage density does not meet those targets. Table 3.3 shows a comparison of the theoretical storage densities of hollow glass micro spheres (S38 and optimized) with the DOE targets 2017 and ultimate [9].

	glass spheres		DOE targets	
	S38	optimized	2017	ultimate
γ_G (wt%)	2.4	14.2	5.5	7.5
γ_V (kg/m ³)	6.0	17.3	40.0	70.0

Table 3.3: Comparison of gravimetric and volumetric hydrogen storage densities of hollow glass microspheres (S38 spheres and optimized spheres) compared with the DOE targets for hydrogen storage densities [9]. For optimized spheres a wall thickness safety factor of $S_f = 2$ was used.

Storage densities as a function of the shell thickness

In the last subsection it became clear, that the gravimetric storage density γ_G of hollow glass micro spheres increases with decreasing pressure, for with decreasing pressure the required sphere shell thickness is also decreasing. In contrast to that, the volumetric storage density has a maximum at a certain ratio of shell thickness to radius. This is due to the fact that the volumetric storage density is proportional to the sphere inner volume and the maximal allowed pressure inside the sphere. The inner volume of the sphere decreases with increasing shell thickness whereas the maximal pressure increases with increasing shell thickness.

p_E can be expressed by the ratio ε of sphere shell thickness d to sphere radius r :

$$p_E = \varepsilon \frac{2\sigma}{S_f}, \quad (3.15)$$

Using expression (3.15) and inserting it into equations (3.13) and (3.14) or (3.8) and (3.11), yields the gravimetric and volumetric storage density as a function of ε for optimized spheres.

$$\gamma_{G,opt}(\varepsilon) = \frac{1}{1 + \frac{\rho_{gl}RT}{M_{H_2}} \left(\frac{1}{(1-\varepsilon)^3} - 1 \right) \left(\frac{S_f}{2\sigma \cdot \varepsilon} + B \right)} \quad (3.16)$$

$$\gamma_{V,opt}(\varepsilon) = f \frac{M_{H_2}}{RT} \cdot \frac{(1-\varepsilon)^3}{\frac{S_f}{2\sigma \cdot \varepsilon} + B} \quad (3.17)$$

By deriving equation (3.17) and setting it to zero, the optimum ratio of shell thickness and sphere radius can be determined. Equation (3.18) gives the ratio ε for maximum volumetric storage density as a function of the tensile strength, the safety factor and the total virial coefficient B , which is temperature dependent (compare equation (3.4)),

$$\varepsilon(\gamma_V = \max) = -\frac{S_f}{3B\sigma} + \sqrt{\frac{2S_f^2 + 3S_f B\sigma}{18B^2\sigma^2}} \quad (3.18)$$

Figure 3.8 shows the behaviour of the gravimetric and volumetric storage density as a function of ε assuming different extraction temperatures T_E and safety factors S_f .

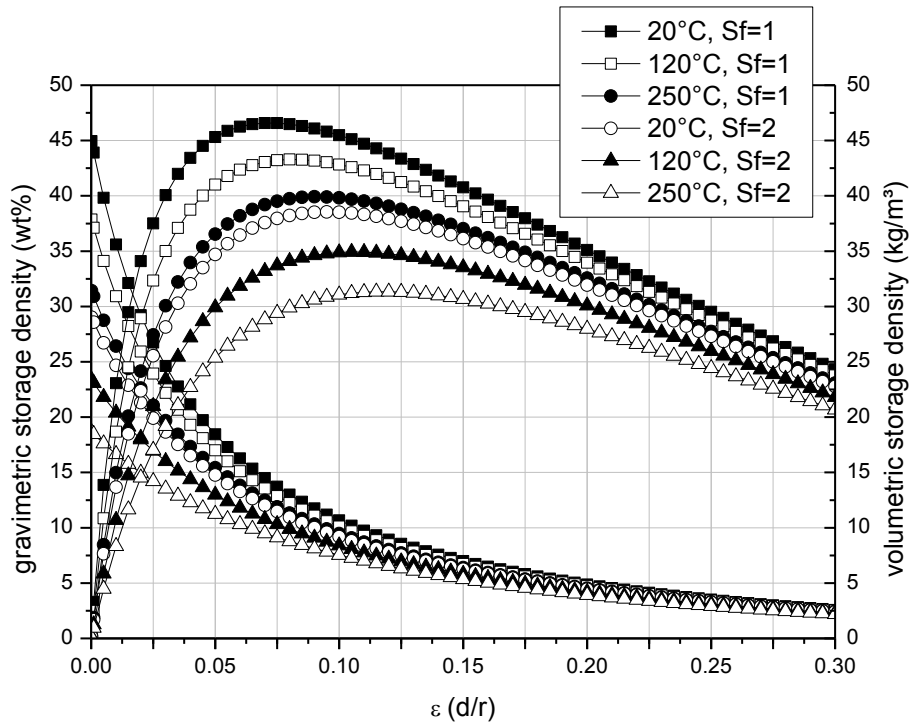


Figure 3.8: Gravimetric and volumetric storage densities of hollow glass microspheres as a function of ε , which is the ratio of shell thickness d to radius r of the spheres; illustrated for different safety factors S_f and extraction temperatures T_E ; the gravimetric storage density decreases with increasing shell thickness, whereas the volumetric storage density increases to a maximum before dropping again.

The maximum volumetric density is between $\varepsilon = 0.07 - 0.11$ this corresponds to maximum hydrogen pressures inside the spheres of $p = 232 - 728$ MPa, using equation (3.15) p. 43. It is obvious that such high pressures are not feasible for storing hydrogen. Energy losses due to the compression process would be much too high.

3.2.2. Hydrogen releasing process by temperature induced diffusion

Hydrogen permeation through glass can be described by two mechanisms: diffusion and chemical reaction of H_2 with glass. As an example hydrogen reduces ions like Fe^{3+} , Ce^{4+} or Sn^{4+} forming OH groups, e.g. $H_2 + 2(=SiO)^- + 2Fe^{3+} \leftrightarrow 2(=SiOH) + 2Fe^{2+}$. The reaction rate is much faster than the diffusion rate, making diffusion the limiting factor. The general form of the permeability $K(T)$ is given by [4, p. 777]:

$$K(T) = K_0 T^n \exp\left(\frac{-Q_K}{T}\right), \quad (3.19)$$

where the constants K_0 , n and Q_K are determined empirically. Some researchers use K_0 and Q_K while n is set equal to 1, [16, 30, 36, 57], whereas others use the standard Arrhenius law for which $n = 0$, [17, 31, 38]. Sometimes the values of K_0 and Q_K are expressed as a function of content of glass network formers, e.g. SiO_2 , B_2O_3 , and P_2O_5 denoted by G (mol%) or the amount of modifier oxides, e.g. CaO , Na_2O , MgO , SrO , and NaO , denoted by M [4]. Table 3.4 gives a summary of permeability constants K_0 and activation energies Q_K , which have been summarized by L. Pilon in [4] from different authors. For sake of completeness the original authors are also given [38, 58, 59, 60, 61, 62, 63, 64, 65]. In general, hydrogen permeability increases with G and decreases with M as can be seen in the suggested expressions. The resulting values of $K(T)$ can vary by several orders of magnitude depending on glass composition as has also been shown experimentally in [39]. The permeability can be considered to be independent of pressure to up to 100 MPa [4].

Composition	n	$K_0 \times 10^{-17}$ (mol/Pa m s)	$Q_K(\text{K})$	Source
Soda-lime glass (72% $\leq G \leq 100\%$)	0	8100	17330 - 127.8 G	[58] in [4]
Silicate glasses	1	$3.4+8 \times 10^{-4} M^3$	$3600 + 165 M$	[59] in [4]
Soda-lime glasses ($M = 19\%$)	1	20	5600	[59] in [4]
Vitreous silica (see [60])	0	58.1	4234	[61] in [4]
Vitreous silica (quartz)	0	8688	4469	[62] in [4]
Vitreous silica (quartz)	0	7409	4539	[63] in [4]
Pyrex (borosilicate) (D2)	0	10.7	4529	[64] in [4]
Pyrex (borosilicate)	1	2.787	4026	[65] in [4]
Pyrex (borosilicate) (D2)	0	23.1	4199	[38] in [4]

Table 3.4: Summary of permeability constants K_0 and activation energies Q_K of different glasses for hydrogen. Both, the permeability constant and the activation energy vary with the composition of the glass. G is the amount of glass network formers (in mol%), M the amount of modifying oxides (in mol%). The values were summarized and converted to same dimensions by L. Pilon, University of California, Los Angeles in [4]. Most correlations were found in the 1960ies and 1970ies.

For extraction behaviour calculations of S38 and optimized glass spheres the relations of Shelby (1974) is used [65], which was also used by Kitamura 2009 [36]. For ideal gas the pressure inside the spheres as a function of time is given by:

$$p(t) = p_{\infty} + (p_0 - p_{\infty})e^{-Ct}, \quad (3.20)$$

with the initial pressure inside the sphere p_0 , the ambient pressure p_{∞} and

$$C = K(T) \frac{3RT}{d \cdot r}. \quad (3.21)$$

From this equation it can be concluded that the diffusion rate decreases with increasing radius and shell thickness. Since larger spheres necessitate thicker shells to withstand the pressure, as we have seen before in equation (3.1), the diffusion rate can be nicely set by changing the sphere size. Larger spheres and/or thicker shells result in slower diffusion, smaller spheres and/or thinner shells result in faster diffusion.

Using the real gas equation (see eq. (3.2) and (3.3), p. 36) the hydrogen pressure inside the sphere becomes:

$$p(t) = \frac{p_0 - p_{\infty} + (1 + p_0 B(T)) \cdot p_{\infty} e^{Ct(Bp_0+1)}}{B(p_{\infty} - p_0) + (1 + p_0 B(T)) e^{Ct(Bp_0+1)}} \quad (3.22)$$

The detailed derivations of equations (3.20) – (3.22) are given in the appendix in section 9.1.3.

Figure 3.9 shows a comparison of pressure development in a sphere at room temperature using ideal gas and real gas equations. The initial pressure was set to $p_0 = 47.6$ MPa which corresponds to a loading pressure of 85 MPa at 250 °C. It can be seen that for real gas the pressure drops faster in the beginning than for an ideal gas. The difference is about 20% and can be estimated by a factor

$$\frac{p(t)_{ideal}}{p(t)_{real}} = B(T)p_0 \cdot (1 - e^{-Ct}) + 1. \quad (3.23)$$

For this the ambient pressure p_{∞} was assumed to be zero, which is acceptable due to the fact that usually $p_{\infty} \ll p_0$.

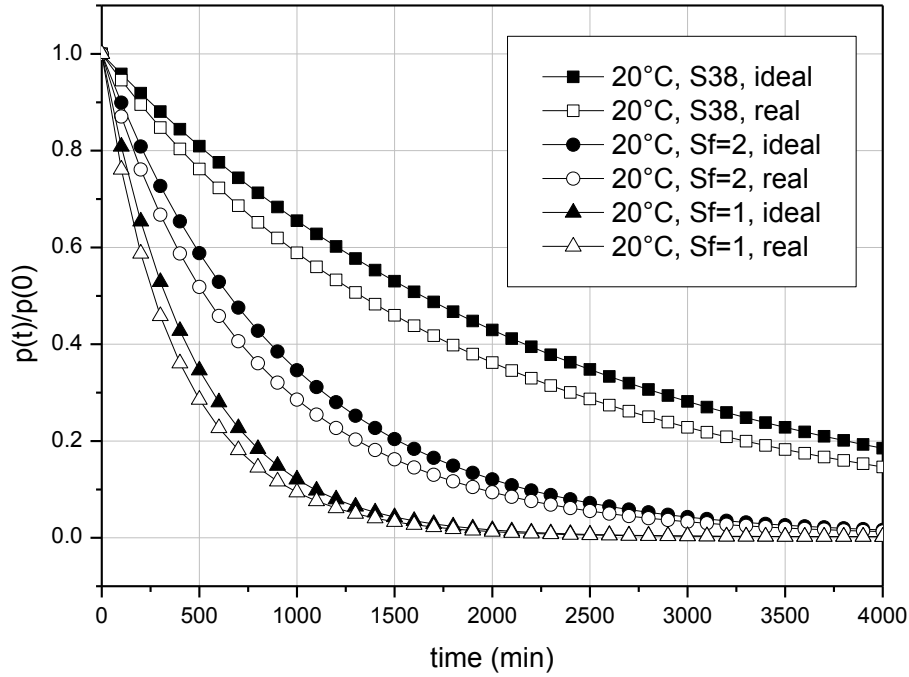


Figure 3.9: Comparison of diffusion behaviour of different microspheres at room temperature for real gas and ideal gas using the relation for borosilicate glass of [65]; radius $r = 14 \mu\text{m}$, shell thickness corresponding to radius, safety factor and a loading pressure of 85 MPa at 250 °C, i.e. $d_{sfl} = 0.13 \mu\text{m}$, $d_{sfl2} = 0.26 \mu\text{m}$ and $d_{s38} = 0.75 \mu\text{m}$. The loading pressure corresponds to 48 MPa at room temperature and is the initial pressure to which the pressure in the graph is normalized.

Figure 3.9 also shows that spheres with this dimension would leak hydrogen in large amounts even at room temperature. As an example, after only 6 hours one half of the loaded hydrogen would have left spheres with an radius $r = 14 \mu\text{m}$ and a shell thickness of $d = 0.13 \mu\text{m}$. The time constant when the pressure has dropped to $1/e$ times the initial pressure should be in the range of 100 days [33]. Using the diffusion correlation for ideal gas (equation (3.20)) and again assuming $p_\infty = 0$, the half time can be written as (compare [57])

$$t_{1/e} = \frac{d \cdot r}{3 \cdot K(T) \cdot RT} \quad (3.24)$$

Using equation (3.12) this can be rewritten to

$$t_{1/e} = \frac{r^2 p_0 S_f}{6\sigma \cdot K(T) \cdot RT} \quad (3.25)$$

Figure 3.10 shows the permeability time constants $t_{1/e}$ at 20 °C (= leakage time t_{leak}) for different sphere radii and safety factors for two different glasses, i.e. borosilicate glass and soda lime glass. The permeability data was taken from Shelby (1974) [65] for borosilicate glass and from Souers (1978) [59] for soda lime glass. It is conspicuous that at 20 °C soda lime glasses behave rather different than borosilicate glasses and meet $t_{1/e} = 100$ days at sphere radii of $r = 18 - 38 \mu\text{m}$, depending on the safety factor. Borosilicate spheres of the same size would already be nearly empty within 15 days, which makes borosilicate glass not applicable for hydrogen storage.

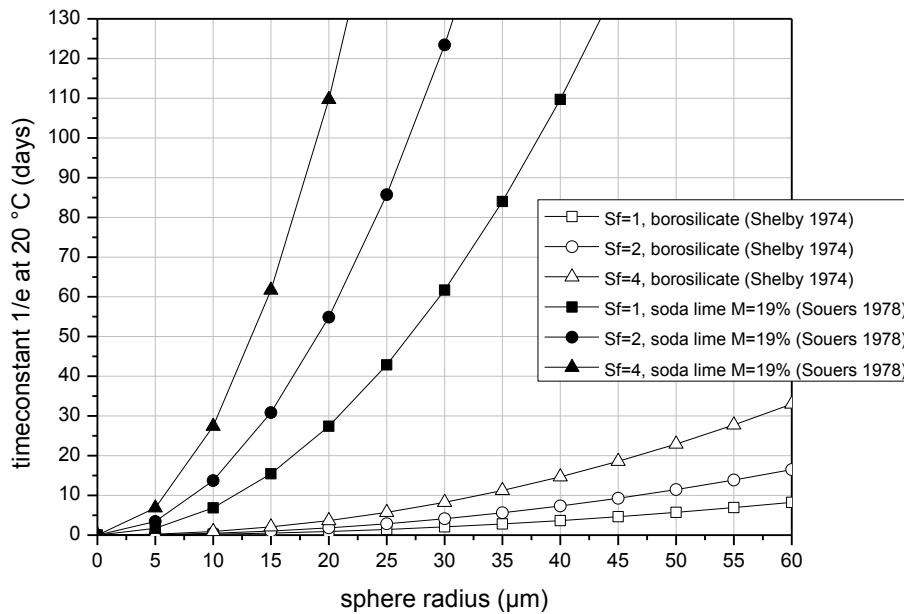


Figure 3.10: Comparison of the permeability time constant at 20 °C, which is the time needed for the pressure to drop to $1/e \times$ initial pressure; given for soda lime glass and borosilicate glass for different sphere radii. Soda lime glass has much higher permeability time constants, thus much lower hydrogen leak rate than borosilicate glass

On the other hand, when comparing the same spheres at 250 °C, which would be the hydrogen extraction temperature, the situation is quite different (see Figure 3.11). At 250 °C the permeability time constants $t_{1/e}$ (= extraction time t_{extr}) of soda lime spheres and borosilicate spheres are rather similar and reach values of less than 10 minutes. So even as soda lime glass has very low leakage at room temperature, feasible hydrogen release rates could be realized for extraction temperatures of $T_E = 250$ °C.

As an example soda lime glass spheres with a radius of $r = 25 \mu\text{m}$ and a shell thickness of $d = 0.65 \mu\text{m}$, which corresponds to a safety factor of $S_f = 2$, have a leakage time of $t_{leak} = 86$ days at 20 °C and a extraction time of $t_{extr} = 8.8$ minutes at 250 °C.

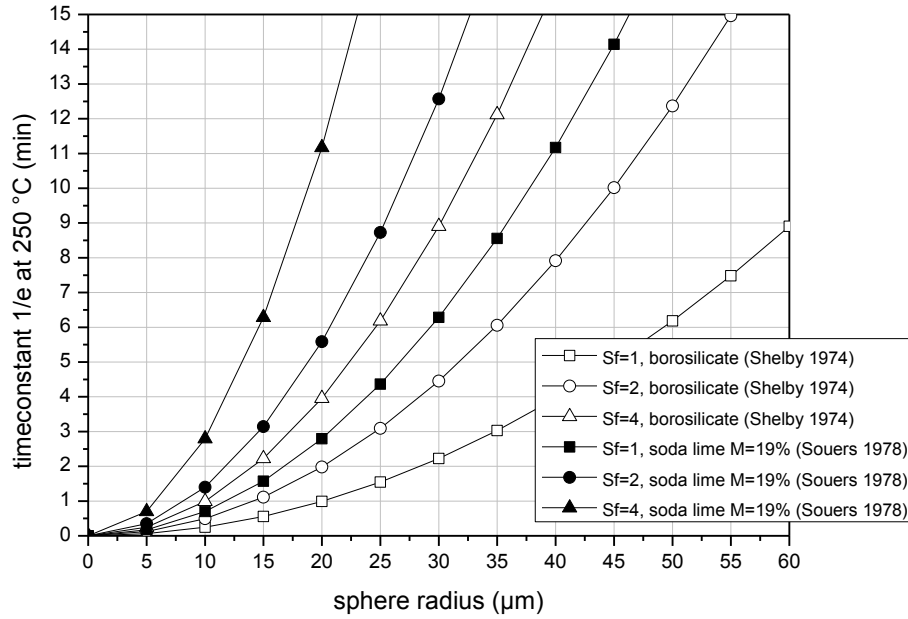


Figure 3.11: Comparison of the permeability time constant at 250 °C, which is the time needed for the pressure to drop to $1/e \times$ initial pressure; given for soda lime glass and borosilicate glass for different sphere radii. At 250 °C soda lime glass and borosilicate glass have similar hydrogen extraction time constants. Extraction time constants of less than 10 minutes are feasible.

In order to compare the same sphere dimensions for borosilicate and soda lime spheres, the difference of tensile strength of soda lime glass and borosilicate glass was neglected. In fact, the tensile strength of soda lime spheres exceeds the tensile strength of borosilicate glass, making this assumption acceptable (see Table 3.2, p. 35).

Hydrogen diffusion experiments with 3M™ S38HS hollow glass microspheres that have been carried out at the Vienna Institute for Atomic and Subatomic Physics by Dyrnjaja et al. [66] were compared with the permeability relation in [65] and showed good agreement.

In this section it was shown that it is possible to synthesize spheres, which meet the demands of permeability. Soda lime spheres have low leakage rates at room temperature and high hydrogen diffusion rates at elevated temperatures of $T_E = 250$ °C. As already mentioned in the beginning of chapter 3, the temperature must not be too high, because of the resulting high vapour pressure of water in the proposed system.

If it would be possible to better control the permeability to decrease the extraction temperature for the releasing process and at the same time keep low diffusion rates at room temperature, the storage densities could be increased. Decreasing the extraction temperature from 250 °C to 100 °C would increase the storage densities by about 40%; from $\gamma_G = 14.2$ wt% and $\gamma_V = 17.3$ kg/m³ densities to $\gamma_G = 20.2$ wt% and $\gamma_V = 24.5$ kg/m³.

The following chapter will deal with a combined storage material containing chemical hydride and hollow glass microspheres.

3.3. Combination of glass microspheres with a hydrolytic system

The previous chapters gave an overview of different hydrogen storage materials and systems. Moreover hydrogen storage in hollow glass microspheres was discussed in detail including storage densities and the releasing process.

In this section a combined system of hollow glass microspheres and NaBH₄ hydrolysis will be described. To do this, first the hydrolysis of NaBH₄ itself will be explained. Secondly, the proposed combined system will be described, before discussing gravimetric and volumetric storage densities. Furthermore, theoretical aspects of the proposed system, such as possible glass sphere hydride ratios, packing densities, thermal limits and water requirements will be investigated.

3.3.1. Hydrolysis of sodium borohydride NaBH₄

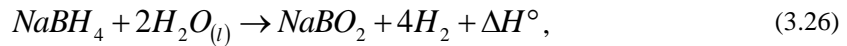
As already mentioned in section 2.2.2, irreversible hydrolysis is possible for a number of different hydrides, e.g. NH₃BH₃, NaBH₄, LiBH₄, CaH₂, NaAlH₄ [5, 20, 67]. Despite this fact, this section will focus only on NaBH₄, since that hydride was actually used in the experiments due to its promising properties and good availability. This section will deal with the hydrolytic reaction, water requirements, resulting material storage densities, some proposed systems and the recycling process of NaBH₄.

The hydrolysis of NaBH₄ has to be catalysed in order to react completely, as will be discussed in detail in section 6. In this section only a very short overview over possible catalysts will be given.

Sodium borohydride (NaBH₄) has a gravimetric hydrogen density of $\gamma_G = 10.66$ wt% and a volumetric hydrogen density of $\gamma_V = 114.03$ kg/m³, which is higher than that for compressed or liquid hydrogen and well within DOE-targets 2017, i.e. 5.5 wt% and 40 kg/m³. This makes NaBH₄ a very interesting material for hydrogen storage. Moreover sodium borohydride is stable in dry air and easily handled like common chemicals, compared with other hydrogen storage materials. NaBH₄ solutions are not flammable and the reaction products are environmentally benign, the H₂ generation rate is easily controlled, the reaction product NaBO₂ can be recycled and H₂ can be generated even at low temperatures [68]. Some of these advantages do not account for the storage system proposed in this thesis, like low temperature hydrolysis, but it becomes clear why NaBH₄ is a very interesting candidate for hydrogen storage applications.

NaBH₄ can either be stored as a stabilized aqueous solution, where a certain amount of NaBH₄ is dissolved in water and stabilized against self-hydrolysis by NaOH, or as a solid in powder form or as granulate.

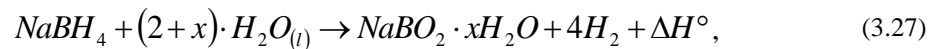
The ideal hydrolytic reaction can be written as



where ΔH° is the enthalpy difference calculated from property tables given in *CRC Handbook of Chemistry and Physics, 88th Edition* (2008) [3] (see also Table 3.5). The enthalpy difference results to $\Delta H = -216.8$ kJ/mol (compare [69]). Resulting material storage densities are $\gamma_G = 10.9$ wt% and $\gamma_V = 111.6$ kg/m³.

Water requirements

In contrast to the ideal reaction, when using solid NaBH₄ or highly concentrated solutions of NaBH₄, the products of the hydrolysis form hydrated borates. The favoured hydrated metaborates correspond to NaBO₂·2H₂O and NaBO₂·4H₂O. Both borates become completely anhydrous at elevated temperatures, i.e. NaBO₂·2H₂O at 350 °C, NaBO₂·4H₂O above 400 °C [70, 71]. Furthermore the borate has a lower solubility than the hydride. The solubility of NaBH₄ in water at 25 °C is 55g/100g water, whereas the solubility of NaBO₂ is 28g/100 g water [69] (see Table 3.5). As a result the solubility of the hydride is not a limiting factor, since more hydride can be dissolved in water than can react, but is limited by solubility of the borate, thus by the excess of water. The reaction equation must be more accurately written as [71]:



where x is the water excess factor. To keep the liquid state of NaBO₂ the concentration of NaBH₄ at 25 °C should be below 14g/100g water, which corresponds to $x = 13.05$. The resulting storage densities result to $\gamma_G = 2.6$ wt% and $\gamma_V = 26.25$ kg/m³. The large quantity of water needed to keep the solution liquid is the major drawback of sodium borohydride hydrolysis. To reduce the water requirements, water recovery from the fuel cell has been proposed [71], where water generated by the fuel cell is re-used for the hydrolytic reaction. That decreases the water excess factor to $x = 9.05$ and increases material storage densities to $\gamma_G = 3.4$ wt% and $\gamma_V = 34.33$ kg/m³.

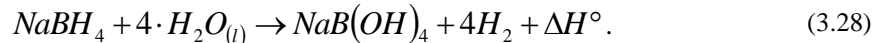
Following this approach the company Millennium Cell demonstrated hydrolysis of NaBH_4 solutions with fuel cell power sources for various applications, including the modification and testing of a Chrysler Natrium passenger vehicle in 2003, as reported in Klebanoff 2013, p. 82. The main issues were the requirement of large amounts of excess water on-board the vehicle and precipitation of NaBO_2 . Millennium Cell essentially concluded that the solution-based NaBH_4 approach was not feasible to reach the DOE-targets in terms of storage density and costs [6].

	density (kg/m^3)	enthalpy (kJ/mol)	molar weight (g/mol)	solubility in water (g/g)
H_2O	997	-285.8	18.015	-
H_2	0.082	0.0	2.016	-
NaBH_4	1070	-188.6	37.833	0.55
NaBO_2	2460	-977.0	65.800	0.28
NaB(OH)_4	-	-1558.6	101.830	-

Table 3.5: Physical and chemical properties of reaction compounds and materials at normal conditions [3, 69, 71]

In short, when NaBO_2 solubility is taken into account in order to only handle liquids, the material storage densities decrease rapidly.

When neglecting the solubility the hydration of the borate NaBO_2 still has to be taken into account. For this particular reaction the water excess factor then results to $x = 2$ [67] and equation (3.27) can be rewritten to



The reaction enthalpy changes accordingly to $\Delta H^\circ = 226.8 \text{ kJ/mol}$. Neglecting the solubility of NaBO_2 and recovering fuel cell water would yield very high values of material storage densities, i.e. $\gamma_G = 21.3 \text{ wt\%}$ and $\gamma_V = 228.07 \text{ kg/m}^3$. However, this would necessitate a cartridge system, where educts (NaBH_4) and products (NaBO_2) remain in the same containment. The cartridge would also have to work as the reaction chamber. Since no fluid pumping would be possible the required catalyst must be added to NaBH_4 solid. Considering the space for water the volumetric storage density is decreased to the value of the ideal reaction, i.e. $\gamma_V = 111.63 \text{ kg/m}^3$. This concept is the basis for the system proposed in this thesis, where the hydrolysis of solid sodium borohydride shall be promoted by catalyst coated hollow glass microspheres.

Table 3.6 shows a summary of storage densities of NaBH_4 hydrolysis under different presumption, i.e. ideal reaction, with respect to NaBO_2 solubility and with implemented water recovery from the fuel cell.

NaBH ₄ hydrolysis	γ_G (wt%)	γ_V (kg/m ³)
ideal reaction	10.9	111.63
considering NaBO ₂ solubility	2.6	26.25
considering NaBO ₂ solubility and fuel cell water recovery	3.4	34.33
considering fuel cell water recovery, but neglecting NaBO ₂ solubility	21.3	111.63
DOE-targets 2017 (ultimate)	5.5 (7.5)	40 (70)

Table 3.6: Summary of achievable hydrogen material storage densities considering different aspects of the reaction; if solubility is taken into account the storage densities are much lower.

Reaction kinetics

The formation of basic hydrated metaborate increases the pH-value of the NaBH₄-solution, inhibiting the reaction even though it is strongly favoured thermodynamically. This results in slow kinetics and limited hydrogen generation capacity of only 7-8% by self-hydrolysis of NaBH₄ at room temperature [71, 72, 73]. This self-hydrolysis is also the reason why NaBH₄-solutions have to be stabilized for long time storage. This is usually done by adding 4 – 10 wt% of NaOH to the solution [69, 72, 74, 75]. Self-hydrolysis was studied by Schlesinger et al. [76] in the 1950's in dependence of both pH-value and temperature. According to Retnamma et al. [73], Kreevoy and Jacobson (1979) reported the reaction rate empirically as:

$$\log\left(t_{1/2}\right) = pH - (0.034 \cdot T - 1.92), \quad (3.29)$$

where the half-time of NaBH₄ decomposition $t_{1/2}$ is given in minutes and temperature T in Kelvin. Thus high pH and low temperature stabilize the solution against self-hydrolysis. This relation accounts for pH in the range of 7 to 10 and temperatures of 15 to 35 °C.

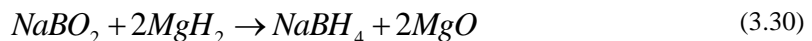
In order to increase reaction rates of pure NaBH₄ or a stabilized NaBH₄-solution the hydrolysis reaction can be promoted thermally or by adding a catalyst. Since the hydrogen release process should work under mild conditions, catalysts are much more investigated. Already in 1953 Schlesinger et al. investigated acid catalysis and metal catalysis for NaBH₄ hydrolysis [76]. Today, research is focused on metal catalysis (Co, Ru, Ni, Pt, Fe, Pd, Rh, Cu,

Zn, and more) which was currently summarized by Demirci (2015). Investigated support materials are carbons, TiO_2 , $\gamma\text{Al}_2\text{O}_3$, LiCoO_2 , Ni foam, Polymers, Oxides and Zeolites and others [77]. Most research groups study catalysed hydrolysis of NaBH_4 -solution rather than NaBH_4 as a solid, because fluids are much easier handled than solids [69, 72, 74, 78, 79, 80, 81, 82]. Others used NaBH_4 powder and mixed it with the catalyst before adding water to initiate the hydrolysis [83, 84, 85, 86, 87]. A more detailed overview of potential catalysts will be given in chapter 6.

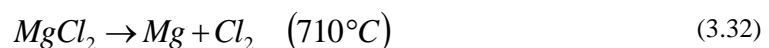
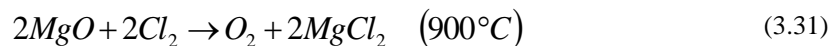
Thermally promoted hydrolysis was investigated by Kojima et al. (2004) [83]. They reached H_2 yields from 2.4% to 37% at temperatures of 23 °C to 200 °C and concluded that without a catalyst hydrogen generation is not sufficient. Another method for NaBH_4 hydrolysis is to use water steam instead of a catalyst which was investigated by Marrero-Alfonso et al. (2007) [70]. They concluded that 85% hydrogen yield is possible within 200 minutes. The energy to vaporize the water could be provided by the hydrolytic reaction. However, amounts of water vapour require a large volume, which might decrease volumetric storage density of the total system.

Recycling of NaBO_2 and pricing of NaBH_4

The reversibility of the hydrolytic reaction is a key issue for the use of the hydride as an energy carrier, thus there are many works regarding recycling of NaBO_2 to NaBH_4 . However, most publications focused on one process only [88, 89, 90, 91]:



Recycling of MgO was only addressed by Kojima and Haga (2003) and Ouyang et al. (2014) [92, 93]. Kojima and Haga (2003) proposed a complex process of several steps using coke to reduce MgO , whereas Ouyang et al. (2014) proposed a much simpler process (see Figure 3.12) with chlorine:



The calculated efficiency of this process is only 49.91%, which is below the DOE-target of 60%. The efficiency could be increased using carbothermal reduction in a solar furnace as

reported in [93, 94]. However, this would necessitate the use of coke similar to the process proposed by Kojima and Haga (2003) which is not desirable, because of CO₂ concerns.

In short, recycling efficiencies of NaBO₂ to NaBH₄ must be increased in order to establish NaBH₄ as a potential hydrogen carrier. Thus the recycling process is still a subject of research.

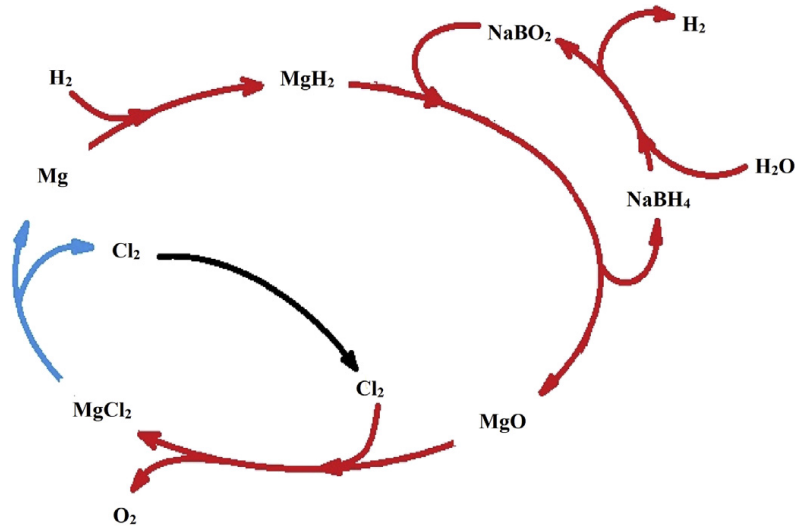


Figure 3.12: Recycling process of NaBO₂ proposed by Ouyang et al. (2014) [93]; NaBO₂ is reduced by MgH₂, which is reduce by Cl₂, Mg is again hydrogenated to reduce NaBO₂

The price of NaBH₄ has decreased since 1999 from 85 €/kg [67], to 67 \$/kg in 2000, to 46 \$/kg in 2006 [95] and has dropped to about 25-30 €/kg in 2014 [96] (assuming 1 € ≅ 1.2 \$). The NaBH₄ pricing over the last 15 years is illustrated in Figure 3.13.

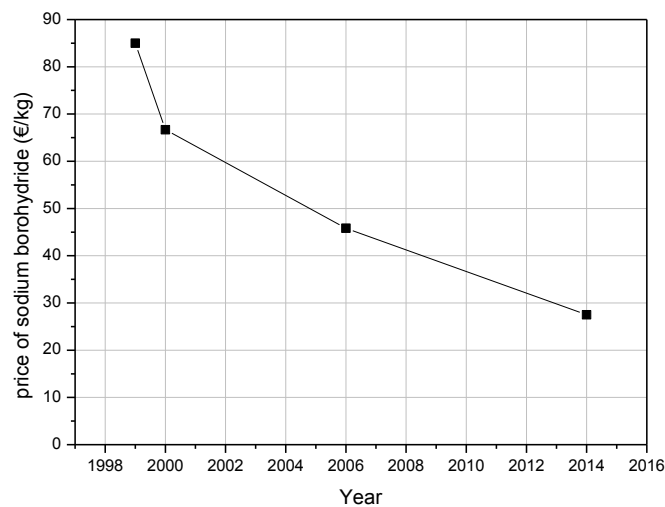


Figure 3.13: NaBH₄ price over the last 15 years

In 2008 the DOE published a no-go recommendation for sodium borohydride for on-board automotive hydrogen storage. The main issues of NaBH₄ as hydrogen storage material for on-board vehicular applications can be summarized [95]:

- Storage capacity targets
- NaBO₂ recycling, and
- Cost

As was shown, since then costs have decreased to 30 €/kg NaBH₄ which corresponds to 281 €/kg H₂. This is far beyond the goal of 2.8-5.6 €/kg, which is the 2017 and ultimate DOE-target [9], assuming a prize of 1.4 €/kg. The one time system costs of the storage system should not be beyond 333 €/kg H₂.

As described, the recycling process is still a subject of research. The storage capacity will be addressed in the following chapter.

3.3.2. Description of the proposed hydrogen storage system

In section 3.2.2, it became clear that in order to release hydrogen captured in the spheres in a feasible time, i.e. $t_{extr} < 10$ minutes, a temperature of 250 °C has to be applied to induce a sufficiently fast diffusion process. As it was shown, the necessary heat can be supplied by a furnace, a heating wire or an infrared lamp [35]. However all these methods require energy on-board the vehicle and reduce the electrical efficiency of the total system. In addition, it was shown that a hydrogen storage system consisting only of hollow glass microspheres on the one hand exceeds the DOE-targets in terms of gravimetric storage density, but will never meet them in respect to volumetric storage density. To overcome both issues Keding and Tajmar (2008) proposed a method to combine hollow glass microspheres with a hydrolytic system [22].

As suggested in the patent, a hydrolytic reaction shall be used to generate hydrogen and the necessary heat, i.e. $\text{NaBH}_4 + 2\text{H}_2\text{O} \rightarrow \text{NaBO}_2 + 4\text{H}_2 + \text{heat}$, to induce the diffusion process in the hollow glass microspheres. For this, hollow glass microspheres are mixed into an aqueous NaBH₄ solution, which is stabilized by added NaOH. To initiate the hydrolytic reaction of the stabilized solution, a catalyst has to be utilized. This catalyst should be applied to the surface of the spheres to guarantee heat evolution at the sphere shells, where it is needed. Using a liquid solution has two advantages: first, the empty space between the spheres is used, since the spheres only have a packing factor of about 63%, thus increasing storage densities; second, with the spheres floating in a liquid, they can be transported much easier than as a solid. For the total system to work, hollow glass microspheres and hydride solution are stored in separate tanks and put together in a reaction chamber. The residual materials, i.e. empty hollow glass microspheres

and NaBO_2 -solution or solid, have to be stored in an additional tank and recycled off-board the vehicle. Off-board recycling is the major drawback of the system. Figure 3.14 illustrates the proposed hydrogen storage and releasing method [22].

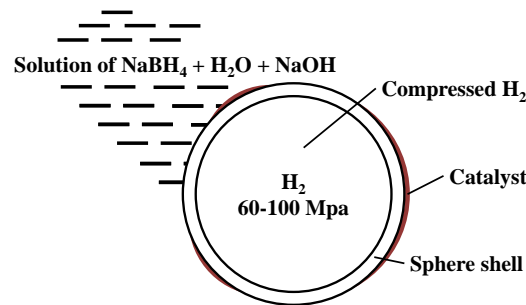


Figure 3.14: Illustration of the hydrogen storage system proposed by Keding and Tajmar (2008) [22]; hollow glass microspheres are pressurized with hydrogen to up 100 MPa and partly coated with a catalyst to initiate the hydrolytic reaction, which generates the heat to induce the diffusion process.

In contrast to the system proposed by Keding and Tajmar (2008) the system proposed in this thesis does not use a solution, but rather sodium borohydride as a solid in the form of a fine grained powder. As illustrated in Figure 3.15 a-d solid sodium borohydride is mixed with hollow glass microspheres, which are coated with a catalyst (a). When adding water to the powder mixture the sodium borohydride dissolves and reacts with the water (b). This reaction is additionally promoted by the catalyst. Without a catalyst the reaction would stop when a certain pH-value is reached as was already explained. As NaBH_4 reacts with water, heat is liberated (c), thus also promoting the chemical processes. The resulting elevated temperature induces the diffusion process of pressurized hydrogen inside the spheres through their shells (d). This process is quite similar to the one proposed by Keding and Tajmar (2008), however, there is a main advantage in using a solid hydride.

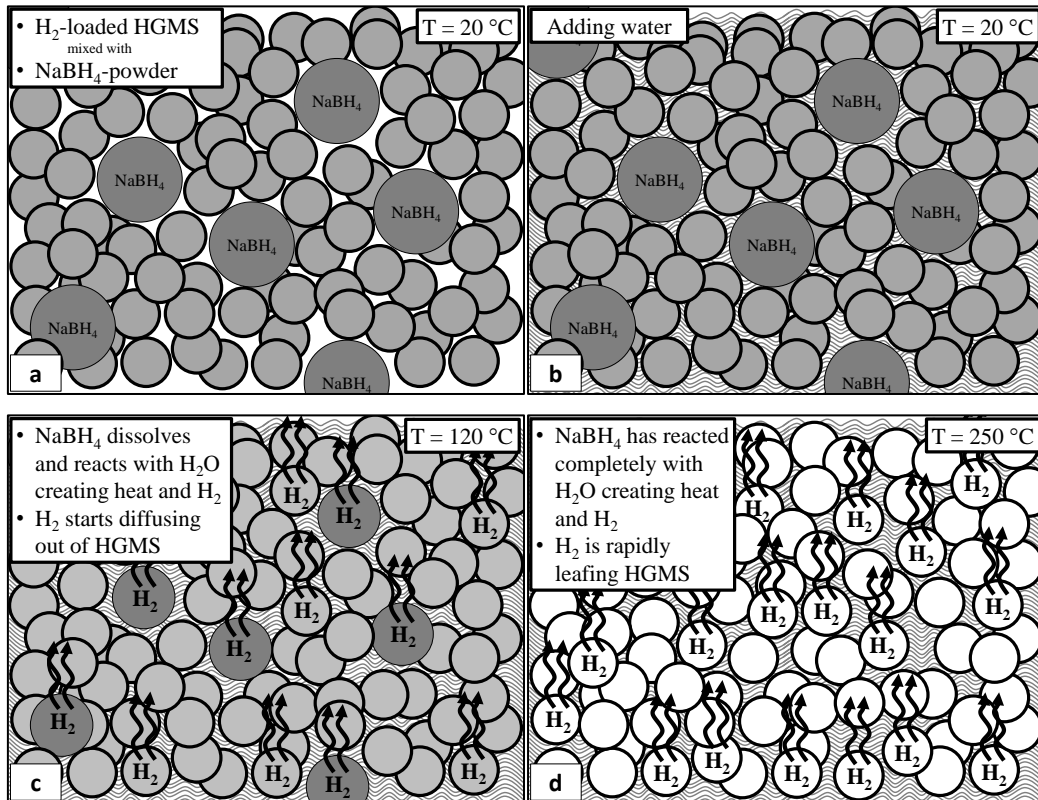


Figure 3.15: a) Sodium borohydride is mixed with catalyst coated, hydrogen loaded hollow glass microspheres; b) water is added from a water reservoir; c) NaBH₄ dissolves in water and reacts with H₂O releasing H₂ and heat, thus increasing the temperature in the reaction chamber, diffusion of hydrogen through the sphere shells starts slowly; d) NaBH₄ has completely reacted with water and the temperature has risen to 250 °C enabling a fast extraction of hydrogen

As illustrated in Figure 3.16 when using solid hydride material it is possible to re-use the water necessary for the hydrolytic reaction. For that the tank of the glass sphere-hydride mixture has to be separated in many smaller sections, each working as a reaction chamber, enabling water cycling. The cycle consists of four steps: first, water from a small reservoir tank (a) is injected into one glass sphere-hydride containing cell b). In the cell, hydrogen is generated as described in Figure 3.15. The hydrogen released by the cell can be buffered in a low-pressure vessel c) to enable the start-up of the engine, or it can be directly forwarded to the fuel cell d). In the fuel cell hydrogen is converted to electricity and water, which is again stored in the water reservoir and used for another glass sphere-hydride filled cell. This cycling of water process would increase the gravimetric and volumetric storage densities dramatically, as will be shown in section 3.3.3.

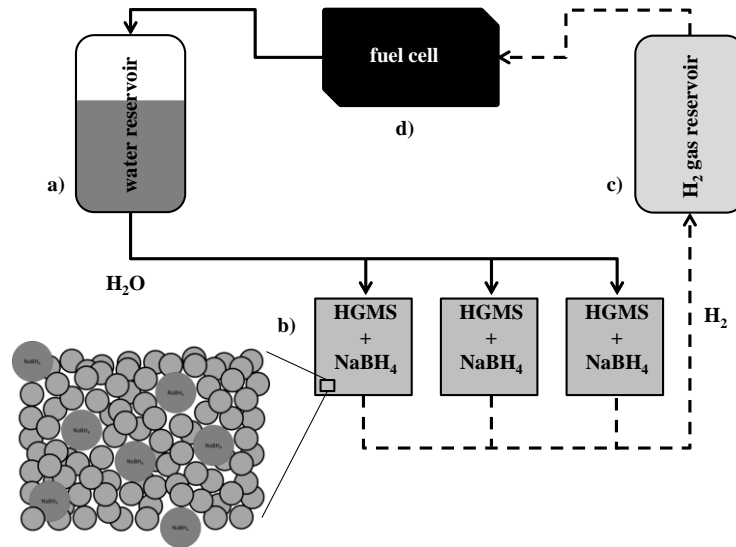


Figure 3.16: Proposed hydrogen storage system; water that is necessary for the hydrolytic reaction is generated by the fuel cell, thus increasing the storage density of the system dramatically; water from the reservoir a) is added to one glass sphere-hydride containing cell b), generated hydrogen is either buffered c) or converted to electricity and water d), the generated water is again stored in the reservoir and can be used for another cell

In the next section the gravimetric and volumetric storage densities of the proposed system will be discussed. Furthermore, theoretical aspects of the proposed system, such as possible glass sphere hydride ratios, packing densities, thermal limits and water requirements will be investigated.

As mentioned a catalyst has to be applied to the sphere surface which will be the topic of chapter 4.

Chapter 6 will give a survey of potential catalysts and explain the experiments to characterize the selected catalysts.

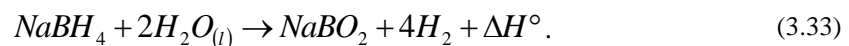
3.3.3. Study on combined glass sphere hydrolytic storage system

In sections 3.2.1 and 3.3.1 the storage densities of hollow glass microspheres and sodium borohydride have been evaluated. Now the storage densities of the proposed combined system will be investigated.

First, assumptions and restrictions of the system will be described. After that hydrogen storage densities of the proposed system and the theoretical aspects, such as ratio of hollow glass microspheres to hydride, water requirements, packing densities of hollow glass microspheres and hydride and thermal limits will be examined.

Restrictions and assumptions

- **Diffusion temperature:** A sufficiently fast diffusion process requires high temperatures of about $T = 250 - 400$ °C as was shown before in section 3.2.2. This necessitates a certain amount of hydride to liberate the required heat.
- **Vapour pressure:** The hydrolysis of the hydride necessitates water, whose temperature is also increased in the course of the reaction. This increases the vapour pressure of water which might be an issue. At 300 °C the vapour pressure of water is 8.58 MPa [23], which would make a heavy pressure vessel indispensable. At 250 °C the pressure drops to already only 3.98 MPa [23], which would roughly halve the weight of a required pressure vessel. However, solubility of NaBO₂ has also to be taken into account. The relation for vapour pressure of NaBH₄ or NaBO₂ solution is not known to the author, but from the results acquired by Marrero-Alfonso et al (2007) and Andrieux (2012) [71, 97], where hydrate formation and de-hydration of NaBO₂ were investigated, it can be suspected that it is much higher than of pure water.
- **Hydrolysis reaction equation:** In section 3.3.1 it was shown that water management is very important for the hydrolytic reaction. There the so-called water excess factor x was introduced, which is most commonly set to 2, when the hydrolysis is carried out near room temperature. If carried out at elevated temperatures sodium metaborate is de-hydrated, thus releasing water, i.e. $\text{NaB(OH)}_4 \rightarrow \text{NaBO}_2 + 2\text{H}_2\text{O}$. According to Marrero-Alfonso et al (2007) the water content of NaBO₂· x H₂O is below 10% at 250 °C [71]. This is also supported by Andrieux et al. (2012), who revised the phase diagram of NaBO₂-H₂O in 2012 and found that at 250 ± 2 °C the hydrated metaborate consist only of pure NaBO₂ and vapour [97]. Considering these facts the hydrolysis reaction equation used in the following study is assumed as



It seems that the system has a sweet spot at 250 °C in terms of vapour pressure, NaBO₂ solubility and hydrogen diffusion velocity.

- **Water requirements:** One glass sphere-hydride filled cell has to be supplied with sufficient water for the hydrolytic reaction and to cover both, hollow glass microspheres and hydride completely. It has to be mentioned that too much water reduces the reachable temperature, because of its high specific heat.

- **Thermal management:** Heat losses to the environment are neglected as well as heat from the fuel cell that might be utilized to preheat the water before injected to one glass sphere-hydride filled cell.
- **Packing factor:** For hydride powder and hollow glass microspheres the same packing factor of $f = 0.63$ is assumed.

System hydrogen storage densities

First, the following table shall give an overview of all used variables and suffixes (Table 3.7).

main variable	description	suffix	description
m	mass	G	gravimetric
γ	storage density	V	volumetric
V	volume	sph	spheres
f	packing factor	hy	hydride
ρ	density	w	water
M	molar weight	b	borate
r	sphere radius		
d	shell thickness		

Table 3.7: Overview of used variables and suffixes

The gravimetric storage density $\gamma_{G,sys}$ and the volumetric storage density $\gamma_{V,sys}$ of the combined system can be written as

$$\gamma_{G,sys} = \frac{m_{sph} \cdot \gamma_{G,sph} + m_{hy} \cdot \gamma_{G,hy}}{m_{sph} + m_{hy} + m_w - m_{w,fuelcell}}, \quad \text{for } m_{w,fuelcell} < m_w, \quad (3.34)$$

$$\gamma_{G,sys} = \frac{m_{sph} \cdot \gamma_{G,sph} + m_{hy} \cdot \gamma_{G,hy}}{m_{sph} + m_{hy}}, \quad \text{for } m_{w,fuelcell} \geq m_w, \quad (3.35)$$

$$\gamma_{V,sys} = \frac{m_{sph} \cdot \gamma_{G,sph} + m_{hy} \cdot \gamma_{G,hy}}{V_{sph} + V_{hy} + V_w - V_{w,fuelcell}}, \quad \text{for } V_{w,fuelcell} < V_w, \quad (3.36)$$

$$\gamma_{V,sys} = \frac{m_{sph} \cdot \gamma_{G,sph} + m_{hy} \cdot \gamma_{G,hy}}{V_{sph} + V_{hy}}, \quad \text{for } V_{w,fuelcell} \geq V_w. \quad (3.37)$$

Equations (3.34) and (3.36) only apply as long the water released from the fuel cell is less or equal to the water needed ($m_{w,fuelcell} < m_w$, $V_{w,fuelcell} < V_w$). If more water is produced by the fuel

cell than is needed, these factors can be neglected. In the following discussion the different parameters will be elaborated.

In order to simplify these equations, a factor of the ratio ζ of hydride mass to mass of hollow glass microspheres is introduced, which strongly influences storage density. It is defined as the mass ratio of NaBH₄ to hydrogen loaded hollow glass microspheres:

$$\zeta = \frac{m_{hy}}{m_{sph}} \quad (3.38)$$

The amount of water to cover the hollow glass microspheres and the hydride is given by (derived in appendix 9.1.4)

$$m_w = \rho_w m_{sph} \frac{1-f}{f} \left(\frac{\gamma_{G,sph}}{\rho_{H_2}} \frac{1}{(1-\varepsilon)^3} + \zeta \cdot \frac{1}{\rho_{hy}} \right) \quad (3.39)$$

The amount of water which is released from the fuel cell $m_{w,fuelcell}$ is given by the amount of hydrogen stored in the spheres and the hydride:

$$m_{w,fuelcell} = \frac{M_w}{M_{H_2}} (m_{sph} \cdot \gamma_{G,sph} + m_{hy} \gamma_{G,hy}) \quad (3.40)$$

With these three relations the equation (3.34)-(3.37) can be written as

$$\gamma_{G,sys} = \frac{\gamma_{G,sph} + \zeta \cdot \gamma_{G,hy}}{1 + \zeta + \rho_w \frac{1-f}{f} \left(\frac{\gamma_{G,sph}}{\rho_{H_2}} \frac{1}{(1-\varepsilon)^3} + \zeta \cdot \frac{1}{\rho_{hy}} \right) - \frac{M_w}{M_{H_2}} (\gamma_{G,sph} + \zeta \cdot \gamma_{G,hy})} \quad (3.41)$$

for $\zeta < \chi$,

$$\gamma_{G,sys} = \frac{\gamma_{G,sph} + \zeta \cdot \gamma_{G,hy}}{1 + \zeta}, \quad \text{for } \zeta \geq \chi \quad (3.42)$$

$$\gamma_{V,\text{sys}} = \frac{\gamma_{G,\text{sph}} + \zeta \cdot \gamma_{G,\text{hy}}}{\frac{2-f}{f} \left(\frac{1}{(1-\varepsilon)^3} \frac{\gamma_{G,\text{sph}}}{\rho_{H_2}} + \zeta \cdot \frac{1}{\rho_{hy}} \right) - \frac{1}{\rho_w} \frac{M_w}{M_{H_2}} (\gamma_{G,\text{sph}} + \zeta \cdot \gamma_{G,\text{hy}})} \quad (3.43)$$

for $\zeta < \chi$,

$$\gamma_{V,\text{sys}} = \frac{f \cdot (\gamma_{G,\text{sph}} + \zeta \cdot \gamma_{G,\text{hy}})}{\frac{1}{(1-\varepsilon)^3} \frac{\gamma_{G,\text{sph}}}{\rho_{H_2}} + \zeta \cdot \frac{1}{\rho_{hy}}}, \quad \text{for } \zeta \geq \chi \quad (3.44)$$

The value χ corresponds to a value ζ when $m_{w,\text{fuelcell}} = m_w$ (respectively $V_{w,\text{fuelcell}} = V_w$), that is, the amount of water needed to cover spheres and hydride is the same as is produced in the fuel cell. Above this value the equations become simpler (as shown), since sufficient water is available. The value χ can be expressed by

$$\chi = \gamma_{G,\text{sph}} \cdot \frac{\frac{M_w}{M_{H_2}} - \frac{1-f}{f} \frac{\rho_w}{\rho_{H_2}} \frac{1}{(1-\varepsilon)^3}}{\frac{1-f}{f} \frac{\rho_w}{\rho_{hy}} - \frac{M_w}{M_{H_2}} \gamma_{G,\text{hy}}}. \quad (3.45)$$

For ε the expression of equation (3.12) can be used, so one can either use radius and shell thickness or safety factor, pressure and tensile strength as input parameters. For ρ_{H_2} the correlation in equation (3.6) of chapter 3.2.1 can be taken. Typical values for χ for different spheres safety factors S_f and S38 spheres are: 2.00 ($S_f=1$), 1.19 ($S_f=2$), 0.68 ($S_f=4$) and 0.61 (S38) kg of spheres per kg of NaBH_4 . These values account for a hydrogen extraction pressure of 85 MPa at a temperature of 250 °C and a packing density of $f=0.63$.

Since χ has to be positive, the packing factor has a maximum value, which can be derived by either assuming the terms above and below the fraction to be positive or to be both negative. In this case, in order to get a physically possible solution, both terms are assumed to be negative. The maximum packing density results to:

$$f < \frac{1}{\frac{M_w}{M_{H_2}} \frac{\rho_{H_2}}{\rho_w} (1-\varepsilon)^3 + 1} \quad (3.46)$$

Of course, the packing density cannot exceed the packing density of hexagonal close packing.

Stoichiometric restrictions for the ratio of hollow glass microspheres to hydride

For the hydrolytic reaction at least 2 mole of water per mole of NaBH_4 are necessary (equation (3.33)), which can be written as

$$\frac{m_w}{M_w} \geq 2 \frac{m_{hy}}{M_{hy}} \quad (3.47)$$

This means that a sufficiently large volume between hydride and spheres is required for water uptake. This of course strongly depends on the packing factor f , but also on the amount of spheres mixed with hydride powder. NaBH_4 powder alone could only have a packing factor of about $f = 0.45$ in order to have sufficiently empty volume between powder particles for water uptake. To guarantee the necessary volume at a given packing factor, i.e. $f = 0.63$, when adding spheres, the ratio of hydride to spheres has an upper limit. The upper limit of ζ can be derived by inserting equation (3.39) in (3.47), which ensures the presence of enough water for the hydrolysis to take place:

$$\zeta_{stoich} \leq \frac{\gamma_{G,sph}}{\rho_{H_2} \left(\frac{2}{\rho_w} \frac{f}{1-f} \frac{M_w}{M_{hy}} - \frac{1}{\rho_{hy}} \right)} \quad (3.48)$$

Typical values for ζ_{stoich} are 11.62 ($S_f=1$), 6.50 ($S_f=2$), 3.33 ($S_f=4$) and 2.71 (S38) kg of NaBH_4 per kg of spheres.

Temperature restrictions

As was already discussed, heat has to be released by the hydrolytic reaction in order to reach a sufficiently high temperature for diffusion. The heat released by the stoichiometric reaction can be calculated by energy conservation:

$$m_{hy} h_{hy} + m_w h_w = m_b h_b + m_{H_2} + Q. \quad (3.49)$$

Using equation (3.38) and relations for the masses:

$$m_w = 2 \frac{M_w}{M_{hy}} m_{hy}, \quad m_b = \frac{M_b}{M_{hy}} m_{hy}, \quad m_{H_2} = 4 \frac{M_{H_2}}{M_{hy}} m_{hy}, \quad (3.50)$$

Q can be expressed as

$$Q_{reaction} = \zeta \cdot m_{sph} \left(h_{hy} + 2 \frac{M_w}{M_{hy}} h_w - \frac{M_b}{M_{hy}} h_b - 4 \frac{M_{H_2}}{M_{hy}} h_{H_2} \right). \quad (3.51)$$

The resulting temperature can be estimated using the specific heat of the present compounds according to the following relation:

$$Q_{spec} = m \cdot c_p \Delta T. \quad (3.52)$$

The main two assumptions are:

- The specific heats of the different compounds are assumed as temperature independent.
- Regarding the specific heat, only reaction products and residual water are taken into account.

For the present system equation (3.52) yields

$$Q_{spec} = (m_{w,res} c_{p,w} + m_b c_{p,b} + m_{H_2} c_{p,H_2} + m_{glass} c_{p,glass}) \cdot \Delta T. \quad (3.53)$$

Some of the added water is consumed due to the hydrolytic reaction. The residual water, which has to be heated up, can be calculated by

$$m_{w,res} = \rho_w m_{sph} \frac{1-f}{f} \left(\frac{\gamma_{G,sph}}{\rho_{H_2}} \frac{1}{(1-\varepsilon)^3} + \zeta \cdot \frac{1}{\rho_{hy}} \right) - 2 \cdot \zeta \cdot m_{sph} \frac{M_w}{M_{hy}}, \quad (3.54)$$

where the first term describes the water needed to cover the sphere-hydride mixture and the second the water consumed during the reaction (compare with equation (3.39)).

Hydrogen mass and glass mass can be given by the relations

$$m_{H_2} = m_{sph} \left(\zeta \frac{4M_{H_2}}{M_{hy}} + \gamma_{G,sph} \right) \quad \text{and} \quad m_{glass} = m_{sph} (1 - \gamma_{G,sph}), \quad (3.55)$$

where the first term of the hydrogen mass describes hydrogen released by the reaction and the second term the hydrogen released by the hollow glass microspheres.

Inserting relations (3.54) and (3.55) into (3.53) and setting $Q_{spec} = Q_{reaction}$ yields the resulting temperature increase of the system. The temperature increase has the form

$$\Delta T = \frac{C_1}{C_2 + \frac{1}{\zeta} \Gamma}. \quad (3.56)$$

Besides compound parameters, the constants C_1 , C_2 and Γ depend on the packing density f , shell thickness to radius ratio ε , the gravimetric storage density of the spheres $\gamma_{G,sph}$ and the hydrogen density. They are given by:

$$C_1 = \frac{1}{M_{hy}} (M_{hy} h_{hy} + 2M_w h_w - M_b h_b - 4M_{H_2} h_{H_2}) \quad (3.57)$$

$$C_2 = \frac{1}{M_{hy}} \left\{ \left(\frac{1-f}{f} \frac{\rho_w}{\rho_{hy}} M_{hy} - 2M_w \right) \cdot c_{p,w} + 4M_{H_2} \cdot c_{p,H_2} + M_b \cdot c_{p,b} \right\} \quad (3.58)$$

$$\Gamma = \left(\frac{1-f}{f} \frac{\rho_w}{\rho_{H_2}} \frac{1}{(1-\varepsilon)^3} \cdot c_{p,w} + c_{p,H_2} - c_{p,glass} \right) \cdot \gamma_{G,sph} + c_{p,glass} \quad (3.59)$$

In the following section the resulting storage densities and temperatures will be illustrated and discussed.

3.3.4. Discussion of resulting material storage densities of the proposed hybrid system

In this section the resulting characteristics of the proposed system will be discussed, where hydrogen loaded hollow glass microspheres and NaBH_4 powder are mixed together. When water is added, the chemical reaction of NaBH_4 and water releases hydrogen and heat. The released heat results in a temperature increase, which induces the diffusion process of hydrogen that was captured inside the spheres.

The assumed parameters were discussed in the sections before and are summarized below:

- packing factor, $f = 0.63$
- ratio of sphere shell thickness and radius, $\varepsilon = d/r = 0.061$ for S38, $\varepsilon = p_E S_f / 2\sigma$ when safety factor is used
- safety factors, $S_f = 1, 2$ and 4
- extraction pressure $p_E = 85$ MPa at an extraction temperature of $T_E = 250$ °C
- tensile strength of glass, $\sigma = 3.31$ GPa
- gravimetric storage density of hollow glass microspheres according to equation (3.13), i.e. 25.2 wt% ($S_f = 1$), 14.1 wt% ($S_f = 2$), 7.2 wt% ($S_f = 4$) and 5.9 wt% for S38 glass spheres
- For the hydrolytic reaction 2 mole of water per mole of NaBH_4 are necessary.

The material parameters of water, hydrogen, hydride, borate and glass are given in Table 3.8.

	density (kg/m ³)	specific heat (J/molK)	enthalpy (kJ/mol)	molar weight (g/mol)
H ₂ O	997	75.3	-285.8	18.015
H ₂	0.082	28.8	0.0	2.016
NaBH ₄	1070	86.8	-188.6	37.833
NaBO ₂	2460	65.9	-977.0	65.800
		specific heat (kJ/kgK)		
borosilicate glass	2230	0.750	-	-

Table 3.8: Properties of participating compounds and materials [3] [24]; values for solids and liquids account for near room temperature, values for gases for 25 °C and 101.325 kPa

Figure 3.17 illustrates the gravimetric storage densities of the hybrid system as a function of ζ , which is the ratio of hydride to spheres. The gravimetric storage density increases with the amount of added hydride up to a certain point, when the curve makes a sharp bend at $\zeta = \chi$. Before the bend at lower ζ values additional water has to be added in order to cover the whole hydride-sphere mixture. Above that value enough water can be supplied by the fuel cell and the gravimetric storage density approaches the gravimetric storage density of the hydride. Storage densities that would yield temperature differences above 500 K are not illustrated, since such high temperatures would not be feasible in any domestic process or in a vehicle. Moreover, as already explained before, high temperatures yield high water vapour pressures, making a high pressure vessel necessary. In the figure, points that yield the same temperature difference are connected with red lines. At the target temperature difference of $\Delta T = 250$ K gravimetric storage densities of 8 wt% to 16 wt% can be reached. This is below the maximum gravimetric storage density of both, hollow glass microspheres and hydride, which have been calculated before to

$\gamma_{G, sph, max} = 25.2 \text{ wt\%}$ and $\gamma_{G, hy, max} = 21.3 \text{ wt\%}$. As a result, from a gravimetric storage density point of view, it seems not very promising to develop a hybrid system, combining hollow glass microspheres and NaBH_4 .

Still, it can also be observed that by combining those two systems a higher gravimetric storage density than for the hydride alone can be achieved, albeit only for spheres with $S_f = 1$ and resulting temperature differences above 350 K. Moreover, when costs are taken into account the hybrid system might be much cheaper per kg of released hydrogen than that of the hydride alone. The cost aspect will be discussed later on.

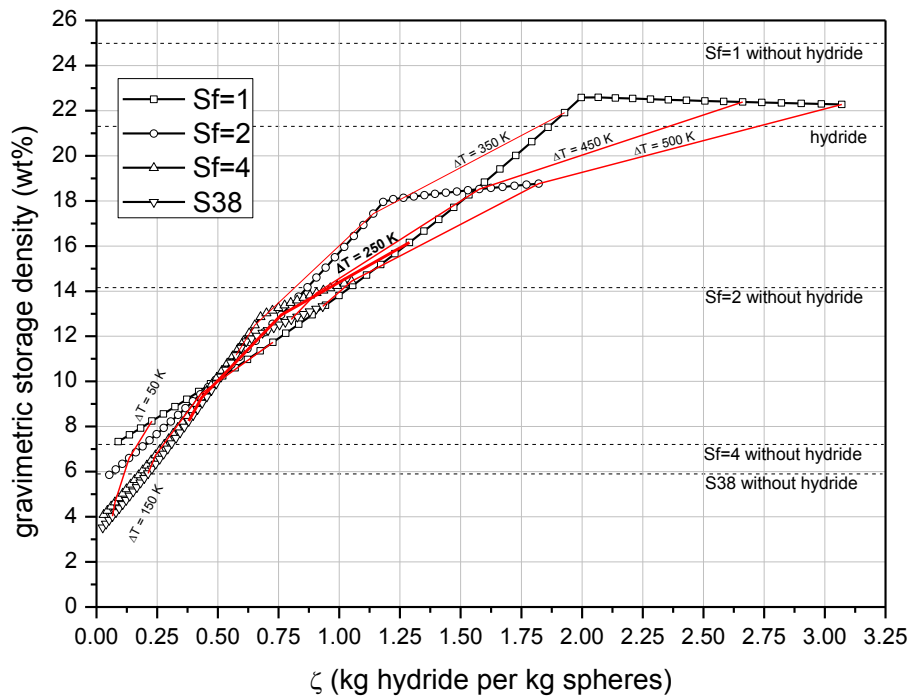


Figure 3.17: Gravimetric hydrogen storage density of the proposed system for different sphere dimensions as a function of ζ , which is the ratio of hydride to spheres mixture; points which would yield the same temperature difference are connected with red lines; at the target temperature difference of 250 K gravimetric storage densities between 8 wt% and 16 wt% can be achieved, depending on used sphere dimensions (safety factor S_f); the dotted lines illustrate the storage density of the hollow glass microspheres without hydride and the hydride alone

Figure 3.18 illustrates the volumetric storage densities of the hybrid system as a function of ζ . In contrast to the gravimetric storage density the volumetric storage density is dramatically increased by adding the hydride. Whereas the volumetric storage density of the hollow glass microspheres alone is quite low, i.e. 18.30 kg/m^3 ($S_f = 1$), 17.34 kg/m^3 ($S_f = 1$), 16.00 kg/m^3 ($S_f = 1$) and 15.5 kg/m^3 (S38), the hybrid system yields much higher volumetric storage densities. The achieved volumetric storage densities of $\gamma_{V, sys} = 30 \text{ kg/m}^3$ at a temperature difference of $\Delta T = 250 \text{ K}$ are however much lower than for the hydrolysis alone, i.e.

111.63 kg/m³. Generally it can be observed that the volumetric storage density increases almost linearly with the amount of added hydride. The bend at $\zeta = \chi$ is not as pronounced as could be observed in Figure 3.17, since the volume of additional water is low compared to the volume of the sphere-hydride mixture.

It can be concluded that the proposed system makes sense from a volumetric storage density point of view, when considering the cost aspects, since NaBH₄ is very expensive as was shown in section 3.3.1.

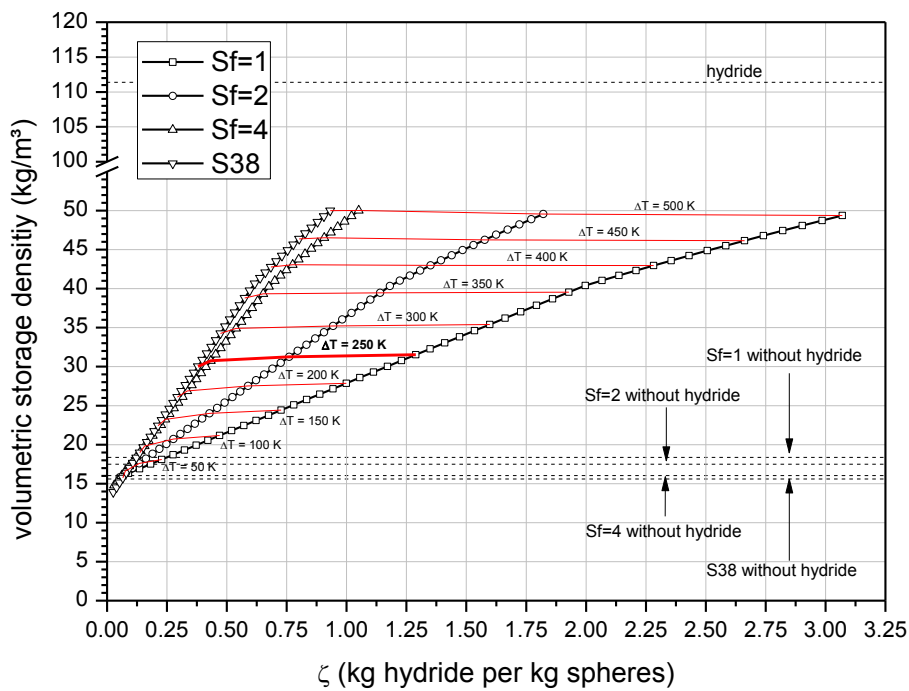


Figure 3.18: Volumetric hydrogen storage density of the proposed system for different sphere dimensions as a function of ζ , which is the ratio of hydride to spheres mixture; points which would yield the same temperature difference are connected with red lines; at the target temperature difference of 250 K the volumetric storage density is slightly above 30 kg/m³, regardless of the sphere dimensions (safety factor S_f); the dotted lines illustrate the volumetric storage density of the hollow glass microspheres without hydride and the hydride alone

As an overview Figure 3.19 shows the volumetric versus the gravimetric storage density of the hybrid system, also including the storage densities of the pure compounds, i.e. hydrogen loaded hollow glass microspheres with different wall thicknesses and the hydride alone, assuming a hydrolytic reaction. Again a sharp bend can be observed, which corresponds to $\zeta = \chi$. Before the bend, additional water has to be added in order to cover the whole hydride-sphere mixture. At higher gravimetric storage densities enough water can be supplied by the fuel cell and both volumetric and gravimetric storage densities approach the storage density of the hydride. It can be seen that the hybrid system has much higher volumetric storage densities

than hollow glass microspheres alone. However, the expensive hydrolytic reaction has much higher theoretical values. When comparing the hybrid system with the DOE-targets it becomes obvious that the gravimetric storage density is well within the targets. In contrast, when looking at the volumetric storage densities it becomes clear that the hybrid system can only meet the DOE-targets at higher temperature differences than were intended. Thus, in order to reach those targets, either a pressure vessel for 16 MPa ($T_{sat} = 350\text{ °C}$) has to be used, which would reduce the storage densities, or the excessive heat is given off to the ambient.

Additional equipment such as valves and tanks, etc., which would also reduce the storage densities have been neglected in all calculations and assumptions. It might be that higher pressures of 16 MPa are not a major issue, and that the additional equipment has only a minor impact on the more critical volumetric storage density. However, this is not a subject of discussion in this work. Before discussing other possible ways to increase the storage densities, a cost estimation of the hybrid system will be made.

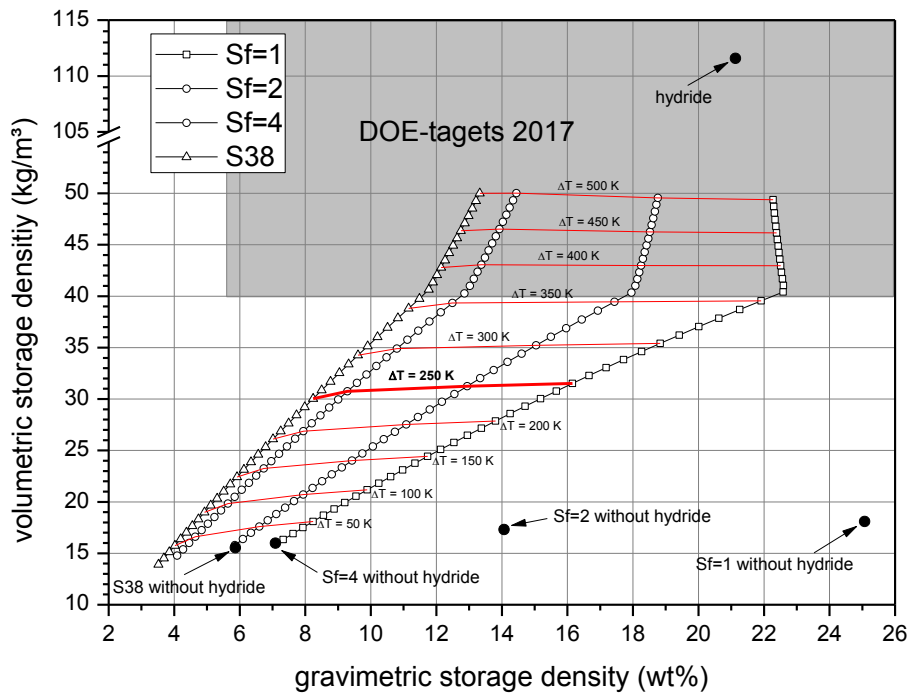


Figure 3.19: Volumetric storage density versus gravimetric storage density for different spheres dimensions (safety factor S_f); the black dots illustrate the storage densities of the pure compounds, i.e. hollow glass microspheres without hydride and hydride NaBH_4 itself under the assumption of a hydrolytic reaction; red lines connect points with the same temperature difference of different sphere dimensions; the grey area corresponds to the DOE-targets for the year 2017

3.3.5. Costs of the hybrid system

The target price for hydrogen in mobile applications which is postulated by the U.S. Department of Energy is 2-4 \$/gge (gasoline gallon equivalent), which corresponds to $c_{H_2, target} = 1.67\text{-}3.34$ €/kg H₂ (1 gge \cong 0.997 kg H₂, 1 € \cong 1.2 \$) [9] [98]. At the moment hydrogen price is at about $c_{H_2} = 7$ €/kg, so this price will be used for the comparison [29]. In 2017-targets the price of the tank system (without hydrogen) should not exceed $C_{tank} = 333$ € per kg H₂ stored ($C_{tank} = 222$ €/kgH₂ stored, ultimate target) [9].

The method used to compare target costs with the costs of the proposed system is to calculate the overall life time costs of both the systems divided by the total driving distance D . The target total driving distance is $D = 240,000$ km [9]. Assuming a driving range $d_{drive} = 100$ km/kg hydrogen [6] (p. 127) [11] this results to a total hydrogen mass of $m_{H_2, total} = 2,400$ kg in the lifetime of a vehicle. The tank should have a storage capacity $S_{tank} = 5$ kg H₂ [9]. The cost of the target system per 100 km $C_{km, DOE}$ using the actual hydrogen price c_{H_2} is then given by

$$C_{km, DOE} = \frac{S_{tank} \cdot C_{tank}}{D} + \frac{c_{H_2}}{d_{drive}} \quad (3.60)$$

Resulting costs for a driving distance of 100 km are:

- 7.69 €/100 km (actual hydrogen price, 2017 target tank cost)
- 7.46 €/100km (actual hydrogen price, ultimate target tank cost)
- 4.03 €/100 km (target hydrogen price 3.34 €/kg, 2017 target tank cost)
- 3.70 €/100 km (target hydrogen price 3.34 €/kg, ultimate target tank cost)
- 2.08 €/100 km (target hydrogen price 1.67 €/kg, ultimate target tank cost)

At this point it has to be mentioned that gasoline prices in the USA are about half of the prices in the EU. As a result hydrogen prices of 4-6 €/100 km are acceptable for the EU-region.

The cost of one kg hydrogen in the hybrid system depends on the costs of hydrogen c_{H_2} , hydride c_{hy} and on the ratio of hydride to spheres ζ . It also depends on the gravimetric storage density $\gamma_{G, sph}$ of hollow glass microspheres and the gravimetric storage density of the hydride. Even though the hollow glass microspheres can be recycled, it cannot be assumed that the recycling efficiency is 100%. Therefore, due to recycling losses, the costs of hollow glass microspheres c_{sph} have to be taken into account. The losses strongly depend on the original sphere quality [26] as already described in section 3.2.1. According to 3M™ losses due pressurizing to maximum pressure are about $R_{loss} = 10\%$ [25].

The cost of one kg hydrogen in the hybrid system c_{hybrid} (€/kg H₂) results to

$$c_{\text{hybrid}} = \frac{c_{\text{sph}} R_{\text{loss}} (1 - \gamma_{G,\text{sph}}) + c_{\text{H}_2} \gamma_{G,\text{sph}} + \zeta \cdot c_{\text{hy}} \gamma_{G,\text{hy}}}{\gamma_{G,\text{sph}} + \gamma_{G,\text{hy}}} \quad (3.61)$$

In this first estimation of the costs of the hybrid system additional equipment such as valves, vessels, containers or metering equipment are neglected. The parameters taken into account are only the costs of the pure materials, i.e. hollow glass microspheres, sodium borohydride and hydrogen. The costs of these materials are given in Table 3.9 [29] [96] [99] [100]:

material	cost (€/kg)
spheres [99, 100]	~10.0
hydride [96]	~27.5
hydrogen [29]	~7.0

Table 3.9: Overview of material costs

Figure 3.20 shows the resulting costs in a gravimetric-volumetric storage density diagram. The costs are given in €/kg H₂. The costs drop with increasing gravimetric storage density, which is most welcome. However, costs increase with increasing volumetric storage density. As previously mentioned, the volumetric storage density was identified as being the more critical aspect, because of low resulting storage values.

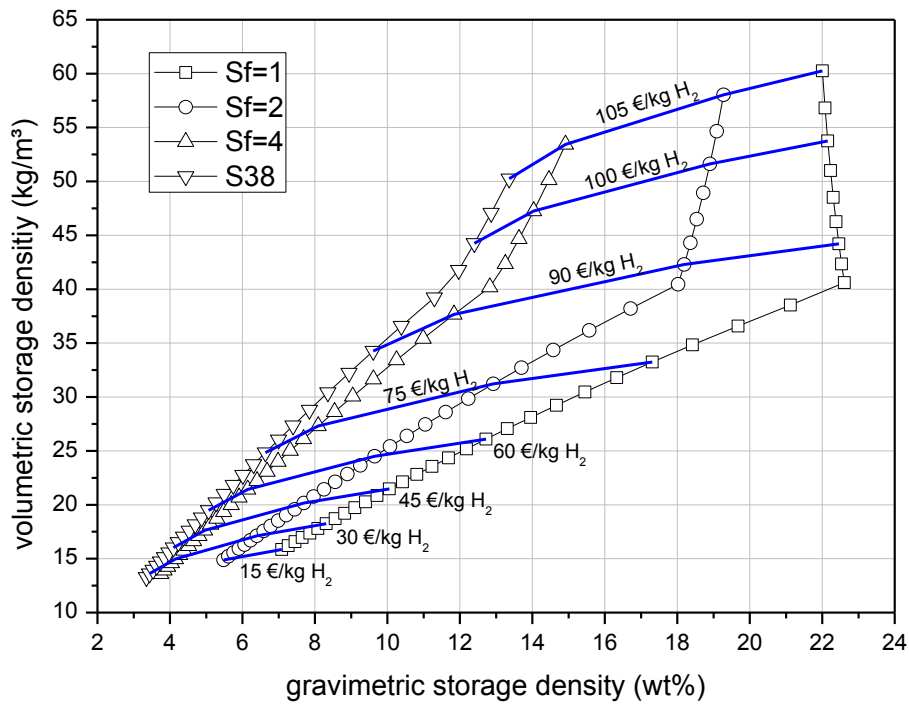


Figure 3.20: Costs of one kg hydrogen as a function of the gravimetric storage density and the volumetric storage density, assuming a hydrogen price 7 €/kg

It can also be observed, that the costs behave similar to the temperature, which is because of the high hydride cost. The hydride is responsible for both temperature increase and dramatic cost increase. Comparing the cost of hydrogen per kg of the hybrid system with DOE-target costs it becomes clear, that the costs of the proposed system are 1-2 orders of magnitude higher than of the ultimate target system.

To calculate the costs per km driving distance is very simple in case of a cartridge system, since there is no extra tank:

$$C_{km,hybrid} = \frac{c_{hybrid}}{d_{drive}} \tag{3.62}$$

Resulting costs per 100 km driving distance are given in Figure 3.21 as a function of the volumetric storage density for different sphere safety factors S_f compared with current hydrogen costs and DOE-target costs. A higher safety factor corresponds to a higher sphere shell thickness (see section 3.2.1). It becomes obvious that at the moment the costs of proposed hybrid hydrogen storage system are far beyond the targeted costs. This is mainly due to the high costs of hydrogen out of NaBH_4 , which are at about 130 €/kg hydrogen. In Figure 3.21 the curves converge asymptotically towards that value. Of course the price of hydrogen also has an effect on the resulting costs, albeit small.

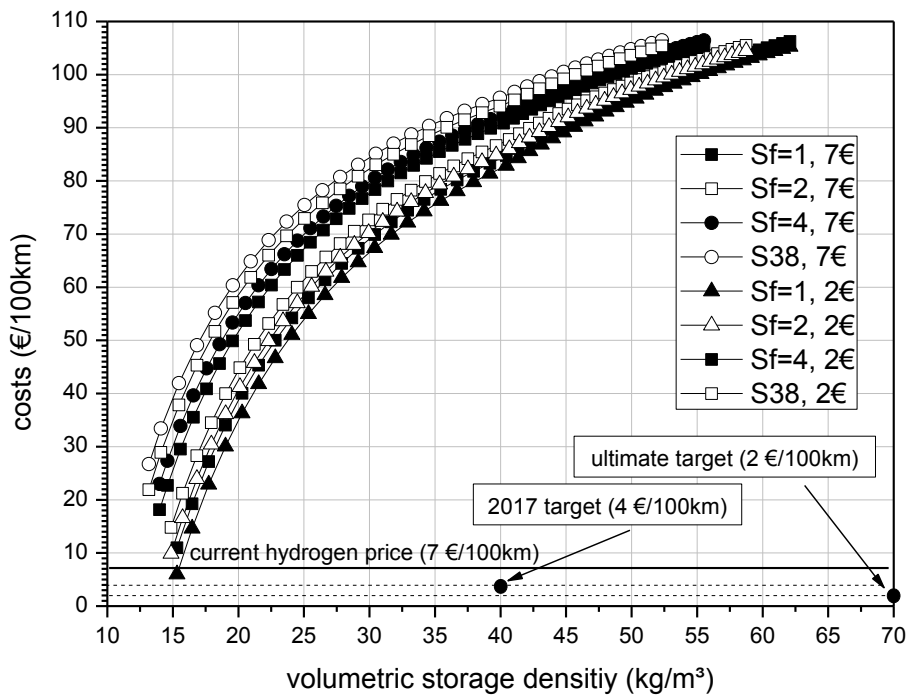


Figure 3.21: Costs for driving distance of 100 km as a function of the volumetric storage density for different safety factors S_f an hydrogen prices; compared with the actual hydrogen price and US target prices

It has to be mentioned, that DOE-target prices refer to a US setting, where fuel in general is much cheaper than in the EU. Due to this fact, the target prices for the EU can be nearly doubled compared to the prices given in Figure 3.21.

Influence of hydrogen, hydride and hollow glass microspheres costs

In order to get a feeling of the influence of hydrogen, hydride and hollow glass microspheres costs on the total system costs, a sensitivity study was carried out. For this, base costs as shown in Table 3.9 are assumed. System parameters are: hollow glass microspheres with safety factor of $S_f = 1$, ratio of hydride to spheres $\zeta = 1$, extraction temperature $T_E = 250$ °C, packing factor of $f = 0.63$.

Figure 3.22 shows the result of the sensitivity study, where the influence of compound prices to total costs was investigated. It became clear that the costs of the hydride have a major influence on the total costs. To reach cost regions near the DOE-targets however, the cost of spheres must be reduced as well. The target prices of all three compounds can be roughly estimated and are given in Table 3.10. Hydrogen costs have to be cut by 70%, hollow glass microspheres costs by 90% and the costs of sodium borohydride have to drop by not less than 98.4%. These numbers seem to be unachievable. Taking into account the price drop of the hydride of 7.8% per year since 1999 (see Figure 3.13), it can be estimated that it would take another 50 years to reach target prices of the hydride. However, mass production and new ways of synthesising NaBH_4 could also result in a dramatic and much faster price drop.

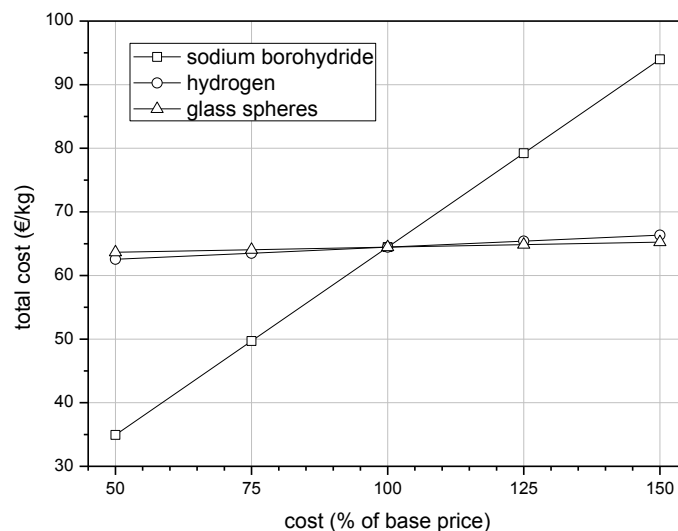


Figure 3.22: Sensitivity study on hydride, hydrogen and glass sphere costs; costs of sodium borohydride have the biggest effect on total costs

material	current costs in €/kg	target costs in €/kg (% of current cost)
spheres	~10.0	1 (10%)
hydride	~27.5	0.45 (1.6%)
hydrogen	~7.0	2 (29%)

Table 3.10: Overview of current costs and target costs to reach DOE-targets

3.3.6. Outlook on further increasing storage densities

It was shown that the reachable gravimetric storage densities of the proposed hybrid system are well within DOE-targets. On the other hand the resulting volumetric storage densities are too low and do not reach those targets. Besides utilizing high pressure vessels or giving off the excessive heat, there are other methods which can be considered to further increase the volumetric storage densities:

- Decrease of the extraction temperature and thus increase hydrogen density within the hollow glass microspheres: As was discussed in section 3.2.2, the hollow glass microspheres have to withstand the hydrogen pressure at the extraction temperature in order not to be crushed. This temperature was estimated at 250 °C to enable a sufficiently fast diffusion process, at a pressure of 85 MPa. If it were possible to further reduce that critical diffusion temperature (extraction temperature) to e.g. 150 °C, this would increase the hydrogen density inside the spheres – at 150 °C and 85 MPa hydrogen density is higher than at 250 °C and 85 MPa. In order to decrease the critical diffusion temperature, the glass permeability has to be further optimized. This measure would also further increase the gravimetric storage density.
- Another way to increase the volumetric storage density is to increase the packing factor f . For the presented calculations a packing factor of $f = 0.63$ was used, which accounts for random close packing of mono-sized spheres [55]. The random packing density can be increased when using a binary distribution, i.e. particles with size x mixed with particles with size y . With this method, random close packing of up to $f = 0.765$ can be reached [101], however, not higher than given in equation (3.46). This accounts for spheres and for hydride particles. This measure would not influence the gravimetric storage density significantly.

A comparison of those two measures is given in Figure 3.23, where hollow glass microspheres with a safety factor of $S_f = 1$ are taken as an example. It can be seen that both measures influence the resulting volumetric storage density significantly. By decreasing the necessary extraction temperature from 250 °C to 150 °C, the volumetric storage density can be increased by about 4 kg/m³. Higher packing factors can increase the volumetric storage density by about 6-11 kg/m³. Thus both measures together yield an increase of 10 to 15 kg/m³; achieving a result 14-21% closer to the DOE-targets, i.e. 70 kg/m³.

However, both measures would require additional research; especially, reducing the diffusion temperature but at the same time achieving a slow diffusion at room temperature is a very difficult task.

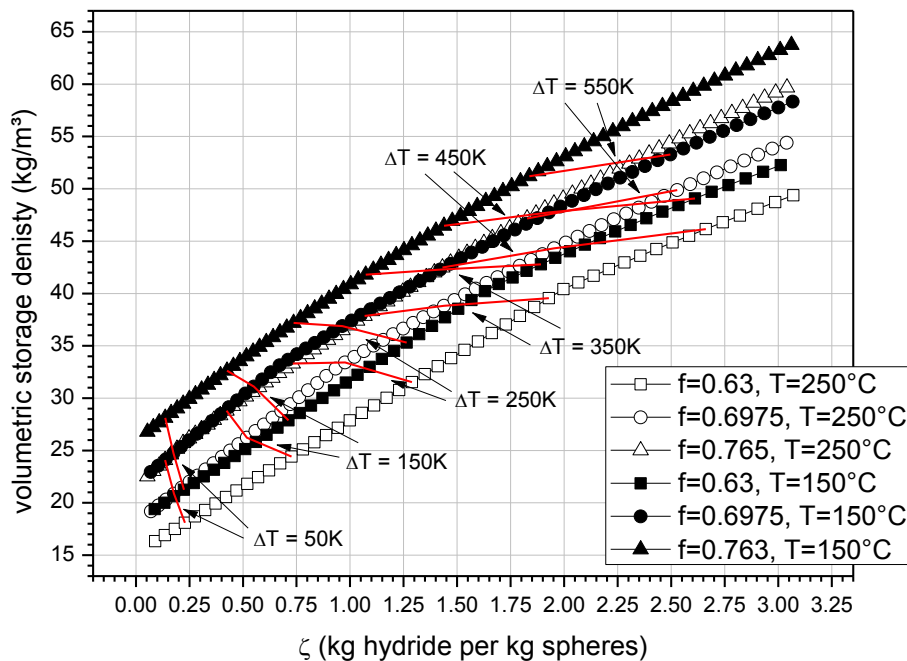


Figure 3.23: Influence of the packing factor and the extraction temperature on the volumetric storage density as a function of ζ , the ratio of hydride to spheres; hollow glass microspheres with a safety factor of $S_f = 1$ are used in this comparison; resulting temperatures are also given (red lines)

3.3.7. Summary of hybrid system analysis

The main arguments for the use of a hybrid system rather than hollow glass microspheres alone were: first, the volumetric storage density can be drastically increased compared to hollow glass microspheres alone; second, the costs can be significantly reduced when compared with a stand-alone hydrolytic system. It became clear that the achievable gravimetric storage densities of $\gamma_{G,sys} = 8-20$ wt% are well within DOE-targets. However, it was also found that the volumetric storage densities of $\gamma_{V,sys} = 30-50$ kg/m³ are within 2017 targets but below the ultimate targets and more research has to be done to further increase the volumetric storage density (see also Table 3.11). Moreover, it was shown that the current costs of the proposed system are much too high and fall far short of the DOE-targets. The most cost-intensive factor is sodium borohydride, thus making it the critical component. In order to reach acceptable costs the compound prices have to be cut dramatically, i.e. 98% for sodium borohydride, 90% for hollow glass microspheres and 70% for hydrogen.

In conclusion the remaining bodies of research are:

- permeability of glass
- realizing higher packing densities in a feasible way
- recycling of and costs of sodium borohydride NaBH₄
- costs of hydrogen
- costs of spheres
- kinetics of the hydrolytic reaction will be discussed in section 6

	DOE-2017	DOE-ultimate	hybrid system
γ_G (wt%)	5.5	7.5	8-20
γ_V (kg/m ³)	40.0	70.0	30-50

Table 3.11: Resulting hydrogen storage densities of the hybrid system compared with DOE targets [9]

As already explained at the beginning of chapter 3.3 the spheres have to be coated with a catalyst in order to induce and accelerate the hydrolytic reaction. The development of this coating process will be described in the next chapter.

4. Coating of hollow glass microspheres

As was shown in section 3.3.2 it is necessary to apply a catalyst to the surface of the hollow glass microspheres to increase the reaction kinetics. There are several ways for coating non-conductive granulates like hollow glass microspheres, i.e. electroless plating, sol-gel coating, chemical vapour deposition in fluidized beds and sputter deposition. All methods will be described briefly in the following sections, including their advantages and disadvantages. Focus, however, will lie on the sputtering process, as this was the chosen coating method.

Furthermore, the development of the apparatus to uniformly coat hollow glass microspheres by sputtering will be described in detail. Oxide films have been applied as catalyst carriers by pulsed magnetron sputtering, which will also be discussed in this section.

Deposited film materials were Al, Cu, Pt, Ru, Ti, TiO₂ and combinations thereof. Al and Cu were used for tests on the coating apparatus, since they are well characterized and inexpensive. Pt and Ru were used as noble metal catalysts with TiO₂ as catalyst carrier and Ti as bonding layer. In this section, however, only Cu, Al and TiO₂ coatings will be described, whereas the catalyst coatings will be dealt with in section 6.

4.1. Overview of possible coating methods

This section will deal with possible coating methods to apply metal and oxide films on hollow glass microspheres, i.e. wet chemical methods: electroless plating, sol-gel coating and ferrite plating, and vapour deposition methods: (plasma enhanced) chemical vapour deposition in fluidized beds and sputter deposition.

4.1.1. Electroless deposition – Overview

Electroless deposition encompasses any process that continuously deposits metal from an aqueous medium. Metal ions of the solution are reduced at the catalytic surface of the substrate which is, in course of the process, coated by the metal. The deposited metal also works as a catalyst for the reduction, which is why this process is called autocatalytic. The process always includes an oxidation and a reduction. Thus it is a redox reaction, which requires a reducing agent which can be oxidized, whereas the metal ions are reduced [102].

One of the most important electroless plating processes is nickel plating, which is why this process will be briefly described as an example.

Electroless nickel

For electroless nickel deposition the following compounds are necessary:

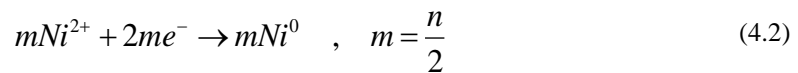
- a nickel cation source: nickel sulphate, nickel chloride or nickel acetate
- a reducing agent: sodium hypophosphite ($\text{NaH}_2\text{PO}_2 \cdot \text{H}_2\text{O}$), sodium borohydride (NaBH_4), dimethylamine borane ($(\text{CH}_3)_2\text{NHBH}_3$) or hydrazine ($\text{N}_2\text{H}_4 \cdot \text{H}_2\text{O}$)

The resulting redox reaction can be written as:

Oxidation:



Reduction:

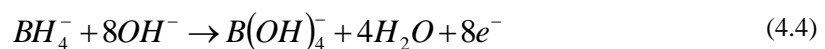


Overall:



where *Red* is the reducing agent and *Ox* the resulting oxide. However, the experimentally observed reaction characteristics indicate that the reactions are considerably more complex than described by simple stoichiometric equations [102]. As an example, the reaction with a borohydride as reducing agent is given:

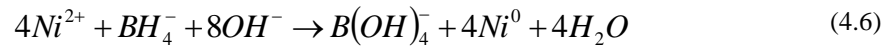
Oxidation:



Reduction:



Overall reaction:



The characteristics of electroless nickel plating include the evolution of hydrogen gas accompanying the reduction of nickel. Furthermore, the deposit is not pure nickel but contains phosphorus, boron or nitrogen depending on the reducing used agent. As mentioned before, the reduction reaction takes place only on the surface of certain metals and must also take place on the deposited metal in order to increase film thicknesses. Finally, the utilization of the reducing agent for depositing metal is considerably lower than 100 percent [102].

In general, the number of metals that can be electrolessly deposited is rather limited due to the characteristics of the reaction. In addition, the resulting films are not pure but always contain compounds of the reducing agent of less than 1 percent. Possible pure metal coatings include copper, silver, gold, nickel, cobalt, platinum, palladium (Cu, Ag, Au, Ni, Pt, Pd) [102, 103, 104, 105, 106, 107]. Using the proper reducing agent binary alloys can be realized, with Ni-P coatings being the most established ones. Other examples of binary alloys deposited electrolessly are Co-P and Co-B [102, 108, 109]. By co-deposition also ternary alloys can be realized, e.g. Co-Fe-(Sn, Pd), Ni-Co-P, Ni-W-P and Ni-Ce-P [110, 111, 112, 113].

4.1.2. Electroless plating on microspheres

Most works, dealing with the coating of hollow glass microspheres and similar particles by electroless plating, focus on enhancing microwave absorbing properties by increasing the conductivity of the spheres or changing the magnetic properties. The coated particles are still lightweight and can be mixed into polymers for electromagnetic shielding [104, 108, 109, 110, 114, 115, 116, 117, 118, 119].

To coat hollow glass microspheres or similar particles (cenospheres), the surface of the spheres has to be sensitized, which basically means to catalytically activate the surface. Commonly used activators are: PdCl₂, SnCl₂, AgNO₃ [104, 108, 109, 110, 114, 115, 117, 118, 120]. This process is quite expensive due to these required activators in combination with the large total surface of the spheres [120].

The coating process can be divided into the following steps:

- pre-treatment of spheres: washing in distilled water and/or coarsening the surface with for example NaOH
- sensitizing the spheres in an aqueous solution containing PdCl₂, SnCl₂ or AgNO₃.
- drying
- plating in plating solution as described before

- washing and drying

The process is also presented in Figure 4.1 leaving out the drying and washing procedures.

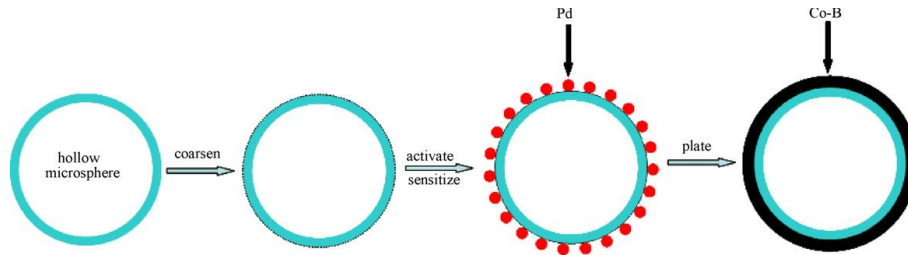


Figure 4.1: Schematic of the coating procedure of hollow glass microspheres by electroless plating, PdCl₂ is used activation agent and a Co-B film is deposited; taken from [109]

Besides coating spherical objects, this coating method is also applied in the fields of catalysis, optics and biotechnology [107].

The main advantage of electroless deposition is that no expensive equipment such as high voltage power supplies or vacuum systems is necessary. Moreover, the whole process works under ambient conditions, with no need for extreme temperatures or pressures (low and high). However, as became clear, the number of metals and alloys that can be electrolessly deposited is very limited. Completely pure metal element coatings are not possible due to the process characteristics. In addition, it is very expensive to coat hollow glass microspheres with this process due to the high costs of sensitizing agents and the large surface of the hollow glass microspheres. Furthermore the whole procedure is quite complex due to the several necessary steps which include washing, heating and drying.

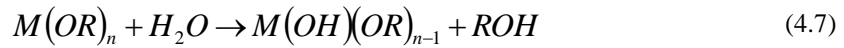
4.1.3. Sol-gel deposition – Overview

The sol-gel process is a wet chemical process to synthesize glassy or ceramic materials, as well as composites, at mild conditions. It can be used for a wide range of compositions (mostly oxides) in various forms, i.e. thin films, monoliths, composites, porous membranes, powders and fibres. Non-oxides that can be formed include nitrides, sulphides, carbides and fluorides [121].

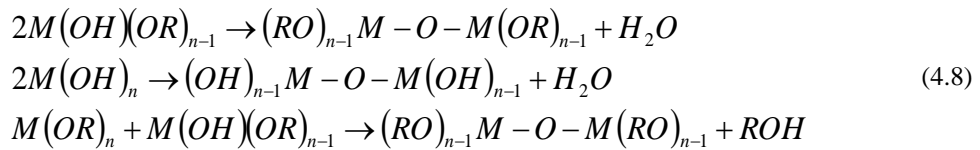
The chemical reaction starts from an ion or a molecular compound and forms a three-dimensional network through oxygen bond formation between the ions. Therefore, first a sol or a homogeneous dispersion of molecular precursors like metal alkoxides, organometallic compounds, metal salts or oxides has to be prepared. By evaporating solvent the viscosity

increases and the sol gelatinises forming colloids, polymer chains or clusters, building a three dimensional network. At this stage the gel can be aged at certain temperatures to influence the final material. After that the gel is dried, e.g. by heating or ultra violet irradiation, and residual water and solvents are evaporated. During this process parameters can be chosen either to densify the network, forming a film or aerogel, or collapse it to a powder, forming a xerogel [121, 122].

Throughout the whole sol-gel process hydrolysis and condensation reactions occur, where the hydrolytic reactions produce aliphatic alcohol, which evaporates, and the (poly)condensation process leads to the forming of metal-oxygen-metal bonds. The hydrolytic reaction can be written as



and the (poly)condensation in three steps as



When using water as a solvent the reaction is very complex, since hydrolysis, condensation and aggregation occur almost simultaneously due to the double role of water as ligand and solvent. To avoid the issues of an aqueous solution other solvents can be used, e.g. organic solvents [121, 122].

Since the hydrolysis is quite slow, the reaction is usually accelerated by adding acids or bases as catalysts. These catalysts have a major impact on the final structure of the derived network. Generally, acids result in a more polymer-like expanded structure, while bases result in a more particle like morphology. Other parameters apart from pH that influence the structure of the derived material are the precursor types, the solvent concentration, aging time in gel condition and the temperature (aging and drying) [121, 122].

The silicon-based sol-gel process represents the most important reaction for industrial applications. Typical precursors of that process are: tetramethoxysilane $Si(OCH_3)_4$ (TMOS) and tetraethoxysilane $Si(OCH_2CH_3)_4$ (TEOS). Apart from the silicon-base process metal-based systems became more and more important during the development of sol-gel chemistry. Today the sol-gel process is used for materials for electronic, optic, magnetic and catalytic

applications. There are several differences between silicon and metals in sol-gel chemistry; however, they will not be discussed in this work. More information can be found in [121, 122].

To vary resulting material parameters, the sol-gel films can be doped with metal and other compounds by adding a doping agent to the sol. As an example, the main starting compounds of a Al/Mg doped ZnO film would be: Zinc acetate dehydrate ($\text{Zn}(\text{CH}_3\text{COO})_2 \cdot 2\text{H}_2\text{O}$) as base material, 2-Methoxyethanol ($\text{C}_3\text{H}_8\text{O}_2$) as solvent, aluminium nitrate nonahydrate ($\text{Al}(\text{NO}_3)_3 \cdot 9\text{H}_2\text{O}$) and magnesium acetate ($\text{Mg}(\text{CH}_3\text{COO})_2 \cdot 4\text{H}_2\text{O}$) as dopant source [121, 122, 123].

4.1.4. Sol-gel coatings on microspheres

Even though the sol-gel process can be used to manufacture hollow glass microspheres as mentioned in section 3.1.6, this section will only deal with coating hollow glass microspheres and other particles by the sol-gel process. Despite intensive research, only few works about the coating of hollow glass microspheres by the sol-gel process were found [124, 125, 126, 127, 128, 129]. Other works refer to some other particles, e.g. diamonds, carbon powder or other powders, e.g. [130, 131, 132].

The works dealing with the coating of microspheres focus strongly on TiO_2 thin films and only one work was found which discusses another coating material, i.e. SnO_2 . In these works the pursued applications were on photonics [124], photo catalysis for air and water treatment [125, 127, 129], and electronics [126].

The coating procedure itself is similar to the electroless plating procedure [124, 126, 127].

- pre-treatment of spheres: washing in distilled water and/or coarsening the surface with, for example, NaOH
- dispersing the spheres in the precursor solution, e.g. titanium tetraethoxide $\text{Ti}(\text{OC}_2\text{H}_5)_4$ ethanolic solution
- filtering and drying
- (washing)
- (sintering)

The main advantages of the sol-gel process are its versatility regarding film morphology. Structure, texture and porosity, and shape of the coating material can be influenced by process parameters. Furthermore nanoparticles can be incorporated and large and/or bent-shape substrates can be coated easily. Any oxide and some non-oxides can be fabricated, also with uniform doping. No expensive equipment like vacuum chambers is necessary. On the other hand, no metal coatings are possible, which is one main disadvantage. Furthermore, due to

stress by shrinkage of the gel upon drying, the coating can easily crack above a critical thickness. Thick coatings above 2 μm can only be achieved by adding organic components. In addition, multicomponent materials are difficult to handle due to preferential precipitation of a particular oxide during sol formation [121].

4.1.5. **Ferrite plating**

Ferrite plating will not be described in detail, since only one work addressing hollow glass microspheres was found.

Crystalline spinel ferrite films with various compositions can be formed directly from an aqueous solution at temperatures from 24 °C - 100 °C, i.e. $(\text{Fe},\text{M})_3\text{O}_4$, where $\text{M} = \text{Fe}, \text{Co}, \text{Ni}, \text{Zn}, \text{Al}, \text{Cr}, \text{Ti}$, etc. [133]. Wei et al. (2007) used this method to plate magnetic Fe_3O_4 films on hollow glass microspheres for electromagnetic shielding [134]. Like in other wet chemical methods, this method does not require any expensive equipment and works at mild conditions. The main disadvantage, however, is the limited number of compounds that can be deposited.

4.1.6. **Chemical vapour deposition (CVD)**

The most common way to coat powder-like substrates is chemical vapour deposition (CVD) in fluidized bed reactors [135]. Due to the similarity of chemical vapour deposition and sputtering, both are vapour deposition processes, the methods for coating powders with CVD will be described in more detail than previous wet coating methods.

CVD processes are widely used in industry due to their versatility to deposit a very large variety of elements and compounds including metals, semiconductors, oxides, nitrides and carbides. The deposits range from amorphous to epitaxial layers, having a high degree of perfection and purity. However, there is a limited number of possible coatings, since there does not exist a volatile compound of every desired solid material [136, pp. 60-76, 137].

In the CVD process gaseous reactants are transported into the reaction chamber, react at the surface of the substrate, either activated thermally, catalytically (gold particles for nanowire formation) or plasma enhanced (PECVD). Solid reaction products form a film; whereas gaseous product compounds are pumped out of the reaction chamber (see Figure 4.2). Today not only thin films but also more complex structures like nanowires can be realized by CVD processes [137, p. 298, 138].

The pressure of CVD processes varies with the desired coating. There are low pressure (1-100 Pa), hot filament (1-2000 Pa) and atmospheric pressure (100 kPa) CVD processes. Typical process temperatures range from 150-1300 °C depending on precursor materials and desired

film. As an example, metal coatings of Cu, Pt and Ru can be deposited at rather low temperatures of about 250-500 °C [139, 140], TiO₂ at temperatures of about 420-900 °C [141, 142] and Si films 800-1200 °C [143]. Due to the necessary high temperatures thermal decomposition of the substrate material can be an issue. As a result the substrate materials are limited. To decrease the required temperature, a plasma can be applied (plasma enhanced/assisted chemical vapour deposition). In the plasma-enhanced chemical vapour deposition (PECVD) method, reactive radicals, ions, and atoms/molecules in the gas phase are generated by plasma rather than by temperature. While plasma-enhanced methods are very useful to lower the substrate temperature, the deposited films are typically less conformal and often contain more surface impurities than competing methods [137, p. 303].

The typical steps that occur in CVD reactions are [137, 143]:

- gas-phase precursor molecules enter the deposition zone,
- physisorption to the substrate surface through weak van der Waals interactions,
- dissociation by thermolysis, catalysis or other means,
- the desired species is left at the surface forming strong covalent bonds,
- former ligands desorb and leave the deposition chamber via the carrier gas flow,
- surface diffusion of chemisorbed species to thermodynamically favoured positions and nucleation
- Transport of reacting gaseous species to the surface.

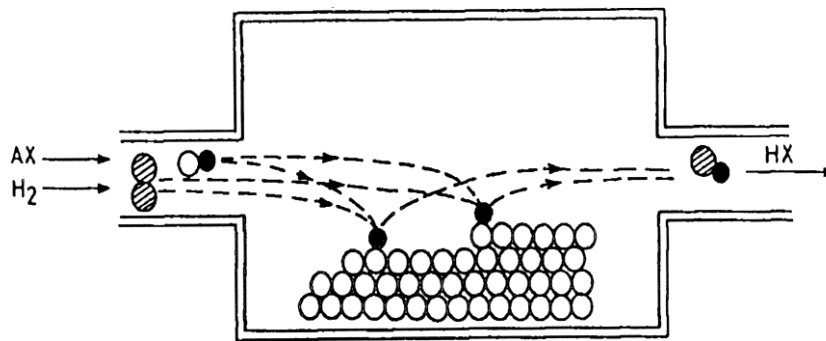


Figure 4.2: Schematic of the chemical vapour deposition (CVD) process; reactants enter the reaction chamber, react at the substrate surface where a solid is formed, residual reaction products leave the reaction chamber; taken from [136, p. 61]

CVD reactions fall into four different categories [136, p. 62]:

- Thermal decomposition reactions (pyrolytic reactions), e.g.:



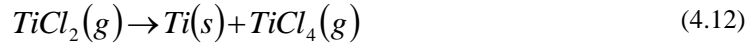
- Reduction reactions, e.g.:



- Displacement reactions, e.g.:



- Disproportionation reactions, e.g.:



These different types of reactions can be involved simultaneously during one CVD process.

4.1.7. Chemical vapour deposition on hollow glass microspheres

Even though no literature was found on the coating of hollow glass microspheres by chemical vapour deposition or plasma enhanced CVD, the principle of coating small particles by these processes is very well studied. For this, some technical solutions have been devised, i.e. fixed bed, flat hearth, rotary cylinders, pneumatic conveying, vertical moving beds and fluidized beds (see Figure 4.3), where fluidised beds are most commonly used to get a uniform coating of the particles. Vahlas et al. gave a detailed report of chemical vapour deposition in fluidised beds, which will be shortly summarised in following [135].

In fixed bed and flat bed, the particles do not move and the reactive gas flows through and over the powder, respectively. In this mode the particles have contact areas with each other and with the walls, which is the major drawback, since it is impossible to coat the entire surface of each particle. Furthermore, in the case of chemical vapour infiltration, diffusion might be limited, affecting the contact between the gas reactants and the inner powder particles resulting in inhomogeneous deposition. For high desired film thicknesses clogging phenomena can occur. Due to these drawbacks, upscaling of these processes is problematic, which is another disadvantage. To overcome these issues the particles have to be moved relative to each other and to the reactor wall. Technical solutions to induce relative particle movement are rotary cylinders, pneumatic conveying, vertical moving beds and fluidized beds (see Figure 4.3). With these measures it is expected that each particle presents its entire surface to the gaseous reactants during the process and is thus fully coated [135].

The most frequently used method to treat powders by CVD is by maintaining them in a fluidised bed regime. For this, gas is injected from the bottom of the bed of solid particles through a gas-distributing plate (grid), allowing the particles to behave like a liquid. For this purpose the gas flow rate has to be above a critical limit. It has to be mentioned that the ratio of surface to volume of the particle is much higher compared to flat substrates like wafers (up to 6 orders of magnitude). As a result gaseous precursors are very often totally consumed after a

short distance beyond the entrance into the fluidised-bed reactor (some centimetres in a laboratory scale apparatus). Fortunately, this is compensated by the permanent mixing of the particles, thus ensuring uniform films. In addition, the strong convection leads to good mass transfer and desired isothermal conditions throughout the bed [135].

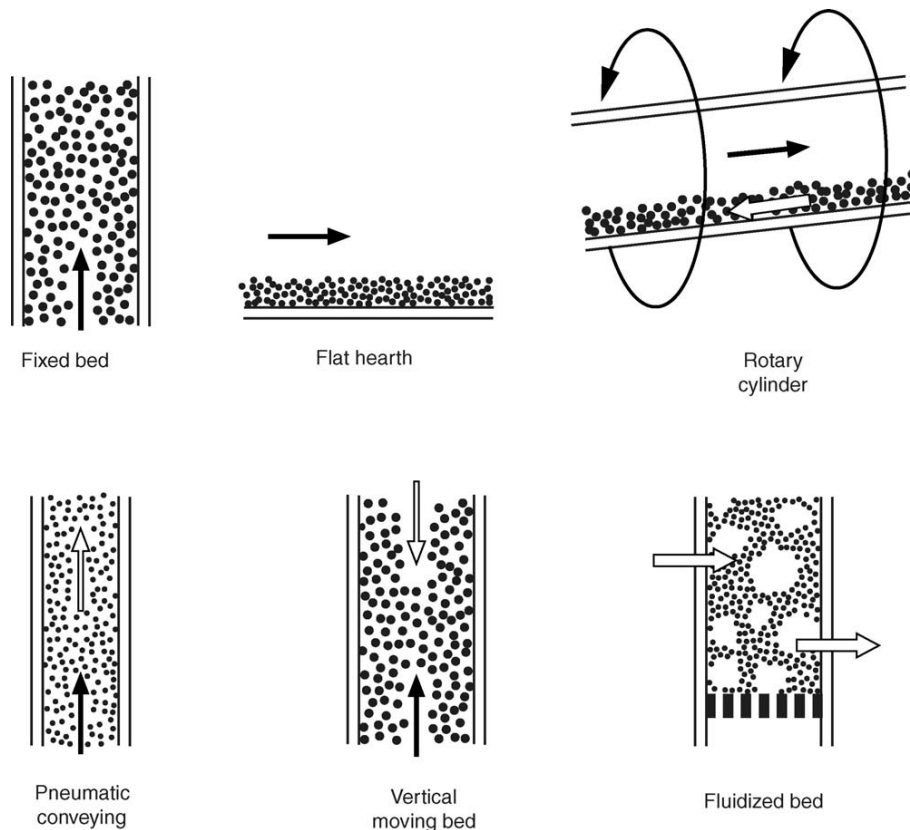


Figure 4.3: Contacting modes for CVD on powders in gas–solid reactors, taken from [135, p. 4]

Limitations arise due to the handling of powders themselves in the fluidised bed and additionally due to simultaneous CVD operation. Possible issues are: required pressure and temperature for the particular CVD process, deposition on the reactor walls and on or in the gas distributor, clogging of the bed due to high deposition rates and/or to low-quality fluidization, homogeneous nucleation and handling of the CVD precursors (purity, volatility, toxicity, etc.) [135].

As already mentioned, it is also possible to realise a plasma enhanced chemical vapour deposition process in a fluidised bed, as shown by the group of von Rohr [144, 145, 146, 147] and others [148]. Figure 4.4 shows a typical setup of a PECVD apparatus with a fluidised bed reactor. The setup can be divided into three parts, the reaction section with the microwave plasma source, the cyclone section, where residual gas is separated from powder particles, and

the feed section, where the particles are fluidised by argon gas flow (< 1 sccm) and fed to the riser tube [147].

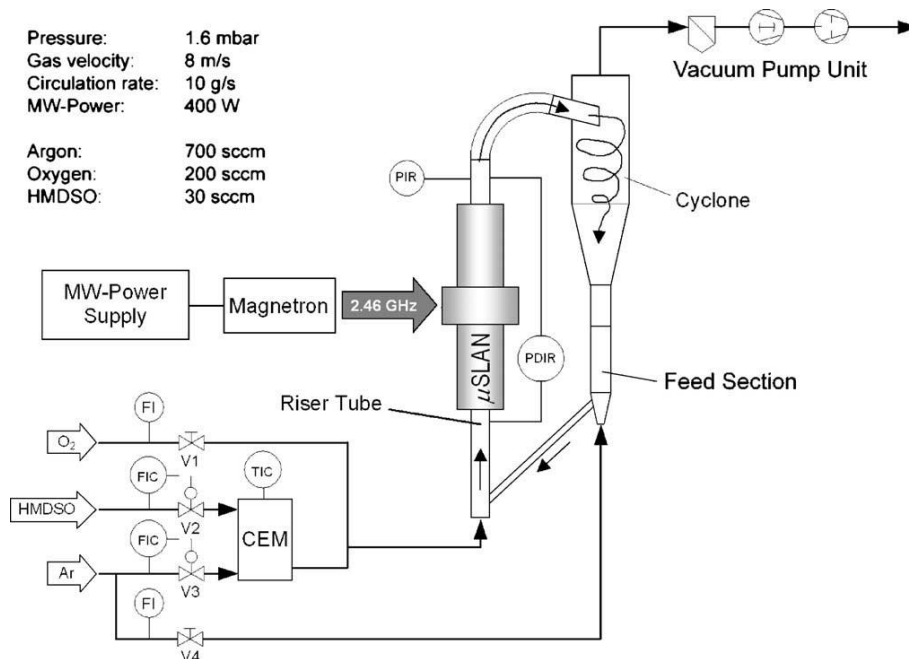


Figure 4.4: Typical setup of a plasma enhanced vapour deposition apparatus with fluidised bed reactor; reaction section with the microwave plasma source; cyclone section, where residual gas is separated from powder particles; feed section, where the particles are fluidised; taken from [147]

A specific problem of FB-PECVD processes is that plasmas hardly penetrate a dense bed (fixed or even fluidized). In some cases this can be achieved by increasing power density (typically 10 W/cm^3 in the case of pure argon) with the risk of creating hot spots and the local melting of particles. This is why the plasma is usually generated at a position where particles are diluted, i.e. in the riser tube (with particle densities of $\sim 50 \text{ g/l}$) [135, 144].

Examples for particles coated by chemical vapour deposition in a fluidised bed reactor are: silicon oxide on NaCl crystals for characterization of the process [144], TiO₂ and V₂O₅/TiO₂ on glass beads and silica gel powder for photo catalysis [145, 148, 149], alumina on abrasive SiC particles [146] and SiO_x films on silica gel particles [147]. The alumina coatings on abrasive particles yielded granular films with attrition at the edges [146].

It appears that the film formation strongly depends on the substrate morphology. Whereas smooth substrates yield dense and coherent films, rough surfaces induce pronounced column growth [147].

It can be concluded that both CVD and PECVD bear the potential for thin film deposition on hollow glass microspheres in a fluidised bed reactor, though no publication regarding this

specific topic was found. The advantages of such an approach would be that the spheres could be coated on every side simultaneously and thus uniformly, which is not possible with standard physical vapour deposition methods (PVD) due to their line of sight characteristics. However, there also exist methods for coating powders with PVD processes, as will be shown in the next section. Another benefit of CVD is that a large variety of materials can be deposited. Still, there are some disadvantages. The overall process only offers a limited choice of materials, since fluidised bed and CVD parameters have to match and agglomeration of particles can also become an issue. Furthermore, an applicable precursor has to be available for the desired coating also with respect to the fluidized bed, which is not always the case. In addition, when using CVD rather than PECVD the high required temperatures can also be an issue for some substrates.

4.1.1. Magnetron Sputtering

Another method to coat hollow glass microspheres is magnetron sputtering, which will be discussed in detail in the next section, since it is one main topic of this thesis.

4.2. Methods for coating hollow glass microspheres by magnetron sputtering

This section will deal with coating hollow glass microspheres by magnetron sputtering. For this, the principle of magnetron sputtering will first be briefly described. After that, an overview of possible methods to coat powder particles by sputtering will be given, before describing the coating system developed in this work. An additional topic regarding TiO₂ films deposited on planar glass and hollow glass microspheres by pulsed DC magnetron sputtering will be addressed afterwards in section 5.

4.2.1. Magnetron Sputtering

Magnetron sputtering is one of the most widely used methods for thin film deposition. It can be utilized to manufacture nearly every metal coating or metal composite as well as nitride, oxide, carbide, fluoride and arsenide layers with controlled stoichiometry, thus making magnetron sputtering a most versatile coating method. The possibility to coat large area substrates and the easy-to-handle process parameters of magnetron sputtering enable a wide range of industrially important applications, i.e. hard coatings, wear-resistant coatings, low friction coatings, corrosion resistant coatings, decorative coatings, catalytic coatings and coatings with specific optical or electrical properties [150, 151, 152].

First it has to be mentioned that magnetron sputtering is a high vacuum and high voltage process. The following two paragraphs describe the principle of magnetron sputtering (taken from Kelly and Arnell (2000) [150] with minor adaptations).

“In the basic sputtering process, a target (or cathode) plate is bombarded by energetic ions generated in a glow discharge plasma, situated in front of the target. The bombardment process causes the removal of target atoms <(sputtering)>, which may then condense on a substrate as a thin film. Secondary electrons are also emitted from the target surface as a result of the ion bombardment, and these electrons play an important role in maintaining the plasma. The basic sputtering process has been known for many years and many materials have been successfully deposited using this technique. However, the process is limited by low deposition rates, low ionisation efficiencies in the plasma, and high substrate heating effects. These limitations have been overcome by the development of magnetron sputtering and, more recently, unbalanced magnetron sputtering.” [150]

“Magnetrons make use of the fact that a magnetic field configured parallel to the target surface can constrain secondary electron motion to the vicinity of the target (see Figure 4.5). The magnets are arranged in such a way that one pole is positioned at the central axis of the target and the second pole is formed by a ring of magnets around the outer edge of the target. Trapping the electrons in this way substantially increases the probability of an ionising electron-atom collision occurring. The increased ionisation efficiency of a magnetron results in a dense plasma in the target region. This, in turn, leads to increased ion bombardment of the target, giving higher sputtering rates and, therefore, higher deposition rates at the substrate. In addition, the increased ionisation efficiency achieved in the magnetron mode allows the discharge to be maintained at lower operating pressures (typically, 0.1 Pa, compared to 1 Pa) and lower operating voltages (typically -500 V, compared to -2 to -3 kV) than is possible in the basic sputtering.” [150]

The principle of magnetron sputtering is given in Figure 4.5: Positively charged ions of the plasma are accelerated towards the target. The resulting bombardment sputters the target and removed target particles are transported towards the substrate and condense on its surface. Using a magnetic field the secondary electrons of the sputtering process are trapped near the target increasing the plasma density, thus increasing erosion rate at the target and the deposition rate at the substrate. Figure 4.5 shows a bottom up configuration, where the target is below the substrate. The positions can be changed, with either the target in the top position, as was used in this work, or in horizontal alignment. The sputtering process has a line of sight characteristic, which basically means, that objects which are not in the target particle beam are not coated.

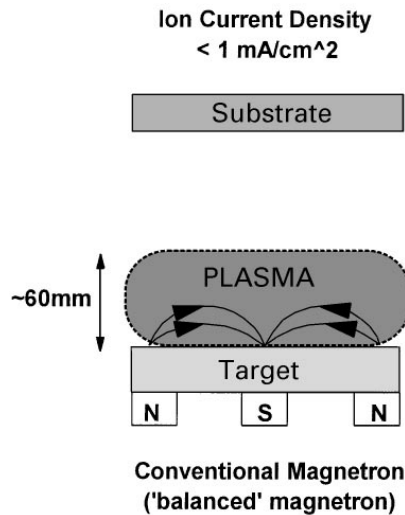


Figure 4.5: Principle of magnetron sputtering, taken from [150]

Different sputter source configurations

There are several different source configurations for magnetron sputtering, which will be shortly explained in the following:

- Common diode direct current magnetron sputtering as was described before.
- Triode magnetron sputtering with an additional heating filament to increase electron and thus plasma density [153].
- Radio frequency sputtering (RF), where a frequency of 13.56 MHz is coupled to the target via an impedance matching network and blocking capacitor. The target and the counter-electrode, which may be the substrate holder, act as the two electrodes. Due to higher mobility of the electron both electrodes acquire a negative bias with respect to the plasma and the target is eventually bombarded with ions (sputtering). Usually the vacuum chamber works as counter electrode, resulting in only minor or none substrate sputtering [153].
- Dual magnetron (DMS) or TwigMag™ systems, where two sputtering sources alternately work as cathode [154].
- Pulsed DC magnetron sputtering, where direct current is pulsed in mid-frequency (5-350 kHz). This method will be described more thoroughly in section 5.2.2.
- High power pulsed magnetrons sputtering (HiPIMS or HPPMS) works similar to pulsed DC magnetron sputtering, only the pulses have much more power (MW) and frequency is much lower (0.5-2 kHz). With this technique highly ionized plasmas can be generated. A very large peak power on the order of megawatts is delivered to

the target in a very short period of time (100-150 μs). This produces a high degree of ionization of the target species [155].

- Unbalanced and balanced magnetron: Whereas all electrons are trapped near the target in a balanced magnetron system, in an unbalanced magnetron some of the electrons can escape and reach the substrate region. This can change and/or improve the deposited film properties due to ionisation events near the substrate [153].

For this work mainly pulsed direct current sputtering was used.

4.2.2. Magnetron sputtering on hollow glass microspheres - review

Although coating plane substrates is state of the art, the coating of powder-substrates, granulates and particles of approximately 2-600 μm diameter by magnetron sputtering is still a difficult task.

This is due to, (i): each side of every single particle has to be exposed to the sputter beam in order to become fully coated; therefore a particle mixing or rotating mechanism is necessary. (ii): small particles of different size and shape become wedged together during the mixing process which prohibits most of the particles from being coated since they are not exposed to the sputtering beam. (iii): in vacuum the particles tend to stick together as coating proceeds, especially when the powder is coated with pure metal. This is because of the absence of any separation layer between the coating of two particles in contact, i.e. air, water film or an oxide layer.

To overcome these issues there were several approaches, as (i): a rotating drum, where the axis of rotation is horizontally and the barrel can be shaped in different ways, e.g. circular [156, 157] with inlets [158, 159], hexagonal [160, 161, 162, 163, 164, 165] or conical [166, 167], and the targets are positioned within the drum or perpendicular beside the drum. (ii): Vibration, where the sample stage is connected to an ultrasonic or electromagnetic vibration generator which keeps the particles tumbling [159, 168, 169, 170, 171, 172, 173, 174, 175, 176], or (iii): tilted rotating vessels, which also can be of different shapes as described in [177, 178, 179, 180], where the last two works [179, 180] were part of this thesis and thus will not be further quoted. Another more exotic approach was done by Kersten et al. (1998) [181] by trapping iron particles in a weak radio frequency plasma and coating them with aluminium by magnetron sputtering. However, the density of the confined particles and thus the yield of modified powder, were rather low. Furthermore, the trapping would not work with the non-conducting hollow glass microspheres.

In the following subsections, the different mentioned approaches will be discussed, before describing the coating mechanism developed in this work in detail.

Rotating Drums

Takehima (1990) [156] describes a rotating drum which is built around the sputter sources and additionally acts as the vacuum chamber. This is similar to the setup proposed by Poelman et al. (2007) [157], but differs however, since in that approach the whole drum with a diameter of 75 cm was located inside a vacuum chamber (see Figure 4.6). Thoth (2006) additionally proposed the use of comb-like inlets to fluidise the particle bed by lifting the powder particles up, so they can fall through the sputtering beam [158]. To lift up particles some inlets in the drum were also realised by Ensinger and Müller (1998) [166, 167], who chose however a conical shape drum with the target aligned horizontally (see Figure 4.7). The group of Abe [160, 161, 162, 163, 164, 165] designed a hexagonal-barrel sputtering system (see Figure 4.8). Due to the rotation of the barrel, the powder is lifted up to a certain level along the wall of the barrel and falls to the bottom of the barrel under its own weight. A vibration mechanism is mounted on the system to agitate the barrel, so that the powder does not adhere to the wall of the barrel and does not agglomerate.

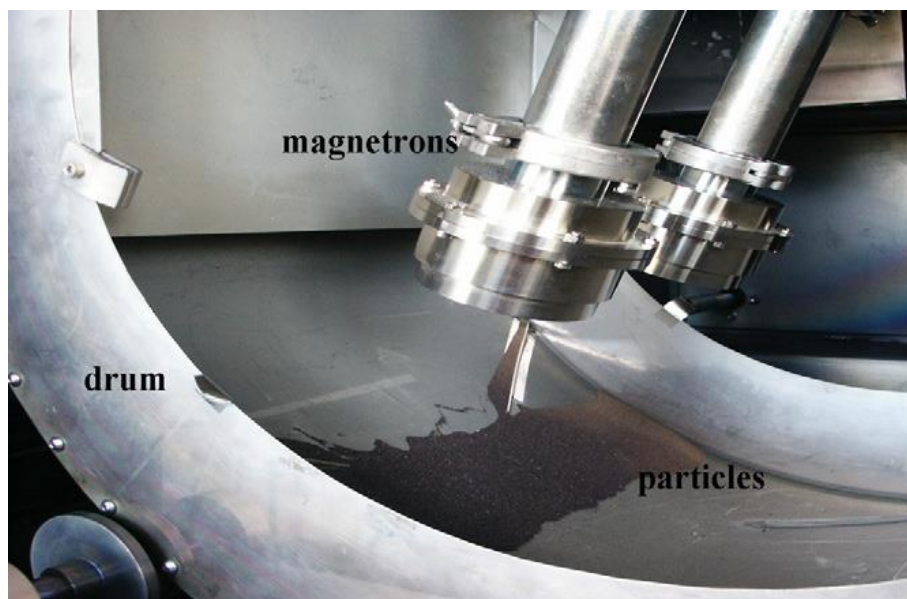


Figure 4.6: Concept for coating powders by magnetron sputtering in a surrounding drum, taken from Poelman et al. (2007) [157]

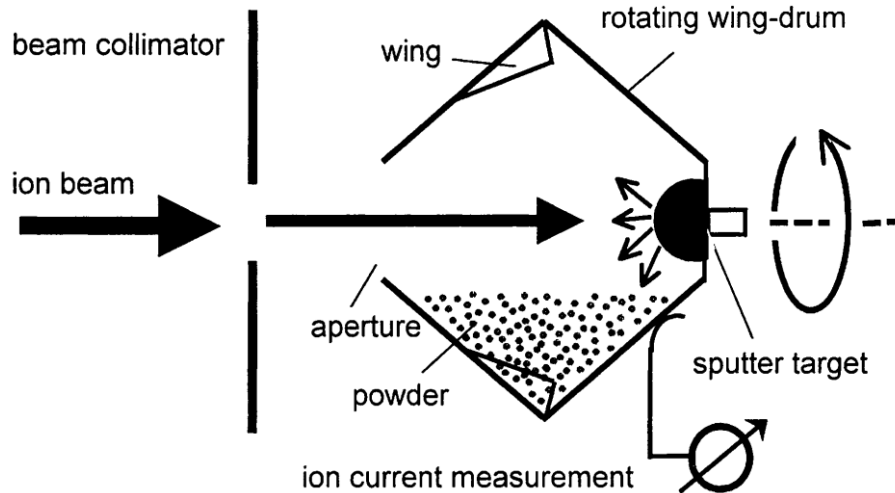


Figure 4.7: Concept for coating powders by ion beam sputtering in a conical shaped drum with wings that lift up the powder material, taken from Ensinger and Müller (2003) [167]

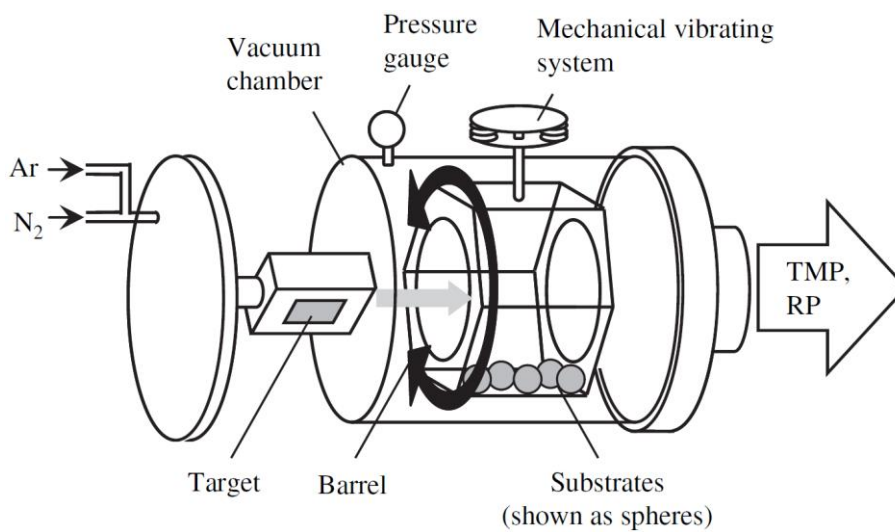


Figure 4.8: Concept for coating powders by magnetron sputtering in a hexagonal shaped drum with a mechanical vibrating system, taken from Taguchi et al. (2009) [165]

The patent of Makowiecki et al. (2002) [159] covers most of the mentioned approaches including different ways to transport the powder to the top of the drum similar to Ensinger and Müller (2003) [167], a tilted drum and agitated substrate carriers to break up clusters.

The shown drum methods can be easily scaled up to several dm³ of powder volume to be coated.

Good vibrations

Yu et al. [168, 169, 170, 171, 172, 173, 174] designed a sample holder connected to an ultrasonic vibration generator in order to coat cenosphere particles uniformly (powder volume 1-3 cm³). A similar setup was used by Fedotov et al. (2013) [175] (powder volume < 1 cm³) and Baechle et al. [176] (powder volume ~20 cm³). Even though some results look promising, upscaling of these deposition devices might be difficult.

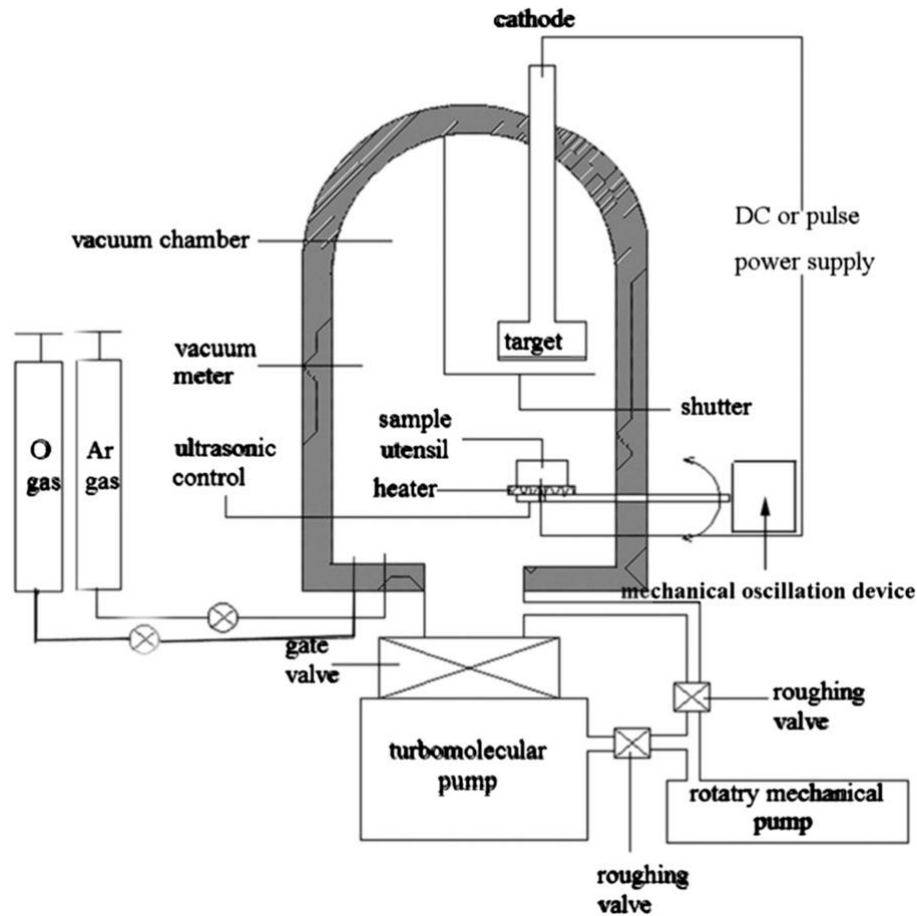


Figure 4.9: Schematic of the apparatus used for coating cenospheres by magnetron sputtering with an ultrasonic vibration generator connected to the sample stage holder, taken from Yu and Shen (2011) [174]

Tilted rotating vessels

The next section will deal with the development of tilted vessels to coat hollow glass microspheres by magnetron sputtering. At this point details of the mentioned literature which was part of this thesis will be given along with additional information.

4.3. Experiments on coating hollow glass microspheres

In previous works of the Thin Films working group at Vienna University of Technology a method for coating granular material by magnetron sputtering was developed (see Figure 4.10). Tilted vessels (3) rotate below the sputtering target to assure good mixing of the granular material (tilt angle α). Furthermore vessel positions can change by rotating the ground plate (1) the vessels are attached to with cantilever arms (2), thus enabling composite coatings by utilizing up to three sputter targets in the vacuum chamber. The vessels and the ground plate are driven by a central friction drive (4,5). The coated substrate materials were diamonds, which have a much higher density than hollow glass microspheres. [177].

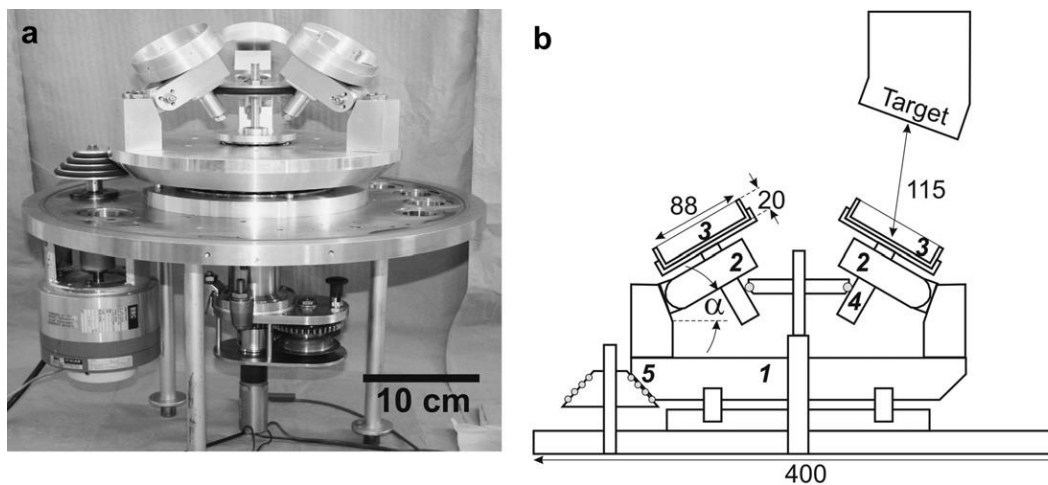


Figure 4.10: Set-up of the particle coating system: (a) photographic image; (b) sketch of the geometric relations, straight numbers are distances in mm, italic numbers relate to details described in the text. Taken from [177]

In order to coat hollow glass microspheres, the author of this work designed a special shaped vessel in his diploma thesis work, published in [178]: It was found that hollow glass microspheres preferentially stick to edges and in corners of common cylindrical vessels. Moreover, it became clear that steep surfaces are necessary to guarantee gliding of the spheres, which would otherwise start to stick to the inner surfaces of the coating vessel. Overcoming these issues resulted in a new vessel design shown in Figure 4.11. The main characteristics of this design were the cone-funnel shaped inner surfaces, which are perpendicular to each other and thus guarantee that each surface is vertical at least once in a rotation period. To prevent simple gliding and to assure mixing of the substrate powder a mixing blade is attached to the inner surface of the funnel part. To further prevent sticking and break apart clusters of spheres that form during the coating process, a percussion mechanism consisting of coach springs which periodically hit the vessel was applied [178].

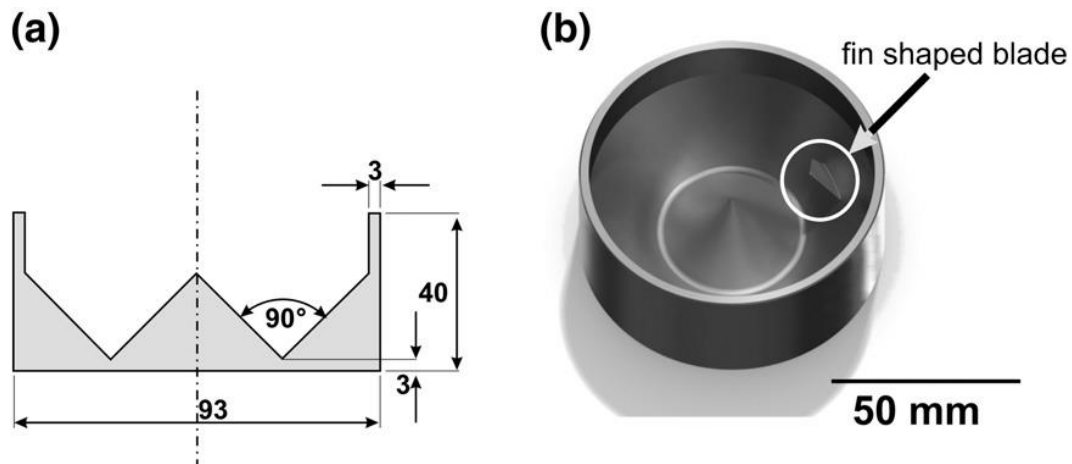


Figure 4.11: Schematic of the special shape coating vessel (a), rendering of the vessel including the mixing blade, taken from [178] (corrected angle)

This section will deal with the improvement of the just described coating mechanism, where the principle of the concussion mechanism was changed from impulse transfer by springs to impulse transfer by gravity. Furthermore, results of coating hollow glass microspheres will be presented.

4.3.1. Substrate: S38 hollow glass microspheres S38

Besides hydrogen storage applications, hollow glass microspheres or glass bubbles have a large variety of applications, e.g. thermal insulation, filling material, composite compound or road marking to name just a few. In this section, the hollow glass microspheres that were used will be characterised and the different pre-treatments of the spheres will be explained.

S38 hollow glass microspheres as delivered by 3M™

For this work hollow glass microspheres type S38 from 3M™ were used. They consist of high grade low-alkali borosilicate glass and have typical diameters of 2-70 μm [25]. A histogram of the glass sphere size distribution shows that most of the spheres have a diameter smaller than 20 μm .

As already mentioned before in section 3.2.1 the radius r of the S38 hollow glass microspheres was determined by measuring the diameter of over a thousand spheres. The measurement was done with scanning electron micrographs and *ImageJ*-Software (v.1.48) and with a particle detection algorithm integrated in *ImageJ* [54]. More details on automatic measurements can be found in the appendix section 9.2.

For the SEM-imaging some spheres were scattered on a glass plate. Then a carbon adhesive tape was pasted on top and stripped off again. The tape was upturned and fixed to the sample carrier of the SEM to analyse the spheres glued to the tape. Another method would be to scatter the spheres directly on the carbon adhesive tape, which might result in another spheres diameter distribution. With the first (top down) method only larger spheres have contact with the tape and thus are glued to the tape, whereas with the second method all spheres sizes are scattered on the tape directly. Since this difference was identified at the very end of this thesis, no additional measurement was carried out for verification for that claim. Still, it is strongly indicated by film thickness measurements carried out by Andreas Eder in course of his PhD thesis.

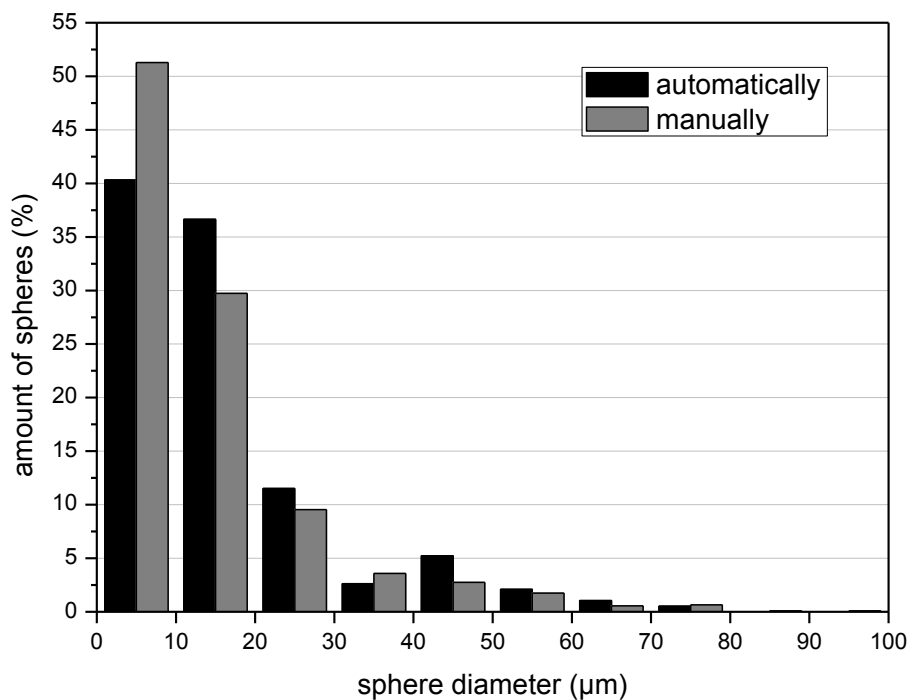


Figure 4.12: Histogram of un-sieved spheres, manually measured (grey) and automatically measured (black)

It became clear that the particle detection algorithm underestimates small sized spheres, thus for further calculations, like total surface of the spheres, the manually recorded data was used.

The mean diameter of the spheres is a critical dimension for coating, since it defines the total surface of the batch of spheres which are to be coated. Yet, there are four different ways to calculate the mean diameter and there is only one correct calculation method for coating applications. A linear approach yields the actual mean diameter of spheres, but does not take into account that most of the spheres are rather small and do not add much to the total volume. A surface area weight approach addresses the total surface of the spheres but just like the linear

approach does not consider the volume of the spheres. When using the volumetric weight diameter, which was applied for hydrogen storage densities in section 3.2.1, on the other hand, the surface is not taken into account. As a result, a combination of volumetrically and surface area weight diameter has to be used. The mean diameter d_{mean} of hollow glass microspheres with respect to surface and volume equation (4.13) can be calculated by:

$$d_{mean} = \frac{6 \cdot \sum_{i=1}^k V_{sph,i}}{\sum_{i=1}^k A_{sph,i}}, \quad (4.13)$$

where $V_{sph,i}$ is the volume and $A_{sph,i}$ is the surface area of sphere i . Table 4.1 gives the values for differently calculated diameters. It becomes clear that the method to calculate the mean diameter strongly influences the outcome, and thus the estimation of the total surface of batch of hollow glass microspheres. The diameter that actually has to be used for total area calculations is about twice the diameter of the other methods, thus decreasing the total surface area of the spheres.

linear mean diameter (μm)	area weight mean diameter (μm)	volumetrically weight mean diameter (μm)	combined weight mean diameter (μm)
14.21	19.04	23.71	40.39

Table 4.1: Comparison of differently calculated mean sphere diameters, the combined weight mean diameter must be used for coating applications

To calculate the surface A_{tot} of a volume V_0 of spheres is now very easy. The number of spheres in the volume is multiplied with the surface of a sphere using the mean diameter d_{mean} . After cancelling terms, this results to a total surface of:

$$A_{tot} = \frac{6 \cdot V_0 \cdot f}{d_{mean}}, \quad (4.14)$$

where f is the packing factor (usually $f = 0.63$). This results in a specific surface of $A_{spec} = 93.6 \text{ m}^2/\text{dm}^3$ ($\sim 0.27 \text{ m}^2/\text{g}$) for as delivered S38 hollow glass microspheres.

It has to be mentioned that the hollow glass microspheres from 3M™ are treated with silicic acid particles which work as anti-caking agent (see Figure 3.5 and some following figures). This agent shall guarantee good trickling behaviour for easy handling [25].

S38 sieved with 50 µm mesh

In the course of the experiments the trickling behaviour of the spheres in vacuum was examined. For that the spheres were sieved and thus separated into batches of bigger and smaller spheres. Sieving was carried out manually and later with a sieving machine with a sieve of 50 µm mesh size (from Retsch GmbH). Figure 4.13 shows a histogram of the sieved glass sphere size distribution. There are still spheres of small diameters (<20 µm) in the batch; most of the spheres, however, are larger and have a diameter of 30-70 µm. Again the discrepancy between automatically and manually measured sphere diameters is visible.

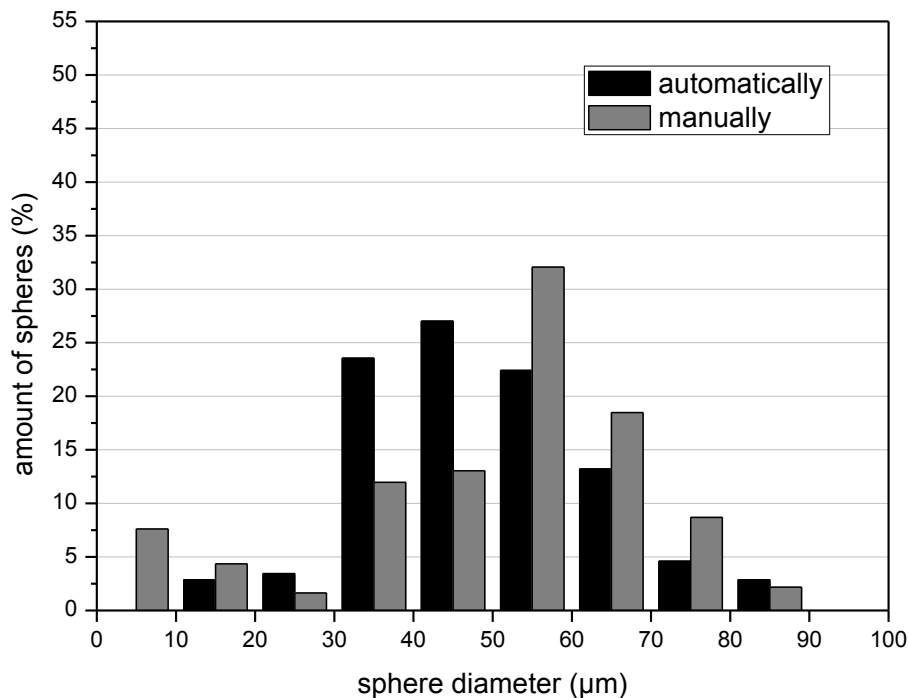


Figure 4.13: Histogram of sieved spheres with 50 µm mesh size, manually measured (grey) and automatically measured (black)

For calculating the mean diameter d_{mean} and the resulting specific surface A_{spec} the same method as before is used. The mean diameter results to $d_{mean} = 60.25 \mu\text{m}$ and the specific surface to $A_{spec} = 62.74 \text{ m}^2/\text{dm}^3$.

Figure 4.14 and Figure 4.15 show optical micrographs of un-sieved and sieved (mesh 50 µm) S38 hollow glass microspheres. As expected there are much less small spheres in the sieved sample.

S38 washed

It was found that spheres as delivered also contained broken spheres and shards. The shards worsen the trickling behaviour and broken spheres cannot store any hydrogen. For that reasons these broken particles were sorted out for catalyst coatings by washing the spheres. The method will be described in more detail in section 6.

When measuring sphere diameters of un-sieved and un-washed spheres, broken spheres and shards have not been taken into account, which is why the diameter of washed spheres can be assumed to have the same distribution as of the un-sieved spheres. Table 4.2 gives an overview of mean diameters and specific surfaces of hollow glass microspheres as delivered and sieved spheres (mesh 50 μm).

	mean diameter	specific surface
un-sieved spheres	40.39 μm	93.60 m^2/dm^3
sieved spheres (50 μm mesh)	60.25 μm	62.74 m^2/dm^3

Table 4.2: Mean diameter and specific surface of hollow glass microspheres, where the diameter was weight with a combinations of volume and surface

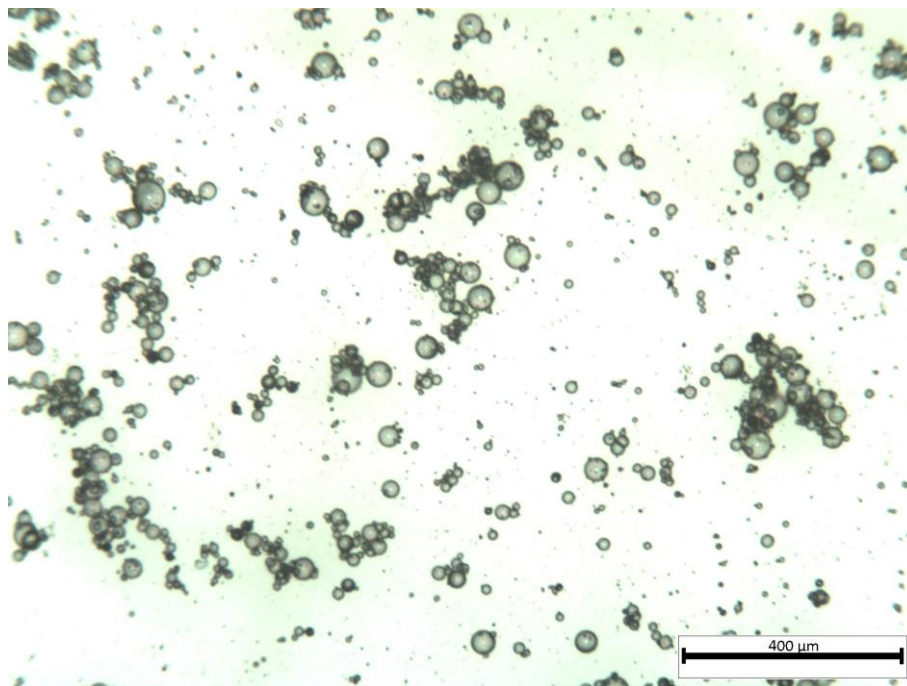


Figure 4.14: Un-sieved S38 hollow glass microspheres, image taken with optical microscope, 50 x magnification

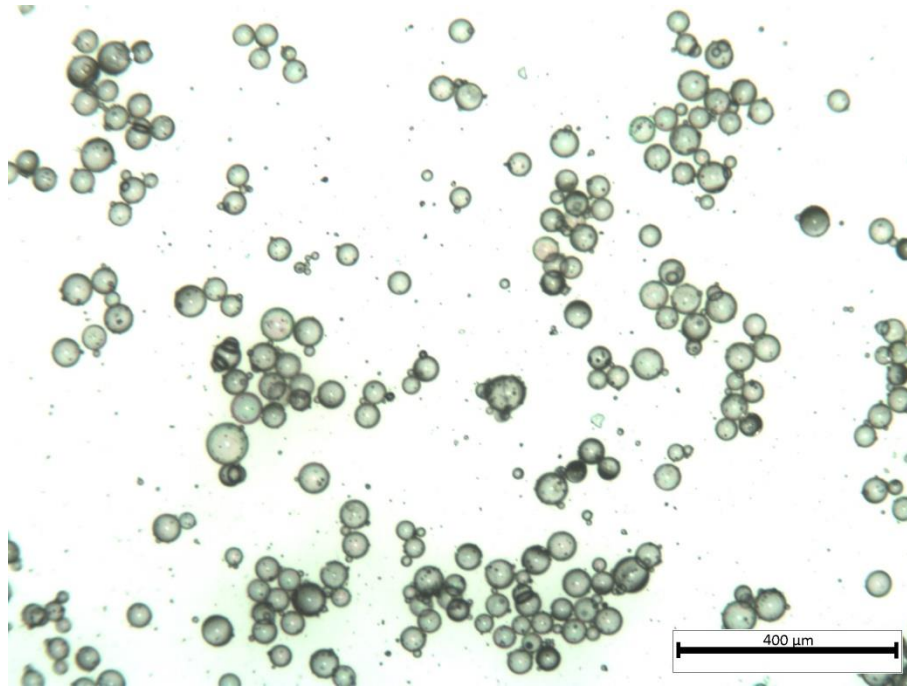


Figure 4.15: Sieved S38 hollow glass microspheres, sieve mesh size 50 μm , image taken with optical microscope, 50 x magnification

4.3.2. Coating vessel and concussion mechanism design

As already mentioned in [178], a specially shaped coating vessel was designed to coat powders and other granular substrates. This vessel was tilted at an angle of $\alpha = 45^\circ$ and rotating beneath the sputtering target. The special shape and the tilting angle allowed that during each rotation period every surface of the vessel became vertical, thus enabling the powder to glide off the surface easily. The resulting movement of the powder however, was not sufficient to break up the powder particle clusters that formed during deposition or to prevent sticking to surfaces completely. As a result it was necessary to use a concussion mechanism to induce additional momentum on the particles. This mechanism has been redesigned to work more reliably, to be simply constructed and to be easily up-scaled.

The basic design of the coating vessel and the concussion is displayed in Figure 4.16, where the coating vessel is put into a bigger plate, the so called concussion plate. The coating vessel can be characterized by the following elements: a smooth inner surface (a), concave to the centre of the vessel and convex to the outer rim of the vessel, thus resulting in surfaces that are tilted into opposite directions on the rim and in the centre of the vessel. Upon tilting the vessel this guarantees that granulate is always located on a steep surface thus facilitating the sliding of particles. To lift and mix the particles a small fin is fixed on the outer rim inside the vessel (b). Experiments have shown that the fin does not have to be very large; it only has to transport a

certain amount of material to an elevated position to create particle trickling and thus stir the particles gently. At a later stage of the experiments, the fin was replaced by a small cylindrical rod to have a better defined geometry. For this work a coating vessel with an outer diameter of 93 mm was used.

The new concussion mechanism consists of a rotating plate with a larger diameter than the coating vessel (Figure 4.16). It has outer rim walls (2) so that the coating vessel (1) can move and glide within the plate and roll along its outer rim. Furthermore there are bolts attached to the outer wall of the plate pointing radially to the centre of the plate. When the coating vessel is put into the rotating plate (Figure 4.17, A), the bolts lift the coating vessel (B) up to a certain point where the barycentre of the coating vessel is no longer supported by the bolt (C) and the coating vessel glides down (D). When the coating vessel hits the wall of the plate (E), additional momentum is generated and, as a result of the concussion, formed particle clusters fall apart and particles that formerly stuck to surfaces are set free. For the experiments the concussion plate had an inner diameter of 124 mm.

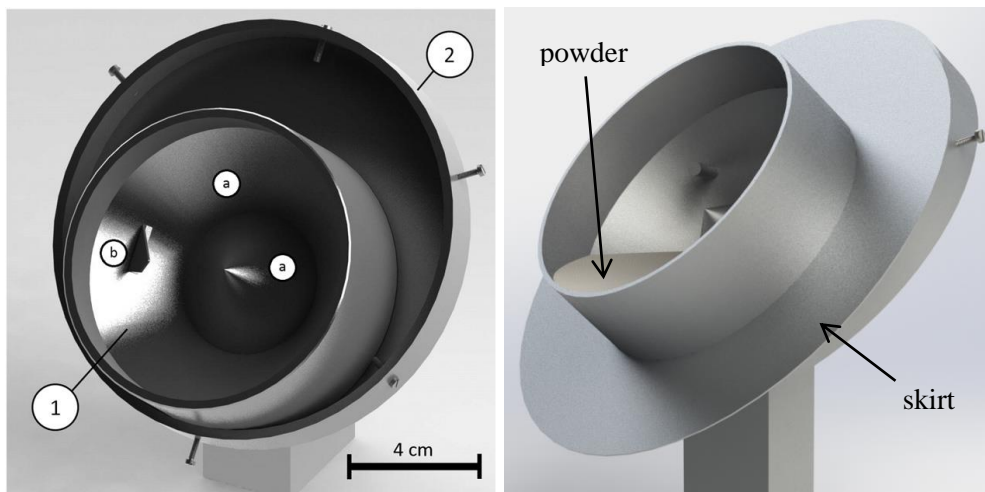


Figure 4.16: a) left: rendering of the powder coating apparatus: a coating vessel (1) with steep surfaces (a) and fin (b), concussion plate (2) which lifts the coating vessel periodically with the bolts screwed in the wall; b) right: same setup but with protection apron and cylindrical fin

It was found that the coating vessel sometimes stopped gliding down the plate and instead moved in circles as it was stuck to the plate. There were two reasons for this behaviour: first, both the coating vessel and the plate were made of aluminium which caused galling. Secondly, in the course of the deposition and the movement of the coating vessel, the inner surface of the plate became more and more rough. To prevent the sputtering beam reaching the plate, a skirt was added to the coating vessel (see Figure 4.16 b). This skirt also had the positive effect of being a heat spreader, thus reducing the temperature of the coating vessel and the powder

material inside. The main issue with temperature was due to the two component adhesive that was used to glue the different parts of the vessel together. The adhesive dissociated at higher temperatures caused by longer sputtering periods and/or higher sputter powers. The adhesive was also used to smooth edges of the inner surface of the coating vessel. To overcome the adhesive issue, parts of the coating vessel were screwed together rather than glued. To prevent galling of aluminium components, i.e. coating vessel and concussion plate, a thin stainless steel plate of the size of the plate's inner surface was put into the plate. With the stainless steel plate and the skirt the movement of the coating vessel could be guaranteed for arbitrary deposition times up to several hours. Construction sketches can be found in the appendix

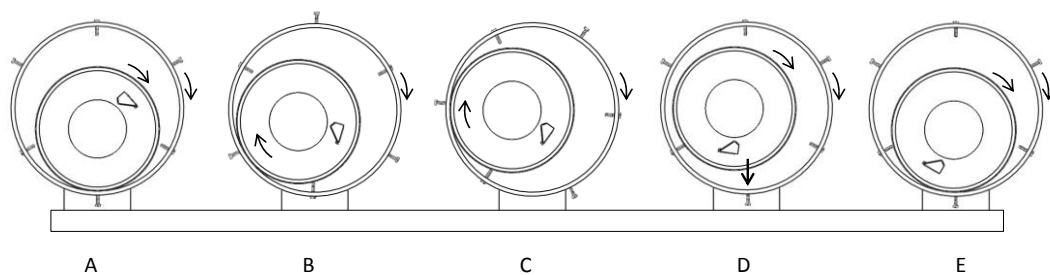


Figure 4.17: Movement of the concussion plate and the coating vessel: (A) coating vessel is in bottom position, (B) coating vessel is lifted up by a bolt, (C) coating vessel is in top most position and starts to roll over the bolt, (D) the vessel glides down the surface of the concussion plate, (E) the coating vessel hits the wall of the plate which results in a concussion that breaks up clusters that form during deposition.

This system enabled uniform coatings on a hollow glass microspheres and diamonds, though diamonds will not be further discussed due to non-disclosure agreements. The amount of powder that could be coated with that system was 20 ml per batch. However, only recently the PhD colleague Andreas Eder scaled up the system and optimized the geometry, so that now a volume of more than 1000 ml can be coated uniformly in one run.

Impact velocity of the coating vessel

In this section impact velocities of the coating vessel when hitting the concussion plate wall for different angular velocities of the plate and different bolt lengths are calculated. As it was shown in Figure 4.17 the movement of the coating vessel is quite complex. To calculate the impact velocity of the coating vessel and to determine the influence of geometrical parameters, the moving parts were modelled in Wolfram Mathematica 6 (see appendix section 9.4). The aim was to find parameters for the maximum impact velocity, which is proportional to the momentum transferred to the spheres and thus to the ability to break up clusters. Therefore the

parameters which influence the impact velocity v , i.e. bolt length d and angular velocity ω of the concussion plate, were varied. Figure 4.18 shows that higher angular velocities as well as longer bolts yield a higher impact velocity. Assuming a constant time for rolling over a bolt, at higher angular velocities the vessel is lifted higher during rolling over the bolt. With longer bolts the coating vessel is also lifted higher (compare Figure 4.17), which results in a higher impact velocity. The theoretical maximum impact velocity was calculated using the energy conservation law to $v_{max} = 641$ mm/s. This maximum occurs when the coating vessel slides from the topmost position of the concussion plate to the lowermost position. Friction between the coating vessel and the concussion plate was neglected in these calculations.

In the experiments an angular velocity of $\omega = 4.5$ rad/s and a bolt length of $d = 5$ mm was used which results in an impact velocity of $v_{impact} = 355$ mm/s. It has to be mentioned that the impact velocity is only the radial component of the coating vessels total velocity relative to the concussion plate. Furthermore it should be noted that the theoretical calculations were done after the construction and feasibility tests, which is why the dimensions of the vessel and the plate as well as the experimental parameters regarding the concussion were not changed in the course of the experiments.

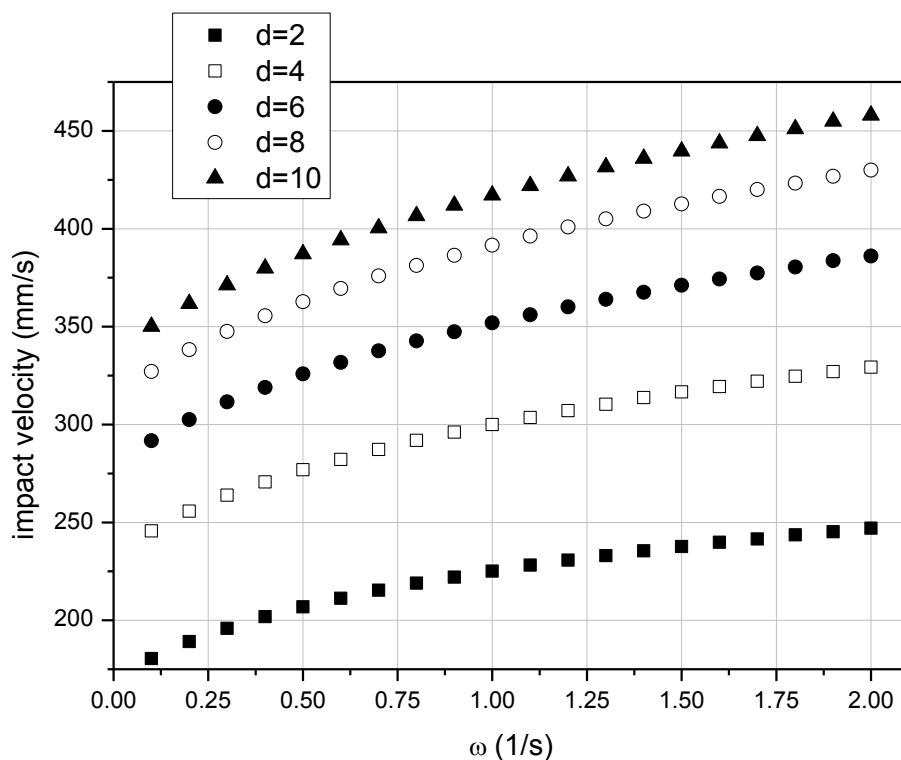


Figure 4.18: Impact velocity v as a function of the angular velocity ω of the concussion plate and the length of the bolts d which lift the coating vessel periodically. Both higher angular velocity and longer bolts yield higher impact velocities.

4.3.3. Coating material and parameters

Hollow glass micro spheres were coated with titanium, aluminium, titanium dioxide, aluminium oxide, platinum and copper. The deposition runs were carried out in DC mode with a 10 cm target for aluminium (Al), aluminium oxide (Al₂O₃), titanium (Ti), titanium dioxide (TiO₂) coatings and a 2 inch target for copper (Cu), platinum (Pt), ruthenium (Ru) and titanium (Ti) coatings. Aluminium oxide and titanium dioxide coatings were deposited in pulsed DC reactive sputtering mode (sputter source: *Advanced Energy Pinnacle™ Plus+ 5x5 kW*). Argon and oxygen partial pressure was regulated with mass flow controllers (*MKS Type 1179*) and a control unit for the mass flow controllers (*MKS Type 647C*). The argon flow was kept constant and the oxygen flow was readjusted to keep the desired oxygen partial pressure. The residual gas was analysed with a quadrupole mass spectrometer (*MKS Microvision 2*).

In addition, trickling experiments of glass micro spheres without a sputter beam were carried out to investigate cluster forming and surface sticking of the particles with the newly designed concussion mechanism. For these experiments 20 ml batches of glass micro spheres were put into the coating vessel at 1.5 Pa argon pressure in the vacuum chamber.

4.3.4. Trickling experiments

In order to achieve uniform coatings on the spheres and a narrow film thickness distribution of the spheres, good trickling behaviour is most important. Thus trickling of spheres was investigated. First experiments with and without concussion but without sputter beam will be described. After that it will be shown that trickling works with every sphere size distribution tested when using the concussion mechanism. Finally, the trickling behaviour under sputter conditions with concussion mechanism will be described and some examples of coated particles will be given.

It has to be mentioned that in atmosphere, spheres of any size distribution trickle inside the rotating coating vessel and do not agglomerate. The air humidity forms a thin layer of water on the surfaces of the spheres and hence influences the trickling behaviour. At lower pressures in the vacuum chamber the trickling is impeded dramatically when pressure decreases below the vapour pressure of water at room temperature. This indicates that the lubricating water layer evaporates, thus leading to higher friction and interlocking of the spheres. According to the *CoolProp* library the vapour pressure of water at room temperature is at $p_{vap} = 2.3$ kPa (23 mbar) [23]. Compared to that, sputtering was usually carried out at pressures of ~ 0.5 -4 Pa (5 -40 $\times 10^{-3}$ mbar). The influence of water on the friction behaviour at low pressures is discussed in several works leading to similar conclusions, e.g. [182, 183].

Trickling experiments were carried out with sieved and un-sieved spheres, where the mesh size of the sieve was 50 μm , as described before. An amount of 8-20 ml of spheres was put into the coating vessel which was placed onto the rotating plate in the vacuum chamber. After evacuating the chamber to 10^{-3} Pa it was filled with argon at 1.5 Pa. Then the rotating mechanism was started and the trickling behaviour of the spheres was observed through a gauge-glass for one hour. These tests were carried out with and without the concussion mechanism.

Trickling experiments without concussion

For these experiments the coating vessel was put into a plate that matched the size of it, so that the coating plate could only rotate but not move in any other way. The tests were carried out according to the procedure described above.

The better part of un-sieved spheres consisted of spheres smaller than 30 μm (see histogram in Figure 4.12), which is why they became wedged together and started sticking onto the coating vessels surfaces quite instantly after starting the experiment. Although there was only little cluster formation which can be explained by the absence of a sputter beam, the trickling nearly stopped completely after 3 minutes, when only about 5% of spheres were still moving at all. After 15 minutes the particle movement in the coating vessel had ceased completely, so that each of these experiments was stopped after trickling could no longer be observed. The bad trickling behaviour can be explained by the size distribution of the spheres and the presence of some broken spheres which promote interlocking of the particles.

Unlike the un-sieved spheres the sieved spheres were trickling during the whole test time of one hour with no significant surface sticking or cluster formation. Due to the absence of smaller and broken spheres the batch had no chance to conglomerate.

The batch of spheres which fell through the sieve showed a similar behaviour to the un-sieved spheres. Rather, they stuck to one another and to the surfaces of the vessel quite instantly after the rotation of the coating vessel started and did not move at all anymore after only one minute. That was why each of these tests was also aborted after 15 minutes. As mentioned above there are broken spheres in the batches of spheres smaller than 50 μm as in the un-sieved ones, although here the ratio of broken to unbroken spheres is even higher. This again promotes sticking.

Figure 4.19 a) and b) show photographs of spheres $> 50 \mu\text{m}$ and $< 50 \mu\text{m}$ after the vacuum chamber was opened and the experiment had been carried out. In Figure 4.19a most of the spheres are at the bottom of the coating vessel, since they glided off the surfaces during the procedure. This indicates good trickling behaviour. In Figure 4.19b the stuck spheres are evenly

distributed which indicates bad trickling behaviour. It was important to switch off the rotation mechanism before opening the vacuum chamber, because the particles started to trickle again under atmospheric conditions when the coating vessel was moved.



Figure 4.19: a) Spheres (8ml) 50 μm sieved ($>50 \mu\text{m}$) are still trickling after 1h rotating in the coating vessel at 1.5 Pa argon; most of the spheres are at the bottom of the coating vessel, which indicates good trickling behaviour; b) spheres (8 ml) 50 μm sieved ($<50 \mu\text{m}$) stick to one another and to the surface quite instantly; the image shows the spheres after 15min rotating in the coating vessel at 1.5 Pa argon; the stuck spheres are evenly distributed in the coating vessel.

Trickling experiments with concussion

For the trickling experiments with the newly designed concussion mechanism similar parameters as for the experiments without concussion were used, i.e. 1.5 Pa argon, 20 ml sphere batches with sieved and un-sieved spheres.

Neither sieved nor un-sieved spheres showed signs of sticking or cluster formation during the test time of one hour. However, it was found that there is a drawback to this mechanism as some of the particles fell out of the coating vessel as a result of the concussion. As mentioned before, these flaws have been eliminated in the course of up-scaling and optimizing the system by a colleague. Now, all particles remain in the vessel and can be coated.

4.3.5. Trickling behaviour of microspheres under sputter conditions

To investigate the trickling behaviour under sputter conditions, hollow glass microspheres were coated by magnetron sputtering with various materials, e.g. Al, Al_2O_3 , Ti, TiO_2 (10 cm target) and Cu, Pt, Ru, Ti (2 inch target). These investigations were also carried out with and

without concussion mechanism. First, results without concussion mechanism will be described, before describing the outcome of experiments utilizing the concussion mechanism.

Coating spheres with a rotating vessel

Since the trickling experiments showed that un-sieved spheres and spheres smaller than 50 µm stop moving completely after 15 minutes at the latest, and the fact that coating promotes sticking, only sphere batches > 50 µm were taken into account when coating without concussion mechanism.

The spheres sieved with 50 µm mesh only trickle a couple of minutes when coated with the rotating coating vessel and without concussion mechanism. As a result not every sphere is coated, let alone uniformly; there are many uncoated spheres and some half coated.

Coating with concussed vessel

As described above, the coating vessel was put into a larger vessel, i.e. concussion plate, where bolts prohibit the coating vessel from rolling but lift it up until it rolls over the bolt and glides down, resulting in a concussion when hitting the plate wall. The periodical gliding down of the coating vessel and hitting the concussion plate wall facilitates the breaking up of clusters which are formed during the coating process. Still, particles tend to form clusters when coated with a metal whereas clusters are not formed when oxide coatings are applied. The trickling behaviour when sputtering oxide layers will be discussed later in more detail. Nevertheless, with the concussion mechanism it is possible to achieve pure metal coatings on spheres and other granular or powder form substrates, because the formed clusters are permanently broken due to the concussion. Figure 4.20 shows titanium coated spheres after one hour sputtering directly after opening the vacuum chamber. Most of the spheres are at the bottom of the coating vessel which indicates good trickling behaviour. The remaining clusters which form and break apart during the whole deposition process are visible.

Cu-coated spheres were analysed with a scanning electron microscope (SEM), using secondary electron detection, energy dispersive X-ray spectroscopy (EDX) and backscattered electron imaging (BSE). Figure 4.21a shows a typical SEM-image of spheres coated with Cu for 60 minutes. A magnification of the marked section of the sphere in the bottom of the image shows the rough surface of the coated sphere (Figure 4.21b). The roughness is a result of forming clusters, where spheres stick together because of the deposited metal, and the breaking apart of these clusters, where the spheres are separated again. In addition the roughness is promoted by silicic acid particles on the surface of the spheres, which are used as anti-caking agent by the manufacturer. The surfaces of the spheres were analysed with EDX. Each Cu-coated sphere investigated showed a significant copper content, varying from 0.6 ± 0.2 at% Cu

to 3.3 ± 0.7 at% Cu corresponding to the varied coating times of 15 to 60 minutes. This indicates a copper coating on each investigated sphere.



Figure 4.20: One hour titanium coated spheres directly after opening the vacuum chamber. The remaining clusters of coated glass micro spheres which form and break apart continuously during the whole coating process can still be seen. Most of the spheres are at the bottom of the coating vessel, which indicates good trickling behaviour.

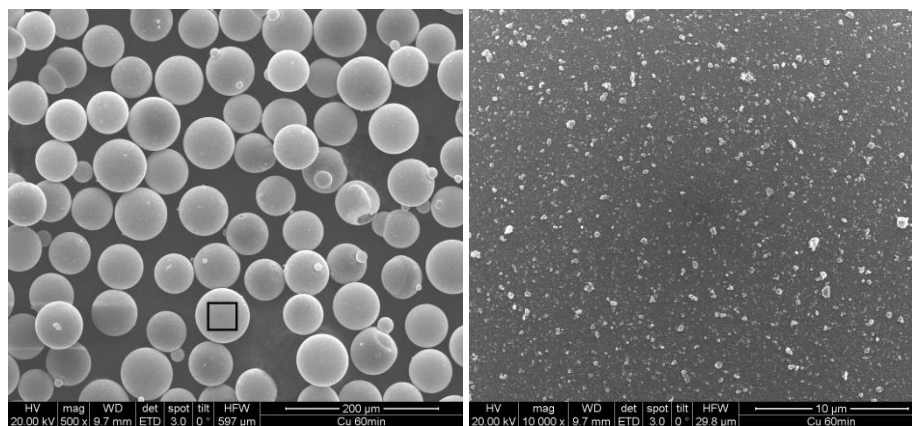


Figure 4.21: a) left: SEM image of Cu-coated hollow glass microspheres (coating time 60 minutes), 500x magnification; b) right: SEM image of the surface of a Cu-coated hollow glass micro sphere, 10,000 x magnification, the rough surface is a result of forming and breaking apart of clusters and of silicic acid

To better distinguish between substrate and film material, BSE images were acquired. The BSE images confirmed that every sphere is coated and that there are no uncoated areas on the spheres. Figure 4.22a shows the continuous Cu-coating on the spheres and no uncoated areas indicated by the constant brightness of the spheres. Uncoated spheres or areas would appear darker in the BSE-image, since the coating consists of Cu and the spheres mainly consist of silica, oxygen and other light elements. In the top right corner of the image is a cracked sphere, where the uncoated inner side of the sphere shell is visible. Figure 4.22 b shows a cross section of a coated sphere shell taken with back-scattered electrons with the copper film on the outer surface. For these measurements the coated spheres were crushed with tweezers before putting them into the electron microscope. The measured film thicknesses of 30 – 50 nm of 60 minutes copper coated spheres are exaggerated due to the edge effect of the measuring method. That is, edges appear brighter and thicker than they actually are. Nevertheless, the investigated cross sections of coated spheres showed uniform films all around the spheres. Film thickness measurements will be briefly discussed in section 4.3.6 including some results of coated hollow glass microspheres.

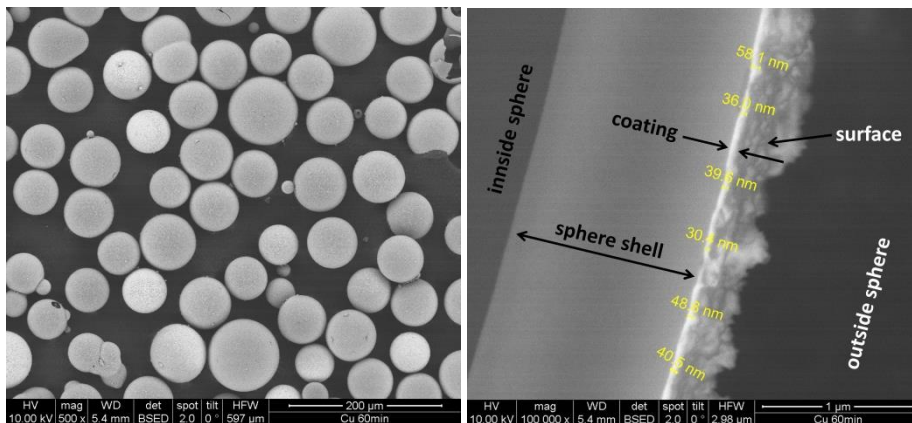


Figure 4.22: a) left: BSE image of Cu-coated hollow glass microspheres with every sphere having a continuous Cu-coating; b) right: BSE image of the cross section of a sphere shell segment with the visible Cu-coating on the outer surface of the sphere shell; measured film thickness of ~ 40 nm is exaggerated due to the edge effect of the measuring method

Optical micrographs of coated spheres are shown in Figure 4.23 and Figure 4.24. Un-sieved spheres were coated with Ti for 1 hour at 200 W sputtering power and sieved spheres were coated with Pt for 10 minutes at 200 W sputtering power. As can be seen in the images, both sieved and un-sieved spheres can be coated with metal films of different film thicknesses. Fragments of broken spheres are visible in the batch of un-sieved spheres (Figure 4.23), but

both, fragments and intact spheres are coated all the same. The images were taken with an optical microscope (*REICHERT POLYVAR MET*) at 50 x magnification.

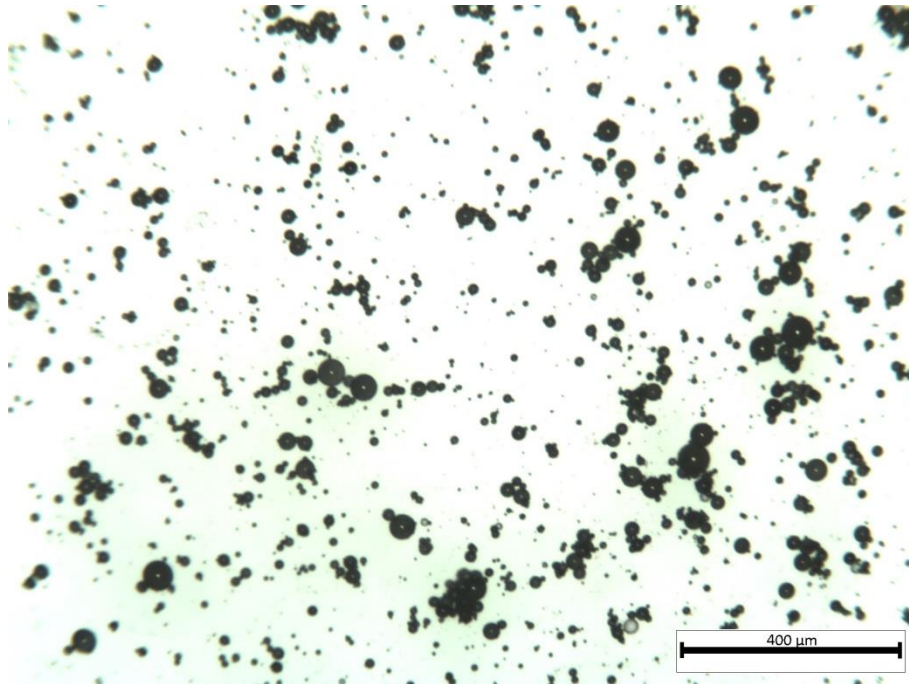


Figure 4.23: Titanium coated un-sieved hollow glass microspheres, coated at P = 200W for 1 h with ST20 sputter source (2 inch target), 50× magnification

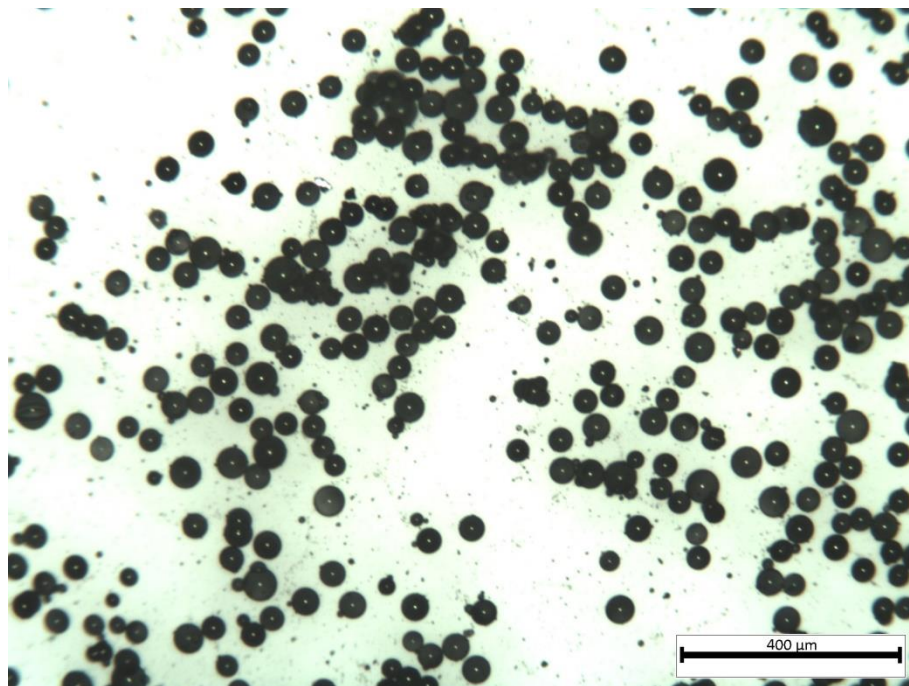


Figure 4.24: Platinum coated hollow glass microspheres > 50 μm, coated at P = 200W for 10 min with ST20 sputter source (2 inch target), 50× magnification

The effect of oxygen on the trickling of hollow glass microspheres

Experiments with aluminium showed that oxygen has a significant effect on the trickling behaviour of the glass microspheres. 10 ml of spheres $> 50 \mu\text{m}$ were put into the coating vessel, which was placed in the concussion plate. Sputtering was carried out with a 2 inch Al target at a power of 200 W. The Argon pressure was fixed at 0.4 Pa, whereas the oxygen partial pressure was varied from 0 to 0.015 Pa.

First the spheres were coated in metallic mode until they began to form clusters after about 20 Minutes. As soon as oxygen was injected into the vacuum chamber cluster occurrence decreased. When the oxygen flow rate was decreased to 1 sccm, which has been the minimum of the flow controller, the spheres started to stick together again. At an oxygen flow rate of 1.5 sccm the cluster occurrence was nearly zero. When the oxygen flow was increased and decreased during 2 hours of coating a the change in brightness of the powder was observed, which indicated the formation of metallic films (dark) and oxide films (brighter).

This behaviour was also observed with titanium and titanium oxide films on hollow glass microspheres. Diamonds showed a similar behaviour.

Baechle et al (2013) made similar observations when coating microspheres with aluminium: *”Exposing the microspheres to an oxygen atmosphere is believed to partially oxidize the outer coating of aluminium on the microspheres, reducing the probability that particles will adhesively bond together.”* [176]

It can be concluded that oxide coatings are much easier to handle than pure metal coatings.

4.3.6. Film thickness measurement

In general, it is difficult to acquire the film thickness of thin films on small objects like hollow glass microspheres. Efforts were made by colleagues, i.e. Harald Mahr and Andreas Eder, to measure the film thickness optically by optical transmission. Though the method itself will not be discussed in this work, some results will be shown in the following.

Results of optical film thickness measurements of copper coated spheres are shown in a histogram in Figure 4.25 with varying coating times. For 60 minutes coating time the mean film thickness results to 16-17 nm which is much less than the back-scattered electron measurement indicated (30-50 nm, exaggeration due to edge effect). It was also observed that with increasing coating time the film thicknesses tend to be more uniform (narrower and higher Gaussian distribution), which is due to prolonged mixing of the powder. Theoretical calculations with the

method described in section 4.3.7 yielded a film thickness of ~ 13 nm, which is in relatively good agreement with the optical measurements.

Table 4.3 lists measured copper film thicknesses compared to calculated values. As expected, the film thickness linearly increases with time. However, there seems to be an offset since a linear extrapolation to a coating time of zero minutes would yield ~ 3 -4 nm film thickness. It has to be mentioned that the optical film thickness measurement method was still under development and optimisation at the time of these measurements. Furthermore, as already discussed in section 4.3.1, the measured mean sphere diameter for calculating the film thickness was assumed too high and the exposed surface to the sputter beam was assumed too low. As both assumption errors cancel each other out, the results of optical measurement and theoretical calculation still show relatively good agreement with each other.

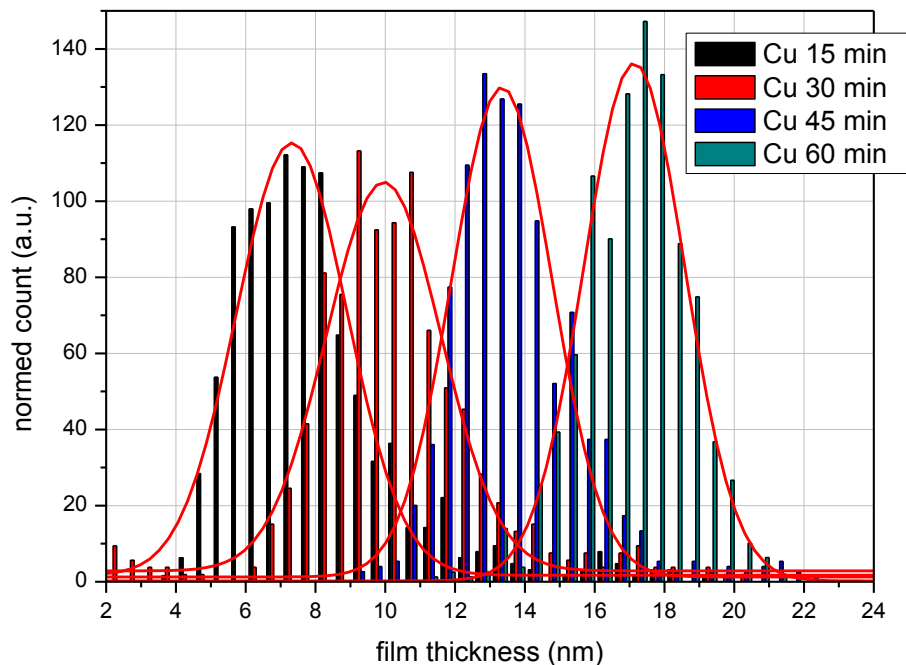


Figure 4.25: film thickness distribution of copper coated hollow glass microspheres (sieved $> 50 \mu\text{m}$), the sphere counts were normed, each sample contains the same number of spheres

sample	optically measured mean film thickness (nm)	calculated film thickness (nm)
Cu 15 min	7.32	3.28
Cu 30 min	9.96	6.56
Cu 45 min	13.34	9.84
Cu 60 min	17.14	13.12

Table 4.3: Mean film thickness of copper coatings on hollow glass microspheres for different coating times (coating power 200 W), measured and calculated

4.3.7. Film thickness estimation and rate determination

As already mentioned, it is difficult to measure the thickness of thin films on hollow glass microspheres, especially for multilayer coatings. At the moment thicknesses of single layer coatings can be acquired via an optical method using light transmission as already mentioned before, which was the work of a colleague and will not be discussed any further. Nevertheless, it was necessary to estimate the resulting film thicknesses on microspheres before deposition to calculate the coating time.

Therefore, the following parameters have to be determined beforehand:

- Mean diameter d_{mean} (or specific surface) of the powder material that has to be coated, as described in section 4.3.1 about the substrates
- surface of the powder material exposed to the sputtering beam S_{exp}
- volume of powder put into the coating vessel V
- packing density of the powder f (packing factor)
- geometry factor of the powder f_{circ} , which is basically the circularity of the particles (for spheres this is 1)
- sputter rate at the coating vessel \dot{x}
- and deposition time t

Thus the film thickness can be expressed by:

$$d_{film} = d_{mean} \cdot \frac{\dot{x} \cdot t \cdot S_{exp}}{6 \cdot V \cdot f \cdot f_{circ}} \quad (4.15)$$

where the factor $6 \cdot V \cdot f \cdot f_{circ} / d_{mean}$ corresponds to the total surface of the powder volume V . In the following the different parameters will be discussed in more detail.

Mean diameter of the powder particles

The method was described in section 4.3.1.

Surface exposed to the sputtering beam

The surface exposed to the sputter beam strongly depends on the filling volume, as is shown in Figure 4.26. A higher filling volume, that is more hollow glass microspheres in the coating

vessel, yields a higher exposed surface. On the other hand, the dependency of the exposed surface on the tilt angle of the coating vessel is negligible. However, the tilt angle strongly influences the maximum capacity of the coating vessel. Whereas at a tilt angle of 45° a maximum of 23 cm^3 can be loaded into the vessel, at a steeper angle of 55° only 11.8 cm^3 can be placed in it. At a lower angle of 35° a much larger amount of 39.6 cm^3 can be loaded into the vessel. At this low angle however, the spheres cannot be coated uniformly due to more agglomeration and adhesion to the coating vessels inner surfaces.

It has to be mentioned that the presented results assume that all of the substrate is always at the bottom most position of the coating vessel, which is the case for diamonds or sieved spheres, but not for un-sieved spheres (compare Figure 4.19 and Figure 4.20). As a result un-sieved spheres actually have a higher exposed surface than assumed in the calculations in Table 4.3. As mentioned before, this error cancels the error made when measuring the mean diameter. Since these facts were found at the very end of the thesis, no additional sphere diameter measurements were carried out.

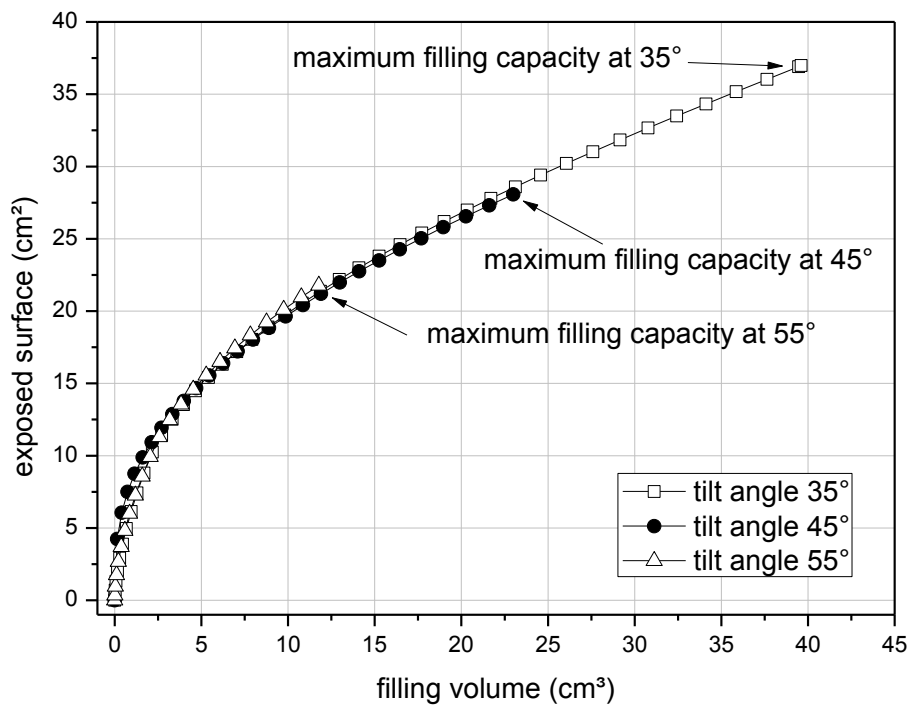


Figure 4.26: Surface of the spheres exposed to the sputter beam as a function of the amount of spheres in the coating vessel (filling volume) at different tilt angles of the coating vessel; the maximum filling capacity is strongly influenced by the tilt angle

Volume of powder put into the coating vessel V

The volume V of hollow glass microspheres put into the coating vessel was measured with a measuring cylinder. Usually a volume of 20 cm³ (20ml) was used which corresponds to an exposed surface of 26.5 cm².

Packing density of powder f (packing factor)

For spheres a packing factor of $f = 0.63$ was used. For diamonds a packing factor of $f = 0.592$ was determined by measuring the weight and the volume.

Geometry factor of the powder f_{circ}

This factor takes into account the non-circularity and surface morphology of powder particles. For instance particles with a craggy or jagged surface have a larger surface than smooth particles. More elliptic or irregular shaped particles can have larger or smaller surfaces than spheres. For spheres the geometry factor is $f_{circ} = 1$. On the other hand, diamonds with the shape of truncated octahedrons have a smaller surface than spheres of the same diameter, thus the geometry factor becomes $f_{circ} = 0.9$.

Sputter rate at the coating vessel \dot{x}

To determine the sputter rate in the coating vessel, a glass plate or a silicon wafer substrate was put into the coating vessel in a horizontal position. The substrate was mounted in a small substrate carrier to obtain a clean brink for film thickness measurement by profilometry. The sputter rates varied from 0.04 nm/s to 2.44 nm/s depending on sputter power, target material, geometry of the whole system and other sputter parameters, i.e. oxygen partial pressure, pulsed sputtering parameters, etc.. The deposition rate is extremely sensitive on the geometry, especially on the distance between target and substrate. In the course of this thesis the geometry was often changed due to utilization of different sputter sources, i.e. 2 inch, 10 cm, 4 inch target diameter, and different coating apparatus configurations. As an example for different deposition rates caused by varying distances Figure 4.27 shows the deposition rate for titanium in the coating vessel. Five Si-substrates were put into the vessel and coated with titanium at 200 W for 60 minutes with the 10 cm sputter source (without rotation). In top down view the vessel seems to be distorted, since the vessel was tilted by 50°. This is illustrated by the elliptic black line at the bottom of the figure. It is striking that the deposition rate has already doubled from the bottom position (4.5, 0) to the middle position (4.5, 2.9) of the vessel. As a result, higher filling

volumes also yield higher deposition rates, since the exposed surface is closer to the sputter target. In appendix section 9.5 an overview of sputtering rates for different configurations is given.

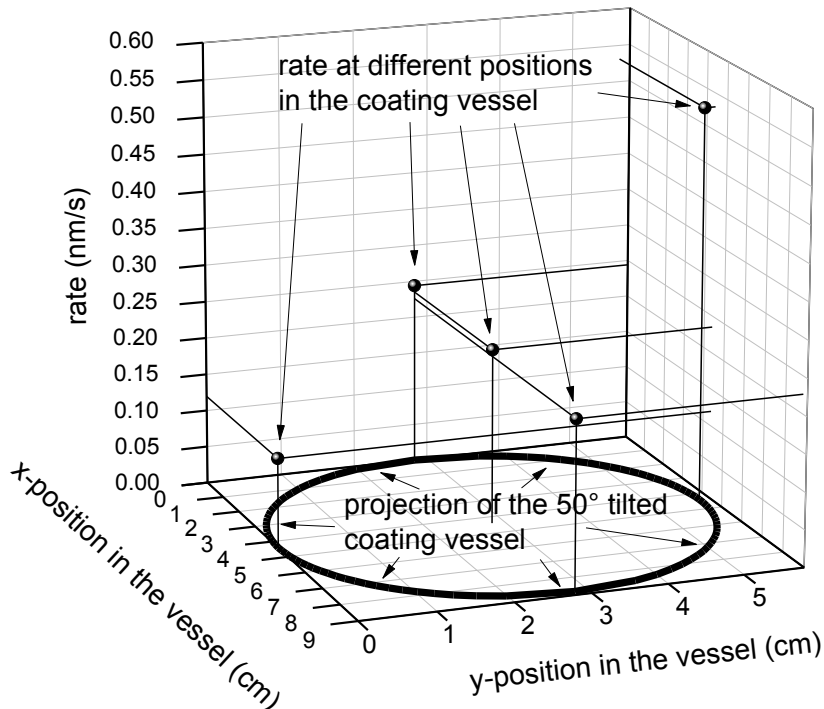


Figure 4.27: Rate of Ti in the 50° tilted vessel (black ellipse) at different positions in the vessel (black balls)

Deposition time t

Deposition times varied from 3-15 minutes for noble metal depositions to 0.3-14 hours for TiO₂ coatings.

4.3.1. Conclusions on coating powders in the concussed coating vessel

Both, metal and oxide films, could be applied on different batches of fine-grained powder by magnetron sputtering, i.e. hollow glass microspheres (2-70 μm), tungsten carbide particles and diamonds. This was achieved by using a tilted special shaped coating vessel in combination with a concussion mechanism, which enables breaking apart powder clusters that form during the deposition process.

It was found that metal coatings promote the cluster formation much more than oxide coatings.

Trickling experiments without magnetron sputtering showed that without the described concussion mechanism the powder becomes immobile in a few minutes in dry conditions, and thus cannot be coated. Only spheres sieved with a 50 μm mesh showed sufficient mobility, but none the less became immobile when coated. When using the concussion mechanism every batch of spheres stayed mobile, and thus could be coated uniformly. This was verified by the means of SEM, EDX and BSE analysis.

The described concussion mechanism and the coating vessel were up-scaled and optimised by a colleague, so that now it is possible to coat one 1 dm^3 of material while particle ejection could be completely eliminated.

A direct comparison with other coating techniques, e.g. fluidised bed chemical vapour deposition or wet chemical methods, has not been carried out. It could happen that coating particles in a fluidised bed leads to more abrasion of the desired coating due to higher particle velocities than in the present setup. However, this is pure speculation and needs to be verified. Still, a most welcome effect of the present apparatus is that coating parameters do not depend on substrate density like in fluidised bed reactors; depositions are completely independent of substrate material. As a result any metal, metal-oxide or –nitride can be deployed on any powder as long as particles are not too small ($> 5 \mu\text{m}$) or are not suitable for vacuum.

5. Reactive pulsed DC magnetron sputtering: Titanium dioxide TiO₂

This section will deal with titanium dioxide thin films on glass substrates as it was chosen as a support material for the catalyst which was applied on glass microspheres. Generally, TiO₂ is one of the more commonly used carrier materials, in special anatase phase TiO₂ [69, 74, 79, 80, 82, 83]. Due to the preferable catalytic properties of as anatase phase TiO₂, that crystalline structure was the main target of the coating experiments. First an overview of possible applications for TiO₂ will be given with a focus on its properties. Then the coating procedure will be described, i.e. pulsed DC magnetron sputtering, including general aspects of reactive sputtering. Finally the results, which were acquired by X-ray-diffractometry (XRD) and scanning electron microscopy (SEM), will be presented together with results of TiO₂ coated hollow glass microspheres.

5.1. TiO₂ – properties and applications

5.1.1. Applications

Titanium dioxide (TiO₂), also called titania, has a wide range of applications. Since its commercial production in the early twentieth century, it has been used as a pigment in paints, coatings, sunscreens, ointments and toothpaste [184, 185]. Today it is also used as anti-reflecting and protective layer for optical coatings, UV filters due to its transparency in visible and near infrared light and its high refractive index [186, 187]. Furthermore titania can be used for oxygen or humidity sensors. Its photocatalytic properties enable applications in the energy

sector: for electrolysis of water to generate hydrogen and dye-sensitised solar cells [185, 188]; for environmental applications: air purification and water treatment [185, 189, 190]; building environment: self-cleaning coatings and non-spotting glass for self-cleaning surfaces [185]; in biomedicine: self-sterilising coatings [185]. Furthermore, TiO_2 can be used in medical applications due to its good blood compatibility [191]. Additionally and most importantly to this work, it often is utilised as a catalyst support material as e.g. hydrolysis of sodium borohydride [68, 69, 74, 77, 79, 80, 82]. Usually the anatase phase is preferred to the rutile phase due to the higher density of localised states at the surface [79, 80, 185]. Thus the deposition of anatase phase films was the main target of the reactive sputtering experiments, which will be described in the following sections. The next section will deal with the structure and properties of the different TiO_2 phases.

5.1.2. Structure and properties

Besides the amorphous phase of TiO_2 there exist three other phases at atmospheric pressure, i.e. rutile, anatase and brookite. While rutile is thermodynamically stable, both anatase and brookite are metastable, where the latter is difficult to synthesise and so is also rarely studied. Another five phases have been found at high pressures (TiO_2 II or srilankite among them), but will not be further discussed, as will the brookite phase [185]. Thus, in the following the focus will lie on rutile and anatase phase TiO_2 . Table 5.1 gives an overview of the basic properties of anatase and rutile. Density and hardness of rutile are higher than of anatase due to the different crystal structure, though it has to be mentioned that both values vary a little depending on literature source. Figure 5.1 shows the structure of anatase and rutile built of “ TiO_6 “-octahedrons. An octahedron consists of one titanium atom in centre and 6 oxygen atoms at the corners, where each oxygen atom is shared by three octahedrons. In the anatase phase these “ TiO_6 “-octahedrons share 4 edges, whereas in the rutile phase they share only 2 edges [185].

Despite the larger experimental band gap of anatase of ~ 3.2 eV compared to ~ 3.0 eV of rutile, the photocatalytic performance of anatase is generally considered superior to that of the more stable rutile. This is attributed to a higher density of localised states, which results in more surface-adsorbed hydroxyl radicals, and slower charge carrier recombination in anatase relative to rutile [185].

Property	Anatase	Rutile
Crystal Structure	Tetragonal	Tetragonal
Atoms per unit cell	4	2
Space group	$I \frac{4_1}{a} md$	$P \frac{4_2}{m} nm$
Lattice parameters (Å)	a = 3.785 c = 9.514	a = 4.594 c = 2.959
Density (kg/m ³)	3894	4250
Refractive index (along axis)	2.49, 2.56	2.90, 2.61
Experimental band gap (eV)	~3.2	~3.0
Hardness (Mohs)	5.5-6	6-6.5

Table 5.1: Properties of anatase and rutile [3, 185]

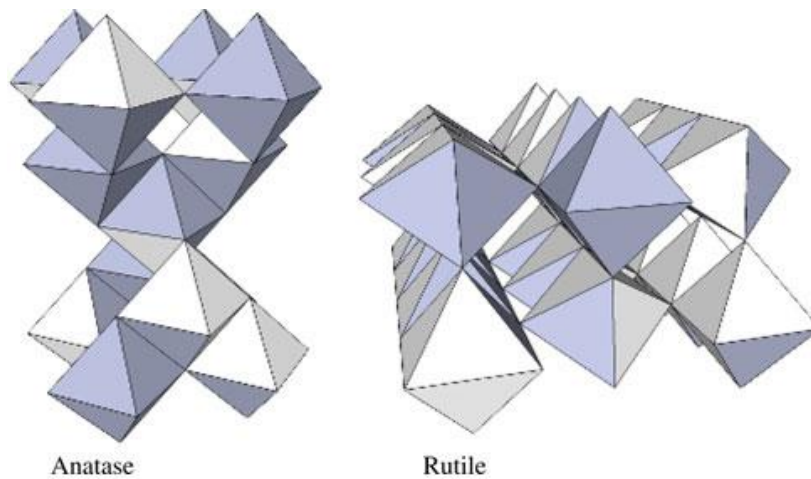


Figure 5.1: Structure of anatase and rutile TiO_2 phases; octahedrons consist of one titanium atom in centre and 6 oxygen atoms at the corners; in anatase phase these “ TiO_6 ” octahedrons share 4 edges, in rutile phase only 2 edges; image taken from [185]

5.1.3. Synthesis and phase transition

In the synthesis of TiO_2 films the initial phase formed is generally anatase, due to a less constrained structure compared to rutile and a lower surface free energy. The synthesis of TiO_2 films can be achieved by various methods, i.e. hydrolysis of TiCl_4 at room temperature, sol-gel synthesis at room temperature, flame pyrolysis of TiCl_4 , solvothermal or hydrothermal, chemical or physical vapour deposition methods. Whereas films deposited at room temperature are usually amorphous, crystalline phases, both anatase and rutile (or mixed), can be realised at elevated temperatures. There is one known way to synthesise rutile near room temperature by

hydrothermal precipitation, however aside from that method, rutile is only obtained by high temperature treatment [185].

At ~600 °C bulk anatase material irreversibly transforms to rutile, though that temperature varies from 400 °C to 1200 °C depending on synthesis method and shape of the TiO₂ material. The phase transition from anatase to rutile is not spontaneous but needs time since it is a reconstruction process, depending on temperature, sample dimensions, grain shape and size, atmosphere and surface area [185].

Which TiO₂ polymorph (amorphous, anatase or rutile) is synthesised depends significantly on synthesis parameters [185]. This also accounts for magnetron sputtering as synthesis method, as will be shown.

5.1.4. TiO₂ thin film preparation methods

There exist various methods for preparing TiO₂ thin films, i.e. spin coating, dip coating, sol-gel coating, plasma impulse chemical vapour deposition, plasma enhanced chemical vapour deposition, reactive evaporation, electron beam evaporation, reactive ion plating, ion beam sputtering, mid frequency sputtering and magnetron sputtering [154, 192]. Nevertheless, the next section will deal with TiO₂ thin films deposited on glass substrates by pulsed DC magnetron sputtering.

5.2. TiO₂ films prepared by reactive pulsed DC magnetron sputtering

This section will deal with TiO₂ thin films deposited on glass substrates by pulsed DC magnetron sputtering. First, general aspects of reactive magnetron sputtering and pulsed DC magnetron sputtering will be described. After that, aspects of reactive pulsed DC magnetron sputtering will be discussed including arcing. Finally, the experimental setup and the sample preparation will be addressed. Results of the deposited TiO₂ films will be shown in the next section. As mentioned before, the main target was to realise anatase phase films.

5.2.1. Reactive Sputtering

Reactive sputtering is used for many applications, including solar control and low-emissivity coatings, barrier layers on packaging, flat panel displays, solar cells, architectural glass, roll or web coatings, coated cutting tools, optical coatings, decorative and functional coatings for plumbing and hardware items, microelectronic devices (barrier layers, high k dielectrics, and

resistive films), automotive windshields and mirrors, micro-electro-mechanical systems (MEMS) devices, surface acoustic wave devices, and transparent conductive oxides [155, 193].

Usually for magnetron sputtering an inert gas, e.g. Ar, is used to create the ions that bombard the metal target. Reactive sputtering, on the other hand, is the sputtering of elemental targets in the presence of chemically reactive gases that react with both the ejected target material and the target surface [151]. Ideally the reaction of ejected target material should only take place at the substrate surface, but in reality it also occurs on the target [194, 155]. Reactive sputtering has become a very popular technique in today's search for new material properties, because of the possibility to deposit a very wide range of compound and alloy thin films including oxides, nitrides, carbides, fluorides or arsenides. Advantages of DC reactive sputtering of elemental targets, i.e. a target consisting of a single element, include [151]:

- it is possible to produce thin compound films of controllable stoichiometry and composition on an industrial scale;
- elemental targets are usually purified more easily, and hence, high-purity films can be produced;
- the complexity and expense of RF systems can be avoided since metallic targets are generally electrically conductive, and hence, DC power can be applied;
- elemental targets are usually easy to machine and bond;
- metallic targets are thermally conductive, which makes the cooling of these targets more efficient – thus, the range of the applied power can be extended (e.g. up to 50 W/cm^2 and higher) without the fear of being cracked; and
- films are deposited at temperatures less than $300 \text{ }^\circ\text{C}$

The most crucial aspect of reactive sputtering is to control the amount of reactive gas in the reaction chamber, since it strongly influences the deposition rate and the properties of the deposited compound. The amount of reactive gas can be either regulated by flow control or partial pressure control [155]; however, it is advised to use partial pressure control, which will become clear in the following.

Flow control

Usually the sputtering yield of the compound material is substantially lower than the sputtering yield of the elemental target material [195]. Since the added reactive gas reacts with the elemental target a compound is formed on the surface of the target, which has a lower sputter yield [155]. In other words, the deposition rate decreases with increasing gas flow due to target poisoning [196]. As an example, the deposition rate of aluminium with oxygen as reactive

gas in compound mode, i.e. the target is fully covered with Al_2O_3 , is only 2-3% of the metal rate [155].

There are two distinct mechanisms by which the compound layers are formed on the target surface: chemisorption of neutral reactive gas species (can occur without glow discharge), e.g. Al with O_2 , and target coverage by ions and atomic species of activated reactive gas (“ion plating”), e.g. Al with N_2 [197].

The compound mode is also referred to as poisoned mode, due to the low rate [155]. To increase the deposition rate and film properties it is possible to operate in a transition region between metal mode and poisoned mode [155]. This mode is not possible with flow control:

The reactive species adsorbs at the target surface and forms a compound, reducing the sputter yield. The compound is sputtered off the target increasing the sputter yield. If more reactive species is supplied to the system than can be eroded, the poisoning of the target and partial pressure of the reactive species increase, thus further decreasing the erosion rate. As a result the target gets completely poisoned. On the other hand, if less reactive species is supplied to the system than is needed, the sputter yield increases with a dropping partial pressure, making even more reactive species necessary. Thus the relationship between the film composition and supply of reactive gas is very non-linear [195]. Furthermore, this leads to a significant hysteresis effect when varying the flow rate of the reactive gas, which is shown in Figure 5.2. When sputtering titanium in DC mode the voltage increases with increasing oxygen flow due to less secondary electron emissions of the compound formed at the target surface. The voltage reaches the maximum at about 2.7 sccm. When the oxygen mass flow is reduced again, first, the voltage remains at high level and starts to drop not before the oxygen flow is below 2.3 sccm.

As a result it is very difficult if not impossible to operate in the transition region with flow control, since any slight disturbance in the process such as an arc event results in rapid poisoning of the target and an increase in the gas partial pressure. As a matter of fact there are some compositions that cannot be deposited with flow control, because the process jumps from under-stoichiometric to over-stoichiometric film composition [155].

In addition, it was reported that depositions in poisoned mode not only have a low rate but also have less than optimal, though reproducible, properties [155, 198]. The latter is mainly due to arcing caused by electrical insulating layer that forms on the target surface and resulting built up charge.

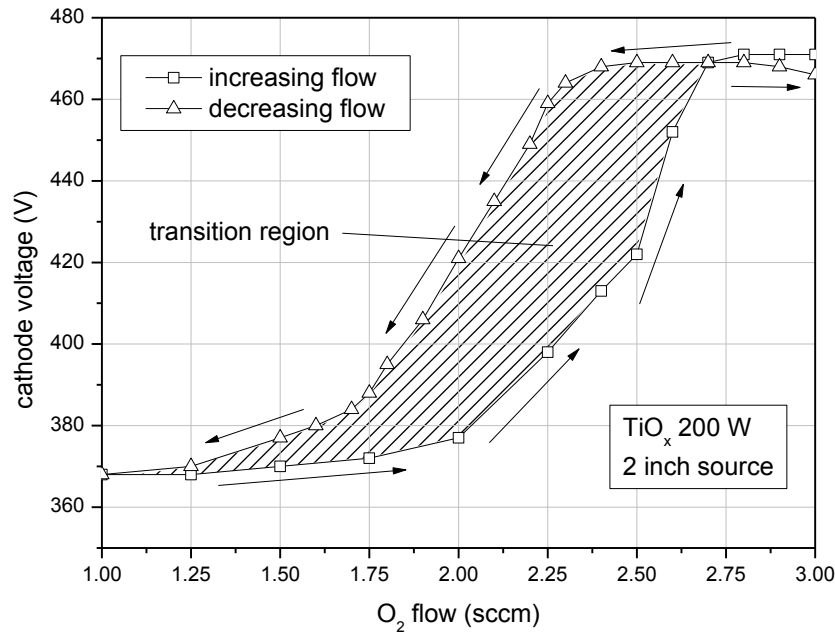


Figure 5.2: Hysteresis effect of the flow rate of the reactive gas; voltage increases with increasing flow and reaches a maximum at ~ 2.7 sccm, but does not decrease before flow rate has dropped to ~ 2.3 sccm.

Partial pressure control

To prevent poisoning of the target the partial pressure of the reactive gas has to be controlled. This requires an active feedback control, but allows operation of the process in the transition region between elemental and poisoned state. Another method would be to increase the pumping speed of the system and thus changing the shape of the reactive gas flow/partial pressure curve. The relationship between the reactive gas flow and the partial pressure then becomes linear. However, increasing costs make this an unattractive solution, particularly for very large deposition system [155, 196].

Advantages of partial pressure controlled systems are: first, transition between the metallic state and the poisoned state is continuous. Second, it is possible to choose an operating point that optimizes the desired film properties and the deposition rate. And third, as a result of the continuous transition of states there is no forbidden region [155].

There are several methods that are commonly used for controlling the partial pressure of the reactive gas during the reactive sputtering process:

- Optical emission spectrometry of the plasma (OES) [151, 199], however this method is not applicable for variable power methods such as the impedance control [198]. The effect of a colour change of the plasma can also be observed with the naked eye,

i.e. when sputtering TiO_x the gas discharge is violet with pure argon and gets whiter when adding oxygen. This was also observed by Lin et al. (2009) [200].

- Mass spectrometry [201].
- Another way to control the partial pressure of the reactive gas is to maintain a constant cathode voltage. Since the cathode voltage has a single valued monotonic functional relationship to the partial pressure of the reactive gas it is possible to use it as a feedback signal. The cathode voltage changes with the partial pressure of the reactive gas in the magnitude of 100-150 V due to decreasing (or increasing) secondary electron emissions (even more for sputtering of aluminium or silicon with oxygen). Now, instead of varying the gas flow, the mass flow and the cathode voltage are fixed. As a result the sputtering power is adjusted and in effect the partial pressure is maintained constant. However, the cathode voltage is also influenced by a change in temperature in the chamber, target erosion, a disappearing anode, outgassing or leaks, fluctuations in argon pressure and other reactive gases. Furthermore it is not possible for all reactive gas/target material combinations due to different chemisorption behaviour (Al chemisorbs O_2 but not N_2) [155, 198, 197, 202, 203, 204].
- To control the partial pressure an impedance control can be implemented using the discharge power as control variable at a fixed reactive gas flow. This allows the stabilisation of the reactive process in the transition region, which cannot be reached by flow control. However, this method cannot be applied for large scale targets, which is due to the well-known problem of lateral inhomogeneities of the target state that can cause severe gradients in the layer thickness and stoichiometry [198]. Malkomes and Vergöhl (2001) briefly describe an algorithm (PID) to simulate the partial oxygen pressure during reactive sputtering. They concluded that from the practical point of view the process can best be controlled with fixed oxygen flow and current/power used as a control parameter [205].
- Total pressure with fixed working gas flow rate: the working gas flow rate is fixed resulting in a fixed pressure. By adding reactive gas its partial pressure and the total pressure increase. For that method the system has to be conditioned, since a temperature increase in the vacuum chamber due to the sputtering process also increases the partial pressure of the working gas and thus decreases partial pressure of the reactive gas. This method was used in this work.

Figure 5.3 shows the voltage as a function of the partial oxygen pressure. Base pressure was set to 1.5 Pa, where the partial pressure of oxygen was controlled by the total pressure in the vacuum chamber. There is no hysteresis visible, though increasing and decreasing the partial

pressure did not give exactly the same pressure for identical partial pressure values. Oxygen partial pressure was varied from 0 to 80 mPa. Most of the TiO_x samples in this work were prepared with an oxygen partial pressure of 33 mPa, since it gave the right stoichiometry, i.e. TiO_2 , and a relatively high deposition rate.

A critical issue of partial pressure control systems were a fast control loop and the response time of the mass flow controllers. However, both issues can be assumed as solved due to developments in recent years in the fields of signal processing and faster responding valves [155, 196].

As already indicated before, the change of the cathode voltage with the partial pressure behaves differently depending on the material of sputtering system and reactive gas, e.g. [155, 206]:

- Decreasing cathode voltage with increasing partial pressure: Al-Ar/ O_2 , Al- N_2 , Si- O_2 , Si- N_2 , Mg- O_2 , Ce- O_2 and Y- O_2
- Increasing cathode voltage with increasing partial pressure: Ti- N_2 , Ta- O_2 , Y- N_2 , Zr- N_2 , Ag- O_2 , Au- O_2 , Cr- O_2 , Nb- O_2 , Pt- O_2 and Re- O_2 .

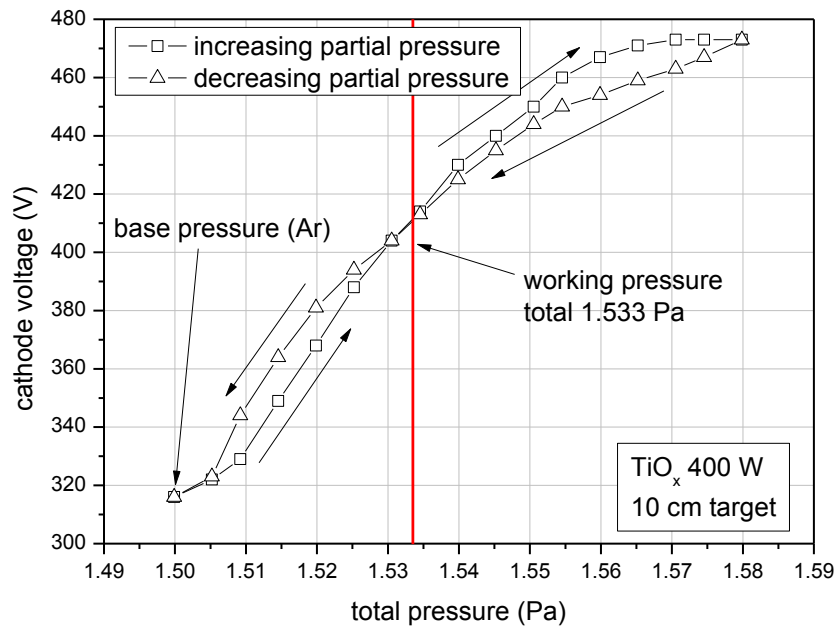


Figure 5.3: With partial pressure control no hysteresis effect occurs; increasing and decreasing partial pressure yields same voltage values; the red line indicates the working pressure of most of the samples produced in this work

This effect can be attributed to secondary electron emission coefficients of the target material and formed compound and the resulting plasma densities. For titanium-oxygen and titanium-nitrogen systems the cathode voltage initially increases with increasing reactive gas partial

pressure due to a reduction of the plasma density caused by subsequent reduction in the ionization collision cross section. Since the compound on the target has a higher secondary electron emission coefficient, and therefore the plasma density increases, the cathode voltage starts to fall with a further increase of reactive gas partial pressure. First the decrease of the plasma density caused by a reduction in the ionization collision cross section is dominant, then the increase in the secondary electron emission for the compound takes over and the cathode voltage decreases [155]. However, this effect was only observed in a very low extent in the course of this work.

Other aspects of reactive sputtering

There are methods to reduce the needed partial pressure and still produce the stoichiometric film with optimum properties by enhancing the reaction of the reactive gas and the sputtered species. These activation techniques include substrate bias, unbalanced magnetrons, or external activation devices such as an inductively coupled plasma source, a microwave source or a laser [155].

For large area application coatings a uniform reactive gas distribution is essential. If the cathode length exceeds 40-50 cm it is recommended to use multiple gas manifolds in combination with multiple and well placed partial pressure sensors (Penning-PEM or oxygen sensors) in order to enable good uniformity [155, 207].

For modelling the reactive sputtering process the so called Berg's model is most commonly used. This model describes the influence of different processing parameters for the reactive sputtering process, while keeping the number of parameters as low as possible. Even though it is only a first order approximation, since the model neglects some effects that may influence the overall process, the predictions fit surprisingly well to most experimentally found results [195]. Nevertheless, the model will not be further discussed in this thesis as it would be beyond the scope and was only mentioned for the sake of completeness.

5.2.2. Pulsed DC magnetron sputtering

Pulsed DC magnetron sputtering is a most advantageous method in controlling structure and composition of TiO_2 thin films due to its easiness to adjust deposition condition and the possibility to adapt the process to large-area coating for industrial purposes [192].

Pulsed DC reactive sputtering, generally, has been widely used to deposit thin films of dielectric materials such as alumina, Al_2O_3 , and titania, TiO_2 , with smooth structure due to the absence of particulates created by micro-arcs [208].

In general, arcing is a serious problem when sputtering insulating layers or reactively in DC mode, which is why arcing will be shortly discussed in the following, including ways to prevent arcing. After that the characteristics and important parameters of pulsed DC sputtering will be explained.

Arcing

A serious problem of reactive DC sputtering or DC sputtering of non-conductive layers is the accumulation of electric charges from the plasma at the target surface. These charges cause mini- or micro-arcs which result in very uneven removal of material from the target electrode and particulate formation. Moreover, arcs lead to more arcs and to inhomogeneities of the target [151, 155, 208].

Undesired effects of arcing are [151, 208]:

- The process becomes unstable, which can be attributed to the disability of the system to recover its original state after switching off the power supply to temporarily suppress arcs, due to the hysteresis effect.
- Arcing reduces the target lifetime, since the surface may be damaged due to a local melting of the target.
- Arcing creates defects in the coatings due to incorporation of droplets of molten target material.
- Severe arcing can even damage the power supply.

To avoid arcing and its undesired effects, the insulating layer can be discharged periodically. This can be achieved by various methods, including radio frequency sputtering and pulsed DC sputtering [151, 155, 208].

Methods to prevent arcing

There are several methods to avoid arcing when sputtering insulating films such as TiO_x [155]:

- With radio frequency sputtering arcing can be completely prevented, though it has some drawbacks. RF sputtering has only about half the deposition rate of DC sputtering but at the same time is more expensive. Furthermore, sputtered films are also deposited on the target, which is not desirable [151, 155, 209].
- Direct current sputtering through a mesh, which prevents the compound formation in the target [155].

- Pulsed direct current sputtering was introduced in the mid-1990s. It has a higher deposition rate compared to radio frequency sputtering, which is the major advantage of this method [155, 209]. A disadvantage of pulsed direct current sputtering of insulating films is that the film can cover the whole inner surface of the vacuum chamber under certain circumstances. This results in an effect known as a disappearing anode. The electrons cannot return to the power supply, the cathode voltage rises and the plasma eventually extinguishes [155].
- Mid-frequency alternating current in a dual magnetron system, which utilises two magnetrons working at a frequency of 40 to 80 kHz. The main advantage of this system is that there is always a clean anode. The disadvantage is that two magnetrons are necessary [155].
- Redundant anode sputtering, where two auxiliary elements work alternately as cathode and anode. This system is cheaper than a dual magnetron system and there is no disappearing anode, since each auxiliary element is cleaned when working as cathode. Still, there is the disadvantage that the auxiliary elements should be made of the same material as the target, to avoid contamination of the target or the substrate with alien auxiliary material [155].
- Arc detection: modern power sources have the ability to detect arc events. When an arc is detected by sensing a drop in the cathode voltage, an increase in cathode current or by a combination of these two events, the power is momentarily stopped to avoid more arcs. However, there is still power stored in the power delivery cable that must be dissipated before the effect of an arc event is over. Sometimes it is necessary to detect and clear an arc and return to full power in less than 1 ms. To minimize the energy that has to be dissipated the power supply cable should be as short as possible [155]

Minimum frequency to avoid arcing with RF or pulsed DC sputtering

The discharge frequency, be it pulsed DC or radio frequency, must be above a minimum to prevent arcing. To estimate that minimum discharge frequency, the time for an arc to occur can be calculated [151]:

$$t_B = \varepsilon_r \varepsilon_0 \frac{E_B}{J_i} \quad (5.1)$$

where ε_r is the dielectric constant of the layer, ε_0 is the permittivity of free space, E_B is the dielectric strength of the insulating layer and J_i is the bombarding ion current density. The voltage breakdown can now be prevented, if the insulating layer can be discharged periodically with a period less than t_B . As an example, for TiO_2 at 400 Watt in transition mode with a 10 cm target, the breakdown time results to $t_b > 2.04$ ns, with $\varepsilon_r = 86\text{-}170$ (anisotropic; for 10-1000 kHz) [3], $\varepsilon_0 = 8.854 \times 10^{-12}$ As/Vm, $E_B > 1000$ V/m [210], $J_i = 37.27$ mA/cm² (erosion area of the target = 2617 mm², compare with Figure 5.3). This corresponds to a minimum frequency of $\nu_{\min} = 480$ MHz, which is far beyond the maximum frequency of $\nu_{\text{pinnacle+}} = 350$ kHz of the pulsed DC power source used in this work, i.e. *Pinnacle® Plus+ 5 kW x 5 kW Power Supply 325 VDC – 800 VDC* with arc detection. This result contradicts practical experience. Even though theoretical calculations predict that a pulse frequency of 5-350 kHz is not sufficient to prevent arcing, experiments carried out in the course of this work did not indicate arcing events once the target was conditioned. Possible reasons for this are: first, the compound formed at the target is not TiO_2 , but rather TiO_x ($x < 2$); and second, the target is never fully TiO_2 -covered.

Pulsed DC (direct current) sputtering

It was shown that pulsed DC magnetron sputtering in mid-frequency (20-350 kHz) is a possible way to prevent arcing when reactively depositing dielectric layers. Periodically reversing the target voltage suppresses arc events at the target and stabilises the reactive sputtering process, thus yielding both, high deposition rates and smooth and uniform films. Other advantages of pulsed DC sputtering technique are its long-term process stability, reduced defect density, improved film properties and enhanced dynamic deposition rates [155, 193].

Belkind et al (2005) described the pulsed DC process as follows (compare with Figure 5.4): *“The power is applied to the target for a time τ_{on} , the ‘on-time’ during which a negative voltage pulse of a few hundred volts is applied to the target. At the end of an ‘on-time’, the power is either switched off for a period of time τ_{off} , the ‘off-time’, or, more commonly, switched to a small positive voltage (about 20V); for that reason the ‘off-time’ is sometimes also referred to as the ‘reverse time’, τ_{rev} . The dielectric surfaces that are charged up during the ‘on-time’ are discharged during the ‘reverse time’. Arc-free operation requires the ‘on-time’ to be sufficiently short to avoid charge build-up that can cause breakdown and arcing and the ‘reverse time’ to be sufficiently long to fully discharge the surfaces in order to avoid charge accumulation in sequential ‘on’ and ‘reverse’ cycles <compare with equation (5.1)>. Typically, the ‘reverse’ time is about 1/10 of the ‘on-time’. Furthermore, the duration of the ‘on-time’ and ‘reverse time’ determines the lowest pulsing frequency ($\nu_c = 1/\tau_{\text{cycle}}$) known as the critical frequency, ν_c , and the highest duty cycle for arc-free pulsed dc reactive sputtering.”* [208]

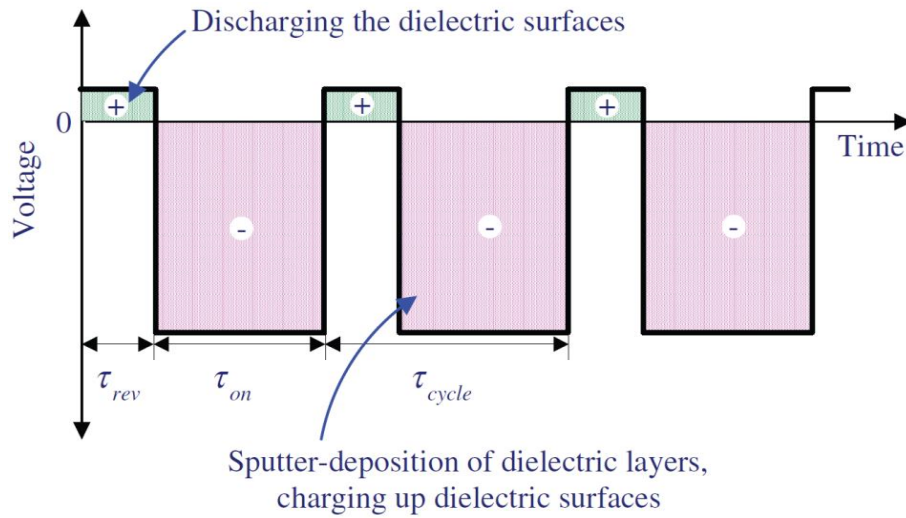


Figure 5.4: Ideal voltage sequence applied to asymmetrical bi-polar pulsed DC sputtering of dielectrics, taken from [208]

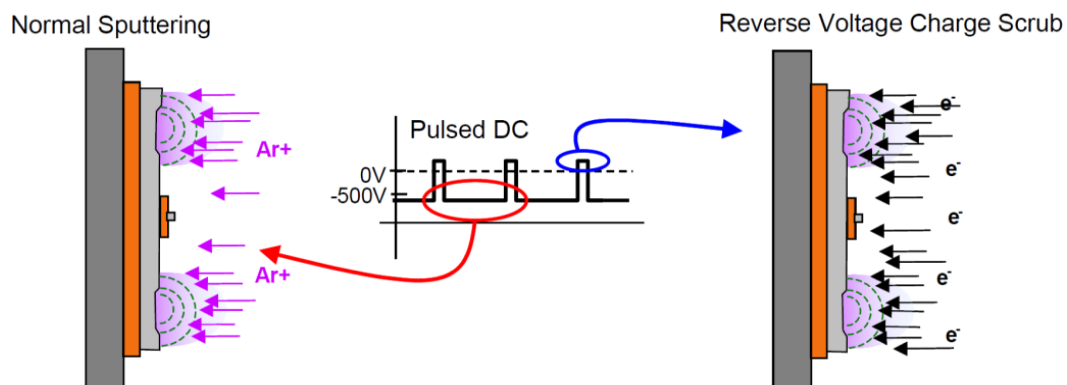


Figure 5.5: Target-schematic of asymmetric pulsed DC power; during the negative pulse, ions are attracted to the target for sputtering (τ_{on}), and during the positive pulse a flux of electrons discharges the target (τ_{rev}), taken from [155]

Since the magnitude and duration of the negative pulse are greater than those for the positive pulse, this type of power is known as asymmetric pulsed power [155].

The two most important parameters for pulsed direct current sputtering are the pulse frequency, which usually is in the range of 20-350 kHz, and the duty cycle with either the on-time or the reverse time as determining parameter. The duty cycle should not be higher than 65-70% to effectively suppress arcing during the deposition of insulating films. Another parameter is the reverse voltage, which, though, was not varied in the course of this work [155, 193]. These mentioned parameters significantly influence the film morphology, foremost the pulse frequency. This is due to the fact that pulsing the discharge significantly modifies the

characteristics of the magnetron plasma, such as plasma density and electron temperatures, and thus the ion energy fluxes to the film [193]. Pulsed DC sputtering causes increased plasma activation in the substrate plane compared to the DC sputter process, i.e. an increased flux and higher energy of ions, electrons and neutral particles, which therefore offers different film properties [154, 211]. However, the relations between the driving voltage waveform and pulsed plasma parameters, as well as their collective impact on the film properties, are not well understood [193].

In conclusion it can be said, that reactive pulsed DC magnetron sputtering offers the means to improve and better manipulate film properties, e.g. structure, morphology and stoichiometry.

Other parameters that influence film properties of TiO_2

Besides pulse frequency duty cycle and partial pressure, there are several other parameters that change film composition and film morphology: substrate material [211], substrate temperature [192, 211], reactive gas flow mode (pulsed or continuous) [196], discharge pressure [186], discharge current [186], energy of the particles impinging on the substrate [154, 211] and bias voltage [155, 212].

Figure 5.6 shows a model for resulting phases of TiO_2 , i.e. amorphous, anatase and rutile, as a function of substrate temperature and particle energy including the corresponding deposition methods, developed by Löbl et al. (1994) [213]. At low particle energies and low substrate temperature the films tend to an amorphous structure. Increasing the substrate temperature first yields anatase phase and then rutile at even higher temperatures. In the region of magnetron sputtering an amorphous, a rutile anatase mixture and pure rutile phase exist depending on the temperature, but no pure anatase can be expected. However, Horprathum et al. (2011) found amorphous films of TiO_2 for substrate temperatures up to 200 °C and anatase phase at temperatures above 300 °C deposited by pulsed DC sputtering [192]. This does not agree with the model of Löbl et al. (1994), though it has to be mentioned that they used silicon substrate, which might work as a seed crystal and promote a certain phase of TiO_2 .

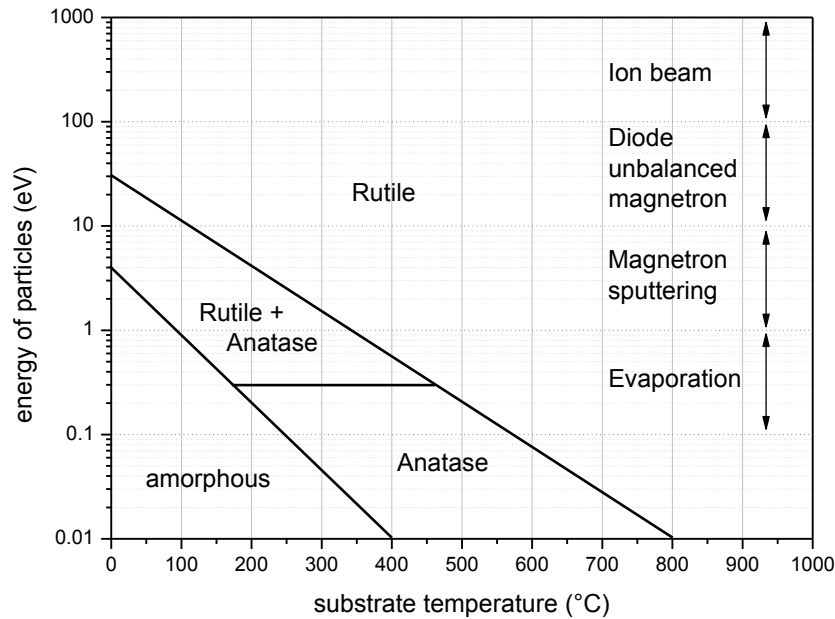


Figure 5.6: Model of TiO_2 deposition giving different phases (amorphous, anatase and rutile) as function of particle energy and substrate temperature; redrawn from [211, 213]

In this work the varied parameters were: pulse frequency, duty cycle and deposition pressure. Additionally the substrate temperature was measured. The next section will describe the experimental setup and the sample preparation.

5.2.3. Experimental setup

The experimental setup for reactively coating glass substrates with TiO_2 consisted of:

- vacuum chamber with diffusion pump
- substrate carrier for holding glass plate substrates
 - with built in Pt100 for temperature measurement
 - 14 cm distance to the target and 3 cm out of central position
- two mass flow controllers, for Ar and O_2 , (MKS Type 1179B)
- 4/8 channel control unit for mass flow controllers (MKS Type 647C)
- Baratron pressure gauge (MKS Type 690)
- Signal converter for the baratron (Type 270B)
- pulsed DC sputter source (Advanced Energy Pinnacle™ Plus+ 5x5 kW)
- sputter source with 10 cm target diameter
- quadrupole mass spectrometer (Alcatel Multi Turboquad), in the course of this work it was later changed (MKS Microvision 2)

5.2.4. Sample preparation

Pre-treatment

Glass plates were cleaned with methanol and a substrate cleaner (*umicore*). Then they were fixed to the sample carrier and put into the vacuum chamber via a vacuum lock. Before coating the pressure in the chamber was at $p_i < 10^{-4}$ Pa (10^{-6} mbar).

Coating parameters

For coating glass plate substrates the following coating parameters were used and/or varied:

- sputter power: $P = 400$ W
- pulse frequency: $\nu = 5$ kHz, 50 kHz, 100 kHz
- reverse time: $t_{rev} = 4$ μ s (also 1 μ s and 2 μ s in pre-tests)
- coating time: $t_c = 60$ min
- argon working pressure: $p_{ar} = 0.4$ Pa, 1.0 Pa, 1.5 Pa
- oxygen partial pressure: $p_{O_2} = 0.033$ Pa

The oxygen partial pressure was set to a value that the voltage is exactly between metal mode and poisoned mode. This was determined before in experiments for characterizing the process, but will not be further discussed in this work. For more information see the diploma thesis of Martin Quirchmayer². With the mentioned parameters it was possible to deposit clear transparent films on glass plate substrates.

Post-treatment

After coating some of the samples were annealed at a temperature of 300 °C.

5.3. TiO₂ thin films – results and discussion

In this section the results of TiO₂ films deposited on glass plate substrates will be discussed. This includes X-Ray diffraction analysis and scanning electron microscope imaging. Additionally substrate temperature was measured and samples were analysed with energy dispersive X-ray spectroscopy to verify the stoichiometry. The measurement methods will not be explained since they are all state of the art methods.

Preliminary experiments showed that the film structure does not significantly depend on the reverse time, thus in the following the reverse time t_{rev} was always set to 4 μ s.

² Diploma thesis: *Herstellung von Titandioxid-Schichten in anataser Phase auf Mikroglasskugeln mit Hilfe von reaktivem Pulsed-DC-Sputtern*, Martin Quirchmair, 2012

5.3.1. X-ray diffraction analysis and scanning electron microscope imaging

Generally, XRD results showed that films become more amorphous with increasing argon working pressure and with increasing pulse frequency. When annealed the samples became more crystalline. This can be observed in the following figures. Before going into details it has to be mentioned that the glass substrate builds an amorphous background in the X-ray diffractogram, since the penetration depth of Cu K- α (1.54 Å) is several tens of microns for light elements and coatings were around 1-2 μm thick [214, p. 2].

Figure 5.7 shows the diffractogram of TiO_2 films deposited on plane glass substrates at a power of 400 W and an argon working pressure of 0.4 Pa with the pulse frequency varied, i.e. 5 kHz, 50 kHz and 100 kHz. It was observed that with increasing frequency the film becomes more amorphous, suppressing the rutile reflex. Figure 5.8 – Figure 5.10 show scanning electron microscopographs of these films (5 kHz, 50 kHz, 100 kHz). With increasing frequency films become smoother and the larger structures become smaller. With closer examination, it is noticeable that there are two types of these larger structures, i.e. erected with round shape in top view (red circles), and lying with irregular shape in top view (black circles). At higher frequencies erected structures are dominating, whereas the irregular structures vanish.

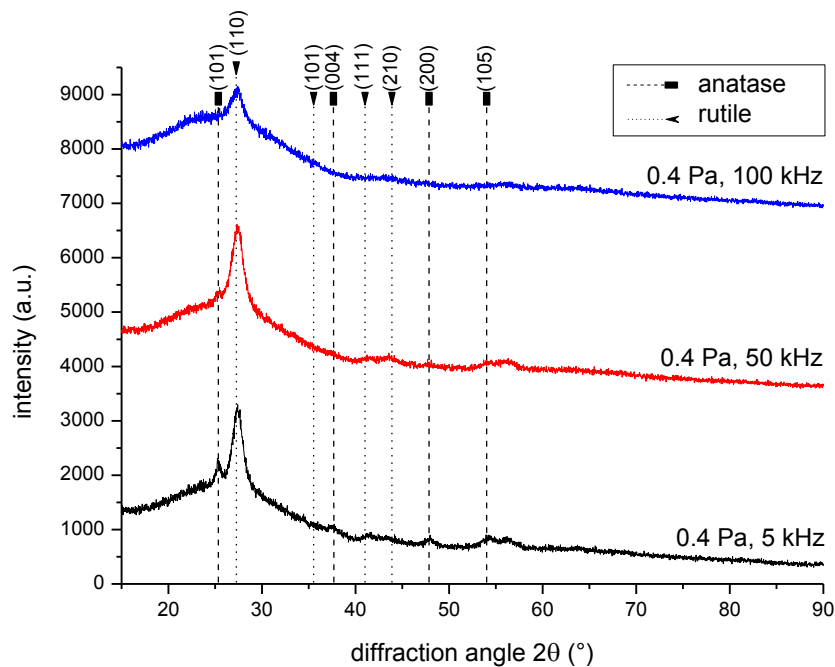


Figure 5.7: XRD-results of TiO_2 sputtered films, deposited at a working pressure of 0.4 Pa, and pulse frequencies of 5, 50 and 100 kHz

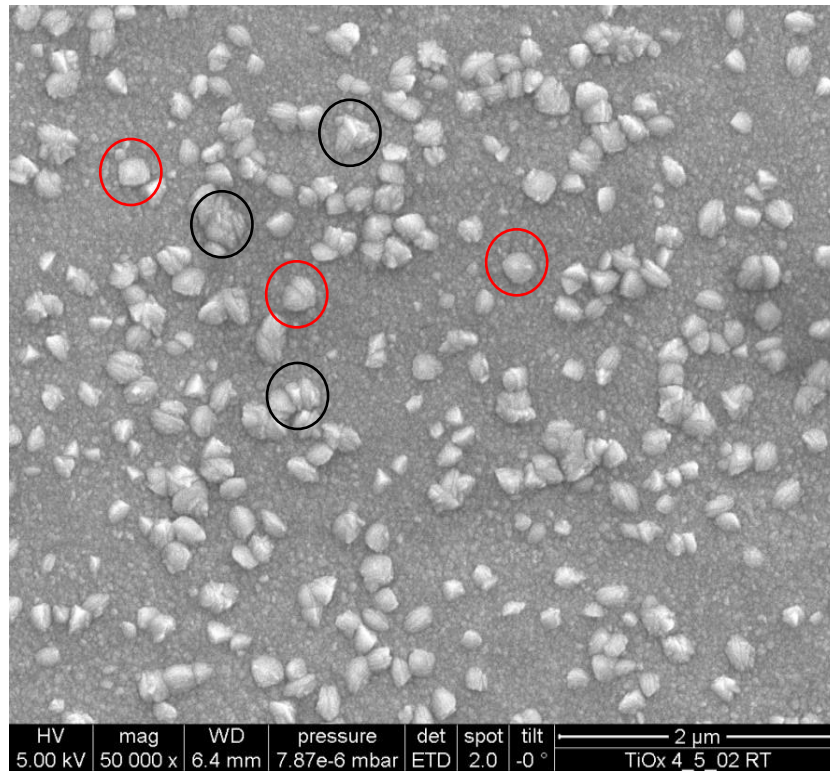


Figure 5.8: SEM-image of TiO_2 sputtered film, deposited at a working pressure of 0.4 Pa and pulse frequency of 5 kHz

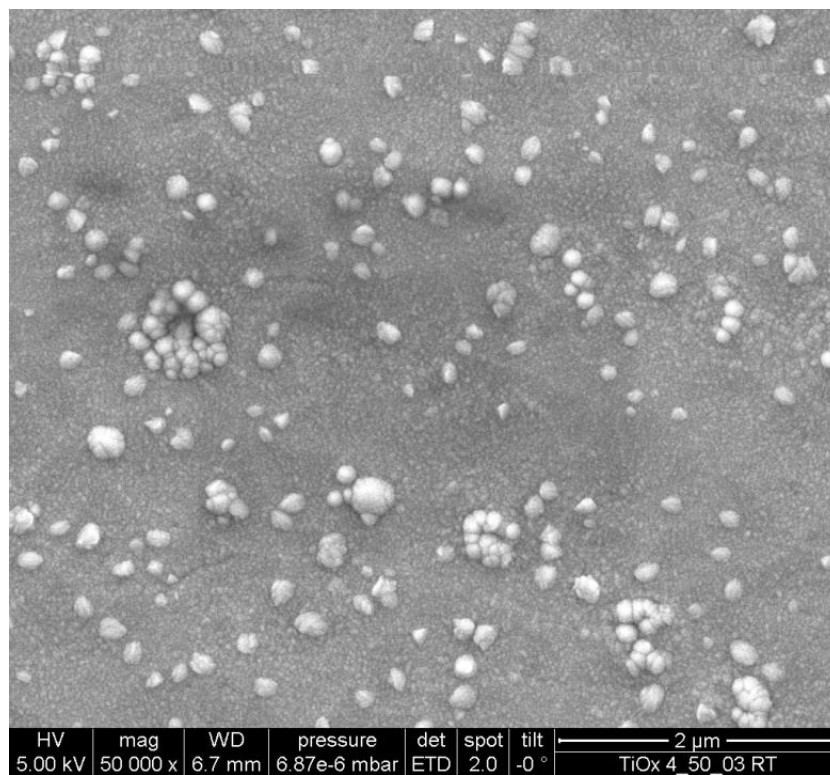


Figure 5.9: SEM-image of TiO_2 sputtered film, deposited at a working pressure of 0.4 Pa and pulse frequency of 50 kHz

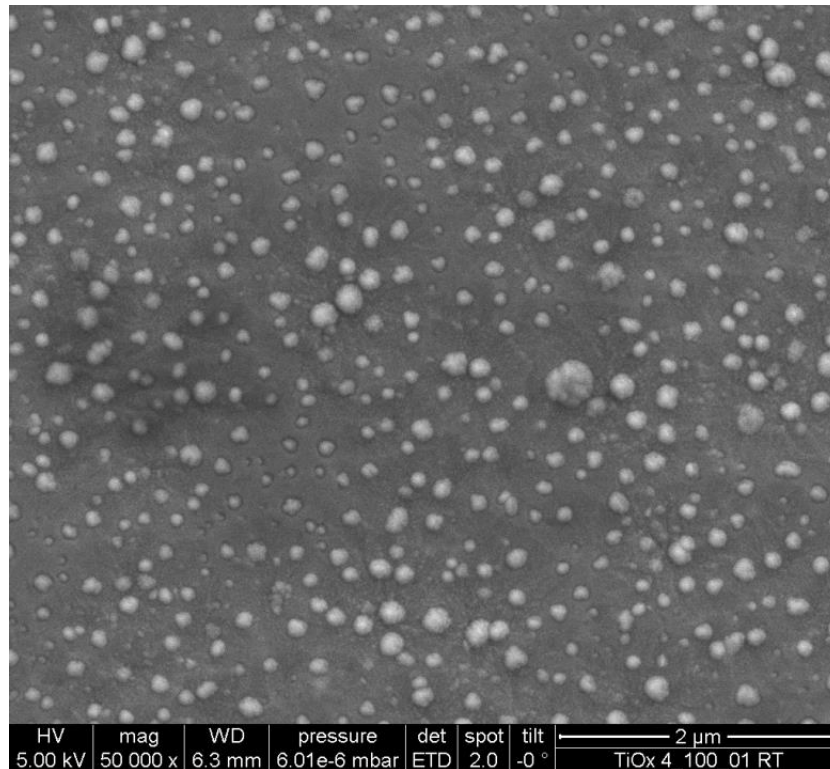


Figure 5.10: SEM-image of TiO_2 sputtered film, deposited at a working pressure of 0.4 Pa and pulse frequency of 100 kHz

These two types of structures indicate the presence of one or the other TiO_2 phase, i.e. anatase and rutile. However, the surrounding, relatively smooth structure also consists of both phases, which is why there is still rutile found with XRD even when there are no lying structures found with SEM. Still, most of the material is amorphous and becomes anatase under annealing at 300 °C. Films that show no anatase, but still have rutile content, which happens due to higher pulse frequencies, developed the anatase structure out of the amorphous phase when annealed. Additionally, rutile content also is increasing under annealing in these films (see Figure 5.11). It has to be mentioned that whereas many reflexes of anatase were found, i.e. (101), (004), (200) and (105), only a single reflex of rutile was found, i.e. (110). It is impossible to be entirely sure of the structure when there is only one single reflex, but it is believed that there is a textured rutile phase in the deposited film. Additionally it was found that the film is strained after annealing, which is indicated by the shift the (004) and (200) reflex, as well as by cracks that were discovered in the film (see SEM image, Figure 5.12). The reflex shift to the right indicates a smaller unit cell and thus a tensile strain, which would be in accordance with the found cracks.

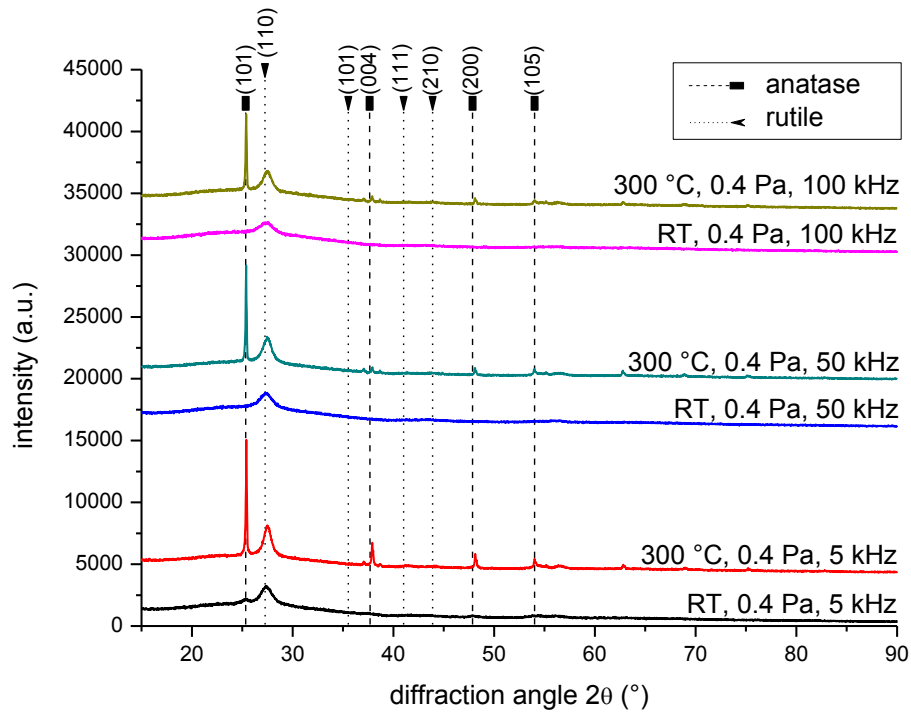


Figure 5.11: XRD-results of TiO_2 sputtered films, deposited at a working pressure of 0.4 Pa, pulse frequencies of 5, 50 and 100 kHz, and annealed at 300 °C

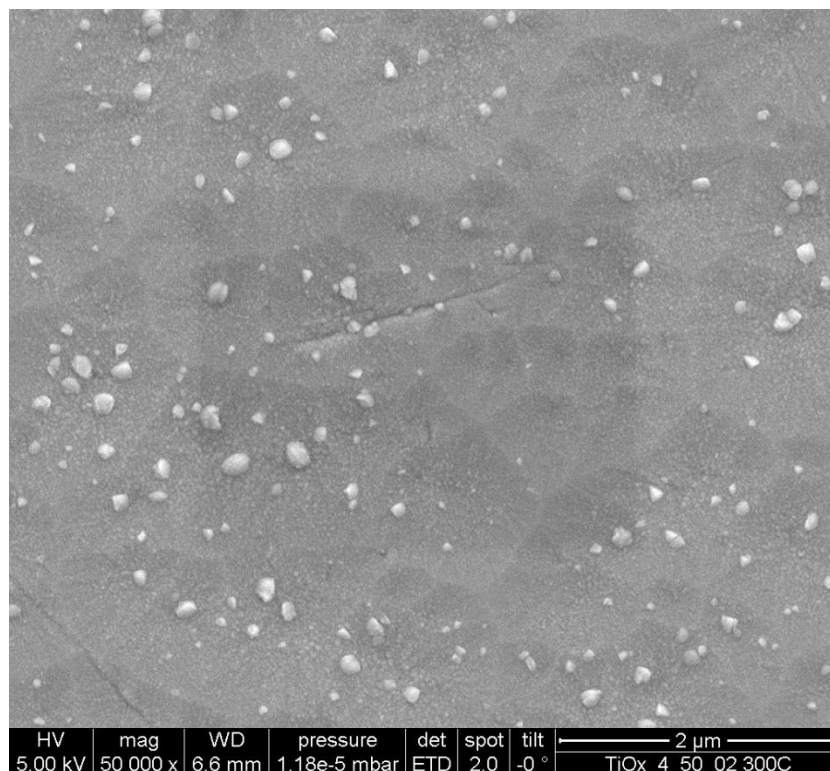


Figure 5.12: SEM-image of TiO_2 sputtered and at 300 °C annealed film, deposited at a working pressure of 0.4 Pa and pulse frequency of 50 kHz; cracks have appeared due to built up of tensile strain in the film caused by the crystallisation process

At higher Ar pressures the films become even more amorphous and the rutile structure is more and more reduced as can be seen in Figure 5.13. Again anatase is formed under annealing, but no rutile if it was not present before annealing (see Figure 5.14). It was found that also at high deposition pressures of 1.5 Pa films become smoother when deposited at higher frequencies, i.e. cauliflower like structure at $\nu = 5$ kHz and more areas with smoother structure at $\nu = 100$ kHz. This is shown in Figure 5.15.

At high working gas pressures (1.5 Pa) and high pulse frequency (100 kHz) the deposited TiO_2 films are completely amorphous but, again, anatase phase is formed when annealed.

In conclusion it was possible to prepare samples with only anatase and only rutile structure. Rutile rich films, however, had a large content of amorphous material which becomes anatase under annealing at 300 °C. Anatase without rutile could only be created at high deposition pressures of $p_{\text{Ar}} = 1.0\text{-}1.5$ Pa and subsequent annealing. Before annealing the pure anatase films were completely amorphous.

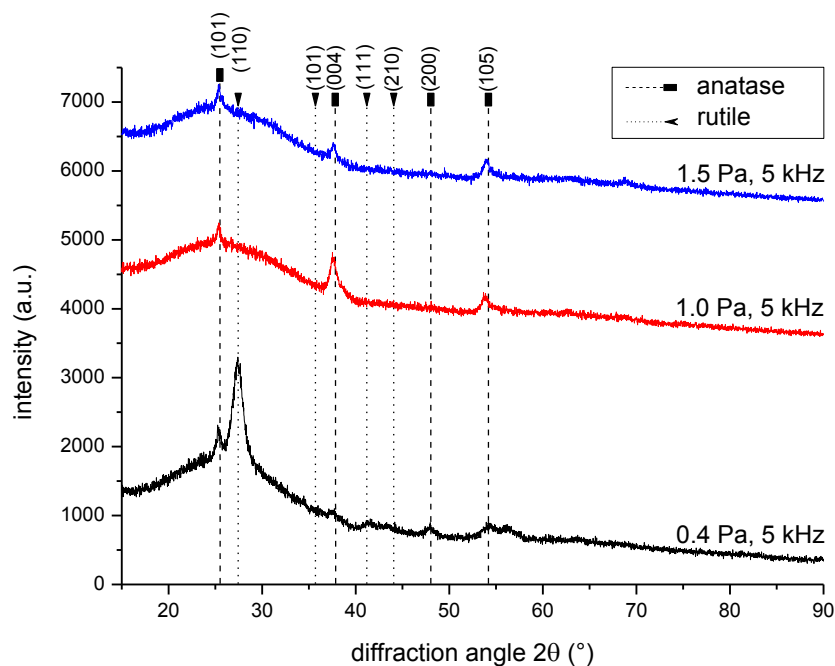


Figure 5.13: Comparison of XRD-results of TiO_2 sputtered films deposited at different working pressures, i.e. 0.4 Pa, 1.0 Pa and 1.5 Pa and a pulse frequency of 5 kHz, at higher working pressures films become more amorphous and rutile is suppressed

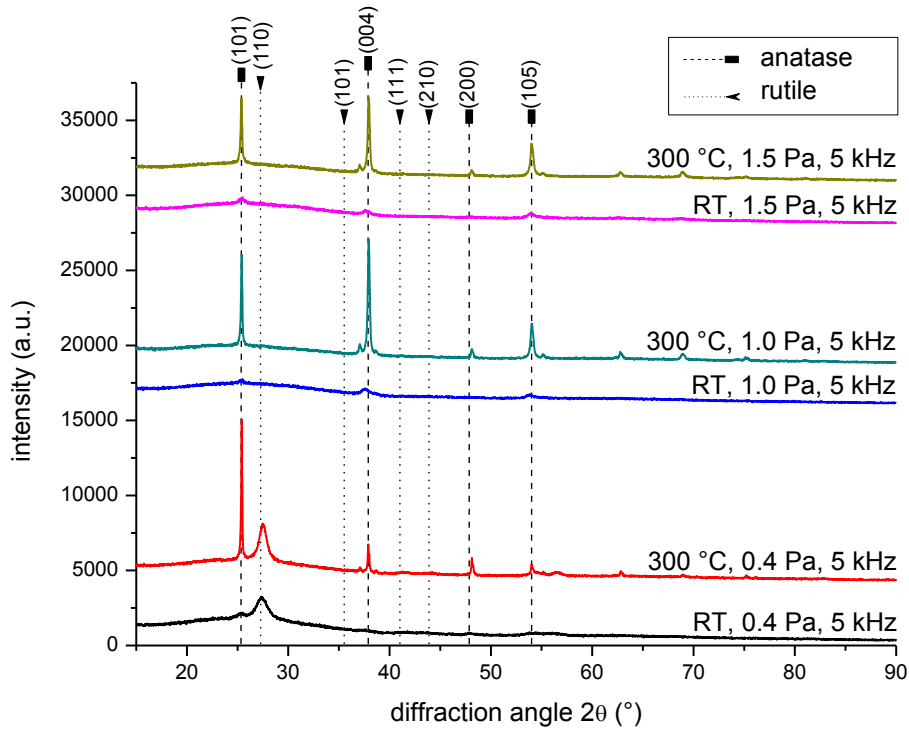


Figure 5.14: Comparison of XRD-results of TiO_2 sputtered films deposited at different working pressures, i.e. 0.4 Pa, 1.0 Pa and 1.5 Pa and a pulse frequency of 5 kHz; before and after annealing; at higher working pressures annealed films have no rutile content

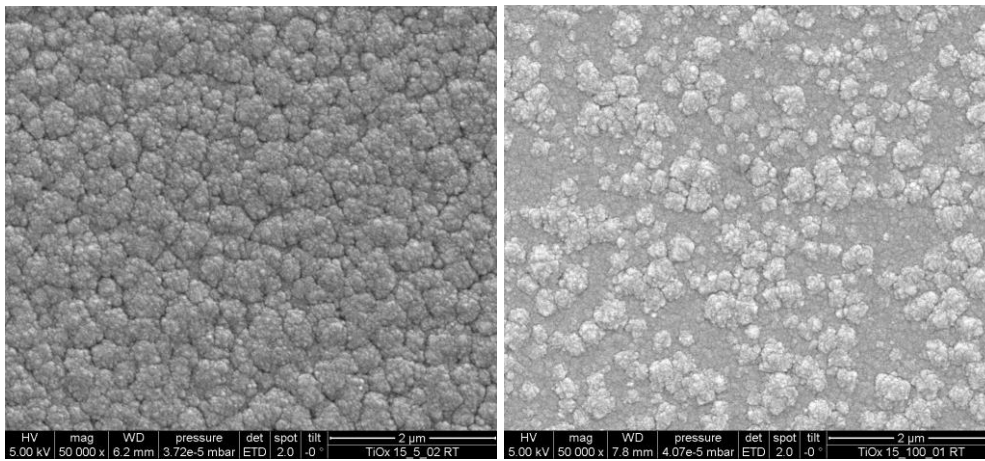


Figure 5.15: Comparison of TiO_2 films deposited at 5 kHz (left) and 100 kHz (right) at a working pressure of 1.5 Pa; at higher frequencies the cauliflower like structure gets smooth regions

These results are in good agreement with the correlations found in [211, 213]. According to Figure 5.6 and taking into account the measured substrate carrier temperature of 100-112 °C, rutile-anatase mixture films would be expected. This was the case when films were deposited at low working pressures and low pulse frequencies. Higher working gas pressures and higher

frequencies on the other hand yielded more amorphous films, which is attributed to the lower sputtered particle energy when hitting the target. High working pressure reduces the sputtering voltage due to a higher ion density and thus decreases the energy of the ions impinging the target. This reduces the energy of the sputtered particles. Additionally, a higher working gas pressure increases scattering of sputtering particles on the way from the target to the substrate, thus again reducing their energy. Furthermore, high frequencies also reduce the voltage on the target and reduce the ion energy which, as before, also reduces the sputtered particle energy. Stoichiometry of the films was verified with EDX.

The following subsections will deal with some more correlations that were found.

5.3.2. Parameters correlating to structure and film thickness

It was found that higher working pressure yields films with higher thickness and more amorphous structure. The structure was already discussed with respect to working pressure in section 5.3.1. In Figure 5.16 it is shown that higher working pressure yields higher film thicknesses, which is because of lower voltage and thus higher ion current. A higher frequency yields thinner films due to a shorter duty cycle, i.e. the sputter voltage is reversed more often. Another effect that influences the film thickness is the particle energy, since particles with higher energy tend to form films with higher density [154, 193].

Additionally it was found, that both the structure of the deposited film and the film thickness strongly depend on voltage and oxygen partial pressure. As was already explained voltage and partial pressure correspond very well to each other. It was found that a slightly lower voltage accompanied by a slightly lower partial pressure yields films with higher film thickness and less amorphous structure (see Figure 5.17). As every deposition was repeated several times, these small differences could be observed and investigated. Most films showed that behaviour, i.e. 0.4 Pa 50 kHz, 1.0 Pa 5 kHz, 1.0 Pa 50 kHz, and 1.5 Pa 50 kHz, 1.5 Pa 100 kHz. Still, additional experiments would be required to investigate this effect more thoroughly (compare [154]).

Correlations with substrate temperature could not be found, as the starting temperature depended on the conditioning time and temperatures in general were very similar to each other at the end of the coating process. They only varied between 100 °C and 112 °C (compare [211]).

The found results are in good agreement with literature [154, 186, 192, 193, 211].

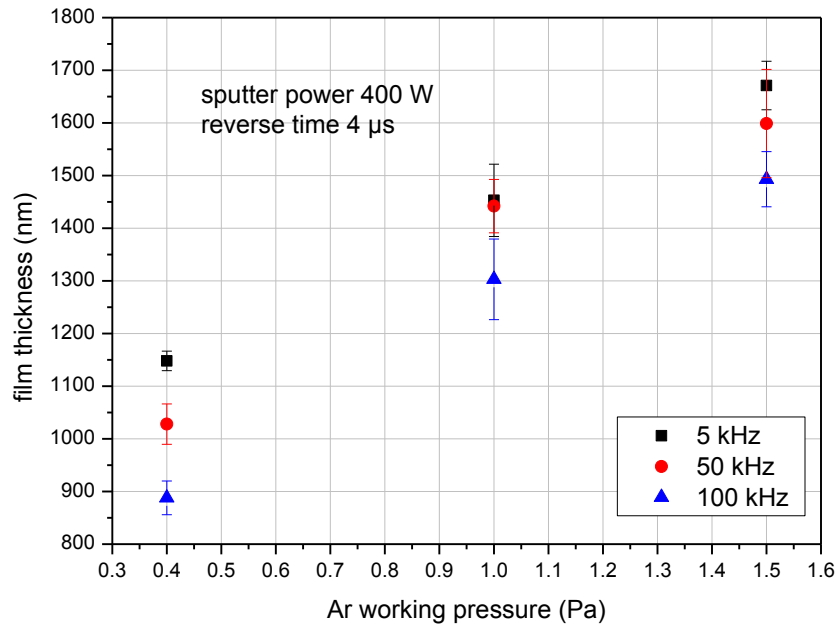


Figure 5.16: Film thickness comparison of TiO_2 on glass deposited at different argon working pressures and different pulse frequencies

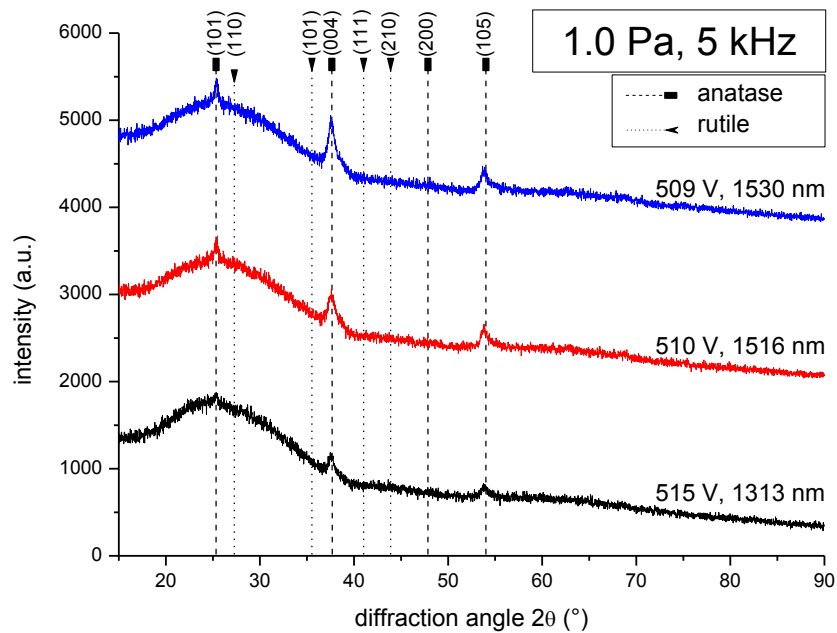


Figure 5.17: Impact of sputtering voltage (effect of oxygen partial pressure) on the structure and the film thickness of TiO_2 films; deposited at 1.0 Pa Ar and $\nu = 5$ kHz

5.4. TiO₂ thin films on hollow glass microspheres

As was shown in the above sections, it was possible to deposit TiO₂ films by pulsed DC magnetron sputtering with anatase phase structure. This coating now had to be applied onto hollow glass microspheres to work as a catalyst carrier to increase the catalytic performance of the noble metal catalyst. For that 20 ml of sieved (> 50 μm) hollow glass microspheres were put into the coating vessel and coated with TiO₂ for 1 and 5 hours. As coating parameters the same that yield anatase phase on plane glass substrate (compare Figure 5.14) were chosen, i.e:

- sputter power: $P = 400$ W
- pulse frequency: $\nu = 5$ kHz
- reverse time: $t_{rev} = 4$ μs (also 1 μs and 2 μs in pre-tests)
- coating time: $t_c = 60$ min, 300 min
- argon working pressure: $p_{ar} = 1.5$ Pa
- oxygen partial pressure: $p_{O_2} = 0.033$ Pa

The films were analysed with scanning electron microscope and x-ray diffraction. Film thicknesses could not be determined thoroughly by these means, because of the lack of contrast between TiO₂ and glass and the low film thickness when using back scattered electrons. The film thickness on the spheres can be estimated to $d \sim 3.5$ nm for 1 hour coating time and $d \sim 17.5$ nm for 5 hours coating time, taking into account the measured deposition rate of 0.38-0.56 nm/s depending on the position inside the coating vessel and using the film thickness calculation method described in chapter 4.3.7. Nevertheless, the typical columnar structure of sputtered films could be observed. Figure 5.18 shows a scanning electron micrograph of 1 hour TiO₂ coated hollow glass microspheres. The columnar structure of the TiO₂ film is slightly noticeable in the cross section of a sphere in Figure 5.19 and in top down view in Figure 5.20. Furthermore, it became clear that anti-caking agent particles are coated to a large extent and also show a film with columnar structure.

Annealing did not have a detectable effect on the films. However, when the coated spheres were washed, the anti-caking agent particles were moved and holes remained where those particles had been before (see Figure 5.21).

It was not possible to achieve film thicknesses that would yield structures like they were observed on plane glass substrate in reasonable time. On plane glass films with thicknesses of about 1 to 2 μm were deposited, whereas the film thicknesses on spheres were in the range of about 4 to 20 nm.

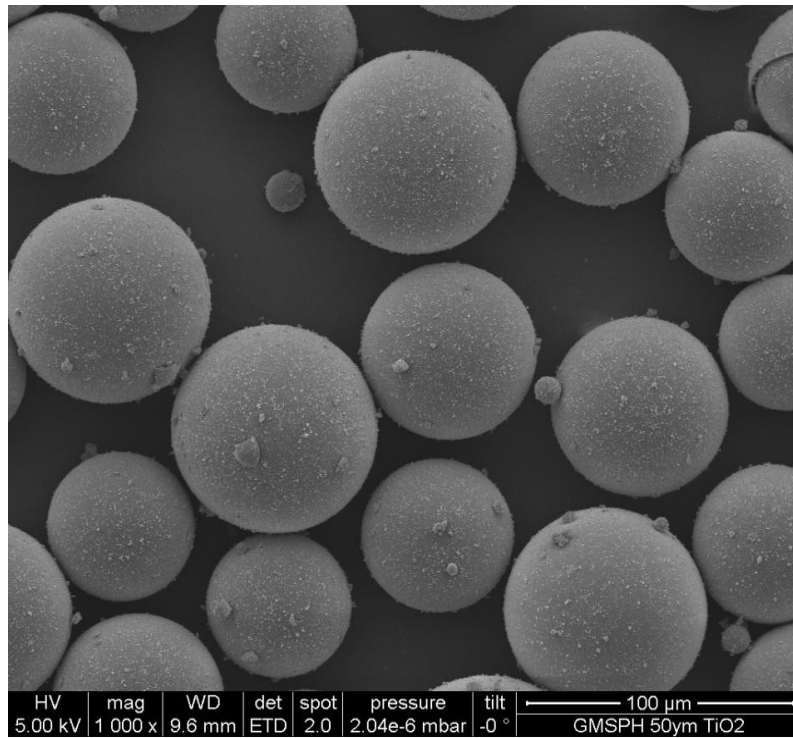


Figure 5.18: Scanning electron microscope image of 1 hour TiO_2 coated hollow glass microspheres

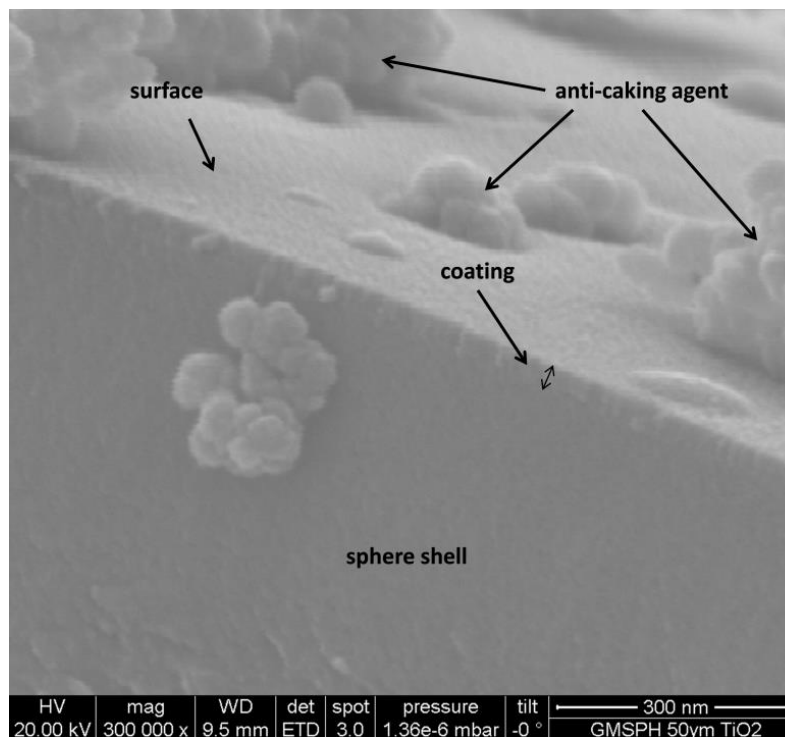


Figure 5.19: Cross section of 1 hour TiO_2 coated hollow glass microspheres, the film has a columnar structure

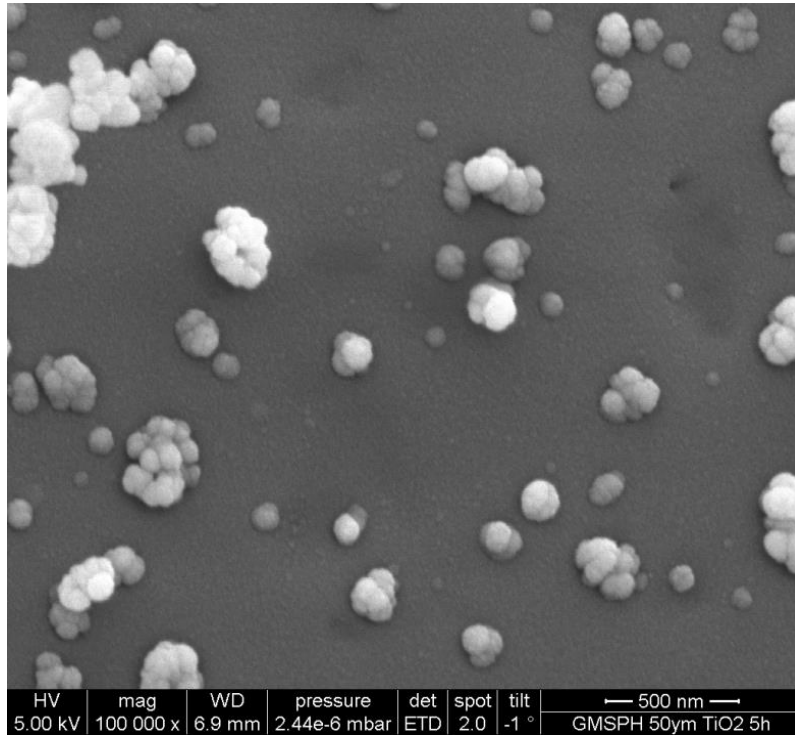


Figure 5.20: Surface of 5 hours TiO_2 coated hollow glass microsphere, the film has a columnar structure, anti-caking agent particles are also coated

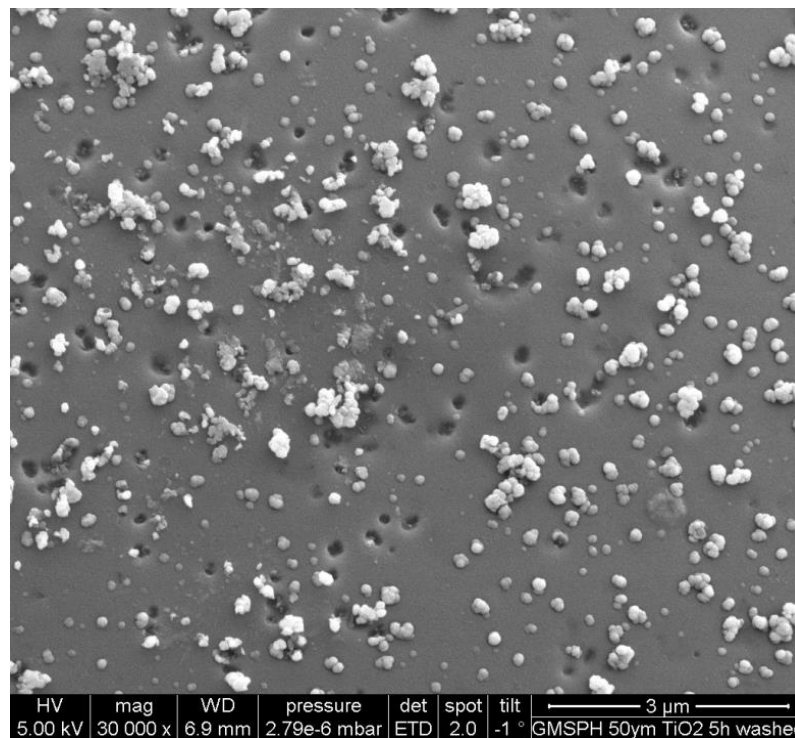


Figure 5.21: Surface of 5 hours TiO_2 coated sphere, that was washed with distilled water; washing moved the anti-caking agent particles and the remaining holes in the coating become visible

5.4.1. X-ray diffraction of TiO₂ films on hollow glass microspheres

The structure of the TiO₂ films on hollow glass microspheres was studied with X-ray diffraction. The samples were measured for 9¼ hours before and after annealing. Annealing was carried out for 6 hours at 300 °C in order to get a more crystalline structure, like it was observed on plane glass substrates. Figure 5.22 shows the diffractograms of hollow glass microspheres coated with TiO₂ before and after annealing, deposited at 1.5 Pa argon pressure, 0.33 Pa oxygen pressure, a power of 400 W, a pulse frequency of 5 kHz a reverse time of 4 µs and 1 hour coating time. It can be clearly seen that only amorphous structure was detected, which mainly consists of the amorphous glass. Still crystalline structure would be detectable, if present. These results are in good agreement with the work of Mukherjee et al. (2014), who studied the morphology of TiO₂ films depending on deposition temperature and film thickness. They concluded that TiO₂ films with a thickness below 25 nm are X-ray amorphous [215]. The film thickness on the spheres was well below that value at $d = 4\text{-}20$ nm. However, most recently in 2015 Bukauskas et al. (2015) published a work, where they found pure anatase phase films of only 9-10 nm thickness by Raman spectroscopy [216]. If a crystalline TiO₂ phase can be detected by Raman spectroscopy on hollow glass microspheres remains to be investigated.

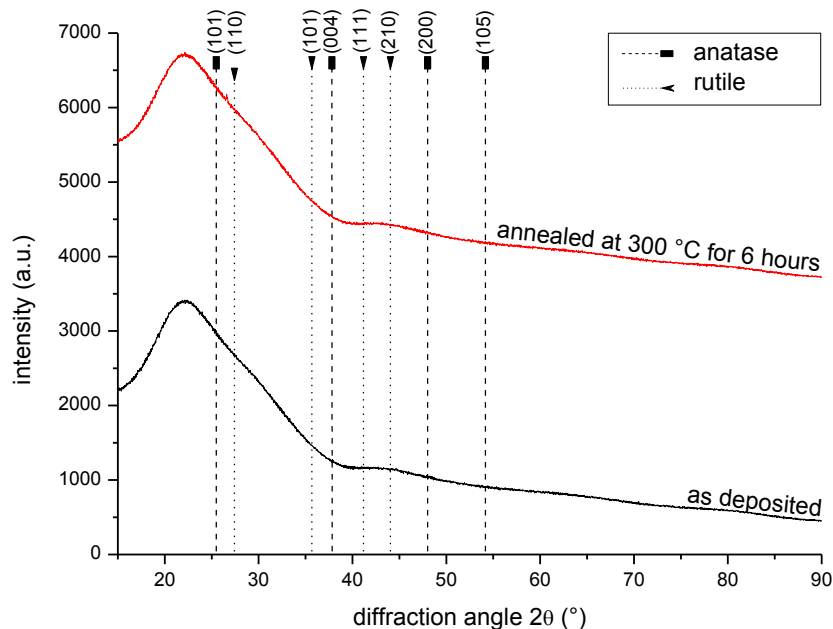


Figure 5.22: XRD results of TiO₂ films on hollow glass microspheres, before and after annealing at 300 °C for 6 hours, both samples show only amorphous structure

It can be concluded that anatase thin films could not be detected on hollow glass microspheres by X-ray diffraction. To yield anatase films higher film thicknesses might be required, which would result in much longer deposition times at the given geometry and deposition rate. Increasing the deposition rate by increasing sputter power or optimizing the deposition geometry, would be recommended in order to yield crystalline phase TiO₂ films on hollow glass microspheres.

Finally, it has to be mentioned that in the end TiO₂ was rather not used as catalyst support, but as a bonding agent between the hollow glass microspheres and the metal catalyst, as will be discussed in chapter 6.

6. Catalyst characterisation

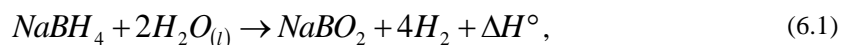
As already discussed in detail in the chapters before, hollow glass micro spheres (type S38) from 3M™ can be filled with hydrogen by the means of a diffusion process at high temperature and high pressure (approx. 250 °C, 70 MPa). After cooling down, hydrogen is trapped inside the spheres unless they are destroyed or heated up again. To release the hydrogen, it is feasible to use an exothermal chemical reaction which itself also produces hydrogen as was described in chapter 3.3. These hydrolytic reactions require a catalyst to work properly [79, 217, 218]. In case of this work it was focused on sodium borohydride (compare with sections 2.2.2 and 3.3.1). The catalyst was applied onto the surface of the spheres by magnetron sputtering using the method described in chapter 4.3.

In this chapter first, a short review of potential catalysts will be given with focus on catalysts that can be applied by magnetron sputtering. After that the experimental setup to characterise the catalyst will be described followed by the sample preparation. Finally results of the tested catalysts will be discussed. As was already mentioned before, in this work powder form NaBH₄ was used rather than a stabilised NaBH₄-H₂O solution. Although this is the main part of this work, it is kept rather short, as it focuses on the final results. These results were acquired after continuously improving the developed methods.

6.1. Overview of potential catalysts

In the course of the hydrolytic reaction (equitation (6.1)) the formation of basic hydrated metaborate increases the pH-value of the NaBH₄-solution, inhibiting the reaction even though it

is strongly favoured thermodynamically. This results in slow kinetics and limited hydrogen generation capacity of only 7-8% by self-hydrolysis of NaBH₄ at room temperature [71, 72, 73].



In order to increase reaction rates of pure NaBH₄, the hydrolytic reaction can be promoted thermally or by adding a catalyst. Therefore, catalysts are already well studied. Already in 1953 Schlesinger et al. investigated acid catalysis and metal catalysis for NaBH₄ hydrolysis [76]. Today, research is focused on metal catalysis (Co, Ru, Ni, Pt, Fe, Pd, Rh, Cu, Zn, and more) which was currently summarized by Demirci (2015). Investigated support materials are carbons, TiO₂, γ -Al₂O₃, LiCoO₂, Ni foam, polymers, other oxides and zeolites and others [77]. Most research groups study catalysed hydrolysis of NaBH₄-solution rather than of the solid NaBH₄, because fluids are easier to handle than solids [69, 72, 74, 78, 79, 80, 81, 82]. Others used NaBH₄ powder and mixed it with the catalyst before adding water to initiate the hydrolysis [83, 84, 85, 86, 87]. In the early stages of NaBH₄ hydrolysis study (50ies and 60ies) also liquid/liquid systems were studied, where aqueous metal salt solutions were used as catalyst [76, 219].

In the following different catalyst synthesis methods will be discussed and catalyst compounds compared.

6.1.1. Catalyst synthesis methods

Because of the sheer number of catalysts and the many ways to synthesise them, this section will only focus on catalysts for NaBH₄ hydrolysis. In principle catalysis can be divided into homogeneous catalysis, where the catalyst and the reactants have the same aggregate state (liquid/liquid or vapour/vapour), and heterogeneous catalysis.

Works about homogeneous catalysis have been carried out, by various groups with being Brown and Brown (1962) one of the earliest, where FeCl₂, CoCl₂, NiCl₂, RuCl₃, RhCl₃, PdCl₂, OsO₄, IrCl₄, H₂PtCl₄ metal salts were dissolved in water and injected into the sodium borohydride solution; with results of catalytic activity in descending order [76, 219]:



In this work solid catalysts were used, which is why the focus lies on these catalysts. In the following, synthesis methods of solid catalysts will be discussed (heterogeneous catalysis).

They either consist of an oxide carrier material (support) and a noble metal or only noble metal particles. More recently also other, none noble metals were investigated. Carrier materials are often used because of their high specific surface area (S_{BET}), their catalytic activity promoting properties and of course to carry the catalyst. Typical specific surface areas (S_{BET}) of commercially available carrier materials are: Sibunit carbon material $S_{BET} = 530 \text{ m}^2/\text{g}$, $\gamma\text{-Al}_2\text{O}_3$ powder $S_{BET} = 170 \text{ m}^2/\text{g}$, TiO_2 powder $S_{BET} = 243 \text{ m}^2/\text{g}$ [79]. These specific areas are about three orders of magnitude larger than the specific surface of hollow glass microspheres used in this work, $S_{BET} = 0.27 \text{ m}^2/\text{g}$.

Impregnation

The most commonly used method to synthesise a catalyst is impregnation of an oxide powder with a metal. Therefore a metal salt is dissolved in water and mixed with the desired carrier material. The carrier material is usually already wetted and the pH value of the mixture adjusted. After that the mixture is dried and annealed for calcination [74, 79, 80]. As an example platinum nitrate can be dissolved in water and mixed with titania powder. The mixture is dried at $250 \text{ }^\circ\text{C}$ and the remaining powder is calcinated at $450 \text{ }^\circ\text{C}$ for 2 hours [69].

Supercritical CO_2 method

Kojima et al (2002) used a method where supercritical CO_2 is utilized [69]. A metal-acetylacetonate (Fe, Ni, Pd, Ru, Rh or Pt) was dissolved into acetone and the resulting solution put into an autoclave with titania powder or cobalt oxide powder. Dry ice was added. After that the autoclave was closed and heated up to $150 \text{ }^\circ\text{C}$ for 2 hours, resulting in a CO_2 pressure of 30 MPa, which is well above the critical point ($\sim 7.38 \text{ MPa}$, $\sim 31 \text{ }^\circ\text{C}$). This caused the titania powder to adsorb the metal-acetylacetonate. After that the titania powder was held at $105 \text{ }^\circ\text{C}$ for 1 hour to yield a metal coating on the titania powder. The result was a catalyst with very high activity compared to catalysts synthesised by impregnation method [69].

Pyrolysis

Pena-Alonso et al. (2007) used a pyrolysis method to activate carbon nanotube paper which was used as the carrier material of the catalyst. The carbon nanotube paper was soaked in a liquid silazane-based precursor and dried. The resulting polymer film was transformed to a ceramic film by pyrolysis ($1100 \text{ }^\circ\text{C}$) [220, 221]. After that a sub-monolayer coating of mixed Pt and Pd atoms was deposited using Pt and Pd bis-allyl pentane solutions [220]. This method yielded results similar to catalysts prepared with the supercritical CO_2 method by Kojima et al. (2002).

In situ formation of the catalyst

Andrieux et al. (2009) used cobalt nanoparticles but concluded that an intermediate cobalt boride species may constitute the catalytic active phase during the hydrolysis [85]. Garron et al. (2009) synthesised Co₂B in situ from Co(H₂O)₆Cl₂ [72].

Electroless deposition

Patel et al. (2010) synthesised a Co-P-B on Ni-foam by chemical reduction of a CoCl₂ + NaH₂PO₂ aqueous solution with NaBH₄ as reducing agent [222].

Pulsed laser deposition

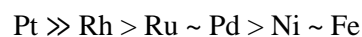
Patel et al. (2010) coated glass substrates by pulsed laser deposition with a Co-P-B film. For that, first Co-P-B was prepared by chemical reduction method and cold pressed in the shape of cylindrical disks in order to be used as a target for laser irradiation. Pulsed laser ablation was carried out under high vacuum [222].

6.1.2. Comparison of catalyst compounds

This section will give a short comparison of the activity of a catalyst depending on used metal and used carrier material. It is important to mention again, that the catalytic performance also strongly depends on the synthesis method.

Noble metal comparison

Kojima et al. (2002) found the following order of catalytic activity using the supercritical CO₂ method and TiO₂ as carrier material [69]:



Pico-scale dispersed platinum on carbon nanotube paper yielded similar results as platinum on TiO₂ synthesised with the supercritical CO₂ method [220].

Demirci and Garin (2008) used the impregnation method to investigate Ru based catalysts on TiO₂ carrier material and found the following order of catalytic activity [74]:

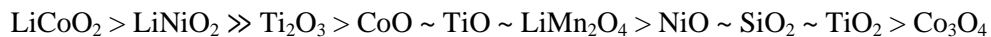


Other promising catalysts are Co nanoparticles investigated by Andrieux et al. (2009) [85], Co₂B nanoparticles investigated by Garron et al. (2009) [72].

Minkina et al. (2010) studied commercially available Rh, Pt and Pd catalysts with Al₂O₃ as carrier material. Although Pt performed best (Pt > Pd >> Rh), these results are not comparable with respect to the compounds, since noble metal content of the catalysts was different for each sample (0.5 % Pt, 1 % Pd and 0.1 % Rh). Furthermore the shape of the catalyst granulates was different [81].

Carrier comparison

Kojima et al. (2002) carried out catalytic experiments of pure metal oxide powder, which is usually used as carrier material. Some of the oxides showed even higher performance than other metal-metal oxide catalysts, e.g. LiCoO₂ > Ru/TiO₂ (supercritical CO₂ method). The performance of the pure oxides in descending order [69]:

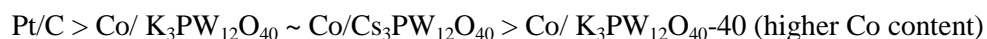


Simagina et al. (2008) used Rh, Ru and Pt on different carrier materials, i.e. Sibunit carbon material with $S_{\text{BET}} = 530 \text{ m}^2/\text{g}$, γ -Al₂O₃ powder with $S_{\text{BET}} = 170 \text{ m}^2/\text{g}$, TiO₂ (anatase) powder with $S_{\text{BET}} = 243 \text{ m}^2/\text{g}$ and TiO₂ (anatase) powder calcinated at 500 °C with $S_{\text{BET}} = 74 \text{ m}^2/\text{g}$. Despite the much larger surface of Sibunit carbon material, its performance as carrier material was inferior to the other tested carrier materials [79]:



Larichev et al. (2010) reported higher activity of Rh on TiO₂ than on Al₂O₃ using the impregnation method [80].

Bennici et al. (2011) investigated Co particles dispersed on two different carrier materials by impregnation. As support materials they synthesised K₃PW₁₂O₄₀ and Cs₃PW₁₂O₄₀ by sol-gel method. They compared the results obtained with a very active commercial catalyst (Pt/C) from Etek [87]:



Crisafulli et al. (2011) investigated the effect of the carrier material using Ru as noble metal. Used carrier materials were activated carbon, CeO₂, TiO₂ and γ -Al₂O₃. Ru was applied to the carrier by impregnation [82].



Effect of pressure on catalytic activity

Kojima et al. (2004) found that increased pressure (0.6 MPa) has a positive effect of the catalyst activity. In their experiments they used Pt/LiCoO₂ and Pt/TiO₂ catalysts, synthesised with impregnation method.

Influence of the preparation method

As is well known, that the activity of a catalyst strongly depends on the way it is synthesised. This was shown by Kojima et al. (2002), who prepared Pt/TiO₂ catalysts in two different ways, i.e. supercritical CO₂ method and impregnation method. The catalyst prepared by the supercritical CO₂ method showed superior activity compared to the catalyst prepared by impregnation [69]. Additionally, it was observed that the order of activity changes comparing Kojima et al. (2002) (supercritical CO₂ method) and Demirci and Garin (2008) (impregnation). In experiments carried out by Kojima et al. (2002) Pt showed the highest activity, whereas in the experiments carried out by Demirci and Garin (2008) Ru showed the highest activity.

Patel et al. (2010) synthesised a Co-P-B catalyst on Ni-foam by electroless deposition and on glass substrates by pulsed laser deposition. The two methods yielded similar results.

Catalyst overview conclusion

As was shown, there are not only many possible catalyst compounds and carrier materials, but there are also many ways to synthesis a catalyst. The synthesis method has a great influence on the catalysts activity. However, no literature about a sputtered catalyst for NaBH₄ hydrolysis was found. In the following the catalytic activity of the found catalyst is summarised:

- Pt \gg Rh > Ru \sim Pd > Ni \sim Fe, all with TiO₂ support (super critical method) Kojima (2002) [69]
- LiCoO₂ > LiNiO₂ \gg Ti₂O₃ > CoO \sim TiO \sim LiMn₂O₄ > NiO \sim SiO₂ \sim TiO₂ > Co₃O₄ (Kojima 2002) [69]
- Rh > Ru \approx Pt \gg Pd, all with Al₂O₃, TiO₂ and Sibunit support, Simagina (2008) [79]

- Ru \approx Ru₂Pt > RuPt \approx RuPt₂ > RuPd > RuAg \approx Pt > RuCu > PtAg, all supported with TiO₂; Ru₂Pt/TiO₂ is in the range of the highest values reported so far in the literature, Demirci (2008) [74]
- Rh/TiO₂ > Rh/ γ -Al₂O₃ Larichev (2010) [80]
- Ru/activated carbon \gg Ru/CeO₂ > Ru/TiO₂ > Ru/ γ -Al₂O₃, Crisafulli (2011) [82]

Since not every possible catalyst can be deposited by sputtering, in the following a list of sputterable catalysts with metal content is given followed by a list of sputterable oxide catalysts [69, 74, 79, 80, 82, 85, 220]:

Sputterable catalysts (metallic):

Rh	Ru ₂ Pt/TiO ₂	Pt/TiO ₂	Co
Rh/TiO ₂	RuPt/TiO ₂	Pt/ γ -Al ₂ O ₃	Co/Al ₂ O ₃
Rh/ γ -Al ₂ O ₃	RuPt ₂ /TiO ₂	Pt/LiCoO ₂	CoB
Ru	RuPd/TiO ₂	Pt/CoO	CoB/Ni
Ru/TiO ₂	RuAg/TiO ₂	Pd	CoB/PdNi
Ru/ γ -Al ₂ O ₃	RuCu/TiO ₂	Ni	CoWB/Ni
Ru/CeO ₂	Pt	NiB	

Sputterable catalysts (oxides):

Co ₃ O ₄	LiMn ₂ O ₄	LiNiO ₂
TiO ₂	TiO	LiCoO ₂
SiO ₂	CoO	
NiO	Ti ₂ O ₃	

6.1.3. Catalyst choice

Whereas the focus of research lied on noble metals such as Pt, Rh and Ru until the year 2010, it shifted more towards Co-B based catalysts in the more recent years to replace noble metals [223]. However, at the beginning of this thesis Rh, Pt and Ru seemed to be the most promising candidates to catalyse the NaBH₄ hydrolytic reaction. Since for sputtering a metal plate (target) of 2 inch diameter and at least 1 mm thickness was necessary, the costs of such a noble metal plate had also to be taken into account. Eventually, Pt and Ru were chosen, even though Rh also looked promising. As sputterable support materials TiO₂ and Al₂O₃ were found most common in literature and since TiO₂ always performed better than Al₂O₃, TiO₂ was chosen as a possible support material. In this work catalyst experiments started with platinum and later went on with ruthenium.

The next section will deal with the experimental setup to characterise the catalysts applied to the surface of hollow glass microspheres by magnetron sputtering.

6.2. Experimental setup for catalyst characterisation

The experimental setup can be divided in two main parts: the reaction chamber unit, where the chemical reaction takes place, and a gas volume measurement unit to measure the amount of released hydrogen. The reaction unit consisted of a three-necked flask, with one port used for a thermocouple for reaction temperature measurement, one port connected to a dropping funnel that was used to inject the water into the reaction chamber and one port connected to the gas volume measurement unit (see Figure 6.1).

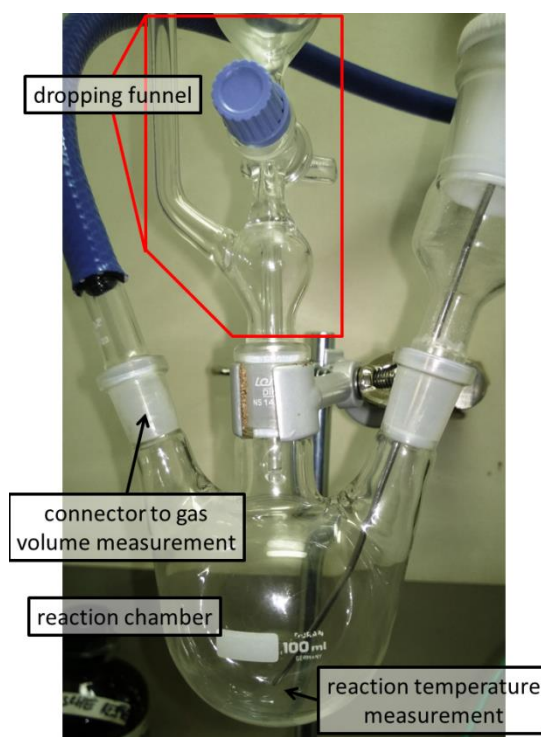


Figure 6.1: Reaction chamber for catalyst experiments, consisting of a three-necked flask connected to the hydrogen outlet, a dropping funnel for water injection and a thermocouple for reaction temperature measurement

The hydrogen gas volume measurement unit consisted of two dropping funnels with each a volume of ~1300 ml (scale 1000 ml), a beaker with a volume of 3000 ml and a balance (*Kern PCB 6000* $g \pm 1$ g; see Figure 6.2). Before each test the air was sucked out of the system with an aspirator so that the water inside the beaker was sucked into the dropping funnels until they

were full, the pressure difference between inside and outside the system being the driving force. When hydrogen is released in the reaction chamber, its volume can be determined by measuring the mass of water in the beaker on the balance. In preliminary experiments only one dropping funnel with a volume of 500 ml was used, which is why only one hose was needed (compare Figure 6.1 and Figure 6.2). Data acquisition was done with a self-written LabVIEW program, a NI-data acquisition system for the thermocouple and a RS232 interface for the balance.

One goal was to investigate the time dependent thermal behaviour of the hybrid hydrolytic system in order to check the whole hydrogen storage concept including hollow glass microspheres. The main question was how fast the temperature would rise when the water was injected. Therefore, no water bath was used nor a pH measurement unit due to its high thermal mass.

Additionally to the reaction temperature measurement the ambient temperature was measured with another thermocouple in order to calculate the temperature difference caused by the hydrolytic reaction.

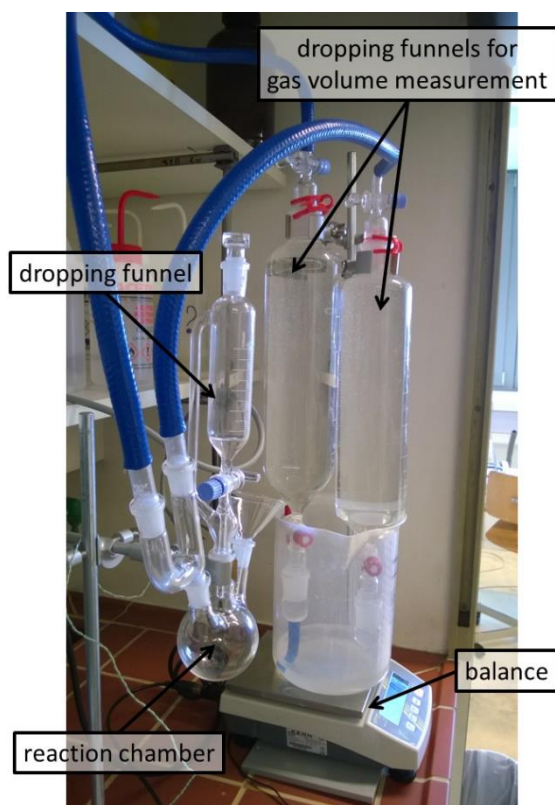


Figure 6.2: Experimental setup for catalyst activity characterisation, with reaction chamber connected to the gas volume measurement section, consisting of two dropping funnels, a beaker and a balance

6.2.1. Experimental procedure

The experimental procedure worked as follows:

- The large dropping funnels for measurement of released gas volume were filled with water by an aspirator.
- The small dropping funnel was filled with 4 ml of water with a pipette, to be injected into the reaction chamber.
- This was followed by a 60 minutes leakage test, to be sure that no air enters the system, which would cause a higher measured gas volume.
- 0.81 g of NaBH₄ (*Venpure™ SF powder, Rohm and Haas*) and 0.81 g of catalyst coated hollow glass microspheres were weighed in with a balance (*Sartorius 110 g ± 0.1 mg*).
- The compounds were mixed in a flask and put into the reaction chamber with a funnel via the thermocouple port (see Figure 6.2 between dropping funnels)
- The thermocouple was re-attached to the three-necked flask.
- After that a 60 minutes leakage test of the whole system was carried out.
- 4 ml of water are injected into the reaction chamber to start the hydrolytic reaction.
- Temperature and displaced water mass were measured for 60 minutes.

6.2.2. Error source analysis

In the following possible error sources of the catalyst characterisation in general and of the hydrogen yield in special will be described and evaluated.

Amount of NaBH₄

The amount of used NaBH₄ in each test varies within the accuracy of the balance that was used (*Sartorius, 110 g, ± 0.1 mg*). A measured error of ± 4 mg was found to be acceptable. This results in an error of ± 0.5 % in released hydrogen and liberated heat due to the hydrolytic reaction.

Amount of hollow glass microspheres

The amount of hollow glass microspheres (0.81 g) was measured the same way as the amount of NaBH₄. However, ± 0.25 % more or less catalytic material does not have a measurable effect on hydrogen yield.

Atmospheric pressure

The atmospheric pressure has no influence on the water level inside the dropping funnels, since the water is held by the pressure difference, which is independent of ambient pressure.

Room temperature

Another possible error could occur due to varying ambient temperatures. This changes the water density and thus the water volume to mass ratio. Furthermore, it changes the density of released hydrogen. Temperature changes of 5 K result in a water density change of 0.1 % and a hydrogen density change of 1.7 %. Thus the total error due to ambient temperature is 1.8 %.

Remaining NaBH₄ in mixing flask or funnel

Due to humidity some of the hollow glass microspheres and NaBH₄ can remain in the flask or the funnel, which is used to put the sphere-hydride mixture into the reaction chamber. Unfortunately this remaining powder could not be quantified due to the very small amount – barely visible with the naked eye. A maximum loss of 0.01 g was estimated, which is why 0.81 g was always weighed in, resulting in 0.8 – 0.81 g of NaBH₄ inside the reaction chamber. The estimated error is 1.2 %.

Air humidity

It was important to operate in air-conditioned rooms, especially in summer when air humidity is much higher. Operating in unconditioned rooms caused the NaBH₄ to adsorb air humidity, which made it useless for further testing. To further prevent air humidity to influence the quality of NaBH₄, the container was kept closed at all time, except when retrieving some NaBH₄. Retrieving and mixing was always done as the last step of each experiment preparation. As a result no tested mixture was exposed to atmosphere longer than 70 minutes before the reaction was initiated. This includes 60 minutes leakage test inside the reaction chamber.

Systematic overestimation: pressure difference and water displacement

As the water displacement method to measure the amount of released hydrogen uses a pressure difference between the inside of the apparatus and the ambient, this pressure difference also influences the result of the measurement. At lower pressure a certain mass of hydrogen takes up more volume. A 60 cm water column in the dropping funnels yields a pressure difference of 5868 Pa, which results in an overestimation of 5.9 % at the beginning of the experiment. However, when hydrogen is released, water is replaced by hydrogen, thus the height of water column decreases and with that the deviation decreases. The deviation decreases to 0 when the water in the dropping funnels and the beaker reach the same level.

Furthermore, it has to be taken into account that water is also displaced by the nozzle and connecting pieces of the dropping funnels which extend into the beaker, as the water level in the beaker rises. At the same water level in the beaker and the dropping funnels, the dropping funnels displace 132 ml of water (glass displaced water). In order to calculate the overestimation, the amount of glass displaced water has to be compared with hydrogen displaced water. The maximum amount of hydrogen that can be released (0.81 g NaBH₄, 21 °C, 0.1 MPa) is 2094 ml. As a result at the beginning of the measurement there is no overestimation due to glass displaced water. The overestimation increases to 6.3 % when water levels in the beaker and the dropping funnel reach the same height.

A linear approximation of both described overestimations is shown in Figure 6.3, including the total overestimation. These overestimations had to be taken into account in data analysis.

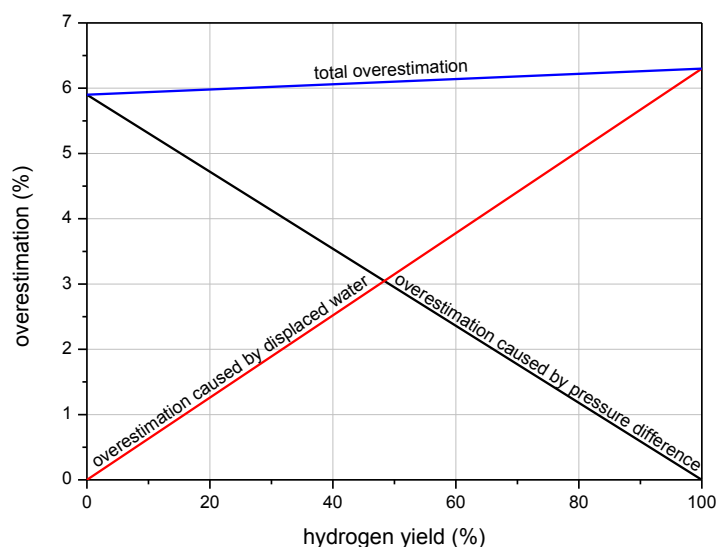


Figure 6.3: Overestimation of hydrogen yield as a function of hydrogen yield

Conclusion regarding error sources

Most of the possible errors are too small to be of any significance or can be corrected by adjustments. However, residual NaBH₄ in flasks and funnels in the course of mixing the powders and loading the reaction chamber had to be taken into account (1.2 %), as well as the influence of the room temperature (1.8 %). This gives a total error of 3.0 %.

The overestimation of hydrogen yield of 5.9 - 6.3 % due to pressure difference and glass displaced water were also taken into account.

6.3. Sample preparation

This section describes the sample preparation, starting from 3M™ S38 hollow glass microspheres as delivered. These steps include washing of the spheres, sieving the spheres and coating the spheres. After tests the experiments were often repeated, therefore the spheres had to be washed again and also treated with acid. Not all of these steps were carried out every time. Furthermore, in the course of the work procedures often changed, i.e. pre-treatment of the spheres, sputter conditions, sputter geometry and post-treatment of the spheres for repeating the catalytic experiment.

6.3.1. Pre-treatment of hollow glass microspheres

Washing

As already mentioned before, broken spheres and shards sink down whereas whole spheres float on the surface of water. Thus to separate spheres and shards they had to be washed. The washing was carried out in a separating funnel by adding distilled water to the spheres and shaking the mixture. After sedimentation of the broken particles at the bottom of the funnel they were purged and the procedure was carried out again. This was done three times. After that the spheres floating at the surface were put into a filtration funnel with filtration paper connected to a suction piston and dried. In the following sample preparation tables the spheres with such a treatment will be declared as “washed”.

Sieving

As was already explained in section 4.3, in order to improve trickling behaviour during the coating process, the spheres were sieved with a 50 µm mesh size sieve. In the course of the experiments the coating procedure was improved so every batch of spheres could be coated. Furthermore, it was found that sieving the needed amount of spheres takes a very long time. As a result sieving was replaced by washing the spheres, to get rid of glass shards.

Still, after washing the spheres they were sieved with a 100 µm sieve to make sure that no lumps remain in the glass sphere powder (spheres are smaller than 100 µm).

Other treatments

In order to investigate the effect of silicic acid on catalysis, which had been added by the manufacturer as anti-caking agent, it was tried to remove the silicic acid from the spheres. This was done by cooking the spheres in distilled water. A significant amount of silicic acid could be removed, although not all. It is likely that washing the spheres in an ammonia or NaOH solution would be a better way to remove the silicic acid. This remains to be investigated.

6.3.2. Catalyst-coating of hollow glass microspheres

After pre-treatment hollow glass microspheres were put into the coating vessel, described in section 4.3. The amount of spheres varied, i.e. 20 or 30 ml, depending on the sputter geometry and used coating vessel.

Sputter geometries

Coatings were first carried out with the sputter sources arranged on opposite ends of the vacuum chamber. The position of the coating vessel could be changed, but only one material could be deposited at a time, either with the 4 inch (10 cm) target or the 2 inch target (see Figure 6.4 a). The 4 inch target was used for Ti and TiO₂ coatings, whereas noble metals were always deposited with the 2 inch, i.e. Pt and Ru.

As was already mentioned before, the coating mechanism was scaled up in the course of the work of Andreas Eder. Therefore the geometry changed. Now there was only one coating vessel positioned in the middle of the vacuum chamber with the sputter sources tilted towards it (see Figure 6.4 b). In that configuration coating vessels of different sizes could be used. For applying catalytic coatings another, larger coating vessel was constructed that could easily hold 30 ml of powder.

All catalytic coatings for preliminary experiments to find a proper catalyst were deposited in the first configuration. When promising candidates had been identified, larger samples became necessary for rigorous testing. In this case the second configuration was used.

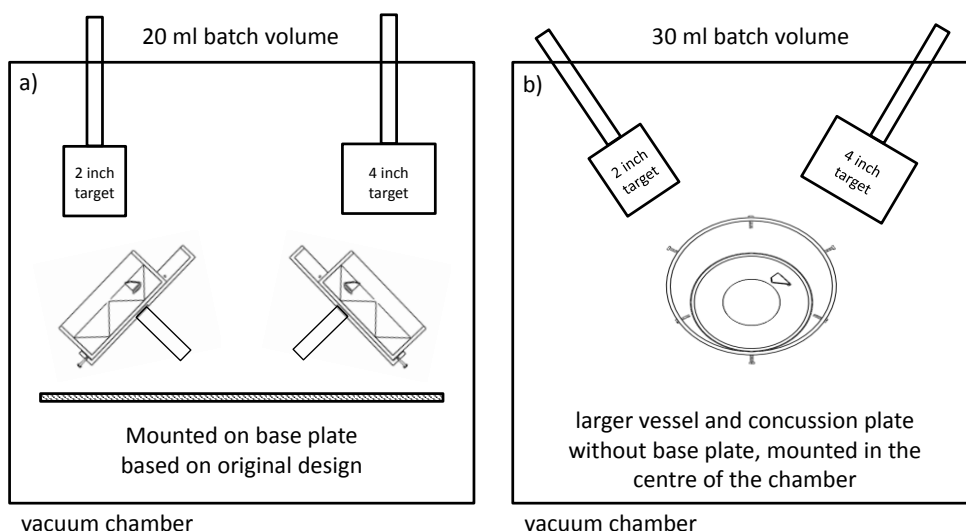


Figure 6.4: Different sputter geometries: a) the coating vessel (20 ml filling volume) can be positioned either beneath the 4 inch target (Ti, TiO₂) or beneath the 2 inch target (noble metal), the coating vessel is mounted on a rotatable base plate. b) a larger coating vessel is positioned in the centre with the sputter sources a tilted towards it (20 or 30 ml filling volume)

Sputter conditions

Table 6.1 shows some examples of deposited films on hollow glass microspheres that were tested for their catalytic activity and their deposition conditions. The chamber configuration refers to the old or new geometry (see Figure 6.4) and the batch volume to the amount of spheres in the coating vessel. The film thickness was measured optically (see section 4.3.6) and calculated (see section 4.3.7 and appendix 9.5). Some samples were annealed at 300 °C. Noble metal deposition was usually carried out at 200 W DC and 0.5 Pa Ar pressure with a 2 inch source. Titanium oxides were usually deposited at 200 or 400 W, 5 kHz, 4 μ s and 0.5 or 1.5 Pa Ar pressure with additional 0.01-0.033 Pa O₂ with a 10 cm or 4 inch source.

To list every deposited film would go beyond the scope of this section.

film & film thickness	batch volume & chamber configuration	sputter conditions
Pt, ~ 1.5 nm	20 ml sieved 50 μ m old	5 min, 200 W DC, 0.5 Pa Ar
Pt, ~ 4.5 nm	20 ml sieved 50 μ m old	15 min, 200 W DC, 0.5 Pa Ar
Pt, ~ 1.5 nm, 300 °C	20 ml sieved 50 μ m old	5 min, 200 W DC, 0.5 Pa Ar, annealed 300 °C
TiO ₂ , ~ 3.5 nm	20 ml sieved 50 μ m old	60 min, 400 W 5 kHz 4 μ s, 1.5 Pa Ar + 0.033 Pa O ₂
TiO ₂ , ~ 3.5 nm Pt, ~ 1.5 nm	20 ml sieved 50 μ m old	60 min, 400 W 5 kHz 4 μ s, 1.5 Pa Ar + 0.033 Pa O ₂ ; 5 min, 200 W DC, 0.5 Pa Ar
Ru, ~ 3.5 nm	20 ml sieved 50 μ m old	5 min, 200 W DC, 0.5 Pa Ar
TiO ₂ , ~ 1.1 nm TiO _x , ~1.3 nm Ti, ~ 1.6 nm Ru, ~ 3.5 nm	20 ml sieved 50 μ m old	20 min, 400 W 5 kHz 4 μ s, 1.5 Pa Ar + 0.033 Pa O ₂ ; 20 min, 400 W 5 kHz 4 μ s, 1.5 Pa Ar + 0.01 Pa O ₂ ; 20 min, 400 W 5 kHz 4 μ s, 1.5 Pa Ar; 15 min, 200 W DC, 0.5 Pa Ar
TiO ₂ , ~ 0.3 nm TiO _x , ~0.4 nm Ti, ~ 0.6 nm Pt, ~ 0.27 nm	20 ml washed new	20 min, 400 W 5 kHz 4 μ s, 1.5 Pa Ar + 0.033 Pa O ₂ ; 20 min, 400 W 5 kHz 4 μ s, 1.5 Pa Ar + 0.01 Pa O ₂ ; 20 min, 400 W 5 kHz 4 μ s, 1.5 Pa Ar; 15 min, 200 W DC, 0.5 Pa Ar
TiO ₂ , ~ 0.15 nm TiO _x , ~ 0.2 nm Ti, ~ 0.3 nm Ru, ~ 0.42 nm	30 ml, washed new	30 min, 200 W 5 kHz 4 μ s, 1.5 Pa Ar + 0.033 Pa O ₂ ; 30 min, 200 W 5 kHz 4 μ s, 1.5 Pa Ar + 0.01 Pa O ₂ ; 30 min, 200 W 5 kHz 4 μ s, 1.5 Pa Ar; 30 min, 200 W DC, 0.5 Pa Ar

Table 6.1: Examples of deposited films on hollow glass microspheres for catalysis tests

6.3.3. Evaluation method

As described in section 6.2, reaction temperature, ambient temperature and hydrogen yield are measured. Figure 6.5 shows the measured data of two typical experiments, i.e. blank spheres and Pt coated spheres. The graph shows the temperature difference in the reaction chamber and the hydrogen yield as a function of time. Measurement time was 1 hour, but the value of the hydrogen yield was always taken at 3500 seconds. Maximum temperature difference was also determined. The theoretical maximum of hydrogen yield and temperature difference were calculated and are also given in the graphic, i.e. with given amount of 0.81 g NaBH_4 : $2,094 \pm 73$ ml of hydrogen (at 21 °C, 0.1 MPa) and $\Delta T_{max} = 84$ K. For estimating the theoretical maximum of the temperature difference only the mass and specific heat of the three-necked flask were taken into account. Other losses like radiation and convection were neglected.

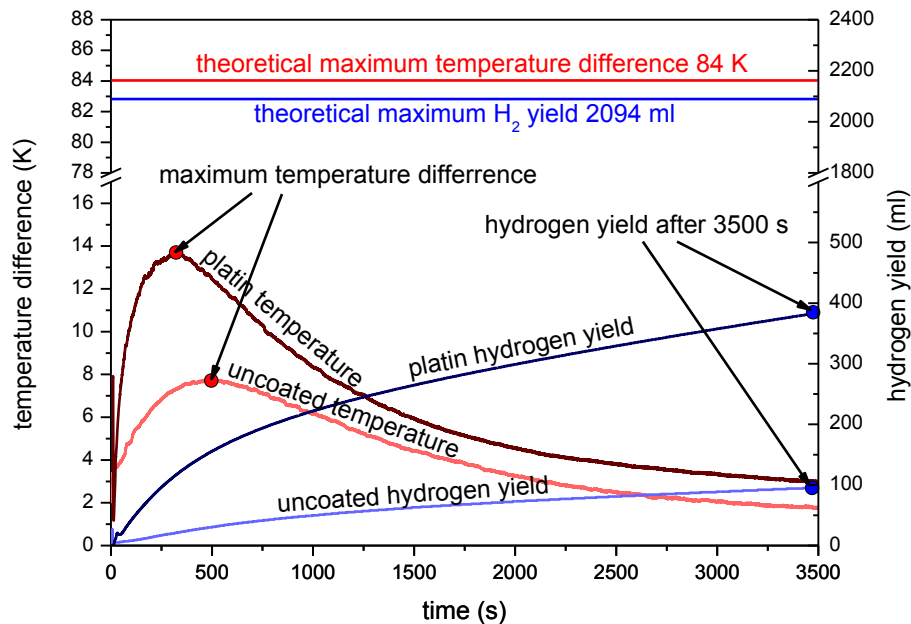


Figure 6.5: Typical characteristic of measured data, temperature evolution and hydrogen yield as a function of time; red dots indicate the maximum temperature, blue dots the measured hydrogen volume that was used for comparisons; theoretical maxima of temperature difference and hydrogen yield are also given

For evaluation the measured maximum temperature and the hydrogen yield at 3500 s were taken. The amount of every batch of coated spheres was enough to carry out at least 3 experiments, although most coatings were tested more often than 3 times.

As can be seen in Figure 6.5, hydrogen is released even when using uncoated spheres. This is because of the self-hydrolysis of NaBH_4 with water as was already mentioned at the beginning

of section 6.1. After 3500 seconds about 5 % of hydrogen were released, which is in good agreement with reported maximum self-hydrolysis of 7-8 % [71].

6.4. Results and discussion

As was already mentioned above the sample preparation often changed in the course of this work. This was mainly due to developing more accurate methods, e.g. pre-treatment, deposition process and catalyst tests. As an example, at the beginning of this work the spheres were coated without any pre-treatment, later that procedure changed to sieving before coating, and in the end spheres were washed and sieved (see section 6.3.1). Additionally, also the coating method changed as it was further developed. Furthermore, arising problems such as film adhesion had to be addressed. As a result, it sometimes became difficult to compare results with each other. In this chapter the effects of different synthesised films will be described, i.e. film thickness, support material, annealing and type of noble metal. The main focus, however, will be on film adhesion and catalyst re-activation, since it became clear that those were the big challenges. The following analysis will first focus only on hydrogen yield rather than maximum temperature, since temperature and hydrogen yield correlate with each other. Hydrogen yield will be given in percent of the theoretical maximum. Later on, also the temperature behaviour will be discussed.

6.4.1. Effect of film thickness - platinum

Hollow glass microspheres were coated with platinum with varying the deposition time between 5 to 20 minutes, which resulted in different film thicknesses. Figure 6.6 shows the hydrogen yield as a function of the film thickness. Apparently hydrogen yield increases with Pt film thickness up to ~ 4.5 nm film thickness, but then drops rapidly at higher film thicknesses.

This can be explained by the film growth mechanism and the size of Pt clusters. As Pt atoms adsorb at the glass surface they start to form clusters. First the number and size of clusters increases, which yields a larger catalytically active surface. As the size of the clusters reaches a certain diameter, the clusters start to coalesce; this dramatically decreases the catalytically active surface. Agustsson et al. (2008) investigated island growth of platinum coatings on amorphous SiO₂ substrates, deposited by DC magnetron sputtering at only 0.05 Pa Ar pressure and 20 W power. They found that coalescence starts between 1.1 nm and 3.3 nm and a continuous film is formed between 2.9 nm and 7.5 nm depending on substrate temperature (RT-400 °C) [224]. This is in good agreement with the explanation above.

This effect was not studied more thoroughly as another catalytic material looked more promising. Furthermore, attempts to analyse the coatings with transmission electron microscopy

failed for now due to the fragile spherical substrate shape. Still it can be concluded that the film thickness, or rather cluster size, has a significant effect on the catalytic activity. Nevertheless, it became clear that pure platinum is not the material of choice, since only hydrogen yields of slightly above 20 % could be achieved.

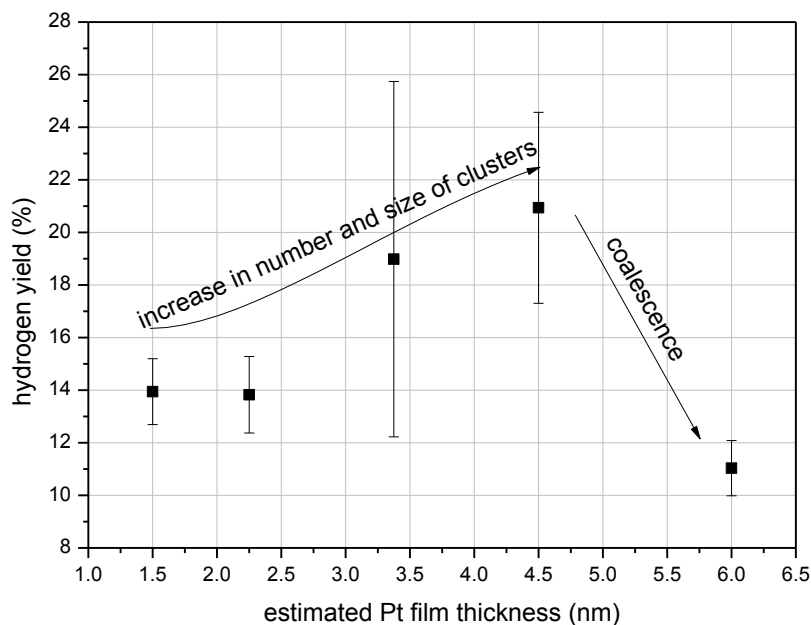


Figure 6.6: Effect of film thickness on hydrogen yield; spheres were coated with platinum

6.4.2. Platinum modifications & ruthenium

Hollow glass microspheres were not only coated with platinum, but also with pure TiO₂, with platinum and TiO₂ as support and ruthenium. Additionally platinum coated spheres were annealed at 300 °C. Figure 6.7 shows a summary of the acquired results. It was found that a pure 3.5 nm TiO₂ coating also has a catalytic effect, however smaller than pure Pt coatings. This is in agreement with literature (see section 6.1.2). A 1.5 nm Pt film supported by 3.5 nm TiO₂ film has a higher catalytic activity than a pure Pt film. Heat treatment of the Pt coating has an even higher impact on the activity. However, compared to Ru all tested variations containing Pt have a much lower catalytic activity. With ruthenium coated spheres a 97 % hydrogen yield was reached. Order of catalytic activity was found to be as follows:

$$\text{Ru (3.5nm)} \gg \text{Pt (4.5nm)} > \text{Pt (1.5nm, 300°C)} > \text{Pt/TiO}_2 \text{ (1.5nm/3.5nm)} > \text{Pt (1.5nm)} > \text{TiO}_2 \text{ (3.5nm)}$$

Since now a most promising catalyst was found, the focus now was on its reusability. Although ruthenium by far showed the best performance, one issue already became apparent at

the first test. The ruthenium film was completely washed off the spheres in the course of the reaction, which of course undermined its reusability. Adhesion interlayers had to be applied. The next two sections will deal with film adhesion of catalytic coatings and the reusability of the catalyst.

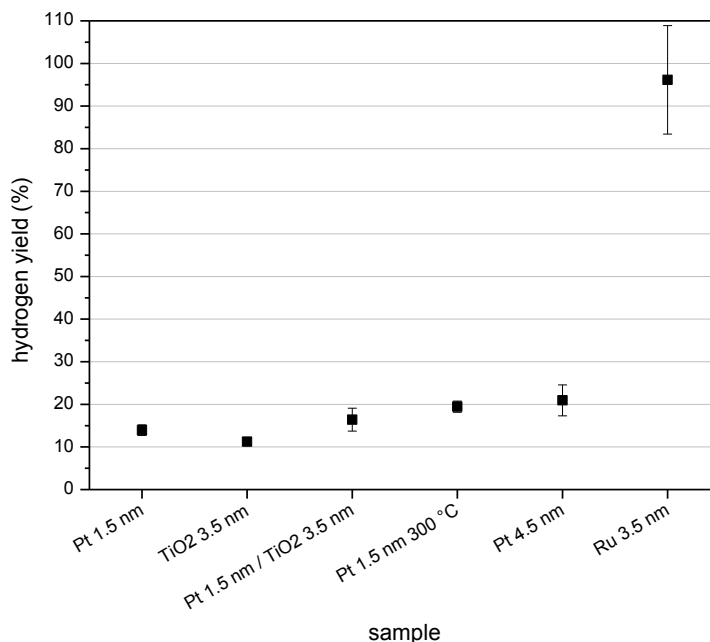


Figure 6.7: Overview of differently prepared samples; ruthenium has by far the highest activity

6.4.3. Film adhesion

The bad adhesion of Ru films was already observed when coating plane glass substrates for rate determination. The Ru films started to pop off immediately after retrieving them from the vacuum chamber.

Whereas the washing off of the Ru film of the spheres was observable with the naked eye, a similar but not as pronounced behaviour was observed with Pt coated spheres. This is shown in Figure 6.8, where images of Pt coated spheres were taken before and after the catalyst test with the back-scattered electron detector of a scanning electron microscope. After repeating the catalyst experiment 2 times it was clearly visible that Pt films are also partly peeled off (indicated by red arrows). It has to be mentioned that the maximum temperature during the catalyst test only reached about 40 °C when using Pt coated spheres, whereas it reached around 90 °C when using Ru coated spheres. Thus Pt coatings might also be washed off completely at higher temperatures.

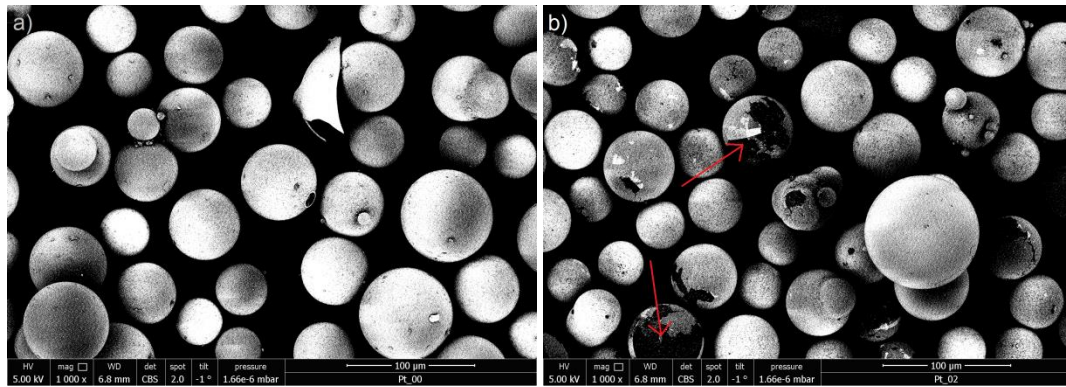


Figure 6.8: Pt coated spheres before and after catalytic experiment, images taken with the back-scattered electron detector; a) films are uniform without defects, b) after 2 uses of the spheres the films are partly peeled off

To overcome the issue of film adhesion, adhesion interlayers were deposited on the spheres before applying the catalyst. Several different interlayer configurations were tried, including Ti-Ru, TiO₂-Ru, reactive sputtered Ru+O₂, a multi-layer coating of TiO₂/TiO/Ti-Ru and TiO₂/TiO₂-Ru-co-sputtered. It was found that the latter two work best, whereas the former three configurations either were washed off again (Ti-Ru, Ru+O₂) or had a decreased catalytic activity (TiO₂-Ru). Table 6.2 gives more detailed information on film preparation parameters.

Figure 6.9 shows a comparison of the differently prepared catalytic coatings with adhesion interlayers. There were two layers that had good adhesion and good catalytic performance, i.e. a multi-layer coating of TiO₂, TiO, Ti and Ru, and a co-sputtered film where first a TiO₂ film was deposited before applying TiO₂ and Ru together at the same time.

film & film thickness	batch volume & chamber configuration	sputter conditions
Ti, ~ 0.4 nm Ru, ~ 0.2 nm	20 ml, washed new	20 min, 400 W DC, 0.5 Pa Ar 15 min, 200 W DC, 0.5 Pa Ar
TiO ₂ , ~ 0.2 nm Ru, ~ 0.2 nm	20 ml washed new	20 min, 400 W 5 kHz 4 µs, 1.5 Pa Ar + 0.033 Pa O ₂ ; 15 min, 200 W DC, 0.5 Pa Ar
RuO _x , ~ 0.25 nm	20 ml washed new	15 min, 200 W DC, 0.5 Pa Ar + 0.033 Pa O ₂
TiO ₂ , ~ 0.15 nm co-(TiO ₂ & Ru), ~ 0.55 nm	20 ml washed new	30 min, 200 W 5 kHz 4 µs, 0.5 Pa Ar + 0.033 Pa O ₂ ; 30 min, 200 W 5 kHz 4 µs & 200 W DC, 0.5 Pa Ar + 0.033 Pa O ₂
TiO ₂ , ~ 0.15 nm TiO _x , ~ 0.2 nm Ti, ~ 0.3 nm Ru, ~ 0.4 nm	30 ml, washed new	30 min, 200 W 5 kHz 4 µs, 1.5 Pa Ar + 0.033 Pa O ₂ ; 30 min, 200 W 5 kHz 4 µs, 1.5 Pa Ar + 0.01 Pa O ₂ ; 30 min, 200 W 5 kHz 4 µs, 1.5 Pa Ar; 30 min, 200 W DC, 0.5 Pa Ar

Table 6.2: Catalyst plus adhesion interlayer films, noble metal was always deposited with the 2 inch target, whereas the interlayer was always deposited with the 4 inch target

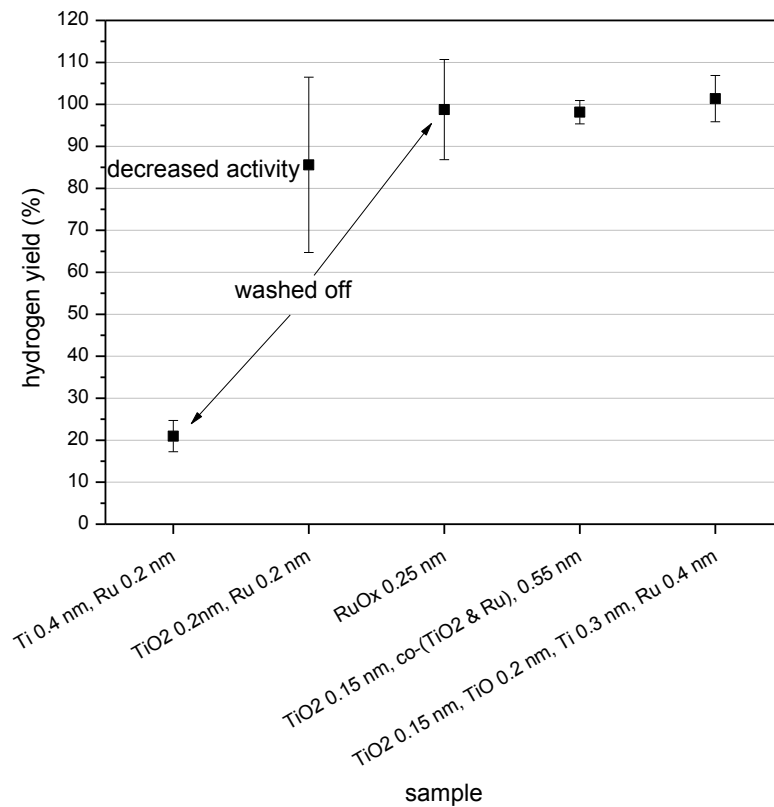


Figure 6.9: Comparison of hydrogen yield of differently prepared catalyst coating with adhesion interlayers

The film integrity of those two coatings was investigated with scanning electron microscopy, but no areas with delaminated films were found. However, the silicic acid particles were removed in course of the catalyst testing and left holes. This was also observed with platinum coated spheres and when washing TiO₂ coated spheres (compare Figure 5.21). Figure 6.10 shows the multi-layer films of TiO₂/TiO/Ti/Ru on a sphere before catalysis, after the first catalysis and after the second catalysis. As can be observed, the silicic acid particles are removed in course of the treatment (testing, washing) and leave holes in the coating. As will be shown in the next section, the catalytic performance decreases rapidly from the first test to the second and it was thought that the removal of the silicic acid particles is the reason for this decrease in catalytic activity. However, this is not the case, as will be shown in section 6.4.4.

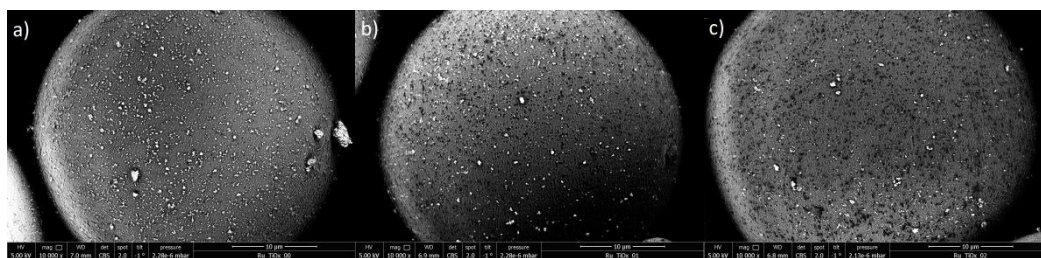


Figure 6.10: Multi-layer TiO₂/TiO/Ti/Ru films on a sphere before testing (a), after first use (b) and after second use (c). Silicic acid particles are removed in course of the treatment (testing, washing) and leave holes in the coating. Images were taken with back-scattered electron detector

6.4.4. Catalyst reusability and reactivation

A catalyst is of no use when it can only be used once. Unfortunately exactly that was the case. All catalysts presented so far yielded much less hydrogen when used a second time. Some examples of this behaviour are shown in Figure 6.11 illustrating the reusability of one Pt and two Ru based catalysts.

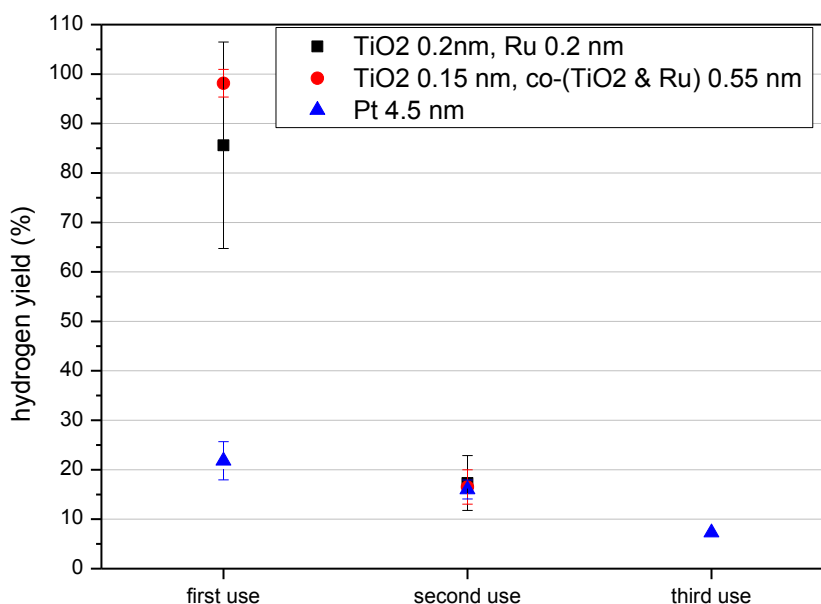


Figure 6.11: Reusability of catalysts; both Pt based and Ru based catalyst have a large decrease in performance once being used

Film adhesion and the decrease of silicic acid particles were thought to be the reason for that decrease in performance. However, since the issue of film adhesion was already solved, the impact of the silicic acid particles had to be investigated more thoroughly. Therefore, catalyst coated spheres were deliberately mistreated by cooking them in distilled water. By doing so,

most of the silicic acid particles could be removed. However, the catalytic tests showed no difference to un-mistreated spheres, thus the silicic acid particles could not be the reason for the dramatic decrease in catalytic performance after the first use.

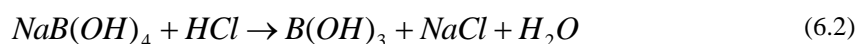
Since film adhesion and silicic acid particles could be excluded, it was thought that the active sites of the catalyst might be blocked by some chemical residuals that could not be removed by washing the spheres with distilled water. Hence, the spheres were additionally washed in diluted acetic acid, which resulted in an increase in their catalytic performance. As acetic acid is a very weak acid it was replaced by diluted hydrochloric acid, which worked even better. The whole recycling procedure worked as follows:

- After ending the experiment the spheres were mixed with 10 ml of distilled water
- Then 2 ml of 64-66 % hydrochloric acid were added
- After thoroughly mixing all was put into a filter adding more distilled water
- The spheres were purged with distilled water 2 more times
- Finally the spheres were dried and could be used for the next test

By using hydrochloric acid it was possible to completely reactivate the catalyst two times. However, it has to be mentioned that material was lost due to the recycling procedure of the spheres (washing, filtering, etc.), which is why the amount of spheres and thus of the number tests decreased from cycle to cycle. Figure 6.12 shows the final results of reusability of catalyst coated hollow glass microspheres. It can be seen that the catalyst could be reactivated completely two times. In the fourth tests a decrease in catalytic performance could be observed, but since both tests could only be carried out once there is no statistics (error bars include measurement accuracy). The decrease in the number of tests due to recycling losses is indicated in the figure.

The effect of acid treatment on uncoated spheres was also investigated. Acid treated uncoated spheres yielded a hydrogen release of 7 %, which is significantly more than untreated spheres of 5 %, but still not in the region of any tested catalyst.

The exact mechanism of acid treatment is not clear and remains to be investigated. However, it can be speculated that it is due to an acid-base reaction. NaBH_4 forms NaB(OH)_4 as one final product of the reaction. This sodium tetrahydroxyborate blocks the active sites of the catalyst. By applying hydrochloric acid the following reaction takes place and unblocks the active site.



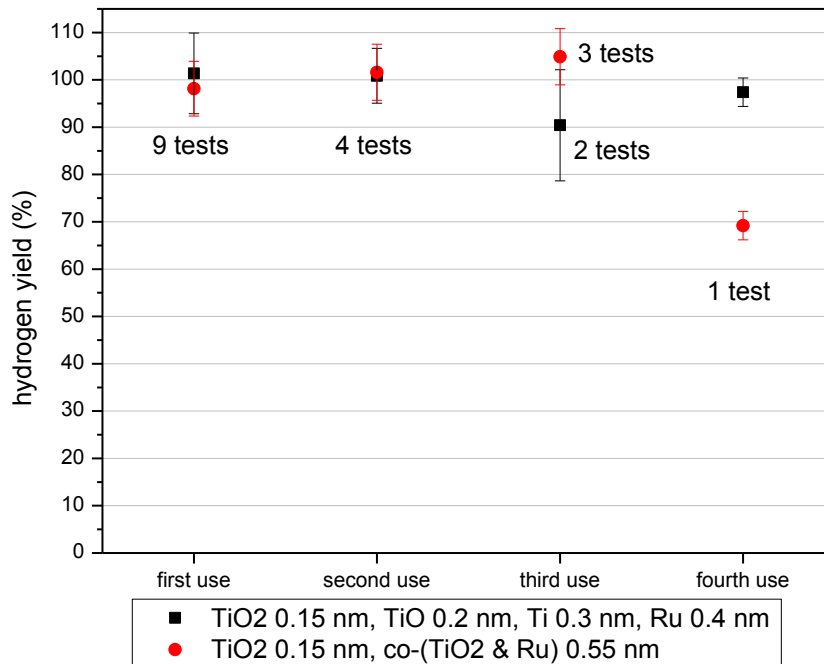


Figure 6.12: Reusability of catalysts after hydrochloric acid treatment; catalysts can be repeatedly reactivated

6.4.5. Temperature behaviour

An important parameter of the whole hydrogen storage system is how fast it reacts on hydrogen demand. A fast response also means that elevated temperatures must be achievable in a short time. Thus not only the reached maximum temperature has to be analysed, but also when this temperature occurs. For that samples of multilayer coated TiO₂/TiO/Ti-Ru and co-sputtered coated TiO₂/TiO₂-Ru spheres were analysed. Figure 6.13 shows an overview of reached maximum temperatures as a function of the time when they were reached for each use of the samples. It became apparent that co-sputtered films not only yield slightly higher temperatures, they also reach them faster than multilayer coatings. Especially the first use of multilayer coated spheres showed lower temperature differences than all other tests excluding the fourth use of the spheres. There is a clear trend that the more often the catalyst coated spheres are used, the longer it takes to reach the maximum temperature, to that extent that it takes nearly half an hour to reach the maximum temperature when using the spheres for the fourth time. Nevertheless, both coatings seem to bear the potential for a catalyst in the proposed hybrid hydrolytic hydrogen storage system.

Finally it has to be mentioned that at such elevated temperatures the reaction is also driven thermally and not only by the catalyst.

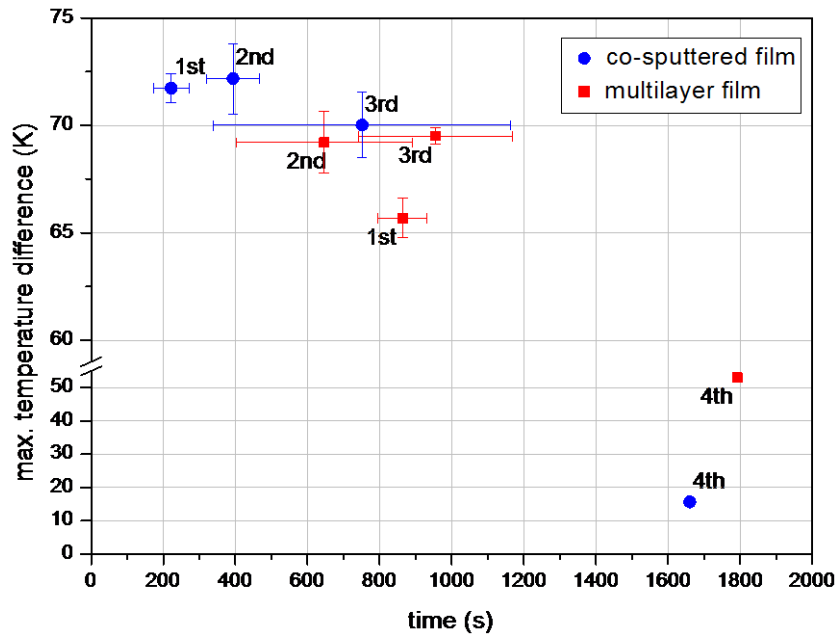


Figure 6.13: Comparison of max. temperature and time of max. temperature of multilayer and co-sputtered coatings, numbers indicate if sample is tested for the first, second, third or fourth time

6.5. Conclusion of catalyst characterisation

It can be concluded that Ru based catalysts applied on hollow glass microspheres by magnetron sputtering have a much higher catalytic activity than Pt based catalysts. It became clear that adhesion of the catalyst is an issue that, however, could be solved by applying adhesion interlayers, e.g. multilayer $\text{TiO}_2/\text{TiO}/\text{Ti}/\text{Ru}$ and co-sputtered $\text{TiO}_2/\text{co}-(\text{TiO}_2-\text{Ru})$. Another issue was the reusability of the catalyst, since all catalysts showed a large decrease in activity after the first use. This was solved by treating the spheres with hydrochloric acid after each experiment. By doing so it was possible to reactivate the catalyst two times. Both developed coatings seem to bear the potential for a catalyst in the proposed hybrid hydrolytic hydrogen storage system, since both repeatedly showed a hydrogen yield of nearly 100 %. However, since co-sputtered films showed a faster temperature increase, which would be necessary to release hydrogen stored inside the hollow glass microspheres, these films would be the catalyst of choice for first storage system tests with hydrogen loaded spheres.

7. Conclusion and outlook

In this work a hybrid concept to store hydrogen was proposed, consisting of catalyst sputter-coated hollow glass microspheres and sodium borohydride. The spheres can be loaded with hydrogen by applying heat and hydrogen pressure. Due to the elevated temperature of around 250 °C hydrogen diffuses through the glass wall into the spheres. After cooling down the hydrogen is trapped and can only be released by applying heat again. To do that, an exothermal hydrolytic reaction shall be used, i.e. sodium borohydride and water, which needs a catalyst to generate a sufficient amount of heat. The catalyst has to be applied to the spheres, so that spheres and catalyst can be recycled.

The main arguments for the use of a hybrid system rather than hollow glass microspheres alone were: first, the volumetric storage density can be drastically increased compared to hollow glass microspheres alone; second, the costs can be significantly reduced when compared with a stand-alone hydrolytic system. It became clear that the achievable gravimetric storage densities of $\gamma_{G,sys} = 8-20$ wt% are well within targets proposed by the U.S. Department of Energy (DOE) (see Table 7.1). Though it was also found that the volumetric storage densities of such a system of $\gamma_{V,sys} = 30-50$ kg/m³ are also within 2017 targets, they are below the ultimate targets. Thus, more efforts have to be made to further increase the volumetric storage density.

	DOE-2017	DOE-ultimate	hybrid system
γ_G (wt%)	5.5	7.5	8-20
γ_V (kg/m ³)	40.0	70.0	30-50

Table 7.1: Resulting hydrogen storage densities of the hybrid system compared with DOE targets [9]

Moreover, it was shown that the current costs of the proposed system are much too high and fall far short of the DOE-targets. The most cost intensive factor is sodium borohydride, thus making it the critical component. In order to reach acceptable costs the compound prices have to be cut dramatically, i.e. 98 % for sodium borohydride, 90 % for hollow glass microspheres and 70 % for hydrogen. This might be achieved with more efficient ways to recycle NaBO_2 , which is the end product of the hydrolytic reaction, an increase in renewable energy and an increased demand of hollow glass microspheres.

Remaining bodies of research regarding the overall concept are:

- permeability of glass, for a more controlled diffusion process
- realizing higher packing densities of hollow glass microspheres in a feasible way
- recycling of sodium borohydride to reduce costs
- costs of hydrogen
- costs of spheres

A main task of the work was to apply a working catalyst on the hollow glass microspheres. For that a coating system based on magnetron sputtering was developed, which made it possible to apply both, metal and oxide films, on hollow glass microspheres and other granular materials of different shapes and size distributions. This was achieved by using a tilted special shaped coating vessel in combination with a concussion mechanism, which enabled breaking apart powder clusters that form during the deposition process.

It was found that metal coatings promote the cluster formation much more than oxide coatings.

Trickling experiments of powders without magnetron sputtering showed that without the described concussion mechanism the powders become immobile in a couple of minutes, and thus cannot be coated. Only spheres sieved with a 50 μm mesh showed sufficient mobility, but none the less became immobile when they were coated. When using the concussion mechanism every batch of spheres stayed mobile, and thus could be coated uniformly. This was verified by the means of SEM, EDX and BSE analysis.

The described concussion mechanism and the coating vessel were up-scaled and further optimised by a colleague, so that now it is possible to coat one 1 dm^3 of material while particle ejection could be completely eliminated.

A direct comparison with other coating techniques, e.g. fluidised bed chemical vapour deposition or wet chemical methods, has not been carried out. However, a most welcome effect of the present apparatus is that coating parameters do not depend on substrate density like in fluidised bed reactors; depositions are completely independent of substrate material. As a result

any metal, metal-oxide or –nitride can be deployed on any powder as long as particles are not too small ($> 5 \mu\text{m}$) or are not suitable for vacuum.

Another goal was to apply anatase phase TiO_2 to the spheres as a catalyst support material. For that experiments of reactive pulsed DC magnetron sputtering were carried out. It was possible to deploy anatase films on plain glass substrates, which then was tried with hollow glass microspheres. However, it has to be concluded that anatase thin films could not be detected on hollow glass microspheres by X-ray diffraction. To yield anatase films higher film thicknesses might be required, which would result in much longer deposition times at the given geometry and deposition rate. Increasing the deposition rate by increasing sputter power or optimizing the deposition geometry, would be recommended in order to yield crystalline phase TiO_2 films on hollow glass microspheres. Nevertheless, TiO_2 films were used as adhesion interlayers for catalytic coatings.

The main goal of the work was to find a working catalytic coating that could be applied on hollow glass microspheres and has a good stability. For that Ru based and Pt based coatings were applied by magnetron sputtering and tested with respect to hydrogen yield and temperature increase. It can be concluded that Ru based catalysts applied on hollow glass microspheres have a much higher catalytic activity than Pt based catalysts. It became clear that adhesion of the catalyst is an issue that, however, could be solved by applying adhesion interlayers, e.g. multilayer $\text{TiO}_2/\text{TiO}/\text{Ti}/\text{Ru}$ and co-sputtered $\text{TiO}_2/\text{co}-(\text{TiO}_2\text{-Ru})$ systems. Another issue was the reusability of the catalyst, since all catalyst showed a large decrease in activity after the first use. This was solved by treating the spheres with hydrochloric acid after each experiment. By doing so it was possible to repeatedly reactivate the catalyst. Both developed coatings seem to bear the potential for a catalyst in the proposed hybrid hydrolytic hydrogen storage system, since both repeatedly showed a hydrogen yield of nearly 100 % of the theoretical value. Nevertheless, co-sputtered films would be the catalyst of choice for first storage system tests with hydrogen loaded spheres, since they showed a faster temperature increase, which would be necessary to release hydrogen stored inside the hollow glass microspheres.

Although a proper working catalyst was found, there are still subjects of investigation, including the effect of catalyst film thickness on hollow glass microspheres and the acid-based reactivation mechanism. The next major step would be tests of hydrogen loaded catalyst-coated hollow glass microspheres with a hydride in a low pressure reaction chamber to induce the diffusion process of hydrogen out of the spheres.

8. References

- [1] International Energy Agency, "IEA Statistics - CO2 Emissions from Fuel Combustion - Highlights," OECD/IEA, Paris, France, 2013.
- [2] U. Eberle, M. Felderhoff and F. Schüth, "Chemische und physikalische Lösungen für die Speicherung von Wasserstoff," *Angewandte Chemie* 121, pp. 6732-6757, 2009.
- [3] R. D. Lide, CRC Handbook of Chemistry and Physics, 88th Edition, Boca Raton, FL: CRC Press, 2007.
- [4] S. Sherif, D. Yogi Goswami, E. K. Stefanakos and A. Steinfeld, Handbook of Hydrogen Energy, Boca Raton, London, New York: CRC Press, Taylor & Francis Group, 2014.
- [5] D. Durbin and C. Malardier-Jugroot, "Review of hydrogen storage techniques for on board vehicle applications," *International Journal of Hydrogen Energy* 38, pp. 14595-14617, 2013.
- [6] L. Klebanoff, Hydrogen Storage Technology - Materials and Applications, Boca Raton, London, New York: CRC Press - Taylor & Francis Group, 2013.
- [7] P. Dodds, I. Staffell, A. Hawkes, F. Li, P. Grünewald, W. McDowall and P. Ekins, "Hydrogen and fuel cell technologies for heating: A review," *International Journal of Hydrogen Energy (article in press)*, 2015.
- [8] U.S. Department of Energy, "Comparison of Fuel Cell Technologies," Office of Energy Efficiency & Renewable Energy, 2015. [Online]. Available: <http://energy.gov/eere/fuelcells/comparison-fuel-cell-technologies>. [Accessed 26 January 2015].
- [9] U.S. Department of Energy, "Technical System Targets: Onboard Hydrogen Storage for Light-Duty Fuel Cell Vehicles," 6 June 2013. [Online]. Available: http://energy.gov/sites/prod/files/2014/03/f12/targets_onboard_hydro_storage.pdf. [Accessed 14 January 2015].
- [10] H. Chen, J. Zheng, P. Xu, L. Li, Y. Liu and H. Bie, "Study on real-gas equations of high pressure hydrogen," *International Journal of Hydrogen Energy* 35, pp. 3100-3104, 2010.
- [11] Toyota™, "Toyota - USA Newsroom; 2016 Mirai Product Information," 17 November 2014. [Online]. Available: <http://pressroom.toyota.com>. [Accessed 27 January 2015].
- [12] R. Ahluwalia, T. Hua, J.-K. Peng, S. Lasher, K. McKenney, J. Sinha and M. Gardiner,

- “Technical assessment of cryo-compressed hydrogen storage tank systems for automotive applications,” *International Journal of Hydrogen Energy* 35, pp. 4171-4184, 2010.
- [13] H. Langmi, J. Ren, B. North, M. Mathe and D. Bessarabov, “Hydrogen Storage in Metal-Organic Frameworks: A Review,” *Electrochimica Acta* 128, pp. 368-392, 2014.
- [14] G. Eklund and O. von Krusenstierna, “Storage and transport of merchant hydrogen,” *International Journal of Hydrogen Energy* 8, pp. 463-470, 1983.
- [15] K. Yan, B. Sellars, J. Lo, S. Johar and M. Murthy, “Storage of hydrogen by high pressure microencapsulation in glass,” *International Journal of Hydrogen Energy* 10, pp. 517-522, 1985.
- [16] B. Duret and A. Saudin, “Microspheres for on-board hydrogen storage,” *International Journal of Hydrogen Energy* 19, pp. 757-764, 1994.
- [17] D. Kohli, R. Khardekar, R. Singh and P. Gupta, “Glass micro-container based hydrogen storage scheme,” *International Journal of Hydrogen Energy* 33, pp. 417-422, 2008.
- [18] S. Dalai, S. Vijayalakshmi, P. Shrivastava, S. Sivam and P. Sharma, “Effect of Co loading on the hydrogen storage characteristics of hollow glass microspheres (HGMs),” *International Journal of Hydrogen Energy* 39, pp. 3304-3312, 2014.
- [19] S. Satyapal, J. Petrovic, C. Read, G. Thomas and G. Ordaz, “The U.S. Department of Energy’s National Hydrogen Storage Project: Progress towards meeting hydrogen-powered vehicle requirements,” *Catalysis Today* 120, p. 246–256, 2007.
- [20] T. Umegaki, J.-M. Yan, X.-B. Zhang, H. Shioyama, N. Kuriyama and Q. Xu, “Boron- and nitrogen-based chemical hydrogen storage materials,” *International Journal of Hydrogen Energy*, pp. 2303-2311, 2009.
- [21] H. Veluswamy, R. Kumar and P. Linga, “Hydrogen storage in clathrate hydrates: Current state of the art and future directions,” *Applied Energy* 122, pp. 112-132, 2014.
- [22] M. Keding and M. Tajmar, “Method and Installation for Storing and Releasing hydrogen”. International Patent WO2008019414 A2, EP2051931 A2, WO2008019414A3, 21 February 2008.
- [23] I. Bell, J. Wronski, S. Quoillin and V. Lemort, “Pure and Pseudo-pure Fluid Thermophysical Property Evaluation and the Open-Source Thermophysical Property Library CoolProp,” *Industrial & Engineering Chemistry Research*, pp. 2498-2508, 13 January 2014.
- [24] N. Bansal and R. Doremus, *Handbook of Glass Properties*, Orlando, FL: Academic Press, Inc., 1986.
- [25] 3M™, „Glass Bubbles: 3M Energy and Advanced Materials: 3M Europe,“ 2015. [Online]. Available: http://solutions.3m.com/wps/portal/3M/en_EU/EU-EAMD/Home/OurProducts/GlassBubbles/. [Zugriff am 5 January 2015].
- [26] K. Yan, X. Xie, B. Li, J. Yuan and J. Zhang, “Influence of the real density and structure imperfection of hollow glass microspheres on the compression strength,” *Materials Science and Engineering A528*, pp. 8671-8675, 2011.
- [27] R. Teitel, “Hydrogen supply method”. California, USA Patent United States Patent 4,211,537, 8 July 1980.
- [28] R. Teitel, “Containing a metal that absorbs hydrogen to form a hydride”. USA Patent United States Patent No 4,302,217 A, 24 Novembre 1981.
- [29] Linde Gas GmbH and E. Klein, Interviewees, *State of the Art of Hydrogen Compression*. [Interview]. 9 1 2015.
- [30] T. Halvordson and J. Shelby, “DOE Final Report: Controlled Permeation of Hydrogen Through Glass,” U.S. Department of Energy, Alfred, New York, USA, 1998.
- [31] A. Akunets, N. Basov, V. Bushuev, V. Dorgogotovtsev, A. Gromov, A. Isakov, V. Kovylnikov, Y. Merkulev, A. Nikitenko and S. Tolokonnikov, “Super-high-strength

- microballons for hydrogen storage,” *International Journal of Hydrogen Energy*, pp. 697-700, 1994.
- [32] J. Shelby, “FY 2008 Annual Progress Report of DOE Hydrogen Program: IV.D.5 Glass Microspheres for Hydrogen Storage,” U.S. Department of Energy, Alfred, New York, USA, 2008.
- [33] M. Herr and J. Lercher, “Hydrogen Storage in Microspheres - Final Report ESTEC,” European Space Agency, Noordwijk, Netherlands, 2003.
- [34] D. Rapp and J. Shelby, “Photo-induced hydrogen outgassing of glass,” *Journal of Non-Crystalline Solids* 349, pp. 254-259, 2004.
- [35] J. Shelby, M. Hall, M. Snyder and P. Wachtel, “A Radically New Method for Hydrogen Storage in Hollow Glass,” U.S. Department of Energy, Alfred, New York, USA, 2009.
- [36] R. Kitamura and L. Pilon, “Radiative heat transfer in enhanced hydrogen outgassing of glass,” *International Journal of Hydrogen Energy* 34, pp. 6690-6704, 2009.
- [37] S. Shetty and M. Hall, “Facile production of optically active hollow glass microspheres for photo-induced outgassing of stored hydrogen,” *International Journal of Hydrogen Energy* 36, pp. 9694-9701, 2011.
- [38] N. Kurita, N. Fukatsu, H. Otsuka and T. Ohashi, “Measurements of hydrogen permeation through fused silica and borosilicate glass by electrochemical pumping using oxide protonic conductor,” *Solid State Ionics* 146, pp. 101-111, 2002.
- [39] X. Qi, C. Gao, Z. Zhang, S. Chen, B. Li and S. Wei, “Production and characterization of hollow glass microspheres with high diffusivity for hydrogen storage,” *International Journal of Hydrogen Energy* 37, pp. 1518-1530, 2012.
- [40] S. Dalia, S. Vijayalakshmi, P. Sharma and K. Choo, “Magnesium and iron loaded hollow glass microspheres (HGMs) for hydrogen storage,” *International Journal of Hydrogen Energy* 39, pp. 16451-16458, 2014.
- [41] P. Ried, M. Gaber, R. Müller and J. Deubener, “Hydrogen permeability of a barium-aluminoborosilicate glass - A methodical approach,” *Journal of Non-Crystalline Solids* 394-395, pp. 43-49, 2014.
- [42] R. Zalosh and S. Bajpai, “Hydrogen microsphere hazard evaluation, in Proceedings of the DOE Thermal and Chemical Storage Annual Contractor’s Review Meeting,” U.S. Department of Energy, Tyson Corner, Virginia, USA, 1981.
- [43] W. Paul and R. Jones, “Production and separation of small glass spheres,” *British Journal of Applied Physics* 3, pp. 311-314, 1952.
- [44] M. Schmitt, J. Shelby and M. Hall, “Preparation of hollow glass microspheres from sol-gel derived glass for application in hydrogen gas storage,” *Journal of Non-Crystalline Solids* 352, pp. 626-631, 2006.
- [45] K.-H. Grote und J. Feldhusen, *Dubbel Taschenbuch für den Maschinenbau* 24. Auflage, Berlin, Heidelberg: Springer, 2014, pp. K6-K7.
- [46] J. Den Hartog, *Strength of Materials*, New York: Dover Publications, 1961.
- [47] G. McLellan and E. Shand, *Glass Engineering Handbook*, 3rd edn. ed., New York: McGraw Hill, 1984.
- [48] R. Doremus, *Glass Science*, 2nd edn. Hrsg., New York: John Wiley & Sons, 1994.
- [49] DIN ISO, DIN ISO 3585:1999-10 Borosilicate glass 3.3 - Properties (ISO 3585:1998), Beuth Verlag GmbH, 1999-10.
- [50] 3M™ and M. Döring, Interviewees, *Mechanical properties of glass used for hollow glass microspheres*. [Interview]. 4 11 2008.
- [51] SAE International, Standard J2601: Fueling Protocols for Light Duty Gaseous Hydrogen Surface Vehicles, International: SAE International, 2014.

- [52] T. Domschke, "Gleichgewichte und Beladungsgeschwindigkeiten eines Niedertemperaturmetallhydrids. ISBN 3-18-143306-3.," VDI-Verlag, Düsseldorf, 1989.
- [53] M. Striednig, S. Brandstätter, M. Sartory and M. Klell, "Thermodynamic real gas analysis of a tank filling process," *International Journal of Hydrogen Energy* 39, pp. 8495-8509, 2014.
- [54] U.S. National Institutes of Health, „ImageJ,“ 17 Novembre 2004. [Online]. Available: <http://rsbweb.nih.gov/ij/index.html>. [Zugriff am 21 February 2015].
- [55] G. Scott and D. Kilgour, "The density of random close packing of spheres," *British Journal of Applied Physics, Series 2, Volume 2*, pp. 863-866, 1969.
- [56] L. Smith and P. Midha, "Computer simulation of morphology and packing behaviour of irregular particles, for predicting apparent powder densities," *Computational Material Science* 7, pp. 377-383, 1997.
- [57] J. Ogden, H. Wallman and J. Watz, "Assessment of infrastructure requirements for hydrogen vehicle refueling stations using glass microspheres for hydrogen storage," *Proceedings of the 1997 U.S. DOE, Hydrogen Program Review*, pp. 197-236, 21-23 May 1997.
- [58] R. Tsugawa, I. Moen, P. Roberts and P. Souers, "Permeation of helium and hydrogen from glass-microsphere laser targets," *Journal of Applied Physics*, 47(5), pp. 1987-1993, 1976.
- [59] P. Souers, I. Moen, R. Lindhal and R. Tsugawa, "Permeation eccentricities of He, Ne, and D-T from soda-lime glass microbubbles," *Journal of the American Ceramic Society*, 61(1-2), pp. 42-46, 1978.
- [60] J. Shelby, Handbook of Gas Diffusion in Solids and Melts, Materials Park, Ohio, USA: ASM International, 1996.
- [61] V. Altomose, "Helium diffusion through glass," *Journal of Applied Physics*, 32(7), pp. 1309-1316, 1961.
- [62] R. Lee, R. Frank and D. Swets, "Diffusion of hydrogen and deuterium in fused quartz," *The Journal of Chemical Physics* 36(4), pp. 1062-1071, 1962.
- [63] R. Lee, "Diffusion of hydrogen in natural and synthetic fused quartz," *The Journal of Chemical Physics* 38(2), pp. 448-455, 1963.
- [64] H. Laska, R. Doremus and P. Jorgensen, "Permeation, diffusion, and solubility of deuterium in pyrex glass," *Journal of Chemical Physics* 50(1), pp. 135-137, 1969.
- [65] J. Shelby, "Helium, deuterium, and neon migration in a common borosilicate glass," *Journal of Applied Physics* 45(5), pp. 325-2149, 1974.
- [66] E. Dyrnjaja, S. Hummel, M. Keding, M.-T. Smolle, J. Gerger and M. Zawisky, "Neutron transmission measurements on hydrogen filled microspheres," *Nuclear Instruments and Methods in Physics Research B* 318, p. 241-244, 2014.
- [67] V. Kong, F. Foulkes, D. Kirk and J. Hinatsu, "Development of hydrogen storage for fuel cell generators. I: Hydrogen generation using hydrolysis hydrides," *International Journal of Hydrogen Energy* 24, pp. 665-675, 1999.
- [68] B. Liu und Z. Li, „A review: Hydrogen generation from borohydride hydrolysis reaction,“ *Journal of Power Sources* 187, pp. 527-534, 2009.
- [69] Y. Kojima, K. Suzuki, K. Fukumoto, M. Sasaki, T. Yamamoto, Y. Kawai and H. Hayashi, "Hydrogen generation using sodium borohydride solution and metal catalyst coated on metal oxide," *International Journal of Hydrogen Energy* 27, pp. 1029-1034, 2002.
- [70] E. Marrero-Alfonso, J. Gray, T. Davis and M. Matthews, "Hydrolysis of sodium borohydride with steam," *International Journal of Hydrogen Energy* 32, pp. 4717-4722, 2007.
- [71] E. Marrero-Alfonso, J. Gray, T. Davis and M. Matthews, "Minimizing water utilization in

- hydrolysis of sodium borohydride: The role of sodium metaborate hydrates,” *International Journal of Hydrogen Energy* 32, pp. 4723-4730, 2007.
- [72] A. Garron, D. Swierczynski, S. Bennici und A. Auroux, „New insights into the mechanism of H₂ generation through NaBH₄ hydrolysis on Co-based nanocatalysts studied by differential reaction calorimetry,” *International Journal of Hydrogen Energy* 34, pp. 1185-1199, 2009.
- [73] R. Retnamma, A. Novais and C. Rangel, “Kinetics of hydrolysis of sodium borohydride for hydrogen production in fuel cell applications: A review,” *International Journal of Hydrogen Energy*, pp. 9772-9790, 2011.
- [74] U. Demirci and F. Garin, “Ru-based bimetallic alloys for hydrogen generation by hydrolysis of sodium tetrahydroborate,” *Journal of Alloys and Compounds* 463, pp. 107-111, 2008.
- [75] V. Minkina, S. Shabunya, V. Kalinin, V. Martynenko and A. Smirnova, “Long-term stability of sodium borohydrides for hydrogen generation,” *International Journal of Hydrogen Energy* 33, pp. 5629-5635, 2008.
- [76] H. Schlesinger, H. Brown, A. Finholt, J. Gilbreath, H. Hoekstra and E. Hyde, “Sodium borohydride, its hydrolysis and its use as reducing agent and in the generation of hydrogen,” *Journal of the American Chemical Society* 75, pp. 215-219, 1953.
- [77] U. Demirci, “The hydrogen cycle with the hydrolysis of sodium borohydride: A statistical approach for highlighting the scientific/technical issues to prioritize in the field,” *International Journal of Hydrogen Energy* 40, pp. 2673-2691, 2015.
- [78] A. Goncalves, P. Castro, A. Novail, C. Rangel and H. Matos, “Modeling of catalytic hydrogen generation from sodium borohydride,” *18th European Symposium on Computer Aided Process Engineering - ESCAPE 18*, 2008.
- [79] V. Simagina, P. Storozhenko, O. Netskina, O. Komova, G. Odegova, Y. Larichev, A. Ishenko and A. Ozerova, “Development of catalysts for hydrogen generation from hydride compounds,” *Catalysis Today* 138, pp. 253-259, 2008.
- [80] Y. Larichev, O. Netskina, O. Komova and V. Simigani, “Comparative XPS study of Rh/Al₂O₃ and Rh/TiO₂ as catalysts for NaBH₄ hydrolysis,” *International Journal of Hydrogen Energy* 35, pp. 6501-6507, 2010.
- [81] V. Minkina, S. Shabunya, V. Kalinin and H. Yoshida, “Hydrolysis of Sodium Borohydride for Hydrogen Generation,” *Proceedings of 18th World Hydrogen Energy Conference 2010*, 2010.
- [82] C. Crisafulli, S. Scire, M. Salanitri, R. Zito and S. Calamia, “Hydrogen production through NaBH₄ hydrolysis over supported Ru catalysts: An insight on the effect of the support and the ruthenium precursor,” *International Journal of Hydrogen Energy* 36, pp. 3817-3826, 2011.
- [83] Y. Kojima, Y. Kawai, H. Nakanishi and S. Matsumoto, “Compressed hydrogen generation using chemical hydride,” *Journal of Power Sources* 135, pp. 36-41, 2004.
- [84] Y. Shang, R. Chen and G. Jiang, “Kinetic study of NaBH₄ hydrolysis over carbon-supported ruthenium,” *International Journal of Hydrogen Energy* 33, pp. 6719-6726, 2008.
- [85] J. Andrieux, D. Swierczynski, L. Laversenne, A. Garron, S. Bennici, C. Goutaudier, P. Miele, A. Auroux and B. Bonnetot, “A multifactor study of catalyzed hydrolysis of solid NaBH₄ on cobalt nanoparticles: Thermodynamics and kinetics,” *International Journal of Hydrogen Energy* 34, pp. 938-951, 2009.
- [86] S. Bennici, A. Garron and A. Auroux, “Maximizing the hydrogen yield in the catalyzed hydrolysis of pure borohydride powders,” *International Journal of Hydrogen Energy* 35, pp. 8621-8625, 2010.

- [87] S. Bennici, H. Yu, E. Obeid and A. Auroux, "Highly active heteropolyanions supported Co catalysts for fast hydrogen generation in NaBH₄ hydrolysis," *International Journal of Hydrogen Energy* 36, pp. 7431-7442, 2011.
- [88] K. Eom, E. Cho, M. Kim, S. Oh, S.-W. Nam and H. Kwon, "Thermochemical production of sodium borohydride from sodium metaborate in a scaled-up reactor," *International Journal of Hydrogen Energy* 38, pp. 2804-2809, 2013.
- [89] A. Figen and S. Piskin, "Microwave assisted green chemistry approach of sodium metaborate dihydrate (NaBO₂·2H₂O) synthesis and use as raw material for sodium borohydride (NaBH₄) thermochemical production," *International Journal of Hydrogen Energy* 38, pp. 3702-3709, 2013.
- [90] T. Ou, A. Giuliano, M. Panizza, A. Barbucci and G. Cerisola, "Thermochemical recycling of hydrolyzed NaBH₄. Part I: In-situ and ex-situ evaluations," *International Journal of Hydrogen Energy* 38, pp. 15269-15274, 2013.
- [91] T. Ou, M. Panizza and A. Barbucci, "Thermochemical recycling of hydrolyzed NaBH₄. Part II: Systematical study of parameters dependencies," *International Journal of Hydrogen Energy*, pp. 15940-15945, 2013.
- [92] Y. Kojima and T. Haga, "Recycling process of sodium metaborate to sodium borohydride," *International Journal of Hydrogen Energy* 28, pp. 989-993, 2003.
- [93] L. Ouyang, H. Zhong, Z. Li, Z. Cao, H. Wang, J. Liu, X. Zhu and M. Zhu, "Low-cost method for sodium borohydride regeneration and the energy efficiency of its hydrolysis and regeneration process," *Journal of Power Sources* 269, pp. 768-772, 2014.
- [94] M. Galvez, A. Frei, G. Albisetti, G. Lunardi and A. Steinfeld, "Solar hydrogen production via a two-step thermochemical process based on MgO/Mg redox reactions - Thermodynamic and kinetic analyses," *International Journal of Hydrogen Energy* 33, pp. 2880-2890, 2008.
- [95] U. Demirci, O. Akdim and P. Miele, "Ten-year efforts and a no-go recommendation for sodium borohydride for on-board automotive hydrogen storage," *International Journal of Hydrogen Energy* 34, pp. 2638-2645, 2009.
- [96] I. Beck, Interviewee, *Prizing of NaBH₄ at S. Goldmann GmbH & Co. KG*. [Interview]. 6 May 2014.
- [97] J. Andrieux, L. Laversenne, O. Krol, R. Chiriac, Z. Bouajila, R. Tenu, J. Counieux and C. Goutaudier, "Revision of the NaBO₂·2H₂O phase diagram for optimized yield in the H₂ generation through NaBH₄ hydrolysis," *International Journal of Hydrogen Energy* 37, pp. 5798-5810, 2012.
- [98] K. Butcher, „U.S. National Work Group Meeting for the Development of Commercial Hydrogen Measurement Standards, Fuel Specifications Subcommittee,“ in *Appendix E: The Starting Point: A Discussion Paper Describing a Proposed Method of Sale and Quality Specification for Hydrogen Vehicle Fuel*, 2008.
- [99] 3M™ und F. Wolff, Interviewees, *General Information about 3M glass spheres*. [Interview]. 28 May 2014.
- [100] Omya GmbH, *Angebot über 3M Glass Bubbles S38 - Nr. 2014-DE-JO-00041-150546*, Gummern, Österreich, 2014.
- [101] K. Lochmann, L. Oger and D. Stoyan, "Statistical analysis of random sphere packings with variable radius distribution," *Solid State Sciences* 8, pp. 1397-1413, 2006.
- [102] G. Mallory and J. Hajdu, *Electroless Plating: Fundamentals and Applications*, Orlando, Florida, Norwich, New York, USA: American Electroplaters and Surface Finishers Society, Noyes Publications/William Andrew Publishing, LLC, 1990.
- [103] J. Hu, W. Li, J. Chen, X. Zhang and X. Zhao, "Novel plating solution for electroless deposition of gold film onto glass surface," *Surface & Coatings Technology* 202, pp.

- 2922-2926, 2008.
- [104] Z. Yan, Z. Tong, Z. Run, C. Jiping and D. Yuexin, "Hollow ceramic microsphere coated with Co by electroless plating and its electromagnetic properties," *Rare Metal Materials and Engineering* 39, pp. 587-592, 2010.
- [105] C.-M. Chen, C.-H. Chen, S.-J. Cherng and T.-C. Wei, "Electroless deposition of platinum on indium tin oxide glass as the counterelectrode for dye-sensitized solar cells," *Materials Chemistry and Physics* 124, pp. 173-178, 2010.
- [106] M. Ayturk and Y. Ma, "Electroless Pd and Ag deposition kinetics of the composite Pd and Pd/Ag membranes synthesized from agitated plating baths," *Journal of Membrane Science* 330, pp. 233-245, 2009.
- [107] Y. Kobayashi, Y. Ishii, H. Yamane, K.-I. Watanabe, H. Koda, H. Kunigami and H. Kunigami, "Fabrication of TiO₂/Pt core-shell particles by electroless metal plating," *Colloids and Surfaces A: Physicochem. Eng. Aspects* 448, pp. 88-92, 2014.
- [108] X. Li, Y.-X. Duan, Y. Zhao and L. Zhu, "Effects of heat treatment on magnetic properties of Co-Fe-plated hollow ceramic microspheres," *Progress in Natural Science: Materials International* 21, pp. 392-400, 2011.
- [109] X. Li, X. Han and P. Xu, "Microstructure evolution and magnetic properties of Co-B coatings electrolessly plated on hollow microspheres," *Applied Surface Science* 255, pp. 6125-6131, 2009.
- [110] S.-S. Kim, S.-T. Kim, J.-M. Ahn and K.-H. Kim, "Magnetic and microwave absorbing properties of Co-Fe thin films plated on hollow ceramic microspheres of low density," *Journal of Magnetism and Magnetic Materials* 271, pp. 39-45, 2004.
- [111] T. Sankara Narayanan, S. Selvakumar and A. Stephen, "Electroless Ni-Co-P ternary alloy deposits: preparation and characteristics," *Surface and Coatings Technology* 172, pp. 298-307, 2003.
- [112] J. Balaraju, Klavati and K. Rajam, "Electroless ternary Ni-W-P alloys containing micron size Al₂O₃ particles," *Surface & Coatings Technology* 205, pp. 575-581, 2010.
- [113] J. Balaraju and M. Chembath, "Electroless ternary NiCeP coatings: Preparation and characterisation," *Applied Surface Science* 258, pp. 9692-9700, 2012.
- [114] S. Shukla, S. Seal, J. Akesson, R. Oder, R. Carter and Z. Rahman, "Study of mechanism of electroless copper coating of fly-ash cenosphere particles," *Applied Surface Science* 181, pp. 35-50, 2001.
- [115] Z. Liu, L. Phua, Y. Liu and C. Ong, "Microwave characteristics of low density hollow glass microspheres plated with Ni thin-film," *Journal of Applied Physics* 100, p. 093902, 2006.
- [116] L. Phua, Z. Liu and C. Ong, "Synthesis, structure and dynamic magnetic properties of double-layered Ni-Fe_{1-x}Co_x hollow microspheres," *Journal of Applied Physics* 41, p. 015001, 2008.
- [117] W.-J. Kim and S.-S. Kim, "Preparation of Ag-coated hollow microspheres via electroless plating for application in lightweight microwave absorbers," *Applied Surface Science* 329, pp. 219-222, 2015.
- [118] M. Han, Y. Ou and L. Deng, "Microwave absorption properties of double-layer absorbers made of NiCoZn ferrites and hollow glass microspheres electroless plated with FeCoNiB," *Journal of Magnetism and Magnetic Materials* 321, pp. 1125-1129, 2009.
- [119] S. Zhou, Q. Zhang, H. Liu, X. Gong and J. Huang, "Microwave absorption performance of magnetic Fe-Ni-P nanoparticles electrolessly plated on hollow glass microspheres," *Materials Chemistry and Physics* 134, pp. 224-228, 2012.
- [120] S. Shukla, S. Seal, Z. Rahaman and K. Scammon, "Electroless copper coating of cenospheres using silver nitrate activator," *Materials Letters* 57, pp. 151-156, 2002.

- [121] S. Zhang, *Nanostructured Thin Films and Coatings - Functional Properties*, Boca Raton, Florida, USA: CRC Press, Taylor & Francis Group, 2010.
- [122] M. Guglielmi, G. Kickelbick and A. Martucci, *Sol-Gel Nanocomposites*, New York, Heidelberg, Dordrecht, London: Springer, 2014.
- [123] D. Fang, K. Lin, T. Xue, C. Cui, X. Chen, P. Yao and H. Li, "Influence of Al doping on structural and optical properties of Mg–Al co-doped ZnO thin films prepared by sol–gel method," *Journal of Alloys and Compounds* 589, pp. 346-352, 2014.
- [124] M. Holgado, A. Cintas, M. Ibisate, C. Serna, C. Lopez and F. Meseguer, "Three-Dimensional Arrays Formed by Monodisperse TiO₂ Coated on SiO₂ Spheres," *Journal of Colloid and Interface Science* 229, pp. 6-11, 2000.
- [125] C. Shifu and C. Gengyu, "Photocatalytic oxidation of nitrite by sunlight using TiO₂ supported on hollow glass microbeads," *Solar Energy* 73, pp. 15-21, 2002.
- [126] M. Haraguchi, F. Komatsu, K. Tajiri, T. Okamoto, M. Fukui and S. Kato, "Fabrication and optical characterization of a TiO₂ thin film on a silica microsphere," *Surface Science* 548, pp. 59-66, 2004.
- [127] J. Xu, H. Yang, Q. Yu, L. Chang, X. Pang, X. Li, H. Zhu, M. Li and G. Zou, "Synthesis and characterization of hollow glass microspheres coated by SnO₂ nanoparticles," *Materials Letters* 61, pp. 1424-1428, 2007.
- [128] G. Mu, X. Pan, N. Chen, C. He and M. Gu, "Synthesis and characterization of hard magnetic composites - Hollow microsphere/titania/barium ferrite," *Applied Surface Science* 254, pp. 2483-2486, 2008.
- [129] L. Sun, S. Wan, Z. Yu and L. Wang, "Optimization and modeling of preparation conditions of TiO₂ nanoparticles coated on hollow glass microspheres using response surface methodology," *Separation and Purification Technology* 125, pp. 156-162, 2014.
- [130] A. Boulle, Z. Oudjedi, R. Guinebretiere, B. Soulestin and A. Dauger, "Ceramic nanocomposites obtained by sol-gel coating of submicron powders," *Acta Materialia* 49, pp. 811-816, 2001.
- [131] H. Suffredini, V. Tricoli, L. Avaca and N. Vatistas, "Sol–gel method to prepare active Pt–RuO₂ coatings on carbon powder for methanol oxidation," *Electrochemistry Communications* 6, pp. 1025-1028, 2004.
- [132] H. Suffredini, V. Tricoli, N. Vatistas and L. Avaca, "Electro-oxidation of methanol and ethanol using a Pt–RuO₂/C composite prepared by the sol–gel technique and supported on boron-doped diamond," *Journal of Power Sources* 158, pp. 124-128, 2006.
- [133] M. Abe, "Ferrite plating: a chemical method preparing oxide magnetic films at 24 - 100°C, and its applications," *Electrochimica Acta* 45, pp. 3337-3343, 2000.
- [134] J. Wei, J. Liu and S. Li, "Electromagnetic and microwave absorption properties of Fe₃O₄ magnetic films plated on hollow glass spheres," *Journal of Magnetism and Magnetic Materials* 312, pp. 414-417, 2007.
- [135] C. Vahlas, B. Caussat, P. Serp and G. Angelopoulos, "Principles and applications of CVD powder technology," *Materials Science and Engineering R* 53, pp. 1-72, 2006.
- [136] R. Bunshah, *Handbook of Hard Coatings*, Norwich, New York, USA: Noyes Publications, William Andrew Publishing, LLC, 2001.
- [137] B. Fahlmann, *Materials Chemistry*, Second Edition, Dordrecht, Heidelberg, London, New York: Springer, 2011.
- [138] K. Dick, "A review of nanowire growth promoted by alloys and non-alloying elements with emphasis on Au-assisted IIIeV nanowires," *Progress in Crystal Growth and Characterization of Materials* 54, pp. 138-173, 2008.
- [139] P. Premkumar, N. Prakash, F. Gaillard and N. Bahlawane, "CVD of Ru, Pt and Pt-based alloy thin films using ethanol as mild reducing agent," *Materials Chemistry and Physics*

- 125, pp. 757-762, 2011.
- [140] I. Szymanska, "Gaseous phase studies of new copper(II) carboxylate complexes with tert-butylamine as potential precursors for chemical vapor deposition (CVD)," *Polyhedron* 50, pp. 200-207, 2013.
- [141] H. Lee, M. Song, J. Jurng and Y.-K. Park, "The synthesis and coating process of TiO₂ nanoparticles using CVD process," *Powder Technology* 214, pp. 64-68, 2011.
- [142] P. Piszczek, Z. Muchewicz, A. Radtke, M. Gryglas, H. Dahm and H. Rozycki, "CVD of TiO₂ and TiO₂/Ag antimicrobial layers: Deposition from the hexanuclear μ -oxo Ti(IV) complex as a precursor, and the characterization," *Surface & Coatings Technology* 222, pp. 38-43, 2013.
- [143] A. Sherman, *Chemical Vapor Deposition for Microelectronics*, Westwood, New Jersey, USA: Noyes Publications, 1987.
- [144] M. Karches, C. Bayer and P. von Rohr, "A circulating fluidised bed for plasma-enhanced chemical vapor deposition on powders at low temperatures," *Surface and Coatings Technology* 116-119, pp. 879-885, 1999.
- [145] M. Karches, M. Morstein, P. von Rohr, R. Pozzo, J. Giombi and M. Baltanas, "Plasma-CVD-coated glass beads as photocatalyst for water decontamination," *Catalysis Today* 72, pp. 267-279, 2002.
- [146] M. Karches, M. Morstein and P. von Rohr, "Encapsulation of abrasive particles by plasma CVD," *Surface and Coatings Technology* 169-170, pp. 544-548, 2003.
- [147] B. Borer and R. von Rohr, "Growth structure of SiO_x films deposited on various substrate particles by PECVD in a circulating fluidized bed reactor," *Surface & Coatings Technology* 200, pp. 377-381, 2005.
- [148] G. Kim, S. Kim and S. Park, "Plasma enhanced chemical vapor deposition of TiO₂ films on silica gel powders at atmospheric pressure in a circulating fluidized bed reactor," *Chemical Engineering and Processing* 48, pp. 1135-1139, 2009.
- [149] M. Song, Y.-K. Park and J. Jurng, "Direct coating of V₂O₅/TiO₂ nanoparticles onto glass beads by chemical vapor deposition," *Powder Technology* 231, pp. 135-140, 2012.
- [150] P. Kelly and R. Arnell, "Magnetron sputtering: a review of recent developments and applications," *Vacuum* 56, pp. 159-172, 2000.
- [151] I. Safi, "Recent aspects concerning DC reactive magnetron sputtering of thin films: a review," *Surface and Coatings Technology* 127, pp. 203-219, 2000.
- [152] G. Bräuer, B. Szyszka, M. Vergöhl and R. Bandorf, "Magnetron sputtering – Milestones of 30 years," *Vacuum* 84, pp. 1354-1359, 2010.
- [153] M. Waite, S. Shah and D. Glocker, "Sputtering Sources," in *50 Years of Vacuum Coating Technology and the growth of the Society of Vacuum Coaters*, Donald M. Mattox and Vivienne Harwood Mattox, eds., Society of Vacuum Coaters, 2007, pp. 42-50.
- [154] J. Szczyrbowski, G. Bräuer, M. Ruske, J. Bartella, J. Schroeder and A. Zmelty, "Some properties of TiO₂ layers prepared by medium frequency reactive sputtering," *Surface and Coatings Technology* 112, pp. 261-266, 1999.
- [155] W. Sproul, D. Christie and D. Carter, "Control of reactive sputtering processes," *Thin Solid Films* 491, pp. 1-17, 2005.
- [156] E. Takeshima, "Process and apparatus for coating fine powders". Chiba, Japan Patent patent number 4,940,523, 10 July 1990.
- [157] H. Poelman, K. Eufinger, D. Depla, D. Poelman, R. De Gryse, B. Sels and G. Marin, "Magnetron sputter deposition for catalyst synthesis," *Applied Catalysis A: General* 325, pp. 213-219, 2007.
- [158] R. Toth, "Apparatus and method of treating fine powders". North Huntington, Pennsylvania, USA Patent patent number: US 2006/0193978 A1, 31 August 2006.

- [159] D. Makowiecki, J. Kerns, C. Alford and M. McKernan, "Sputtering process and apparatus for coating powders". Oakland, California, USA Patent US 6,355,146 B1, 12 March 2002.
- [160] T. Abe, S. Akamaru and K. Watanabe, "Surface modification of Al₂O₃ ceramic grains using a new RF sputtering system developed for powdery materials," *Journal of Alloys and Compounds* 377, pp. 194-201, 2004.
- [161] T. Abe, S. Akamura, K. Watanabe and Y. Honda, "Surface modification of polymer microparticles using a hexagonal-barrel sputtering system," *Journal of Alloys and Compounds* 402, pp. 227-232, 2005.
- [162] S. Akamaru, S. Higashide, M. Hara and T. Abe, "Surface coating of small SiO₂ particles with TiO₂ thin layer by using barrel-sputtering system," *Thin Solid Films* 513, pp. 103-109, 2006.
- [163] T. Abe, H. Hamatani, S. Higashide, M. Hara and S. Akamura, "Surface coating of small SiO₂ particles with a WO₃ thin film by barrel-sputtering method," *Journal of Alloys and Compounds* 441, pp. 157-161, 2007.
- [164] A. Taguchi, T. Kitami, H. Yamamoto, S. Akamaru, M. Hara and T. Abe, "Surface coating with various metals on spherical polymer particles by using barrel sputtering technique," *Journal of Alloys and Compounds* 441, pp. 162-167, 2007.
- [165] A. Taguchi, M. Inoue, C. Hiromi, M. Tanizawa, T. Kitami and T. Abe, "Study of the surface morphology of platinum thin films on powdery substrates prepared by the barrel sputtering system," *Vacuum* 83, pp. 575-578, 2009.
- [166] W. Ensinger and H. Müller, "Noble metal deposition on aluminum oxide powder surfaces by ion beam sputtering," *Nuclear Instruments and Methods in Physics Research B* 141, pp. 693-698, 1998.
- [167] W. Ensinger and H. Müller, "Surface treatment of aluminum oxide and tungsten carbide powders by ion beam sputter deposition," *Surface and Coatings Technology* 163 –164, pp. 281-285, 2003.
- [168] Z. Yu, Z. Shen, Z. Xu and S. Wang, "Fabrication and structural characterization of metal films coated on cenosphere particles by magnetron sputtering deposition," *Applied Surface Science* 253, pp. 7082-7088, 2007.
- [169] X. Yu, Z. Xu and Z. Shen, "Metal copper films deposited on cenosphere particles by magnetron sputtering method," *Journal of Physics D: Applied Physics* 40, pp. 2894-2898, 2007.
- [170] X. Yu, Z. Shen and Z. Xu, "Preparation and characterization of Ag-coated cenospheres by magnetron sputtering method," *Nuclear Instruments and Methods in Physics Research B* 265, pp. 637-640, 2007.
- [171] X. Yu and Z. Shen, "Metal copper films coated on microparticle substrates using an ultrasonic-assisted magnetron sputtering system," *Powder Technology* 187, pp. 239-243, 2008.
- [172] X. Yu, Z. Shen and C. Cai, "Millimeter wave electromagnetic interference shielding by coating expanded polystyrene particles with a copper film using magnetron sputtering," *Vacuum* 83, pp. 1438-1441, 2009.
- [173] X. Yu and Z. Shen, "The electromagnetic shielding of Ni films deposited on cenosphere particles by magnetron sputtering method," *Journal of Magnetism and Magnetic Materials* 321, pp. 2890-2895, 2009.
- [174] X. Yu and Z. Shen, "Photocatalytic TiO₂ films deposited on cenosphere particles by pulse magnetron sputtering method," *Vacuum* 85, pp. 1026-1031, 2011.
- [175] A. Fedotov, S. Grigoriev, E. Lyutikova, P. Millet and V. Fateev, "Characterization of carbon-supported platinum nanoparticles synthesized using magnetron sputtering for application in PEM electrochemical systems," *International Journal of Hydrogen Energy*

- 38, pp. 426-430, 2013.
- [176] D. Baechle, J. Demaree, J. Hirvonen and E. Wetzel, "Magnetron sputter deposition onto fluidized particle beds," *Surface & Coatings Technology* 221, pp. 94-103, 2013.
- [177] J. Hell, M. Horkel, E. Neubauer and C. Eisenmenger-Sittner, "Construction and characterization of a sputter deposition system for coating granular materials," *Vacuum* 84, pp. 453-457, 2010.
- [178] G. Schmid, C. Eisenmenger-Sittner, J. Hell, M. Horkel, M. Keding and H. Mahr, "Optimization of a container design for depositing uniform metal coatings on glass microspheres by magnetron sputtering," *Surface & Coatings Technology* 205, pp. 1929-1936, 2010.
- [179] G. Schmid and C. Eisenmenger-Sittner, "A method for uniformly coating powdery substrates by magnetron sputtering," *Surface & Coatings Technology* 236, pp. 353-360, 2013.
- [180] G. Schmid, C. Eisenmenger-Sittner, J. Hell and M. Quirchmair, "Vorrichtung zum Beschichten eines Substrates aus Teilchen". Vienna, Austria Patent patent number WO 2014/043728 A1, 13 September 2013.
- [181] H. Kersten, P. Schmetz and G. Kroesen, "Surface modification of powder particles by plasma deposition of thin metallic films," *Surface and Coatings Technology* 108-109, pp. 507-512, 1998.
- [182] J. Xu and K. Kato, "The effect of water vapor on the agglomeration of wear particles of ceramics," *Wear* 202, pp. 165-171, 1997.
- [183] J. Andersson, R. Erck and A. Erdemir, "Friction of diamond-like carbon films in different atmospheres," *Wear* 254, pp. 1070-1075, 2003.
- [184] A. Khataee and G. Mansoori, Nanostructured Titanium Dioxide Materials, New Jersey, London, Singapore, Beijing, Shanghai, Hong Kong, Taipei, Chennai: World Scientific Publishing Co. Pte. Ltd., 2012.
- [185] D. Hanaor and C. Sorrel, "Review of the anatase to rutile phase transformation," *Journal of Material Science* 46, pp. 855-874, 2011.
- [186] V. Vancoppenolle, P.-Y. Jouan, M. Wautelet, J.-P. Dauchot and M. Hecq, "D.C. magnetron sputtering deposition of TiO₂ films in argon-oxygen gas mixtures: theory and experiments," *Surface and Coatings Technology* 116-119, pp. 933-937, 1999.
- [187] G. Tian, L. Dong, C. Wei, J. Huang, H. He and J. Shao, "Investigation on microstructure and optical properties of titanium dioxide coatings annealed at various temperature," *Optical Materials* 28, pp. 1058-1063, 2006.
- [188] L. Clarizia, D. Spasiano, I. Di Somma, R. Marotta, R. Andreozzi and D. Dionysiou, "Copper modified-TiO₂ catalysts for hydrogen generation through photoreforming of organics. A short review," *International Journal of Hydrogen Energy* 39, pp. 16812-16831, 2014.
- [189] H. Park, Y. Park, W. Kim and W. Choi, "Surface modification of TiO₂ photocatalyst for environmental applications," *Journal of Photochemistry and Photobiology C: Photochemistry Reviews* 15, pp. 1-20, 2013.
- [190] A. Ayati, A. Ahmadpour, F. Bamoharram, B. Tanhaei, M. Mänttari and M. Sillanpää, "A review on catalytic applications of Au/TiO₂ nanoparticles in the removal of water pollutant," *Chemosphere* 107, pp. 163-174, 2014.
- [191] H. Shao, C. Yu, X. Xu, J. Wang, R. Zhai and X. Wang, "Influence of Ti nanocrystallization on microstructure, interface bonding, surface energy and blood compatibility of surface TiO₂ films," *Applied Surface Science* 257, pp. 1649-1654, 2010.
- [192] M. Horprathum, P. Eiamchai, P. Limnonthakul, N. Nuntawong, P. Chindaudom, A. Pokaipisit and P. Limsuwan, "Structural, optical and hydrophilic properties of

- nanocrystalline TiO₂ ultra-thin films prepared by pulsed dc reactive magnetron sputtering,” *Journal of Alloys and Compounds* 509, pp. 4520-4524, 2011.
- [193] P. Kelly, C. Beevers, P. Henderson, R. Arnell, J. Bradley and H. Bäcker, “A comparison of the properties of titanium-based films produced by pulsed and continuous DC magnetron sputtering,” *Surface and Coatings Technology* 174 –175, pp. 795-800, 2003.
- [194] L. Maissel and R. Glang, *Handbook of thin film technology*, United States of America, New York: McGraw-Hill Company, 1970.
- [195] S. Berg and T. Nyberg, “Fundamental understanding and modeling of reactive sputtering processes,” *Thin Solid Films* 476, pp. 215-230, 2005.
- [196] N. Martin, R. Sanjines, J. Takadoum and F. Levy, “Enhanced sputtering of titanium oxide, nitride and oxynitride thin films by the reactive gas pulsing technique,” *Surface and Coatings Technology* 142-144, pp. 615-620, 2001.
- [197] J. Affinito and R. Parsons, “Mechanisms of voltage controlled, reactive, planar magnetron sputtering of Al In Ar/N₂ and Ar/O₂ atmospheres,” *Journal of Vacuum Science and Technology*, pp. 1275-1284, 1984.
- [198] N. Malkomes, M. Vergöhl and B. Szyszka, “Properties of aluminum-doped zinc oxide films deposited by high rate mid-frequency reactive magnetron sputtering,” *Journal of Vacuum Science and Technology A* 19(2), pp. 414-419, 2001.
- [199] S. Schiller, U. Heisig, K. Steinfelder, J. Strümpfel, R. Voigt, R. Fendler and G. Teschner, “On the investigation of d.c. plasmatron discharges by optical emission spectrometry,” *Thin Solid Films* 96, pp. 235-240, 1982.
- [200] Z. Lin, K. Liu, Y.-C. Zhang, X.-J. Yue, G.-Q. Song and D.-C. Ba, “The microstructure and wettability of the TiO_x films synthesized by reactive DC magnetron sputtering,” *Materials Science and Engineering B* 156, pp. 79-83, 2009.
- [201] W. Sproul and J. Tomashek, “Rapid rate reactive sputtering of a group IVb metal”. USA Patent United States Patent 4,428,811, 4 April 1983.
- [202] H. Gilboa, R. Mosely and H. Hanawa, “Process and apparatus for forming stoichiometric layer of a metal compound by closed loop voltage controlled reactive sputtering”. Patent Patent 5,108,569, 28 April 1992.
- [203] W. Xiong and S. Gupta, “Stable high rate reactive sputtering”. Patent Patent 6,537,428, 25 March 2003.
- [204] C. Köble, D. Greiner, J. Klaer, R. Klenk, A. Meeder and F. Ruske, “DC reactive sputtering of aluminium doped zinc oxide films for solar modules controlled by target voltage,” *Thin Solid Films* 518, pp. 1204-1207, 2009.
- [205] N. Malkomes and M. Vergöhl, “Dynamic simulation of process control of the reactive sputter process and experimental results,” *Journal of Applied Physics* 89, pp. 732-739, 2001.
- [206] D. Depla, J. Haemers and R. De Gryse, “Discharge voltage measurements during reactive sputtering of oxides,” *Thin Solid Films* 515, pp. 468-471, 2006.
- [207] V. Bellido-Gonzalez, B. Daniel, D. Monaghan and J. Counsell, “Proceedings: Glass Performance Days, Finland 2009,” in *Uniformity control in reactive magnetron sputtering*, Tampere, Finland, 2010.
- [208] A. Belkind, A. Freilich, J. Lopez, Z. Zhao, W. Zhu and K. Becker, “Characterization of pulsed dc magnetron sputtering plasmas,” *New Journal of Physics* 7, p. 90, 2005.
- [209] G. Este and W. Westwood, “A quasi-direct-current sputtering technique for the deposition of dielectrics at enhanced rates,” *Journal of Vacuum Science and Technology A* 6 (3), pp. 1845-1848, 1988.
- [210] S. Marinel, D. Choi, R. Heuguet, D. Agrawal and M. Lanagan, “Broadband dielectric characterization of TiO₂ ceramics sintered through microwave and conventional

- processes,” *Ceramics International* 39, pp. 299-306, 2013.
- [211] O. Treichel and V. Kirchhoff, “The influence of pulsed magnetron sputtering on topography and crystallinity of TiO₂ films on glass,” *Surface and Coatings Technology* 123, pp. 268-272, 2000.
- [212] P. Kelly, R. Hall, J. O'Brien, J. Bradley, G. Roche and R. Arnell, “Substrate effects during mid-frequency pulsed DC biasing,” *Surface and Coatings Technology* 142-144, pp. 635-641, 2001.
- [213] P. Löbl, M. Huppertz and D. Mergel, “Nucleation and growth in TiO₂ films prepared by sputtering and evaporation,” *Thin Solid Films* 251, pp. 72-79, 1994.
- [214] M. Sardela, *Practical Materials Characterization*, New York, Heidelberg, Dordrecht, London: Springer, 2014.
- [215] S. Mukherjee, A. Nebatti, F. Mohtascham, S. Schipporeit, C. Notthoff and D. Mergel, “Influence of thickness on the structural properties of radio-frequency and direct-current magnetron sputtered TiO₂ anatase thin films,” *Thin Solid Films* 558, pp. 443-448, 2014.
- [216] V. Bukauskas, S. Kaciulis, A. Mezzi, A. Mironas, G. Niaura, M. Rudzikas, I. Simkiene and A. Setkus, “Effect of substrate temperature on the arrangement of ultra-thin TiO₂ films grown by a dc-magnetron sputtering deposition,” *Thin Solid Films* 585, pp. 5-12, 2015.
- [217] Q. Xu and M. Chandra, “A portable hydrogen generation system: Catalytic hydrolysis of ammonia-borane,” *Journal of Alloys and Compounds* 446-447, p. 729-732, 2007.
- [218] N. Patel and A. Miotello, “Progress in Co-B related catalyst for hydrogen production by hydrolysis of boron-hydrides: A review and the perspectives to substitute noble metals,” *International Journal of Hydrogen Energy* 40, pp. 1429-1464, 2015.
- [219] H. Brown and C. Brown, “New, Highly Active Metal Catalysts for the Hydrolysis of Borohydride,” *Journal of the American Chemical Society* 84(8), pp. 1493-1494, 1962.
- [220] R. Pena-Alonso, A. Sicurelli, E. Callone, G. Carturan and R. Raj, “A picoscale catalyst for hydrogen generation from NaBH₄ for fuel cells,” *Journal of Power Sources* 165, pp. 315-323, 2007.
- [221] S. Shah and R. Raj, “Nanodevices that explore the synergies between PDCs and carbon nanotubes,” *Journal of the European Ceramic Society* 25, pp. 243-249, 2005.
- [222] N. Patel, R. Fernandes, N. Bazzanella and A. Miotello, “Co-P-B catalyst thin films prepared by electroless and pulsed laser deposition for hydrogen generation by hydrolysis of alkaline sodium borohydride: A comparison,” *Thin Solid Films* 518, pp. 4779-4785, 2010.
- [223] N. Patel and A. Miotello, “Progress in CoeB related catalyst for hydrogen production by hydrolysis of boron-hydrides: A review and the perspectives to substitute noble metals,” *International Journal of Hydrogen Energy* 40, pp. 1429-1464, 2015.
- [224] J. Agustsson, U. Arnalds, A. Ingason, K. Gylfason, K. Johnsen, S. Olafsson and J. Gudmundsson, “Growth, coalescence, and electrical resistivity of thin Pt films grown by dc magnetron sputtering on SiO₂,” *Applied Surface Science*, pp. 7356-7360, 2008.

Appendix

9. Appendix

9.1. Microspheres and hydrolysis

9.1.1. Relation for a pressurized thick walled spheres

Referred to in section 3.2.1, p. 34

The maximum pressure inside a thick walled pressurized hollow glass microsphere is given by

$$p_{\max} = \frac{\frac{\sigma}{S_f} + p_a \frac{r_a^3}{r_a^3 - r_i^3}}{\frac{r_i^3}{r_a^3 - r_i^3} \left(1 + \frac{r_a^3}{2r_i^3} \right)}, \quad (9.1)$$

where σ is the glass tensile strength, S_f the safety factor, p_a the ambient pressure, r_a the sphere outer radius and r_i the sphere inner radius.

9.1.2. Pressure inside spheres at different loading and extraction temperatures

Referred to in section 3.2.1, p. 35

The amount of hydrogen n inside one sphere is given by the real gas equation

$$p_L V_{Sp} = nRT_L Z_L(p_L, T_L) \quad (9.2)$$

with loading pressure p_L , sphere volume V_{Sp} , amount of mol n , gas constant R , loading temperature T_L and compressibility factor $Z_L(p, T)$ for loading conditions (equation (9.3)) [10]

$$Z_L = 1 + B_L p_L, \quad (9.3)$$

where $B_L(T)$ is the total virial coefficient for loading conditions, given by [10]

$$B_L = \frac{B_1}{T_L} + \frac{B_2}{T_L^2}. \quad (9.4)$$

The same relation (equation (3.2)) accounts for the extraction pressure p_E

$$p_E V_{Sp} = nRT_E Z_E(p_E, T_E), \quad (9.5)$$

with extraction temperature T_E and compressibility factor $Z_E(p_E, T_E)$ for loading conditions. Since the amount of hydrogen n and the sphere volume V_{Sp} are constant in both cases, the extraction pressure can be expressed to

$$p_E = \frac{p_L T_E}{T_L (1 + B_L p_L) - B_E p_L T_E}, \quad (9.6)$$

with

$$B_E = \frac{B_1}{T_E} + \frac{B_2}{T_E^2} \quad (9.7)$$

and B_L similarly.

As an example we assume a loading temperature of $T_L = 200$ °C, an extraction temperature of $T_E = 120$ °C and a loading pressure $p_L = 85$ MPa, which results in an extraction pressure of $p_E = 70.6$ MPa.

9.1.3. Hydrogen diffusion – pressure as a function of time

Referred to in section 3.2.2, p. 44

For ideal gas the hydrogen molecules that go through the shell of a microsphere with surface A and volume V , with a shell thickness d and a radius r , is given by

$$dn = K(T) \cdot \frac{A}{d} \cdot (p(t) - p_{\infty}) dt \quad (9.8)$$

with $K(T)$ being the permeability. The pressure after a time dt is

$$p(t + dt) = p(t) - dn \frac{RT}{V} \quad (9.9)$$

inserting (9.8) in (9.9) yields

$$\frac{dp}{dt} = -C(p(t) - p_{\infty}) \quad (9.10)$$

where

$$C = K(T) \cdot RT \frac{A}{d \cdot V} = K(T) \cdot \frac{3RT}{d \cdot r}. \quad (9.11)$$

Solving the differential equation (9.10) gives

$$p(t) = p_{\infty} + (p_0 - p_{\infty}) \cdot e^{-K(T) \frac{3RT}{d \cdot r} t} \quad (9.12)$$

For real gas, equation (9.10) has the form

$$\frac{dp}{dt} = -C(1 + Bp(t))(p(t) - p_{\infty}) \quad (9.13)$$

with the compressibility $Z(T, t)$

$$Z(T, t) = 1 + B(T)p(t). \quad (9.14)$$

Equation (9.13) was solved with *Wolfram Mathematica* to

$$p(t) = \frac{p_0 - p_\infty + (1 + p_0 B(T)) \cdot p_\infty e^{Ct(Bp_\infty+1)}}{B(p_\infty - p_0) + (1 + p_0 B(T)) e^{Ct(Bp_\infty+1)}}. \quad (9.15)$$

Initial condition and end condition for both, ideal gas and real gas, were $p(0) = p_0$ and $p(\infty) = p_\infty$.

9.1.4. Amount of water to cover hollow glass microspheres and hydride

Referred to in section 3.3.3, p. 61

The amount of water to cover hollow glass microspheres and the hydride is depending the packing factor and the density of the spheres and the hydride

$$m_w = \rho_w (1 - f) \cdot \left\{ \frac{m_{sph}}{f \cdot \rho_{sph}} + \frac{m_{hy}}{f \cdot \rho_{hy}} \right\}, \quad (9.16)$$

where ρ_{sph} and ρ_{hy} are the true densities of the spheres and the hydride, which is why they were multiplied with the packing factor f . The density of the hydride is a material parameter whereas the density of the spheres depends on the sphere dimensions. The true density of hydrogen loaded spheres is given by

$$\rho_{sph} = \frac{(r^3 - (r-d)^3) \rho_{glass} + (r-d)^3 \rho_{H_2}}{r^3}. \quad (9.17)$$

Using the relation for the gravimetric storage density of hollow glass microspheres

$$\gamma_{G,sph} = \frac{\rho_{H_2} (r-d)^3}{\rho_{H_2} (r-d)^3 + \rho_{glass} (r^3 - (r-d)^3)}, \quad (9.18)$$

the true density of hydrogen loaded spheres can be written as

$$\rho_{sph} = \frac{\rho_{H_2} (r-d)^3}{\gamma_{G,sph} r^3}. \quad (9.19)$$

With $\zeta = m_{sph}/m_{hy}$ and inserting equation (9.19) in (9.16) yields

$$m_w = \rho_w m_{hy} \frac{1-f}{f} \left(\zeta \cdot \frac{\gamma_{G,sph}}{\rho_{H_2}} \frac{r^3}{(r-d)^3} + \frac{1}{\rho_{hy}} \right) \quad (9.20)$$

9.2. Sphere counting algorithm used in *ImageJ*

Referred to in section 4.3.1, p. 97

The diameter of spheres was measured automatically with *ImageJ* software by the “Analyse Particle” function.

- Therefore, first the scale must be set (Analyze → Set Scale).
- After that the threshold has to be set in order to get a binary image (Image → Adjust → Threshold).
- Then the particle analysing function is used (Analyze → Analyze particles). The analysing parameters were:
 - Size: 40-100000 μm^2 ,
 - Circularity: 0.65-1.00,
 - Show: Outlines, Include Holes.

The automatic measurement method gives slightly different results than manual measurement. The difference is caused by the fact that *ImageJ* cannot automatically detect every sphere like the human eye.

9.3. Construction drawings of the concussion mechanism

Referred to in section 4.3.2, p. 102

On the following pages the construction sketches of the coating vessel, the concussion plate and the protection skirt are shown. All other construction drawing can be found on the DVDs inside the thesis.

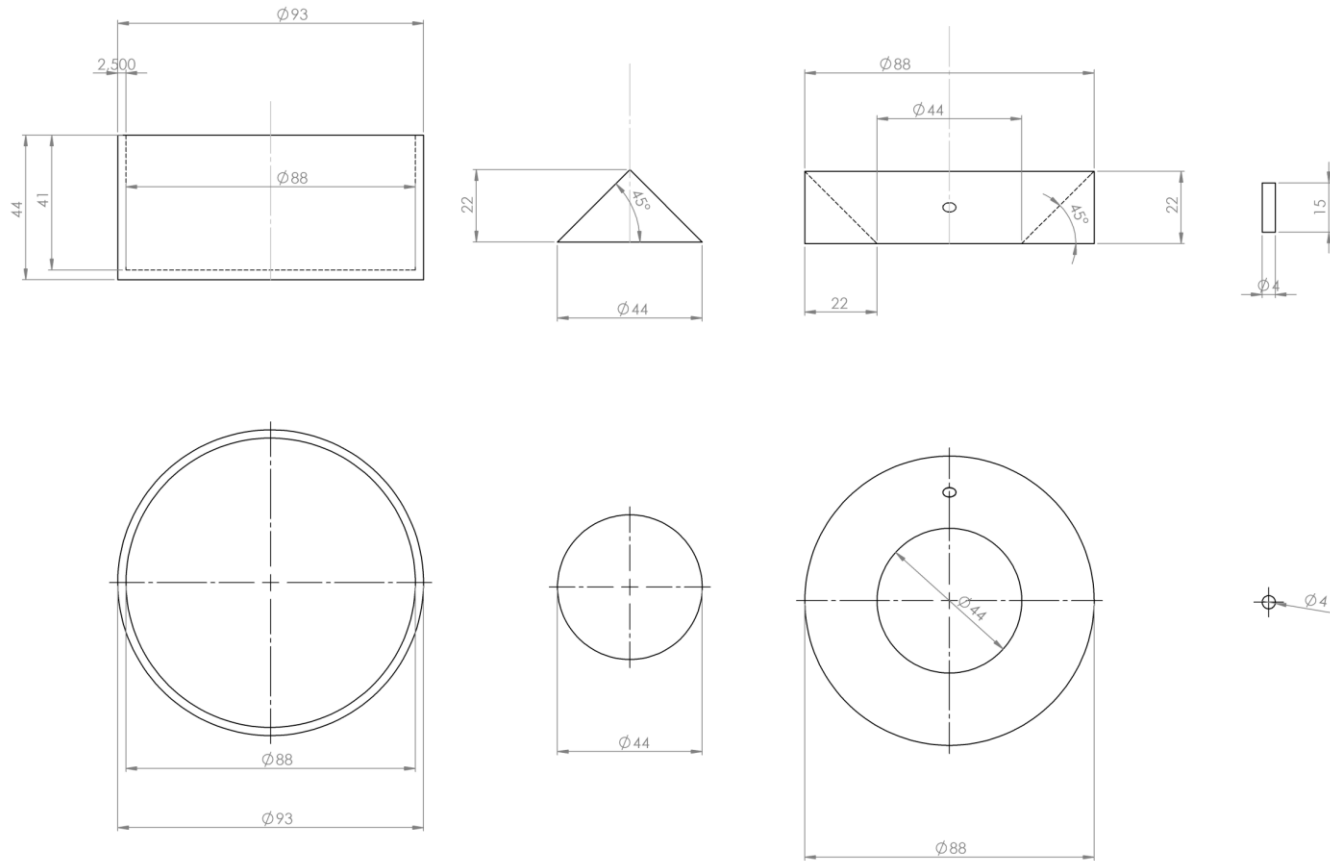


Figure 9.1: Construction drawing of the coating vessel parts

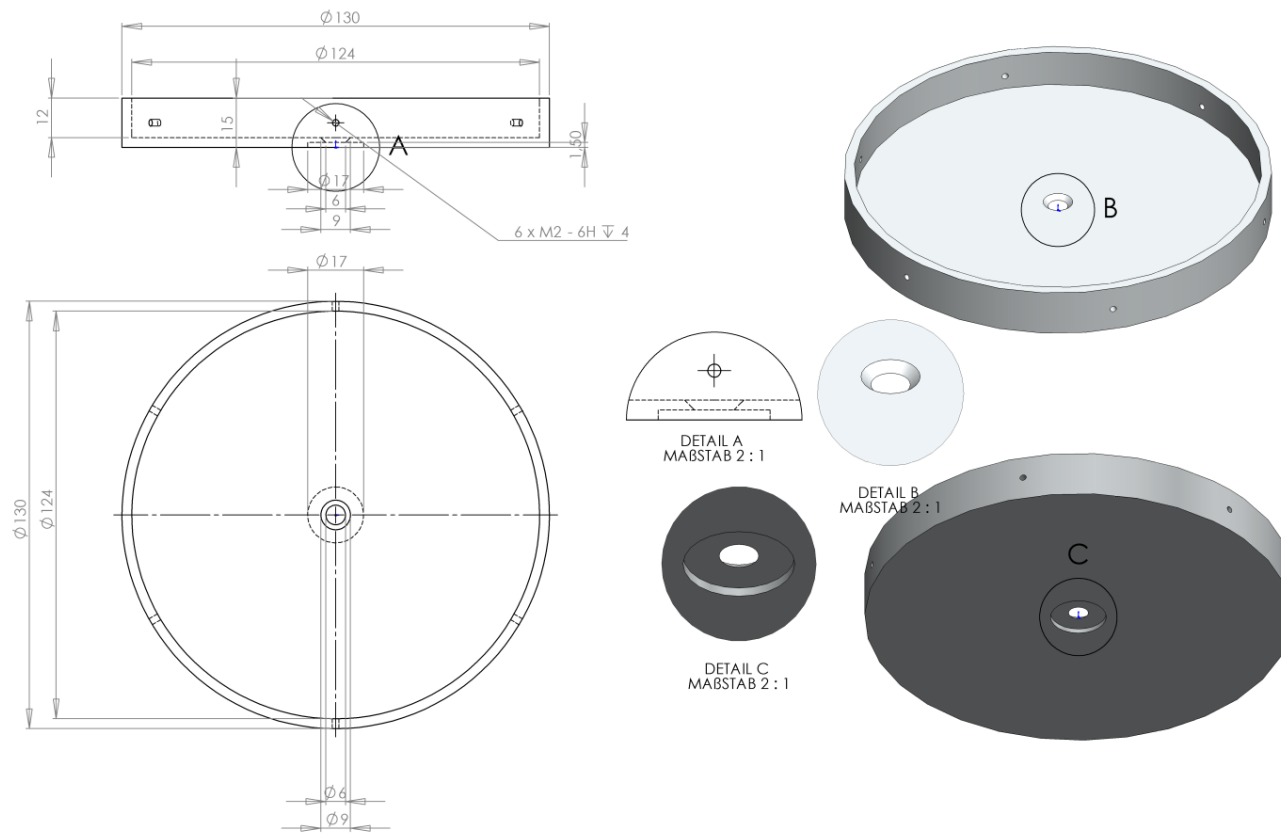


Figure 9.2: Construction drawing of the concussion plate

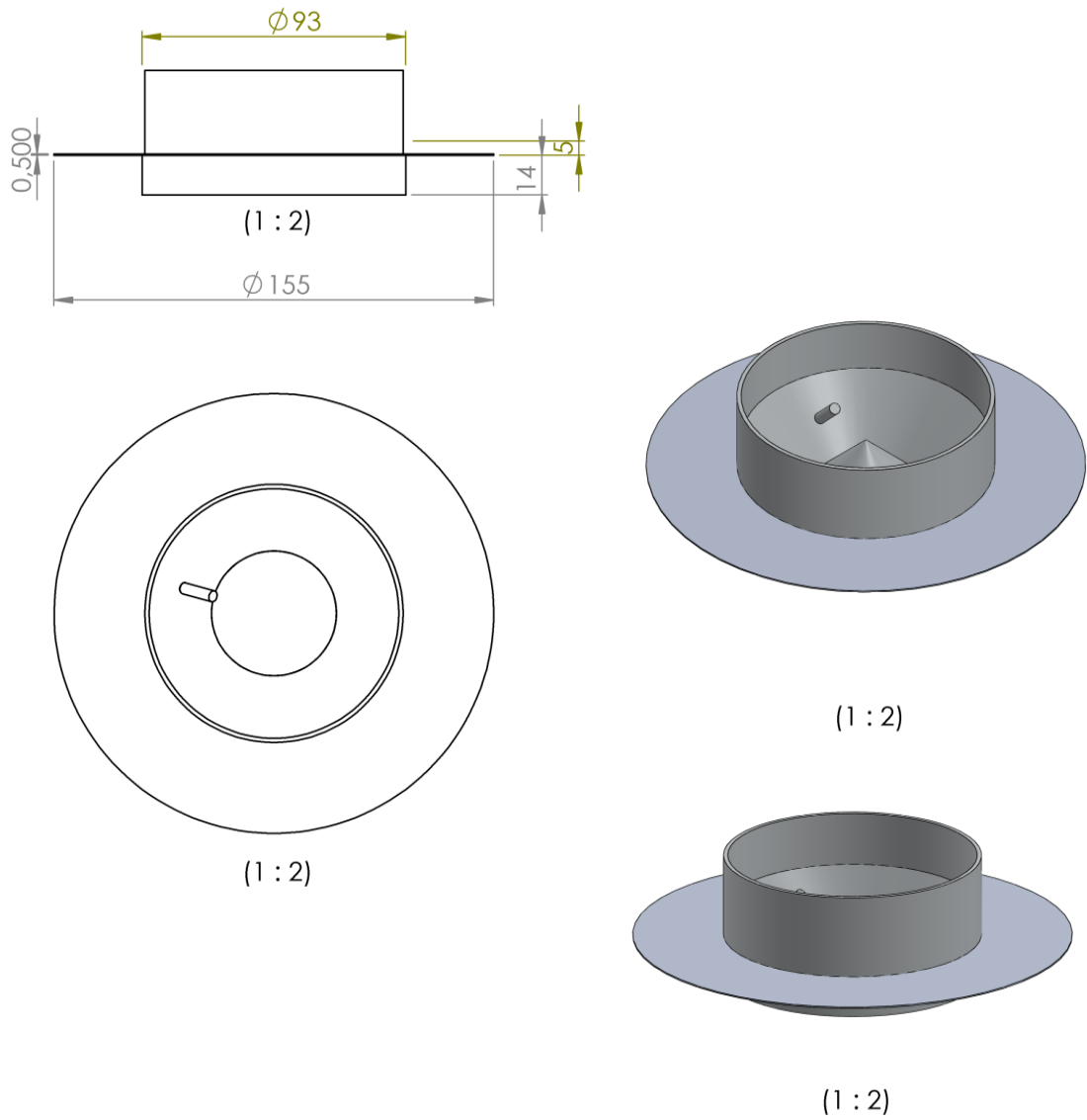


Figure 9.3: Construction drawing of the skirt

9.4. Mathematica model for concussion vessel movement

Referred to in 4.3.2, p. 104

This code describes the movement of the coating vessel inside the concussion plate in

Mathematica 6:

```

Datenspeicherung=1; (* 1=ja, 0= nein*)
(*For[i=1,i<2,i++,*)
ClearSystemCache[]
rs=46.5; (*Radius der kleinen schale 46.5 mm*)
R=62; (*Radius des Tellers mm*)
dot=1; (*Punktgröße*)
d=5; (*wie weit Schrauben hineinragen mm*)
ωR=-0.1; (*Winkelgeschwindigkeit des Tellers rad/s*)
mass=318.27; (*Masse der kleinen schale g*)
Iz=252567; (*Hauptachsenträgheitsmoment der Schale g.mm2*)
Irs=Iz+mass*rs2;
g=9810; (*Erdbeschleunigung mm/s2*)
β=π/2; (*Anstellwinkel der Schale*)
Estoss=0; (*Translationsenergie beim Schalenaufprall g.mm2/s2*)
Erot=0; (*Rotationsenergie g.mm2/s2*)
n=0; (*Schleifenzähler*)
No=3; (*Zahl der Einsätze, Standart=3 *)
dt=0.01;
U=0.15; (*Umdrehungen des Tellers*)

M0={0,rs-R}; (*Schalenmittelpunkt*)
p0={0,rs}; (*Startpunkt im Schalenkoordinatensystem*)
P0=M0+p0; (*Startpunkt im Tellerkoordinatensystem*)
S1={(R-d)*Sin[π/3],-(R-d)*Cos[π/3]}; (*Schraubenstartpunkt 1 im
Tellerkoordinatensystem*)
S2={0,R-d}; (*Schraubenstartpunkt 2 im Tellerkoordinatensystem*)
S3={-(R-d)*Sin[π/3],-(R-d)*Cos[π/3]}; (*Schraubenstartpunkt 3 im
Tellerkoordinatensystem*)
If[Datenspeicherung==1,p={}];
If[Datenspeicherung==1,m={}];

(*Rotation of dome vessel*)
Sh=S1; (*Hubeinsatz*)
Sb=S3; (*Begrenzereinsatz*)
M=M0;
P=P0;
MS=rs;
t=0;
φ=0;

While[φ>-2*π*U,

```



```

While[MS>rs,

  φrs=(R/rs)*ωR*dt;
  Π={{Cos[φrs],-Sin[φrs]},{Sin[φrs],Cos[φrs]}};
  P=M+Π.(P-M);
  φS=ωR*dt;
  Π={{Cos[φS],-Sin[φS]},{Sin[φS],Cos[φS]}};
  Sh=Π.Sh;
  If[Datenspeicherung==1,p={p,{t,P}}];
  If[Datenspeicherung==1,m={m,{t,M}}];
  t=t+dt;
  MS=Sqrt[(M-Sh).(M-Sh)];
];

(* _____ *)
(*Upward moving of dome vessel*)
MSx=-5;
While[MSx<0,
  φS=ωR*dt;
  Π={{Cos[φS],-Sin[φS]},{Sin[φS],Cos[φS]}};
  P=Π.P;
  M=Π.M;
  Sh=Π.Sh;
  If[Datenspeicherung==1,p={p,{t,P}}];
  If[Datenspeicherung==1,m={m,{t,M}}];
  MS=M-Sh;
  MSx=MS[[1]];
  MSy=MS[[2]];
  t=t+dt;
];

(* _____ *)
(*Downward rotation and falling of dome vessel*)
(*Rotationsbeschleunigung über Moment*)
M={M[[1]]*(R-rs)/Sqrt[M.M],M[[2]]*(R-rs)/Sqrt[M.M]}; (*Mittelpunktskorrektur*)
Mrad=R-rs;
L=0;
Mom= MSx*g*mass*Sin[β]; (*Moment*)
L=L+Mom*dt; (*Drehimpuls*)
ωL=-L/Irs;
tfall=0;
While[Mrad-R+rs<=0,
  Mom= MSx*g*mass*Sin[β]; (*Moment*)
  If[ MSy<=0,Mom=0]; (*Wenn der Mittelpunkt der Schale unterhalb von S liegt, wird das
Moment zu 0 *)
  L=L+Mom*dt; (*Drehimpuls*)
  ωL=-L/Irs;
  φS=ωR*dt;
  Π={{Cos[φS],-Sin[φS]},{Sin[φS],Cos[φS]}};
  φL=ωL*dt;

```

```

[]={{Cos[φL],-Sin[φL]},{Sin[φL],Cos[φL]}};
Sh=[] . Sh;
PS=P-Sh;
PM=P-M;

If[MSy>0,
  P=[] . PS+Sh;
  P=[] . P;
  Mvy1=M[[2]];
  Mv1=M;
  MS=M-Sh;
  M=[] . MS+Sh;
  M=[] . M;
  Mvy2=M[[2]];
  Mv2=M;
  vy0=(Mvy2-Mvy1)/dt;
  v=Sqrt[(Mv2-Mv1).(Mv2-Mv1)]/dt;
  ,
  tfall=tfall+dt;
  T={0,vy0-0.5*g*tfall^2};
  P=[] . PM+M;
  P=P+T*dt;
  Mv1=M;
  M=M+T*dt;
  Mv2=M;
  v=Sqrt[(Mv2-Mv1).(Mv2-Mv1)]/dt;

];
If[Datenspeicherung==1,p={p,{t,P}}];
If[Datenspeicherung==1,m={m,{t,M}}];
MS=M-Sh;
MSx=MS[[1]];
MSy=MS[[2]]; (*x und y-Wert des Schalenmittelpunktes bezogen auf die
Stipfelposition*)
Mrad=Sqrt[M.M];
t=t+dt;
If[Mrad-R+rs>=0,Break[]];
];

M={M[[1]]*(R-rs)/Sqrt[M.M],M[[2]]*(R-rs)/Sqrt[M.M]}; (*Mittelpunktskorrektur*)

φ=ωR*t;
[]φ={{Cos[φ],-Sin[φ]},{Sin[φ],Cos[φ]}};

n=n+1;
Switch[Mod[n,No],0,Sh=S1,1,Sh=S2,2,Sh=S3];
Switch[Mod[n,No],0,Sb=S3,1,Sb=S1,2,Sb=S2];
Sh=[]φ . Sh;
Sb=[]φ . Sb;

```

```

M={M[[1]]*(R-rs)/Sqrt[M.M],M[[2]]*(R-rs)/Sqrt[M.M]}; (*Mittelpunktskorrektur*)

(* _____ *)
(*Movement between S*)
ωrs=-ωL; (*Sqrt[2*Erot/Iz];*)
MS=Sqrt[(M-Sh).(M-Sh)];
MSb=Sqrt[(M-Sb).(M-Sb)];
K={M[[1]]*R/Sqrt[M.M],M[[2]]*R/Sqrt[M.M]}; (*Schalenfußpunkt*)
KM=M-K;
KMx=KM[[1]]; (*Hebel der Schlale*)
Mx=M[[1]];
L=0;

While[(Mx<0&&MS>rs)||Mx>0,
  If[MS<rs,L=0;ωrs=0]; (*Wenn Schale rechts an Schraube stößt*)
  If[MSb<rs,L=0]; (*Wenn Schale links an schraube stößt*)
  Mom= KMx*g*mass*Sin[β]; (*Moment*)
  L=L+Mom*dt; (*Drehimpuls*)
  ω=-L/Irs-ωrs; (*+ωR*R/rs*)

  φS=ωR*dt;
  φ={Cos[φS],-Sin[φS]},{Sin[φS],Cos[φS]};
  Sh=φ.Sh;
  Sb=φ.Sb;

  φS=ω*dt;
  φ={Cos[φS],-Sin[φS]},{Sin[φS],Cos[φS]};
  MP=P-M;
  P=φ.MP+M;

  φS=(-ω*rs/R+ωR)*dt;
  φ={Cos[φS],-Sin[φS]},{Sin[φS],Cos[φS]};
  M=φ.M;
  P=φ.P;

  If[Datenspeicherung==1,p={p,{t,P}}];
  If[Datenspeicherung==1,m={m,{t,M}}];
  t=t+dt;

  K={M[[1]]*R/Sqrt[M.M],M[[2]]*R/Sqrt[M.M]}; (*Schalenfußpunkt*)
  KM=M-K;
  KMx=KM[[1]]; (*Hebel der Schlale*)
  Mx=M[[1]];
  MS=Sqrt[(M-Sh).(M-Sh)];
  MSb=Sqrt[(M-Sb).(M-Sb)];
  ];
M={M[[1]]*(R-rs)/Sqrt[M.M],M[[2]]*(R-rs)/Sqrt[M.M]}; (*Mittelpunktskorrektur*)
MS=Sqrt[(M-Sh).(M-Sh)];
φ=ωR*t;

```

```

] (*End of movement loop*)

(*****)
(*Data handling and export*)
If[Datenspeicherung==1,
  p=Flatten[p];
  p=Partition[p,3];
  m=Flatten[m];
  m=Partition[m,3];
  (*Export["P_"<>ToString[rs]<>"_"<>ToString[-ωR]<>"_"<>ToString[d]<>".xls",p];
  Export["M_"<>ToString[rs]<>"_"<>ToString[-ωR]<>"_"<>ToString[d]<>".xls",m];*)

mNoTime=m[[1;;-1,2;;-1]];
pNoTime=p[[1;;-1,2;;-1]];
coordData=Transpose[{m[[1;;-1,1]],mNoTime,pNoTime}];
drawVessel[{t_,{mx_,my_},{px_,py_}}:=Module[{φ,rot},
  φ=t*ωR;
  rot={{Cos[φ],-Sin[φ]},{Sin[φ],Cos[φ]}};
  Graphics[{
    Circle[{mx,my},rs],
    Circle[{0,0},R],
    Disk[{px,py},dot],
    Line[{rot.{(R-d)*Sin[π/3],-(R-d)*Cos[π/3]},rot.{R*SIN[π/3],-R*Cos[π/3]}]},
    Line[{rot.{0,R-d},rot.{0,R}}],
    Line[{rot.{-(R-d)*Sin[π/3],-(R-d)*Cos[π/3]},rot.{-R*SIN[π/3],-R*Cos[π/3]}]}
  ]}
]]

ListAnimate[drawVessel/@coordData[[1;;-1;;5]]]
Export["Vesselanimation.avi",drawVessel/@coordData[[1;;-1;;20]]]
ListPlot[m[[1;;-1,{2,3}]],Joined->True]
ListPlot[p[[1;;-1,{2,3}]],Joined->True]
ClearSystemCache[]

Vessel impact velocity

ωmin=1; (*integer*)
ωmax=60; (*integer*)
ωRstep=0.1;
vel={Ω};
dmin=1; (*integer*)
dmax=10; (*integer*)
For[i=dmin,i≤dmax,i++, (*insert first row*)
  vel={vel,"d"<>ToString[i]}]
For[j=ωmin,j≤ωmax,j++, (*ω-loop*)
  vel={vel,ωRstep*j};
  For[i=dmin,i≤dmax,i++, (*d-loop*)
    ClearSystemCache[];
    rs=46.5; (*Radius der kleinen schale 46.5 mm*)
    R=62; (*Radius des Tellers mm*)
    dot=1; (*Punktgröße*)

```

```

d=i; (*wie weit Schrauben hineinragen mm*)
ωR=-ωRstep*j; (*Winkelgeschwindigkeit des Tellers rad/s*)
mass=318.27; (*Masse der kleinen schale g*)
Iz=252567; (*Hauptachsenträgheitsmoment der Schale g.mm2*)
Irs=Iz+mass*rs2;
g=9810; (*Erdbeschleunigung mm/s2*)
β=π/2; (*Anstellwinkel der Schale*)
Estoss=0; (*Translationsenergie beim Schalenaufprall g.mm2/s2*)
Erot=0; (*Rotationsenergie g.mm2/s2*)
n=0; (*Schleifenzähler*)
No=3; (*Zahl der Einsätze, Standart=3 *)
dt=0.0001;

M0={0,rs-R}; (*Schalenmittelpunkt*)
p0={0,rs}; (*Startpunkt im Schalenkoordinatensystem*)
P0=M0+p0; (*Startpunkt im Tellerkoordinatensystem*)
Sh={(R-d)*Sin[π/3],-(R-d)*Cos[π/3]}; (*Schraubenstartpunkt 1 im
Tellerkoordinatensystem*)

(*Rotation of dome vessel*)
M=M0;
P=P0;
MS=rs;
t=0;
φ=0;

While[MS≥rs,

φrs=(R/rs)*ωR*dt;
□={{Cos[φrs],-Sin[φrs]},{Sin[φrs],Cos[φrs]}};
P=M+□.(P-M);
φS=ωR*dt;
□={{Cos[φS],-Sin[φS]},{Sin[φS],Cos[φS]}};
Sh=□.Sh;
t=t+dt;
MS=Sqrt[(M-Sh).(M-Sh)];
];

(* _____ *)
(*Upward moving of dome vessel*)
MSx=-5;
While[MSx<0,
φS=ωR*dt;
□={{Cos[φS],-Sin[φS]},{Sin[φS],Cos[φS]}};
P=□.P;
M=□.M;
Sh=□.Sh;
MS=M-Sh;
MSx=MS[[1]];

```

```

MSy=MS[[2]];
t=t+dt;
Mtest=M;
];

(*
-----*)
(*Downward rotation and falling of dome vessel*)
(*Rotationsbeschleunigung über Moment*)
M={M[[1]]*(R-rs)/Sqrt[M.M],M[[2]]*(R-rs)/Sqrt[M.M]}; (*Mittelpunktskorrektur*)
Mrad=R-rs;
L=0;
Mom= MSx*g*mass*Sin[β]; (*Moment*)
L=L+Mom*dt; (*Drehimpuls*)
ωL=-L/Irs;
tfall=0;
While[Mrad-R+rs≤0,
  Mom= MSx*g*mass*Sin[β]; (*Moment*)
  If[MSy≤0,Mom=0]; (*Wenn der Mittelpunkt der Schale unterhalb von S liegt, wird
das Moment zu 0 *)
  L=L+Mom*dt; (*Drehimpuls*)
  ωL=-L/Irs;
  φS=ωR*dt;
  R={{Cos[φS],-Sin[φS]},{Sin[φS],Cos[φS]}};
  φL=ωL*dt;
  R={{Cos[φL],-Sin[φL]},{Sin[φL],Cos[φL]}};
  Sh=R.Sh;
  PS=P-Sh;
  PM=P-M;

  If[MSy>0,
    P=R.PS+Sh;
    P=R.P;
    Mvy1=M[[2]];
    Mv1=M;
    MS=M-Sh;
    M=R.MS+Sh;
    M=R.M;
    Mvy2=M[[2]];
    Mv2=M;
    vy0=(Mvy2-Mvy1)/dt;
    vvec=(Mv2-Mv1)/dt; (*vektorielle Geschwindigkeit beim Auftreffen*)
    v=Sqrt[(Mv2-Mv1).(Mv2-Mv1)]/dt; (*Betrag der Auftreffgeschwindigkeit*)
    vrad=vvec.M/(R-rs); (*radiale Gescheindigkeit beim Auftreffen*)
  ,
  tfall=tfall+dt;
  T={0,vy0-0.5*g*tfall^2};
  P=R.PM+M;
  P=P+T*dt;
  Mv1=M;
  M=M+T*dt;

```

```

Mv2=M;
vvec=(Mv2-Mv1)/dt; (*vektorielle Geschwindigkeit beim Auftreffen*)
v=Sqrt[(Mv2-Mv1).(Mv2-Mv1)]/dt; (*Betrag der Auftreffgeschwindigkeit*)
vrad=vvec.M/(R-rs); (*radiale Gescheindigkeit beim Auftreffen*)

];
MS=M-Sh;
MSx=MS[[1]];
MSy=MS[[2]]; (*x und y-Wert des Schalenmittelpunktes bezogen auf die
Stipfelposition*)
Mrad=Sqrt[M.M];
t=t+dt;
If[Mrad-R+rs>=0,Break[]];
];

M={M[[1]]*(R-rs)/Sqrt[M.M],M[[2]]*(R-rs)/Sqrt[M.M]}; (*Mittelpunktskorrektur*)
vel={vel,vrad};
Print[t," ",v," ",vrad];
]];
vel=Flatten[vel];
vel=Partition[vel,i];
(*vel=Transpose[vel];*)
Export["Vessel_Velocity.xls",vel];

```

9.5.Sputter rates of different configurations

Referred to in section 4.3.7, p. 117

The following table shows some examples of sputter rates of different materials at different parameters with different apparatus geometries. In the old apparatus the vessels are arranged as shown in Figure 4.10, whereas the new apparatus setup had just one single vessel in the centre of the vacuum chamber with the sputter sources tilted towards it.

Material	Apparatus	Target size	Parameters	Power (W)	Ar base pressure (Pa)	Rate (nm/s)
Cu	old	2 inch	DC	200	0.5	1.720
Pt	old	2 inch	DC	200	0.5	2.265
Ru ^{*)}	old	2 inch	DC	200	0.5	1.989
TiO ₂	new	4 inch	5 kHz, 4 μs	800	0.5	0.408
TiO ₂	old	10 cm	5 kHz, 4 μs	400	1.5	0.470
Ti	old	10 cm	DC	400	0.5	0.625
Ti	old	2 inch	DC	200	0.5	0.705
Ti	new	4 inch	DC	660	0.5	0.420
Ti	new	2 inch	DC	180	0.5	0.404
Ru	new	2 inch	DC	200	0.5	0.286
RuO _x	new	2 inch	DC	200	0.5	0.351

Table 9.1: Sputter rates in the coating vessel for different parameters

*) Calculated, since Ru films on plane substrate for rate determination with the profilometer always popped off the substrate.

Curriculum vitae

My name is Gerwin Holger Stefan Schmid and I was born in Vienna on 18th of December in the year of 1981. After visiting primary and grammar school I did my military service, before starting the academic studies of Physics at the Vienna University of Technology in 2001. I graduated in 2009 with the degree of Dipl.-Ing.. In the last two years of my study and one year after my degree I worked as a laboratory and later scientific assistant in the *Advanced Materials and Aerospace Technologies* group at *Austrian Institute of Technology* in *Seibersdorf*. After that in the year 2010 I started in the business area of *Sustainable Thermal Energy Systems* in the *Energy Department* of the *Austrian Institute of Technology* in Vienna. Along with that job I began my PhD thesis in the year 2011, which I hope to finish with the present work.

Selected publications:

G. Schmid, C. Eisenmenger-Sittner, J. Hell, M. Horkel, M. Keding and H. Mahr, *Optimization of a container design for depositing uniform metal coatings on glass microspheres by magnetron sputtering*, *Surface & Coatings Technology* 205, pp. 1929-1936, 2010.

G. Schmid and C. Eisenmenger-Sittner, *A method for uniformly coating powdery substrates by magnetron sputtering*, *Surface & Coatings Technology* 236, pp. 353-360, 2013.

G. Schmid, C. Eisenmenger-Sittner, J. Hell and M. Quirchmair, *Vorrichtung zum Beschichten eines Substrates aus Teilchen*. Vienna, Austria Patent patent number WO 2014/043728 A1, 13 September 2013.

G. Schmid, Ch. Reichl, P. Benovsky, Th. Fleckl, G. Pauschenwein, M. Monsberger - *Optische und CFD-gestützte Untersuchung von Ammoniak-Blasenströmungen in Ammoniakwasserlösung zur Entwicklung eines Mikrokanalabsorbers*, *Deutsche Kälte-Klimatagung 2011*, Aachen, November 2011

G. Schmid, Ch. Reichl, T. Fleckl, W. Pink, Ch. Halmdienst, *Optisch- und CFD-gestützte Entwicklung eines Ammoniak-Kanalabsorbers*, *Deutsche Kälte-Klimatagung 2013*, Hannover, November 20ter – 22ter 2013